NON-LINEAR FINITE ELEMENT DYNAMIC ANALYSIS OF TAPERED HOLLOW STEEL POLES FOR PASSIVE BASE ISOLATION

by

TRI LE

Presented to the Faculty of the Graduate School of

The University of Texas at Arlington in Partial Fulfillment

of the Requirements

for the Degree of

DOCTOR OF PHILOSOPHY

THE UNIVERSITY OF TEXAS AT ARLINGTON

May 2008

Copyright © by Tri Le 2008

All Rights Reserved

ACKNOWLEDGEMENTS

I would like to express my sincere gratitude to Dr. Ali Abolmaali, the author's supervising professor, for his continual help and guidance throughout this study. The valuable suggestions made by the members of the supervising committee including Dr. John H. Matthys, Dr. Guillermo Ramirez, Dr. Nur Yazdani, Dr. Frank Lu, and Dr. Shih-Ho Chao are most appreciated and gratefully acknowledged.

A special and warm personal acknowledgement is due to the former chairman, Dr Sia Aderkani, and the chairman, Dr. Nur Yazdani, of the Department of Civil Engineering at the University of Texas at Arlington, for their unrestricted personal counsel during the entire period of the study. Sincere and personal thanks are extended to Raul Fernandez and Farhad Kamangar for their invaluable assistance during the entire experimental phase of the research program. Thanks are also due to Lewis Crow for assisting with his valuable electronics expertise. I also express my gratitude to all my office colleagues.

I would like to express my sincere gratitude to the Texas Department of Transportation (TxDOT) for their financial support throughout this project. In addition, I am thankful to the TxDOT Traffic Control Divisions in Fort Worth, Amarillo, and Dallas for providing locations and bucket trucks for the instrumentation and camera installation.

The last but not the least is the encouragement from my parents, my aunt family, and brother for their devotion, patience, support, and endless love.

March 28, 2008

ABSTRACT

NON-LINEAR FINITE ELEMENT DYNAMIC ANALYSIS

OF TAPERED HOLLOW STEEL POLES FOR

PASSIVE BASE ISOLATION

Tri Le, Ph.D.

The University of Texas at Arlington, 2008

Supervising Professor: Ali Abolmaali

Long tapered poles are commonly used to support Closed Circuit Television (CCTV) Cameras for security and traffic monitoring. Images received from CCTV are normally distorted depending on the wind induced vibration characteristics of the forcing function. To reduce image distortion, three approaches are integrated to optimize the process, which are: (1) development of equations for pole's frequency of vibration in terms of its geometric variables; (2) development of a mechanical damping device to isolate the pole's vibration from that of the camera; and (3) development of an electrical image processing device for image corrections.

The identification of a pole's natural frequency of long tapered hollow steel poles is the most important parameter in the design and calibration of the mechanical damping device. Thus, three-dimensional finite element model analyses, which take

into account the couplings between material, contact and geometric nonlinearities are developed to determine the natural frequency equations for poles commonly used by Texas Department of Transportation (TxDOT) in terms of their geometric variables. A sensitivity study is performed to study the effect of different geometric parameters on the overall natural frequency of the pole. Using the results from the parametric study, empirical formulae between the geometric parameters and the first, second, and third mode natural frequencies for the long tapered hollow steel poles are obtained. Cyclic loading was applied to the model to study the energy dissipation of the pole. In order to verify the Finite Element analysis, data collected from the accelerometers installed on the poles are adopted and analyzed. Natural frequency envelope obtains by varying the pole geometry provided by TxDOT for mechanical isolator device design.

A biaxial mechanical isolator device is developed, specifically aimed at horizontal high-frequency motion abatement in pole-mounted camera applications and similarly conditioned supports. The device works on the principle of force and displacement transmissibility reduction via the use of a lightly damped spring interface with a tuned natural frequency. The isolator is inserted between the top of the structure (pole) and the seat of the camera, and operates by rejecting undesirable high-frequency modal vibrations experienced by the main support; this has the effect of diminishing high-acceleration ground inputs which are principally responsible for image distortion. By design, the isolator trades its high-frequency performance for a low-frequency heave, which does not induce blur but causes limited horizon shift. The developed mechanical device is designed to reduce significantly the high pole vibration

frequencies experienced by the camera. Also the digital algorithm for image stabilization is developed, which is highly effective for low-frequency vibration. For this reason, the proposed mechanical solution is prescribed as an ancillary technique to image processing in installations where high-frequency or displacement conditions prevail at the camera support. Together with the mechanical approach to stabilize the images, image processing is also performed to provide the best stabilized images.

Finally, a test-bed is developed and implemented to perform experiments and analyze the speed and efficiency of different image stabilization algorithms. This algorithm is being integrated with the mechanical device to optimize the vibration reduction process.

TABLE OF CONTENTS

ACKNOWLEDGEMENTS..... iii

ABSTRACT iv

LIST OF ILLUSTRATIONS..... xi

LIST OF TABLES..... xv

Chapter

1. INTRODUCTION…….. 1

1.1 Introduction……..... 1

1.2 Literature Review…… 8

1.2.1 Tapered Hollow Steel Pole …… 8

1.2.2 Bolt Connection…… 11

1.2.3 Damping Device…… 20

1.3 Goals and Objectives …… 22

2. FINITE ELEMENT ANALYSIS ……..... 24

2.1 Introduction……..... 24

2.2 Development of Finite Element Model ……. 26

2.2.1 Symmetric Modeling…… 26

2.2.2 Pre-tension Load …… 27

2.2.3 Contact Modeling …… 30

2.2.4 Material Model …… 33

2.2.5 Yield Criteria 36

2.2.6 Geometric Nonlinearity 38

2.2.7 Numerical Analyses 38

2.3 Model Verification 42

2.4 Eigen Solution and Mode Shapes 46

2.4.1 Lanczos Eigensolver 46

2.4.2 Automatic Multi-level Substructuring (AMS) Eigensolver … 47

2.4.3 Subspace Iteration Method 47

3. PARAMETRIC STUDY 49

3.1 Introduction..... 49

3.2 Selection of Test Cases 50

3.3 Development of the Frequency Equations 55

3.3.1 Basis of Regression Analysis 55

3.3.2 Equations of Pole's Natural Frequency 60

3.4 Comparison Between Predicted
and Experimental Vibrational Frequencies 63

4. ENNERGY DISSIPATION CHARACTERISTIC OF POLES..... 67

4.1 Introduction..... 67

4.2 Material Model 70

4.2.1 Elastic Response 70

4.2.2 Plasticity Theories 72

4.2.3 Stress-strain Relationship 73

4.3 Loading Protocol 74

4.4 Result Discussion 79

5. DEVELOPMENT OF MECHANICAL VIBRATION ISOLATOR 83

5.1 Introduction..... 83

5.2 Theoretical Isolator Design 84

5.3 Practical Isolator Design 87

5.4 Isolator Operational Envelopes 91

5.5 Mechanical Configuration 96

5.6 Prototype Implementation and Test 99

5.7 Lab Testing 102

5.8 Field Testing 103

6. ELECTRONIC IMAGE STABILIZATION FOR TRAFFIC CAMERAS 112

6.1 Introduction..... 112

6.2 Program Algorithm..... 113

6.2.1 Image Stabilization for Traffic Cameras 113

6.2.2 Blocks (Sub-images)..... 114

6.2.3 Target Selection 115

6.2.4 Target Tracking 120

6.2.5 Estimation of Global Motion 121

6.2.6 Motion Compensation 124

7. SUMMARY, CONCLUSIONS, AND RECOMMENDATIONS.....128

7.1 Summary..... 128

7.2 Conclusions……..... 130

7.3 Recommendations……..... 132

Appendix

A. CIRCULAR POLES 134

B. OCTAGONAL POLES 181

C. NATURAL FREQUENCY SENSITIVITY STUDIES
OF CIRCULAR AND OCTAGONAL POLES 216

D. HYSTERESIS PLOT 229

E. IMAGES CORRECTION OF MECHANICAL DEVICE 247

F. IMAGES CORRECTION OF ELECTRICAL DEVICE..... 282

REFERENCES 285

BIOGRAPHICAL INFORMATION..... 293

LIST OF ILLUSTRATIONS

Figure Page

1.1 Typical CCTV camera pole 2

1.2 A typical traffic monitoring center at Florida Highway Traffic Control Center 2

1.3 Traffic video snap shot at low vibration frequency of the pole 3

1.4 Traffic video snap shot at intermediate vibration frequency of the pole 3

1.5 Traffic video snap shot at high vibration frequency of the pole 4

1.6 Typical pole geometric parameters (a) General parameter; (b) Section A-A; (c) Section B-B 5

1.7 Typical mode shapes of 60 ft pole 6

1.8 Schematic and photograph of the device with light ballast 7

1.9 Block diagram of the image stabilization program 7

1.10 Summary of the procedure to accomplish the goal of the study 23

2.1 Typical 3-D models of circular and octagonal poles 28

2.2 Bolt model used in analysis; (a) 3-D bolt model, (b) 3-D bolt model with triangular mesh 29

2.3 Pre-tension load and section 30

2.4 Contact interactions between two surfaces; (a) beginning of step, (b) middle step, (c) end of step. 32

2.5 Nonlinear stress-strain relationships 34

2.6 Newton-Raphson nonlinear schemes 35

2.7 Different mesh densities for H-convergence study;
(a) mesh size 1.25 in., (b) mesh size 0.75 in.,
(c) mesh size 0.5 in., (d) mesh size 0.3125 in.,
(e) mesh size 0.25 in., (f) mesh size 0.2075 in. 40

2.8 Typical mode shapes 41

2.9 Model verification 42

2.10 Convergence study for obtaining the optimum mesh density 43

2.11 Test set up and accelerometers used in the experiments 44

2.12 Comparison between field testing and FEM results 45

2.13 Comparison of the mode shape obtained
from the finite element model analysis
in this study and theoretical solution (Jacobsen-Ayre)
for a typical pole with fixed support 46

3.1 Pole end-plate 52

3.2 Sensitivity analyses for the first mode of octagonal pole
with the changing in: (a) Length, (b) Pole diameter at bottom,
(c) Clearance distance, (d) Plate dimension. 62

3.3 Comparison between predicted and FEM result 64

4.1 The schematic of displacement control of cyclic study 79

4.2 Typical 3-D model of pole end-plate 79

4.3 The Bauschinger effect 71

4.4 Stress-strain hardening curve of material 74

4.5 Loading protocol (AISC 2002) 76

4.6 Loading protocol for 40 ft pole 76

4.7 Loading protocol for 45 ft pole 77

4.8 Loading protocol for 50 ft pole 77

4.9 Loading protocol for 55 ft pole 78

4.10 Loading protocol for 60 ft pole 78

4.11 Dissipated energy vs. pole height 81

4.12 Dissipated energy vs. pole thickness 81

4.13 Dissipated energy vs. bolt diameter 82

4.14 Dissipated energy vs. end-plate thickness 82

5.1 Passive mechanical isolation 84

5.2 Non-dimensional isolation performances 86

5.3 Side view of typical CCTV camera for aerodynamic loading estimates 89

5.4 Wind speed vs. deflection characteristics for case study 91

5.5 Wind speed vs. spring-mass assuming 50% transmissibility for different pole frequencies 92

5.6 Wind speed vs. spring-mass assuming 1.8 Hz pole frequency for different transmissibility ratios 93

5.7 Transmissibility ratios vs. spring-mass assuming 1.8 Hz pole frequency for different wind speeds 94

5.8 Transmissibility ratios vs. spring-mass assuming 4.7 Hz pole frequency for different wind speeds 95

5.9 Transmissibility ratios vs. spring-mass assuming 4.7 Hz pole frequency for different wind speeds 96

5.10 Pigtail connector for typical CCTV cameras 97

5.11 XY table with parallel slides and center clearance 98

5.12 Exploded CAD view of main components in a pole-mounted passive isolator design 99

5.13 Test set up for the mechanical device testing at ARRI laboratory; (a) PC-based data acquisition & control hardware, (b) Close view of the test setup at ARRI Laboratory 102

5.14 Field instrumentation in Fort Worth; (a) Rosedale-I35W, (b) Loop 280-I35W 104

5.15 Field instrumentation in Amarillo; (a) Soncy-I40W, (b) Bell-I40W 105

5.16 Field instrumentation in Dallas (Hampton-I20 East) 106

5.17 Tri-Axis serial accelerometer 106

5.18 Installation of accelerometers on the poles and cameras; (a) in Fort Worth, (b) in Amarillo 107

5.19 Field measurements; (a) Accelerometers installed on the pole and camera in Dallas, (b) Mechanical device installed on the pole in Fort Worth 108

5.20 Field measurements; (a) Mechanical device installed on the pole in Amarillo, (b) Mechanical device installed on the pole in Dallas 109

5.21 Data analysis of the pole at Rosedale-I35W, Fort Worth; (a) acceleration result, (b) vibrational frequency result. 111

6.1 Block diagram of the image stabilization system 113

6.2 Image sequence with selected blocks 115

6.3 Selected target in block j and frame i 116

6.4 Selected targets with largest possible block 117

6.5 Selected targets at the center of each block 118

6.6 Selected targets with maximum standard deviation in each block 119

6.7 Selected targets with maximum entropy in each block 120

LIST OF TABLES

Table Page

2.1 Element Types and Corresponding Element Number 25

2.2 Contact Property for the Model 32

2.3 Material Properties for Steel Poles Used in Analysis 33

2.4 The First Three Natural Frequencies for the Long Tapered Hollow Steel Pole With/Without Geometric Nonlinearity (Hz) 41

3.1 Pre-tension Load Was Used 52

3.2 Independent Parameters Used for Circular Steel Poles 53

3.3 Independent Parameters Used for Octagonal Steel Poles 54

3.4 Error Comparisons Between the Predicted and the FEM Results of Circular Poles 64

3.5 Error Comparisons Between the Predicted and the FEM Results of Octagonal Poles 66

4.1 Independent Parameters of Circular Steel Poles Used for Cyclic Study 68

4.2 Result of Hysteresis Analysis 80

CHAPTER 1

INTRODUCTION

1.1 Introduction

Closed Circuit Television (CCTV) cameras are used to transmit video signals to the monitoring center. The CCTV camera is often used in security sensitive areas such as traffic controls, banks, casinos, airports, or military installations.

Many cities and motorway networks have extensive traffic-monitoring systems, using CCTV to detect congestion and notice accidents. The CCTV camera system can obtain real-time live images of ongoing traffic.

The CCTV camera pole used in traffic monitoring systems has three important structural features: a long tapered pole, a camera installed on the top of the pole, and the connection of the pole to its foundation, as shown in Figure 1.1.

Generally, the images received from the cameras are distorted because of the pole's vibration due to the applied wind load. The image distortion is characterized by the pole's vibration frequency; the higher the frequency of the pole vibration, the more distortion of the images. Distorted images transmitted to the transportation control rooms (Figure 1.2) reduce the efficiency of traffic monitoring.

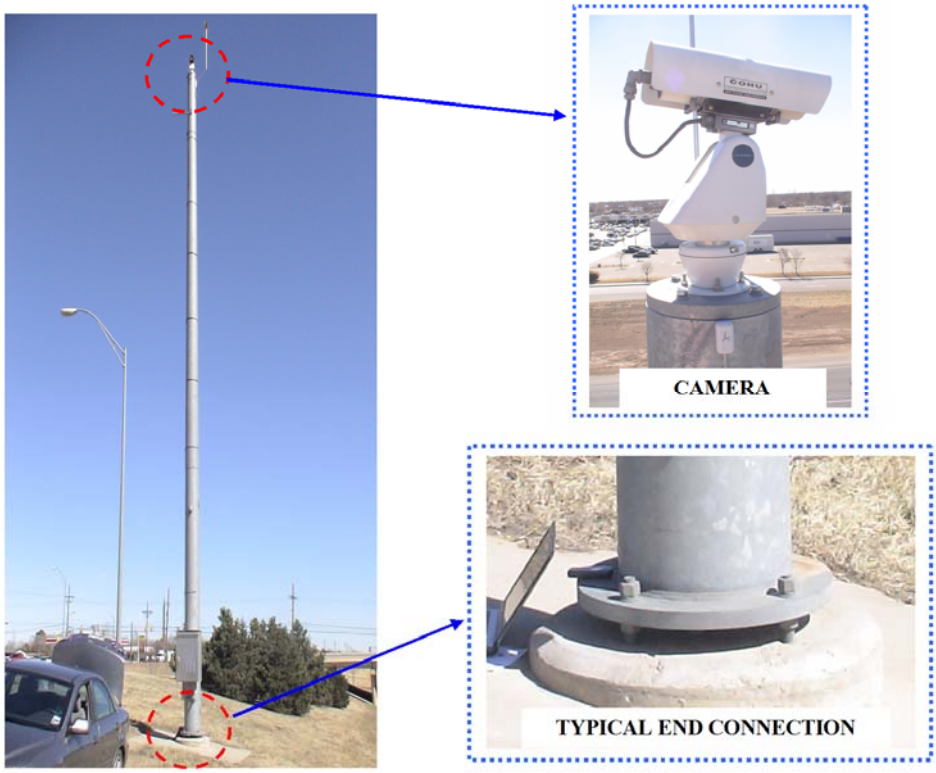

Figure 1.1 Typical CCTV camera pole.

Figure 1.2 A typical traffic monitoring center at
Florida Highway Traffic Control Center.

Figures 1.3, 1.4, and 1.5 show typical distorted images obtained from traffic monitoring centers.

Figure 1.3 Traffic video snapshot at low vibration frequency of the pole.

Figure 1.4 Traffic video snapshot at intermediate vibration frequency of the pole.

Figure 1.5 Traffic video snapshot at high vibration frequency of the pole.

The image distortion is directly related to the pole's dynamic vibration characteristics. This means that, in order to develop a device which will be placed between the camera and the pole, the natural vibration frequencies of the pole need to be studied. The natural vibration frequencies of the poles depend on the pole's geometric parameters such as: height, thickness, base diameter, top diameter, and the parameter defining the pole's connection assembly to the base foundation, as shown in Figure 1.6.

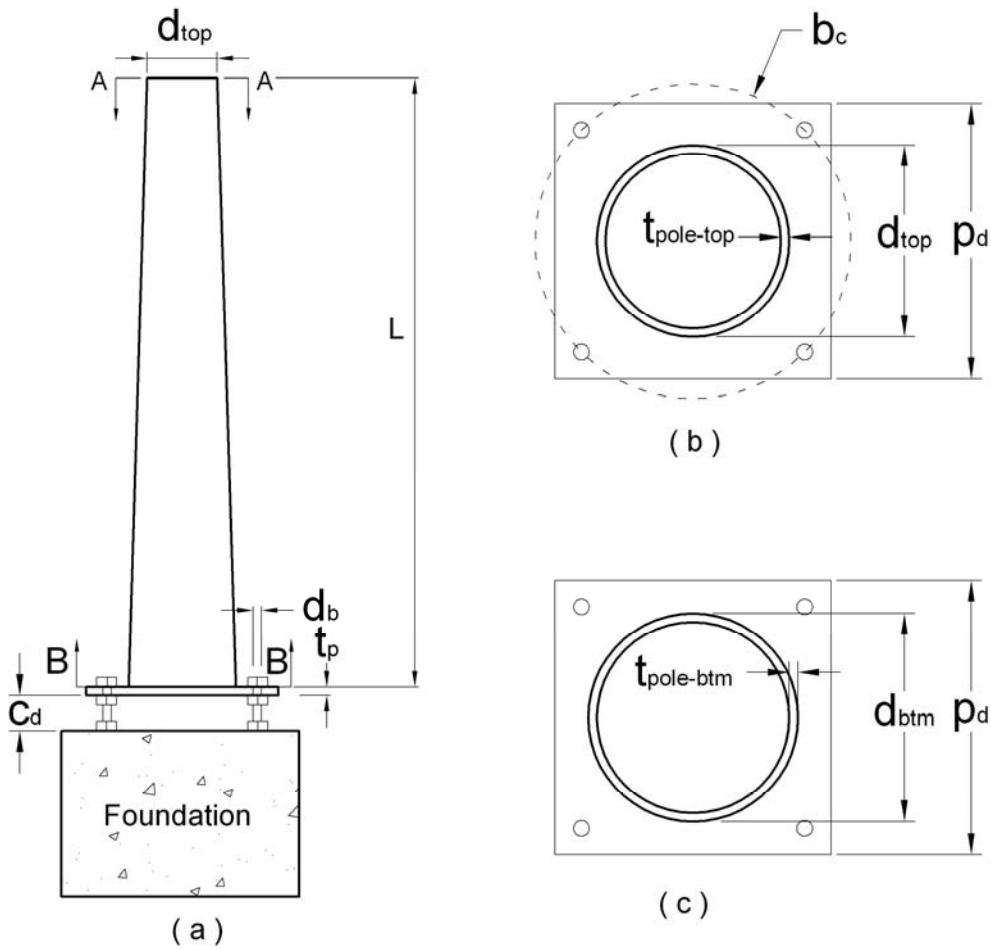

Figure 1.6 Typical pole geometric parameters (a) General parameter; (b) Section A-A; (c) Section B-B.

The classical solution for the frequency of vibration with fixed support was reported by Jacobsen and Ayre, 1958. However, the analysis of tapered poles considering the flexibility of the connection assembly is not an easy task. Indeed, this is identical to the classical problem of the beam-to-column connection where the connection is defined as “semi-rigid”. Traditionally, experimental testing and Finite Element Analysis (FEA) are employed to consider the effects of semi-rigidity into analysis (Abolmaali et al., 2003; and Abolmaali et al., 2005).

In this project, both experimental and finite element analyses (FEA) are employed to develop equations for the natural frequencies of the poles. The finite element model that was developed and verified in TxDOT Project 0-4470 (Jung et al., 2006; and Jung, 2005) was further refined for the study.

The developed model was used to conduct frequency analysis on all the poles with all the possible combinations of geometric variables (80 cases). Figure 1.7 shows typical FEA results from the frequency analysis.

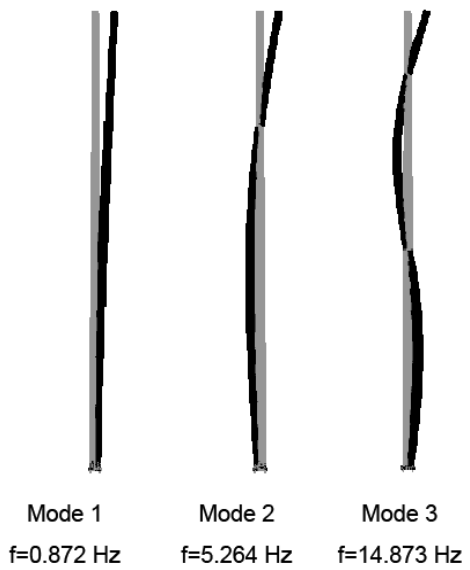

Figure 1.7 Typical mode shapes of 60 ft pole.

The obtained frequency of vibrations was categorized based on different pole sizes. This information was used to develop a mechanical device to be placed between the pole and the camera to eliminate the camera's vibration which led to image distortion. Figure 1.8 shows the schematic and photograph of this device.

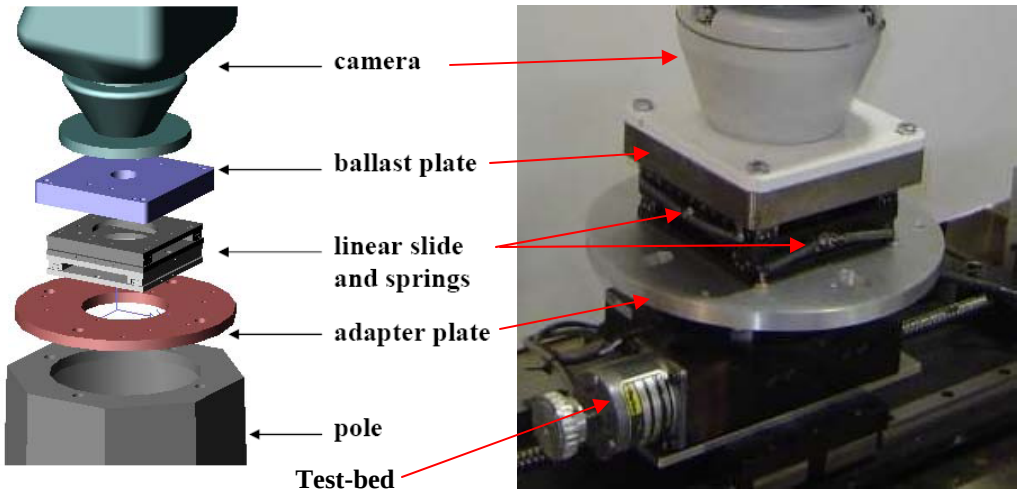

Figure 1.8 Schematic and photograph of the device with light ballast.

Also, an electrical algorithm was developed to remove the unwanted motion (jitter) from the image sequence. The image stabilization program is a Matlab program which can stabilize an input video sequence and display the resulting video. The input video can be selected from a live camera or it may be read from a video file. The algorithm is shown in Figure 1.9.

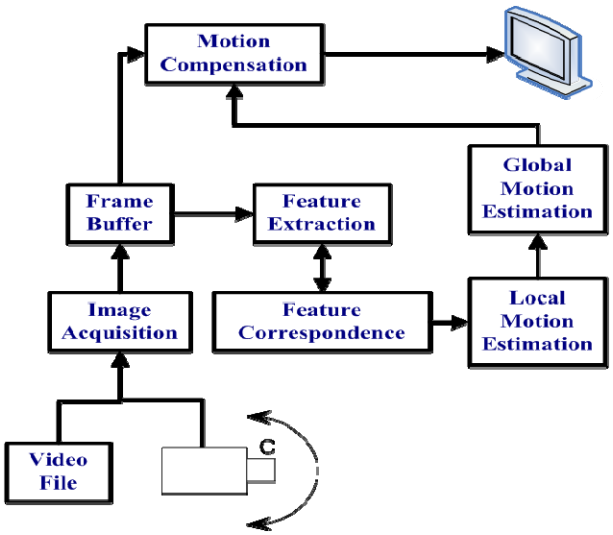

Figure 1.9 Block diagram of the image stabilization program.

1.2 Literature Review

The following is the literature review of the tapered hollow steel pole; natural frequency, bolt connection, and mechanical damping device performed by many researchers.

1.2.1 Tapered Hollow Steel Pole

The information in literature with regard to the dynamic characteristics of the long tapered hollow steel poles is limited. However, there are some codes, reports and publications (Pagnini and Solari, 2001; and Caracoglia and Jones, 2005) regarding the dynamic behaviors of road signs, signals and light poles. But there has not been any essential work done over poles containing CCTV cameras in any literature and the specific requirements on dynamic behaviors of CCTV poles are not documented (Jung et al., 2006). A commonly used tapered pole's height may vary from 20 ft (6.1 m) to 65 ft (19.8 m) depending on the applications, which in turn cause variation of other parameters such as base diameter, top diameter, pole thickness, base plate thickness, and bolt diameter. Also, wind loads vary in different regions and seasons, and the vibrations caused by vehicle traffic affect the pole's deflection and ultimately the images transmitted by the cameras. Thus, prior to the study by Jung et al. (2006), the lack of generalized equations for stiffness and strength of the CCTV poles as the functions of their geometric variables was under scrutiny (Abolmaali et al., 2003). Cameras currently in use are supported by wood, concrete, and steel, while recently fiber-reinforced plastic (FRP) poles have gained wide popularity (Lacoursiere, 1999). State departments of transportation, including the Texas Department of Transportation,

generally use tapered steel poles most often on or near the vicinity of bridge structures (Jung et al., 2006). The California Department of Transportation has recently installed several FRP poles on bridges at different locations (www.dot.ca.gov).

Several investigations on the steel and FRP poles have been performed to predict their load-deflection behavior. Single-pole transmission structures made of wood were studied by Vanderbilt and Criswell (1988). The analysis of the transmission poles utilized Newmark numerical technique to provide the exact solution to the differential equation for large deflections. A computer program was developed for the design and analysis of wood poles. Design equations based on the load resistance factor design (LRFD) format were presented.

Lin (1995) investigated the linear static analysis of tapered FRP poles in terms of various material configurations, geometries, loading condition and boundary conditions. Large deflection analysis was also performed by the finite element model presented. In the linear static analysis, shear strains were not very significant if the pole was in bending, and the layer with the longitudinal fiber orientation would resist most of the load. This study found that the greater the taper ratio, the better the performance was in the practical range. Fibers oriented at an angle (0 to 45 degrees) with respect to the longitudinal direction resulted in economic design.

Kocer and Arora (1996, 1997) developed an optimal design process for steel transmission poles. The geometric properties such as outside diameter at the top of the pole, the thickness of the first and the second piece, and the tapering of the pole were used for design variables. To conduct the design process, the design moment,

compressive stress, bending stress, shear stress, and the deflection were calculated. It was concluded that as the pole tapering increased, other design variables decreased for the optimal design. This study also developed optimal design methods for standardization of steel poles which was developed by discretizing the design variables such as geometric dimensions of the poles, cross-sectional shape, material properties and steel grade, for the pole structure.

Dicleli (1997) investigated the optimum design of steel pole structures. Simple equations and charts for the design of tubular telescopic steel poles of various steel grades and lengths were automatically obtained by the developed program. The pole structures were considered to be subjected to concentrated loads and moments. The program used the unit dummy load method to determine the displacements of the structures.

Polyzois et al. (1998) investigated the dynamic analysis of tapered composite poles with hollow circular cross-section produced by the filament wound technique. The natural frequencies were performed by modal analysis. An analytical model was developed with tapered beam elements including shear effects, which showed good correlation with the finite element results.

Polyzois et al. (1999) presented the results of twelve glass fiber-reinforced plastic poles with various thickness and fiber orientations under cantilever loading. The objective of their study was to compare the analytical results obtained in the study to those of experiments in order to design a series of FRP poles with different safety factors. Modulus of elasticity, Poisson's ratio and shear modulus were calculated by the

rule of mixture (Daniel and Ishai, 2005) and Tsai-Hahn approach. The correlation between the analytical and experimental results was reasonable. It was concluded that a lower factor of safety of 4 can be used for the design of FRP poles.

Ovalization behavior of tapered fiber-reinforced polymer (FRP) poles was presented by Ibrahim and Polyzois (1999). The parameters used in this study were wall thickness and fiber angle. Brazier's modified equation was used to account for the orthotropic properties of FRP poles. This study concluded that the behavior of the FRP poles was non-linear and the critical ovalization load decreased with an increase in the fiber angle.

As a continuation of the work by Polyzois et al. (1999), Ibrahim et al. (2000) conducted twelve full-scale tests on tapered glass fiber-reinforced plastic (GFRP) poles with hollow circular cross section subjected to cantilever bending. The specimens were made of polyester resin reinforced with E-glass fibers by the filament winding process. Theoretical models developed for evaluating the ultimate load were used to determine the optimal cross section of the poles. Fiber orientation and the number of layers were included in the parametric study.

1.2.2 Bolt Connection

For dealing with the dynamic finite element analysis (FEA) of the pole, the role of the bolted connection assembly which supports the pole to the concrete base is considered. Even though using the dynamic (or cyclic) FEA of bolted connection are less noticed in existing literatures concerning the dynamic behaviors of the pole, there are many literatures reported on the static FEA of steel connections.

Early studies by Krishnamurthy et al. (1979) and Krishnamurthy (1980) presented the finite element modeling of bolted connections with varying geometric parameters, support conditions, loading sequence, and material properties. They also compared the results obtained from both 2- and 3-dimensional models.

Krishnamurthy (1981) developed the finite element methodology, specifically for the analysis of unstiffened, four bolt extended end-plate connections. Based on FEA of a large number of geometric configurations of the connection along with a series of experimental tests, the design methodology was developed, which can be found in the 8th edition of the AISC (1980). Krishnamurthy's theoretical result clearly showed that even if enough prying action is presented, it is too conservative to assume prying action to be acting at the edge of the end-plate since this results in thicker than necessary plates.

Kukreti et al. (1984) presented a finite element model for the moment rotation relationship of a bolted steel end-plate connection. A flush end plate connection was used for the FEM and experiments were conducted to verify the model. Parametric study was also conducted on the FEM to determine the effects of various geometric and force related variables. Regression analysis was done on the collected data to develop a prediction equation for the behavior of the connection.

Raj et al. (1987) conducted an analytical study of the behavior of the contact zone and pressure distribution between two circular flat plates connected by a circular bolt. The parameters used in this study are as follows: elastic properties of bolt and materials, bolt head diameter, and thickness of the plates. It was shown that the

elasticity of the bolt and the thickness of the plates played an important role in the load transfer and, consequently, the contact pressure distribution between the plates.

Rothert et al. (1992) studied the 3D FEA of bolted connections including contact. A special finite element rod model was developed to incorporate the deformations of the connecting devices in the analysis of steel frame structures. This model is even capable of describing the complete plasticization of a connection.

Stallings and Hwang (1992) presented a simple bolt pre-tension model in finite element analyses of bolted connections by using temperature changes for the bolts modeled with rod elements. They suggested that two methods presented could be used to produce the desired bolt pre-tensions without elaborate algorithms.

Kulak and Birkemoe (1993) conducted field studies on bolt pre-tension. This study showed that actual pre-tensions were 35% greater than specified minimum pre-tensions. Therefore, bolt pre-tension would be at least 70% of the ultimate tensile strength of the bolt known as proof load.

Gebbeken et al. (1994) presented finite element modeling of bolted steel connections in order to predict their load carrying behavior and to calculate their limit loads. Influence of each geometric variable on connection flexibility has been studied. Gebbeken and others included the effect of material and contact nonlinearities.

Sherbourne and Bahaari (1997) presented a three-dimensional finite element model to determine moment-rotation relationships for steel bolted extended end-plate connections. The end plate considered in the model consisted of a plate welded to the beam cross-section and bolted by two consecutive rows of the two bolts at the tension

flange of the beam and one row of bolts above the compression flange. Plate elements were used for end plate, beam and column flanges, webs, and column stiffeners. Truss elements were used for the bolt shank, and the bolt head and nut were modeled with brick elements. Von mises yield criterion with the associative flow rule was used in the study. The finite element results were compared with the experimental values to verify the model.

Chung and Choi (1996) investigated the effect of bolt pre-tensioning and the shapes of the bolt shank, head, and nut on the behavioral characteristics of the end-plate connections. For the model to simulate the interaction between the end plate and the column flange, a contact algorithm with gap elements was employed.

Chutima and Blackie (1996) investigated the effect of pitch distance, row spacing, end distance and bolt diameter on composite laminate plate joints subjected to tensile loading to consider the effect on the local contact stress distribution.

Hassan et al. (1996) performed FEA of bolted connections for FRP composites. Three-dimensional finite element analysis was conducted on single and muti-bolted connections to determine the failure process, ultimate load distribution among the fasteners, taking into consideration bolt-hole contact problem in the FEM. They used the Tsai-Wu tensor polynomial failure criterion which is applied to the laminate as a whole.

Bursi and Jaspart (1997) collected a set of benchmark problems in finite element modeling of bolted steel connections. The benchmark problems are modeled by finite element and the results are compared with experimental results. This study presented

calibration of a finite element model for isolated bolted end plate steel connection. They also proposed an assemblage of three-dimensional beam finite element to model the behavior of bolts.

Bursi and Jaspart (1998) studied the effect of the most important issues in finite element modeling of the extended end plate connections. These following issues were studied: constitutive relationships, step size, number of integration points, kinematics description, element types, discretization, modeling the bolts, and bolt prestressing. For bolt modeling, they proposed a spin model composed of rigid beam elements (in the bolt head plane) connected to the beam located in the bolt center.

Kukreti and Abolmaali (1998) presented an approach in formulating analytical models to predict the moment rotation hysteresis behavior of top and seat angle connections. Twelve experimental results were used to obtain the prediction equations for the parameters defining the moment rotation hysteresis loops of top and seat angle connections. The parameters considered were initial stiffness, ultimate moment capacity, ultimate rotation, the transition moment, characteristic moment and rigidity parameter. Test results were compared with the results obtained from the regression analysis to show the acceptability of prediction equations. Four different moment rotation hysteresis models: bilinear, elasto-plastic, Ramberg-Osgood, and modified bilinear models were developed from the prediction equations.

Wanzek and Gebbeken (1999) emphasized the importance of through-thickness deformation in the analysis of steel end-plate connections by using three layers of

elements through the thickness of the end-plate. The effects of friction and slip on the response of connections were also considered.

Bahaari and Sherbourne (2000) investigated nonlinear behavior of bolted connections by considering plasticity of the material and changes in the contact area. They presented three-dimensional spar elements to model the bolt shank which were provided to find both the magnitude and distribution of the bolt force within the section. A325 slip critical bolts were used to assemble the connections. Pre-stressing of the bolt shanks was introduced by means of equivalent initial strain. It was shown that preloading was advantageous in improving connection stiffness and in maintaining relatively constant bolt stresses until yield occurred.

Hurrell (2000) provided guidelines on the finite element modeling and analysis of pressure vessel bolted joints. He discussed different modeling issues in bolted connections.

Schafer et al. (2000) studied the effect of triaxiality and fracture in steel connections. Triaxiality is defined as the ratio of the maximum principal stress to the Von-Mises stress. They shown that the triaxiality demands indicate that the fracture of those connections may be governed even when high toughness parent and weld metals is used.

Yang et al. (2000) studied the effect of angle thickness of double angle connections subjected to axial tensile loads, shear loads, and combined loads. The loads were increased monotonically and an elastic-perfectly plastic constitutive law was utilized. The force-displacement curves for axial loading and the moment-rotation

curves for shear loading showed good correlation with those from the three-dimensional finite element analysis (Yang, 1997). Yang et al. concluded that the thickness of the angles had a huge influence on the response of the connection. The initial stiffness increased significantly as the angle thickness increased. The final portions of the curves were almost parallel, but the level of the load or moment increased greatly as the thickness of the angles was increased.

Aref and Guo (2001) addressed the formulation and application of a finite element based large increment method for solving nonlinear structural problems.

Chung and Ip (2001) investigated the structural behavior of cold formed steel bolted connections using finite element method. They have discussed about the three distinctive failure modes as observed; bearing failure, shear-out failure and net-section failure.

Harte and Cann (2001) used FEA to determine the moment-rotation behavior of the pultruded fiber-reinforced plastics beam-to-column connections. The model included bolted assembly, prestress forces and contact surfaces. They stated that the connection stiffness increases as the number of link elements increases, and the rotational stiffness was within 3% of the experimentally obtained. Because of the plane elements used in the model of bolt, web cleats could not be considered. As a result it was suggested that a three-dimensional model of the connection be provided for both the flange and the web cleats.

Kishi et al. (2001) used nonlinear FEA to develop prediction equations based on the power model (Richard and Abbott, 1975; Kishi and Chen, 1990) for the top- and

seat-angle connections. The power model contained three parameters: initial connection stiffness, ultimate moment capacity, and shape parameter. All components of the model were completely independent from each other as assemblages in a real connection. Special attention was given to the bolts which were modeled with eight-node solid elements and divided to consider the effect of shank, head and nut elements on connection behavior. Bolt pre-tension load was 70% of minimum tensile strength of bolt obtained from test data.

Kishi et al. (2001) modeled four finite element analysis models to find out the best estimated moment-rotation characteristics of top and seat angle with double web angle connections. They included bolt shapes accurately and defined contact surfaces, as well. To make the analysis more accurate, first the prestressing is applied and then the load is applied, as would happen in actual practice.

Mofid et al. (2001) presented an analytical model to determine the behavior of a particular steel beam-to-column extended end plate connection in the linear and nonlinear regions. Extensive parametric studies were conducted and the results were compared with nonlinear finite element models as well as with the experimental tests. It was suggested that the initial stiffness of the connection is affected by plate thickness and width, beam depth and the distance between centerline of the bolts. In addition, it was also concluded that the yielding moment depends mainly on the plate thickness, the distance between centerline bolts, the bolt area and the materials.

Zadoks and Kokatam (2001) evaluated the axial stiffness of a bolt using a 3D FEM. The model is loaded by pulling the nodes around the outside of the bolt head in

the axial direction while holding the bottom of the plate fixed. Quasistatic analysis predicts a linear relationship between the reaction force and the axial stretch of the bolt, indicating that the axial stiffness is constant. Dynamic analyses yield the same results if the prescribed accelerations are limited, though the predicted stiffness values are lower than those in the quasistatic analyses.

Citipitioglu et al. (2002) used parametric three-dimensional analysis of finite element studies to predict the overall moment-rotation response of partially-restrained bolted steel beam-to-column connections. It was shown that friction and slip in the model along with the simplicity of changing mesh geometry had more effect on the response of connections with higher moments and stiffer connecting elements. The effect of pre-tension of the bolts in the model was shown to be relatively important, which can vary the ultimate moment by 25 percent. Force-displacement curves were generated in terms of each bolt size and varying total plate thicknesses. Finally, a parametric study was conducted in order to investigate the effects of friction and pre-tension of the bolts on the connection behavior.

Swanson et al. (2002) performed a FEA of T-stubs and compared the results with experimental results. They worked on two sets of models; a 3D T-stub model consisting of brick and wedge elements and several two-dimensional T-stub flange models consisting of rectangular and triangular elements. In both models, effects of material, geometric and contact nonlinearities were incorporated.

Gantes and Lemonis (2003) investigated the influence of equivalent bolt length in the finite element modeling of T-stub connections. They included material, geometric

and contact (with friction) nonlinearities. The numerical results are validated by comparing with the experimental results in the literature. They observed that if bolt length is considered short, the displacements are underestimated (stiff connection) while with longer bolt lengths, the displacements are overestimated and there are some intermediate lengths that can give the same results as experimental results.

Oldfield et al. (2003) worked on modeling of bolted joints under harmonic loads. Equivalent Jenkins element and Bouc-Wen model for a bolted joint are established by fitting the hysteresis loops produced by these simple models with those of a detailed finite element model.

1.2.3 Damping Device

The image distortion of the CCTV camera, which is caused by the pole vibration, is similar in nature to the traditional building vibration subjected to ground motion acceleration. In this analogy, the vibration experienced by the camera is similar to that experienced by a building during an earthquake or other vibratory forces.

The research for passive and active damping systems has gained significant popularity during the recent era. Particularly, since the Northridge and other major earthquakes, the passive control systems were designed to dissipate vibrational energy by absorbing part of the input energy, which reduces structural damage (Hounser et al., 1997). The passive control systems such as seismic isolations are not capable of adjusting to the unexpected external loads or usage patterns. The active control system, on the other hand, is capable of adapting to different loading conditions and to control actuators as a function of response of the system measured with physical sensors.

Both passive and active isolators have been implemented in several buildings throughout the United States and else where (Yang, 2001). Some examples of passive system implementations are the Los Angeles City Hall (Youssef et al., 1995) and the Salt Lake City Building (Mayes et al., 1988), and the most popular active system building implementation is in the building by Kajima Corporation (Yang, 2001).

Comprehensive research studies were conducted in recent years for both active and passive systems. These includes and are not limited to device development, device implementation, device effectiveness, and advanced ductile building connection design. Also, research studies was conducted on the effectiveness of each damping system into the structures and massive single degree of freedom pole system subjected to vibratory forces. The literature in active systems for civil structure is extensive and the following are at their forefront: robust control (Dyke et al., 1995; Jabbari et al., 1995; Magana and Rodellar, 1998; Spencer et al., 1994; Suhardjo, 1990; and Yoshida et al., 1998), DUOX (Ohrui et al., 1994); and another type of HMD system in which small active mass dampers are mounted on a passive tuned mass damper. Reinhorn and Riley (1994) with a sliding hybrid isolation system, Yang and Spencer (1997), Battaini et al. (1998), Spencer and Soong (1999), Dyke et al. (1996a,b, 1998); Jansen and Dyke (2000); Johnson et al. (2001); Ramallo et al. (2001); Spencer et al. (2000); Yi and Dyke (2000); Yoshioka et al. (2002), Symans et al. (1994), Symans and Constantinou (1999), Kurata et al. (1999, 2000), Patten (1999), Akbay and Aktan (1990, 1991, 1995), Dodwell and Cherry (1994), Feng et al. (1993), and Inaudi (1997). The most comprehensive sections

of the prior studies for the passive system are reported by Soong and Dargush (1997), and Soong and Spencer (2002).

1.3 Goals and Objectives

The main objective of this research is to stabilize the image distortion experienced by the CCTV cameras installed at different pole heights, typically used by TxDOT.

To accomplish this objective, two different devices (algorithm) are developed and integrated, which are: mechanical device, electrical device, and the combined algorithm. The developments of both devices require an in-depth understanding and evaluation of the natural vibration frequency of the typical poles. Thus, a continuum FEM) of the pole is developed which was verified by the full-scale experimental tests conducted in TxDOT Project 0-4470. Also, the frequencies obtained from the FEM analyses were verified against those obtained by the field instrumentation of several TxDOT poles subjected to free vibration. The natural frequencies of the poles are identified by considering the different combination of their geometric parameters.

A passive mechanical device was developed to reprieve the vibrational frequencies greater than 1 Hz. Typically, severe image distortions are caused by a pole's frequency of 6 Hz or greater. The electrical device is consequently developed to eliminate the vibrations experienced by the camera for the 1 Hz frequency, which was caused by light wind.

Both devices were tested in the laboratory for image stabilization by subjecting the camera to a wide variety of vibration with different frequencies, known through the

aforementioned FEM analysis. Both the devices were calibrated and optimized through this process. Also, the mechanical device was tested on the selected poles. Figure 1.10 shows a flow chart that summarizes the major activities which leads to the accomplishment of the goals and objectives.

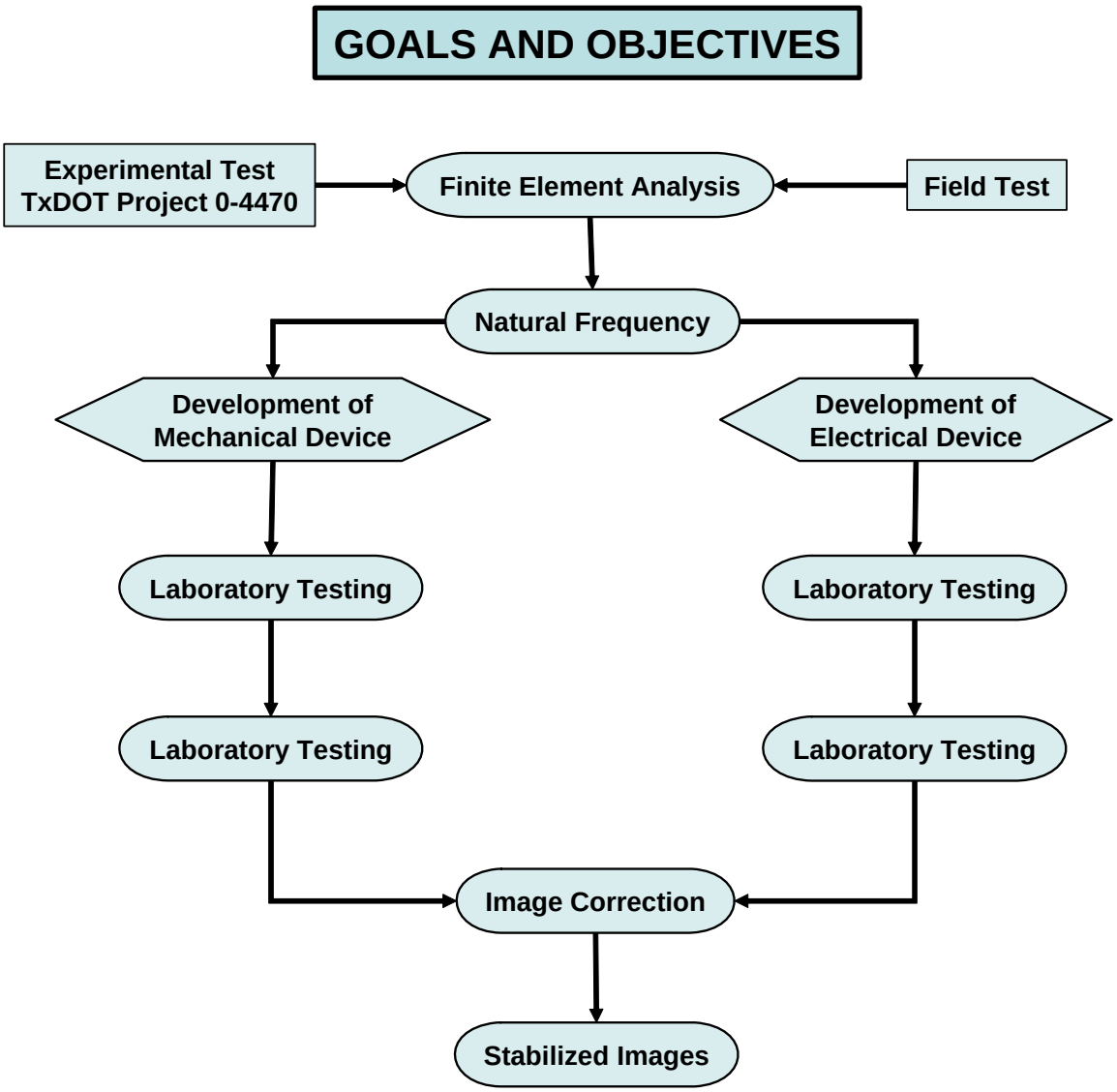

Figure 1.10 Summary of the procedure to accomplish the goal of the study.

CHAPTER 2

FINITE ELEMENT ANALYSIS

2.1 Introduction

A complete nonlinear three-dimensional (3-D) FEM of the typical octagonal and circular tapered poles used by the TxDOT were developed, which consisted of the pole and its connection assembly. The connection assembly consisted of end-plate, bolts, and foundation. Particular attention was devoted to the modeling of the contact surfaces between the bolt shank and the end plate; the bolt heads and the bolt nuts; and the bolt nut and the foundation.

Both three-dimensional shell and solid elements were used to optimize the mesh. In some of the trial models, shell elements for the pole and solid elements for the connection assembly were used. The configuration of the element types used is shown in Table 2.1.

Material, geometric, and contact nonlinearities were incorporated into the analysis algorithm, which is based on the classical monotonic and cyclic plasticity. In the geometric nonlinearity formulation, the large displacement is modeled based on the Almansi (Eulerian) strain which yields to the Cauchy stress tensor from which the total

Lagrangian algorithm was employed. Also the contact nonlinearity was considered for the contacting surfaces which yielded to a coupled iterative nonlinear problem.

Table 2.1 Element Types and Corresponding Element Number.

Element type	Description	D.O.F.	Element shape
C3D4	Tetrahedral Elements	12	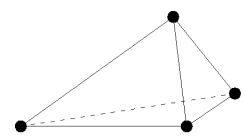
C3D10	Tetrahedral Elements	30	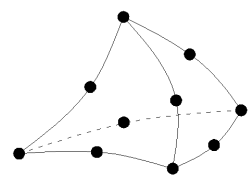
C3D6	Triangular Prisms Elements	18	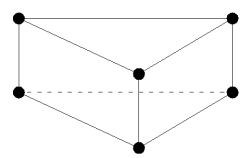
C3D12	Triangular Prisms Elements	36	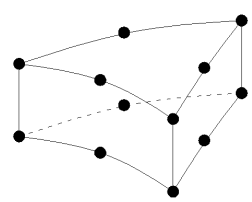
C3D8	Hexahedral Elements	24	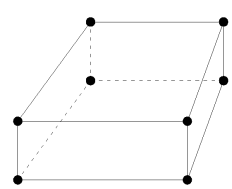
C3D20	Hexahedral Elements	60	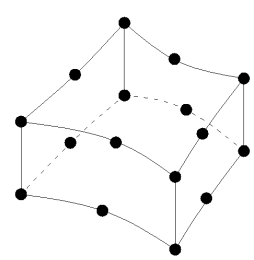

All the classical convergence criteria were employed to check for the converged solution, which includes P-, H-, P-H, and the energy based convergences.

H-convergence is tested by increasing the number of degrees-of-freedom (DOF) of the model as a result of decreasing the element sizes. In the P-convergence, higher order polynomials are used in defining the assumed displacement function, which is equivalent to use higher order elements. The P-H convergence employed both P- and H-methods. Since convergence of the nonlinear problems is monotonically not guaranteed (Razavi et al., 2006), energy-based convergence is more desirable, which thus was adopted.

Also, the H-convergence for each model was tested by using Hilbert L-2 norm, coupled with equating the external and the virtual work done to the internal strain energy at each load increment in the Newton-Raphson marching scheme (Crisfield, 1997).

2.2 Development of Finite Element Model

2.2.1 Symmetric Modeling

Due to the symmetrical nature of the problem with respect to both load and geometry, only one-half of the entire pole's section was modeled (Figure 2.1). Thus, all the nodes at the plane of symmetry were restrained from translation in the three-dimensional space (i.e., local *x, y* and *z*).

2.2.2 Pre-tension Load

In the early FEM modeling of bolted connections pre-tension, effects in the bolts caused by the tightening of each bolt were simulated by applying compressive forces equivalent to proof load (70% of bolt's ultimate tensile strength) to the end-plate at the location of bolt head and nut (Azizinamini, 1985; and Choi and Chung, 1996). These compressive forces were equivalent to the bolt pre-tension force (proof load) per AISC (1999). This type of bolt modeling has traditionally introduced difficulties in monitoring the variation of the bolt forces during the analysis. Thus, in this study the entire bolt shank, bolt head, and bolt nut was modeled with three-dimensional solid elements. The effect of contact surfaces between the bolt head and nut, and the bolt shank and end-plate wall was also included (Figure 2.2). The pre-tensioning force was applied by using the pre-tension element in ABAQUS in which an arbitrary plane was passed through the bolt shank and a predetermined pre-tension force was applied in the plane perpendicular to axial direction (Figure 2.3).

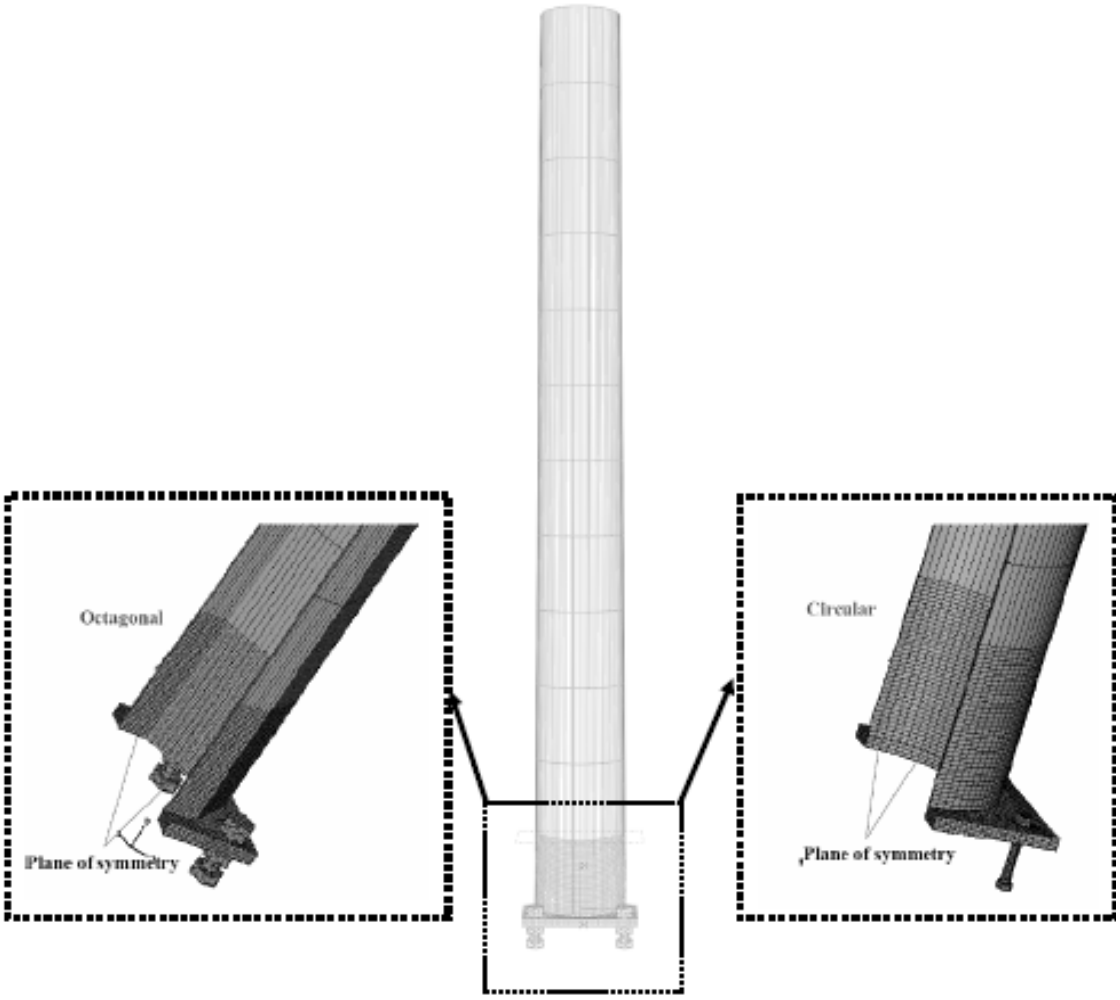

Figure 2.1 Typical 3-D models of circular and octagonal poles.

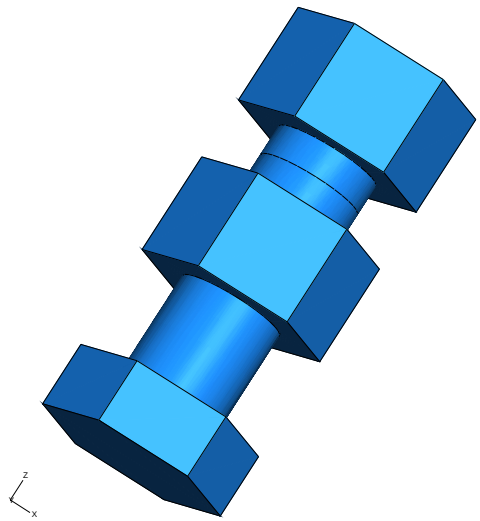

(a)

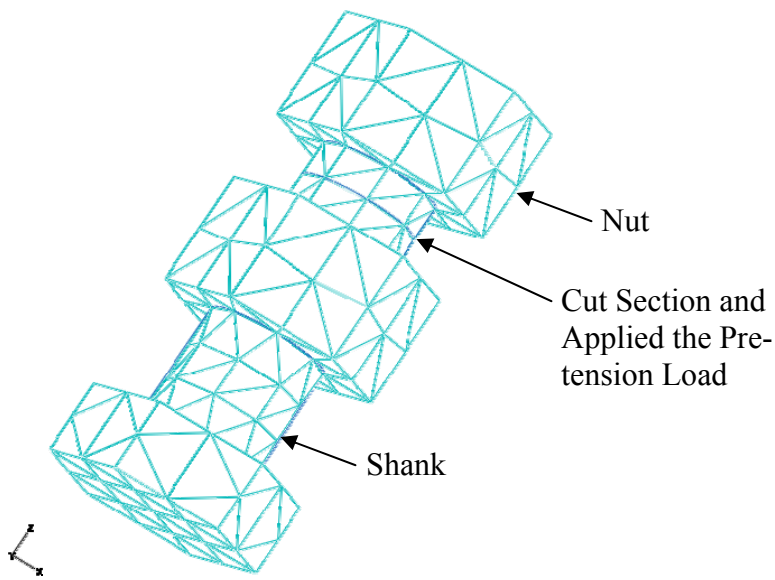

(b)

Figure 2.2 Bolt model used in analysis; (a) 3-D bolt model, (b) 3-D bolt model with triangular mesh

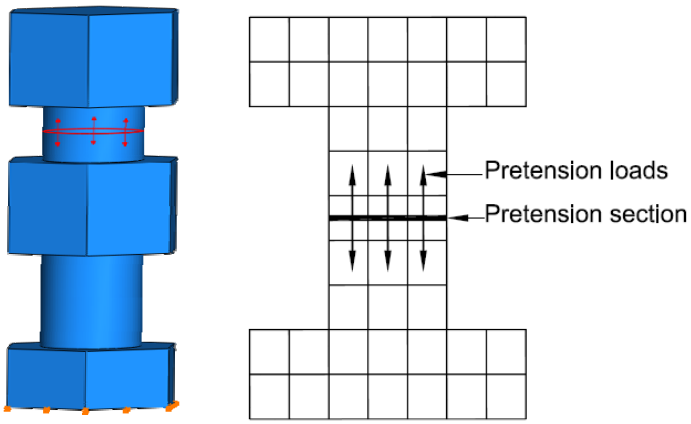

Figure 2.3 Pre-tension load and section.

During the pre-tensioning process, turning of the nut reduces the un-stretched grip length of the bolt, thereby inducing pre-tension. When the desired pre-tension is achieved and the wrench is removed, the new un-stretched grip length becomes locked. The pre-tension element used applies to the same procedure during the loading in the same sequence: first, the specified pre-tension load is applied incrementally to capture the contact effects, and possible nonlinearities induced by material yielding. At this point in the analysis, the pre-tension section displacement is locked for the pre-tensioned bolt. Once all bolts are pre-tensioned and locked, external load is applied incrementally to capture nonlinearities due to material, geometric, and contact. Thus, the analysis is based on non-propositional loading.

2.2.3 Contact Modeling

To avoid numerical penetration between the connecting surfaces, and to model friction for transferring forces between the surfaces, the contact surfaces between the bolt-to-plate and bolt head/shank-to-nut are considered, which introduce nonlinearity in the analysis algorithm. Contact model with small sliding option was applied between

contact pair surfaces, one of which is defined as master surface and the other as slave surface.

The surface-to-surface contact algorithm is employed to simulate the interaction between contact surfaces of the bolt head, the shank, and the nut with the end-plate and bolt holes. In this algorithm, the contact surfaces are defined at the beginning of the analysis. In this case, the top, bottom, and the inner bolt hole surfaces of the end-plate are defined as the master surfaces. The surfaces of the bolts which interact with the end-plate are thus defined as slave surfaces. General constitutive models for the contact behavior are used in the simulation relating the constraint pressure and the shear traction to the penetration distance and the relative tangential motion. Mechanical properties governing the behaviors of the contact surfaces are tangential behavior and normal behavior. One case that can happen during the contact modeling is excessive initial overclosures. If there are large overclosures in the initial configuration of the model at a typical beginning step, as shown in Figure 2.4(a), the incremental iterative procedure is required for converged contact solution, as shown in Figures 2.4(b) and 2.4(c).

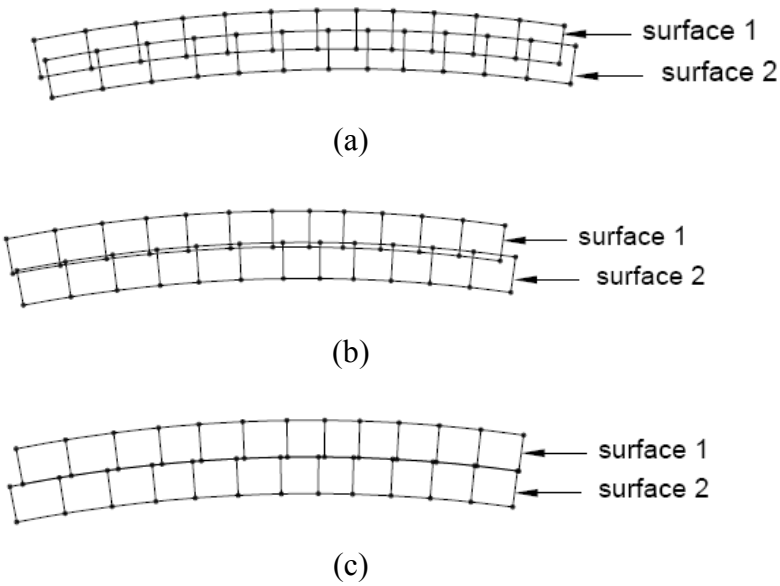

Figure 2.4 Contact interactions between two surfaces; (a) beginning of step, (b) middle step, (c) end of step.

An adequate mesh density was required for regions undergoing plastic deformations to allow contact stresses to be distributed in a smooth fashion. The friction would be a dominant parameter of stiffness at the initial stage of loading. Surface-to-surface and flexible-to-flexible contact types were used in the FEM analysis algorithm since contact between surfaces were deformable finite elements. A coefficient friction of 0.2 which indicates the roughness of the surfaces was used, as observed by Yorgun et al. (2004).

The numerical value and contact parameters that were used for the interaction between the end plate and the bolts is shown in Table 2.2.

Table 2.2 Contact Property for the Model.

Interaction location	Tangential behavior	Normal behavior
End-plate and Bolt Nuts	-Friction formulation : Penalty -Friction coefficient : 0.2	-Pressure Over-closure: Hard contact

2.2.4 Material Model

In general, a complete plasticity theory has three components: (1) a yield criterion that defines the combination of stress components in which initial yielding occurs, (2) a flow rule that deals with the way plastic deformation occurs, and (3) a hardening rule that predicts changes in the yield surface due to the plastic strain.

The material behavior for each pole, end-plate, and bolt was described by the bilinear stress-strain curves, the properties of which are defined in Table 2.3 and Figure 2.5, having a modulus of elasticity of 29,000 ksi (201 GPa), 36 ksi (248 MPa) yield stress, and a Poisson's ratio of 0.29. The material was considered to be isotropic, which was chosen with plasticity-based isotropic hardening rule. These options are often preferred for large strain analysis. The Von Mises yield criterion was adopted in order to obtain the response of the pole in the inelastic region. The initial slope of the curve was taken as the elastic modulus, E, of the material. After several trials to best calibrate the FEM model with the experimental results obtained, the post yield stiffness identified as tangent modulus, E_t , was taken as 1% of the initial stiffness ($E_t = 0.01\ E$). Thus, a bilinear stress-strain relationship for the material was used.

Table 2.3 Material Properties for Steel Poles Used in Analysis.

Material Properties	Pole & End-plate (A36)	Bolt (A325)
Modulus of elasticity (E)	29 Msi (201GPa)	29 Msi (201 GPa)
Yield stress (F_y)	36 ksi (248 MPa)	81 ksi (558 MPa)
Poisson's ratio (υ)	0.29	0.29
Tangential modulus (E_t)	290 ksi (2 GPa)	290 ksi (2 GPa)

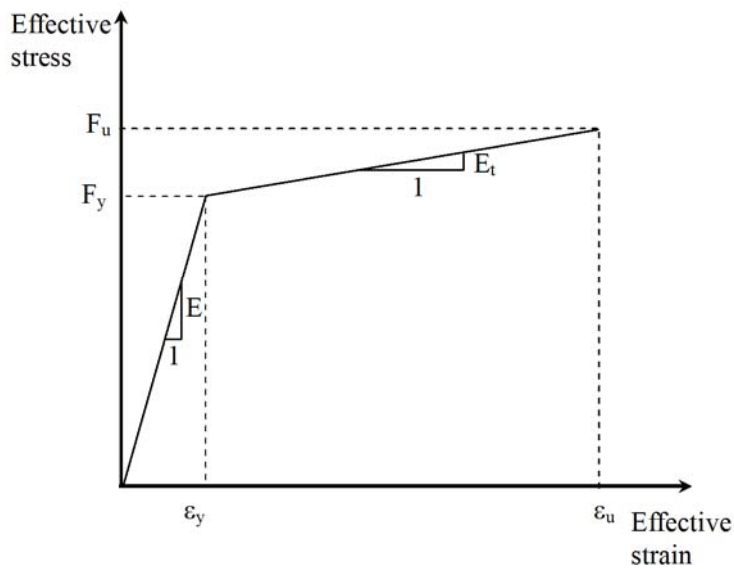

Figure 2.5 Nonlinear stress-strain relationships.

The stress-strain relationship for the material was elastic-plastic strain hardening. Material plasticity and the changes in the contact status area between the contact surfaces along with large deformation are the causes for the nonlinear behavior of bolted connections. This means that the problem in hand refines a coupled nonlinear incremental solution technique which was adopted during the solution process in this study. The loads were applied gradually in increments to characterize actual load history with multiple iterations per load step conducted. Bilinear isotropic hardening option was used for describing the plastic behavior in which the Von Mises criterion is coupled with the isotropic work hardening. Large plastic deformations were expected and observed, thus geometric nonlinearities were incorporated by adopting large strain analysis that accounts for the changes resulting from the shape and orientation of the elements. The large strain procedure places no theoretical limit on the total deformation

or strain experienced by an element, but requires incremental loading to restrict strains from maintaining accuracy in the computations.

The Newton-Raphson procedure was employed for the nonlinear analysis, where the load is divided into a series of load increments applied in several load steps. The tangent modulus at the beginning of each load step was calculated, and it was updated at each iteration with the load step. At the end of each iteration, the unbalanced forces were calculated which was used to solve the incremental system equilibrium equation. A conceptual representation of this nonlinear iteration procedure is shown in Figure 2.6

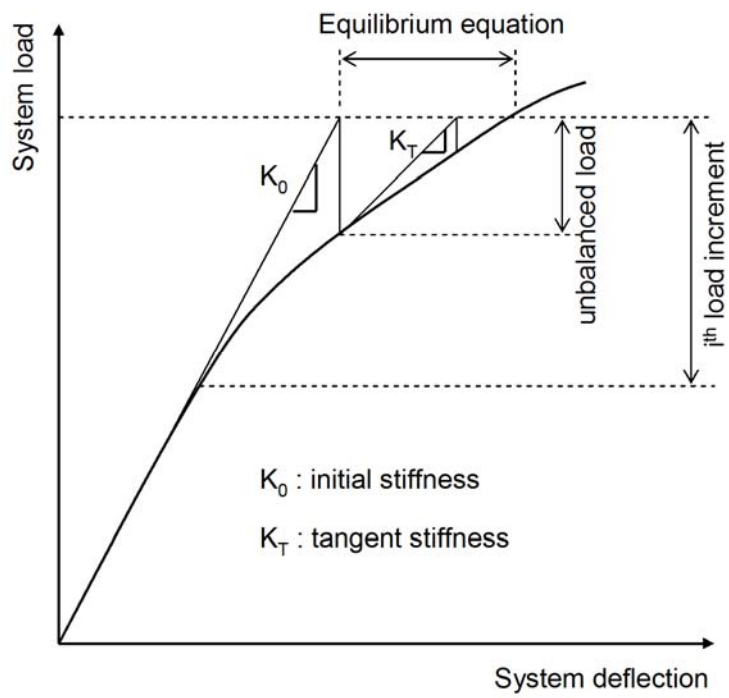

Figure 2.6 Newton-Raphson nonlinear schemes.

2.2.5 Yield Criteria

Several failure theories for yield criteria are discussed in mechanics of materials textbooks (Chen and Han, 1988; Bathe, 1996; Crisfield, 1997; and Morozov, 2004). In one-dimensional problem, yielding is identified with comparison of just one stress component with the yield strength. In multidimensional problems stress tensor is used to identify the state of stress in a continuum subjected to deformation. This stress tensor is decomposed into two parts: hydrostatic and deviatoric. Some materials are pressure dependent, while some are pressure independent in which yield criteria do not depend on the first stress invariant, and they are only defined in terms of the second deviatoric stress invariant. Among the pressure independent criteria, one can name the Maximum Shear Stress and the Von Mises which is called octahedral shearing stress or the maximum strain energy distortion. Von Mises criterion indicates that the yielding happens when the octahedral shear stress reaches a critical value. The approach of the Von Mises yield criterion is as follows:

$$(\sigma_1 - \sigma_2)^2 + (\sigma_2 - \sigma_3)^2 + (\sigma_3 - \sigma_1)^2 > 2\sigma_y^2 \tag{2.1}$$

$$\sigma_{eff} = \sqrt{\frac{1}{2}[(\sigma_1 - \sigma_2)^2 + (\sigma_2 - \sigma_3)^2 + (\sigma_3 - \sigma_1)^2]} > \sigma_y \tag{2.2}$$

Where $\sigma_1, \sigma_2,$ and σ_3 are the principal stresses ($\sigma_1 > \sigma_2 > \sigma_3$) and σ_y is the yield stress of the material obtained from a uni-axial tensile test. When $\sigma_{eff} > \sigma_y$, the element is said to have yielded. To consider the nonlinear behavior, it is convenient to convert stresses to strains, since for the plate material, the stresses remain constant upon

yielding. The principal stresses are transferred to principal strains by the following relationships:

$$\sigma_1 = \mu\{(1-\nu)\varepsilon_1 + \nu\varepsilon_2 + \nu\varepsilon_3\} \tag{2.3}$$

$$\sigma_2 = \mu\{\nu\varepsilon_1 + (1-\nu)\varepsilon_2 + \nu\varepsilon_3\} \tag{2.4}$$

$$\sigma_3 = \mu\{\nu\varepsilon_1 + \nu\varepsilon_2 + (1-\nu)\varepsilon_3\} \tag{2.5}$$

where ν is the Poisson's ratio and μ is calculated using the following relationship:

$$\mu = E / \{(1+\nu)(1-2\nu)\} \tag{2.6}$$

and $\varepsilon_1, \varepsilon_2$ and ε_3 are the principal strains ($\varepsilon_1 > \varepsilon_2 > \varepsilon_3$). Substituting Equations 2.3 to 2.5 into Equation 2.2 gives:

$$(\sigma_1-\sigma_2)^2 + (\sigma_2-\sigma_3)^2 + (\sigma_3-\sigma_1)^2 = \left\{\frac{E}{1+\nu}\right\}^2 \{(\varepsilon_1-\varepsilon_2)^2 + (\varepsilon_2-\varepsilon_3)^2 + (\varepsilon_3-\varepsilon_1)^2\} \le 2(\varepsilon_y)^2 \tag{2.7}$$

or

$$\frac{\sqrt{2}}{2(1+\nu)}\{(\varepsilon_1-\varepsilon_2)^2 + (\varepsilon_2+\varepsilon_3)^2 + (\varepsilon_3-\varepsilon_1)^2\}^{1/2} \le \varepsilon_y \tag{2.8}$$

where ε_y is the yield strain of the material from a uni-axial tensile test. Taking $\nu = 0.5$ for the plastic region, Equation 2.8 reduces to:

$$\frac{\sqrt{2}}{3}\{(\varepsilon_1-\varepsilon_2)^2 + (\varepsilon_2-\varepsilon_3)^2 + (\varepsilon_3-\varepsilon_1)^2\}^{1/2} \le \varepsilon_y \tag{2.9}$$

Therefore, the effective strain, ε_{eff} in any element of the end-plate is calculated in terms of principal strains of the element, as follows:

$$\varepsilon_{eff} = \frac{\sqrt{2}}{3}\left\{(\varepsilon_1 - \varepsilon_2)^2 + (\varepsilon_2 - \varepsilon_3)^2 + (\varepsilon_3 - \varepsilon_1)^2\right\}^{1/2} \tag{2.10}$$

If ε_{eff} is found to be greater than ε_y, then the element is said to have yielded. Von Mises yield criterion is based on this alternative. It has the simple form:

$$f(J_2) = J_2 - k^2 = 0 \tag{2.11}$$

or, written in terms of principal stresses,

$$J_2 = \frac{1}{6}\left[(\sigma_1 - \sigma_2)^2 + (\sigma_2 - \sigma_3)^2 + (\sigma_3\sigma_2)^2\right] = k^2 \tag{2.12}$$

where f is a yield function and k is the yield stress in pure shear. When J_2 exceeds k^2 yielding occurs.

2.2.6 Geometric Nonlinearity

In order to take into account the possible geometric nonlinearity for a long tapered hollow pole, the geometric nonlinearity feature provided by ABAQUS (2006) is adopted. The influence of modeling for with/without geometric nonlinearity algorithm on the natural frequencies for a long tapered hollow pole is discussed in the subsequent section of this study.

2.2.7 Numerical Analyses

Nonlinear dynamic analyses were performed using ABAQUS (2006) software for different cases defined in the next Chapter 3, Table 3.2 and Table 3.3. The natural frequency of the poles and corresponding mode shapes are obtained by using Lanczo's Eigenvalue Extraction Method (ABAQUS 2006). The effects of the self weight is considered in the analysis, and for the modeling, the initial stress and the load stiffness

effects due to preloads and initial conditions, are taken into account. A convergence study is performed for a typical pole case and with different mesh densities, as shown in Figure 2.7, in order to obtain the optimum mesh density. Typical mode shapes and corresponding natural frequencies of a typical pole are shown in Figure 2.8 and Table 2.4, respectively. Also, Table 2.4 presents the effects of the geometric nonlinear algorithm on the natural frequency of the pole, which shows that the frequencies obtained with and without the geometric nonlinearity are almost identical as expected, since Eigenvalue extraction is employed.

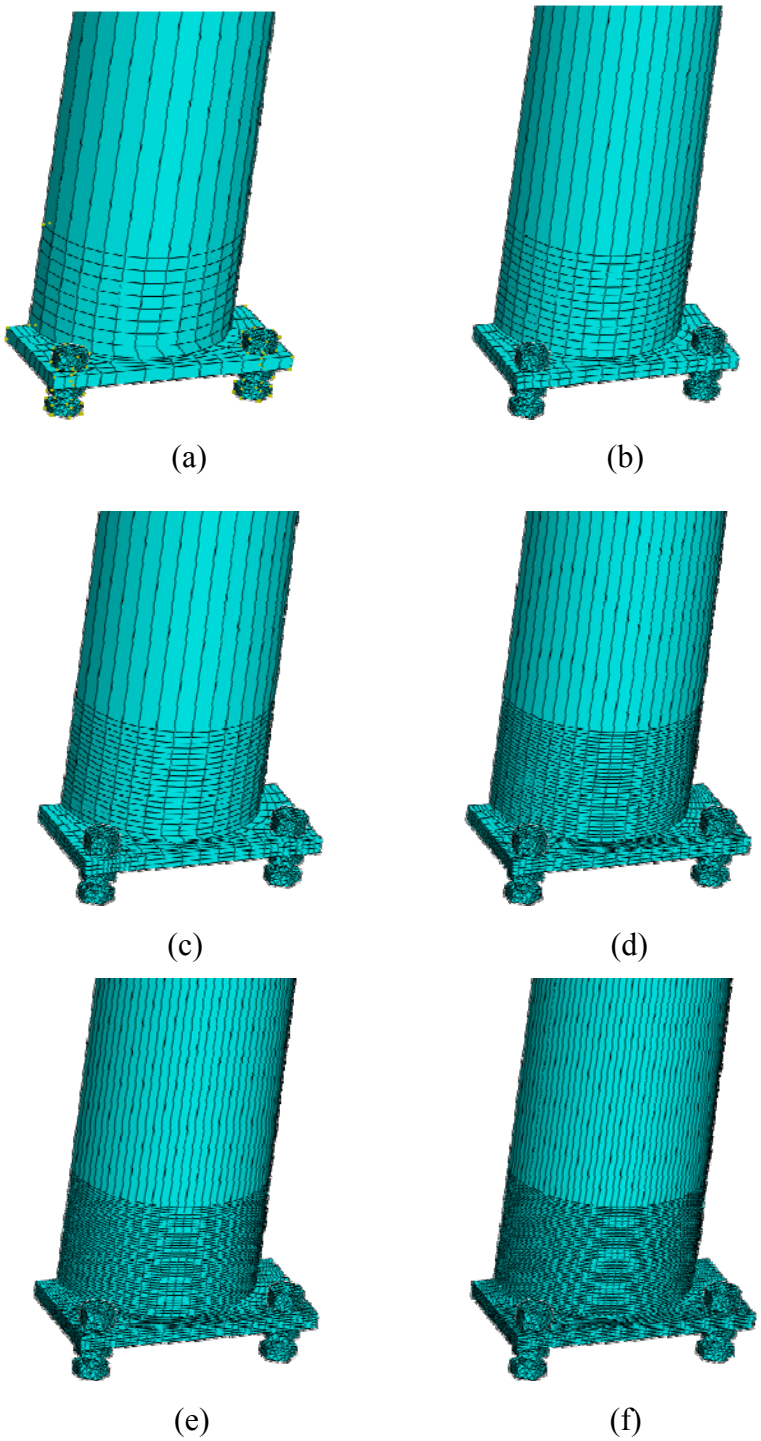

Figure 2.7 Different mesh densities for H-convergence study;
(a) mesh size 1.25 in., (b) mesh size 0.75 in., (c) mesh size 0.5 in.,
(d) mesh size 0.3125 in., (e) mesh size 0.25 in., (f) mesh size 0.2075 in.

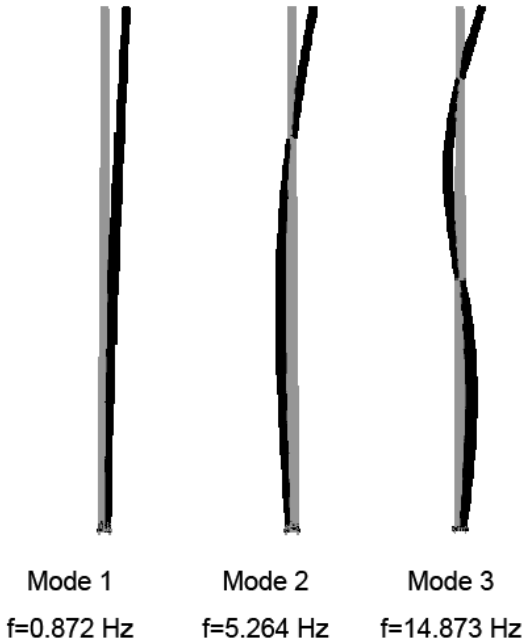

Figure 2.8 Typical mode shapes.

Table 2.4 The First Three Natural Frequencies for The Long Tapered Hollow Steel Pole With/Without Geometric Nonlinearity (Hz).

	Modeling with geometric nonlinearity	Modeling without geometric nonlinearity
Mode 1	0.872	0.884
Mode 2	5.264	5.274
Mode 3	14.873	14.883

Furthermore, it will be shown that the bolt model with corresponding pre-tension forces affect the first three natural frequencies significantly. Also, the modeling pole's connection assembly which introduces the effect of the connection semi-rigidity into the system, causing a less stiff system with lower natural frequencies as compared to those obtained from the pole's model with fixed support.

During the initial analysis step, the pre-tension load, contact interactions, and boundary conditions of the model are applied to introduce the initial condition in the system for the subsequent frequency analysis. In the second step, the Eigenvalue extraction is performed to calculate the natural frequencies and the corresponding mode shape of the model. The procedure for natural frequency extraction is a linear perturbation procedure. It includes initial stress and load stiffness effects due to the pre-tension load and initial boundary conditions (ABAQUS, 2006).

2.3 Model Verification

The finite element model was initially verified by the comparison to the experimental result from TxDOT Project 0-4470, which is shown in Figure 2.9 for the load versus deflection. Figure 2.10 shows the P- convergence study, in which the numbers of elements are increased until the effect of change in the mesh density has little or no impact on the load-deflection plots.

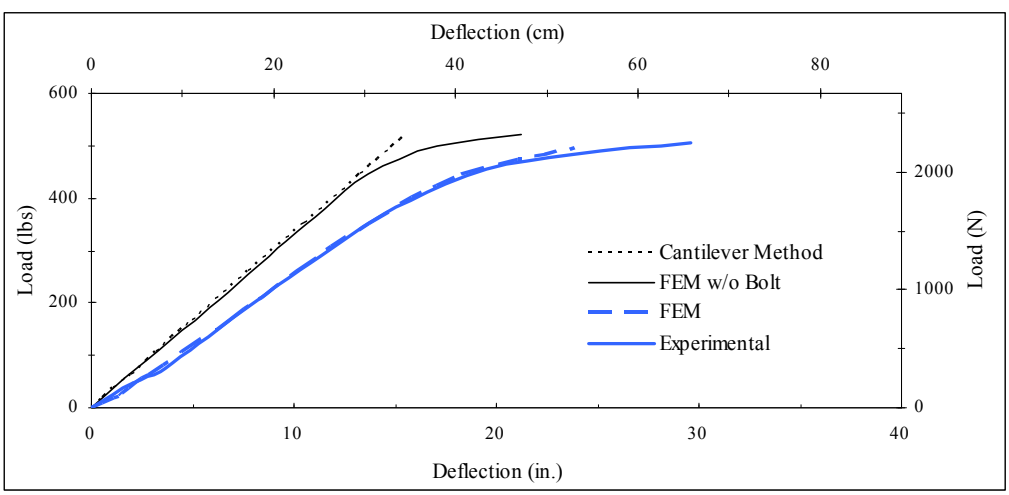

Figure 2.9 Model verification.

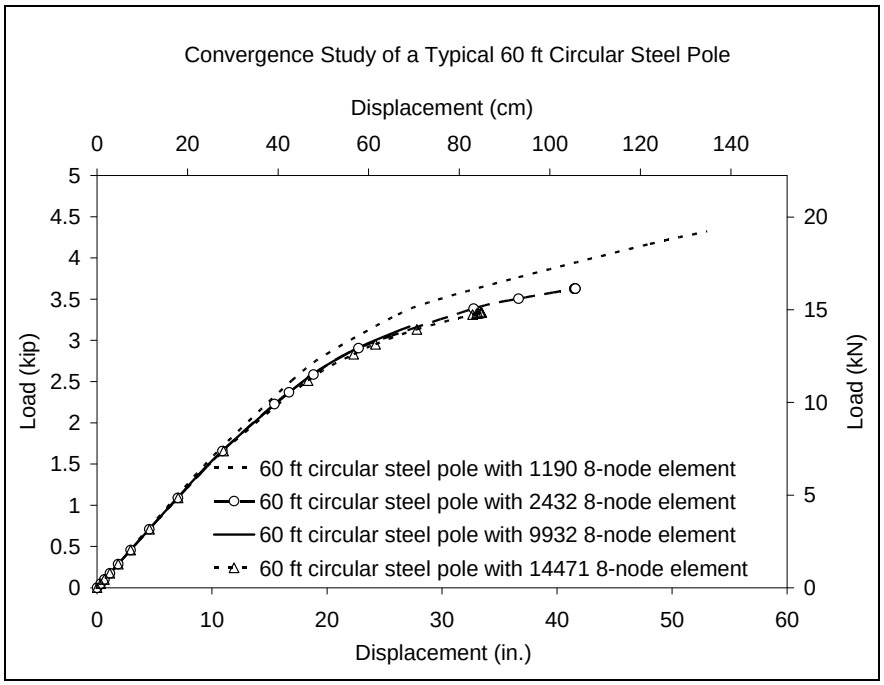

Figure 2.10 Convergence study for obtaining the optimum mesh density.

To further verify the FEM analysis, a field study was conducted in which an actual 60 ft pole located at Rosedale-I35W, Fort Worth, Texas, was instrumented and excited from which the acceleration data were collected. The photographs of instrumentation and test setup are shown in Figure 2.11.

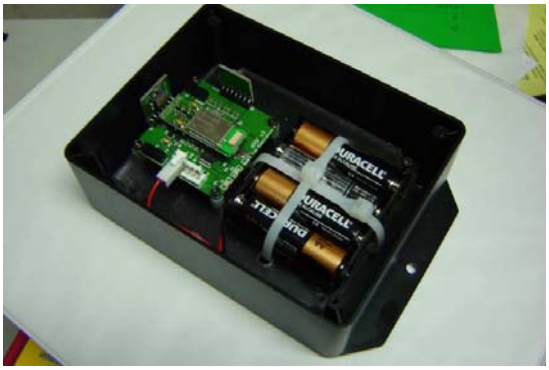

Figure 2.11 Test setup and accelerometers used in the experiments.

Spectral power analyses were conducted and the natural frequency of the pole was obtained and compared with the FEM results. Figure 2.12 shows this comparison.

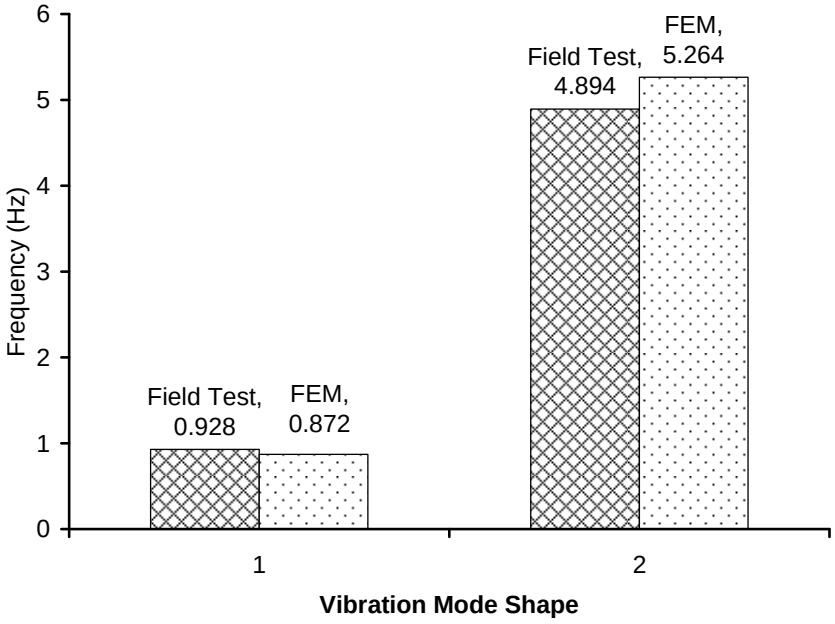

Figure 2.12 Comparison between field testing and FEM results.

Finally, the values of frequencies obtained from the FEM were compared with the classical solution with fixed support (classical solution does not exist for a pole with flexible connection). Figure 2.13 shows that the FEM accurately predicts the frequencies of Eigenvector for the first, the second, and the third modes.

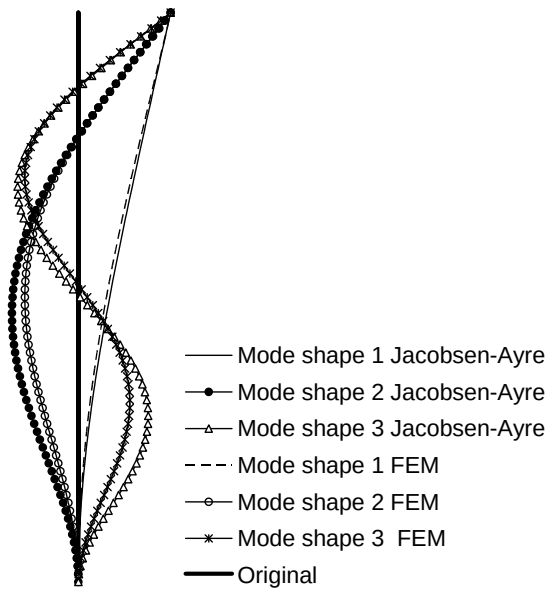

Figure 2.13 Comparison of the mode shape obtained from the finite element model analysis in this study and the theoretical solution (Jacobsen-Ayre) for a typical pole with fixed support.

2.4 Eigen Solution and Mode Shapes

ABAQUS/Standard provides three Eigenvalue extraction methods:

- Lanczos,
- Automatic multi-level substructuring (AMS), an add-on analysis capability for ABAQUS/Standard, and
- Subspace iteration.

2.4.1 Lanczos Eigensolver

For the Lanczos method, the maximum frequency of interest, or the number of Eigenvalues required; ABAQUS/Standard will determine a suitable block size (although you can override this choice, if needed). Both of the maximum frequency of

interest the number of Eigenvalues required, and the actual numbers of Eigenvalues are underestimated, where ABAQUS/Standard will issue a corresponding warning message; the remaining Eigenmodes can be found by restarting the frequency extraction. If the parallel Lanczos Eigensolver is used (i.e., the number of frequency intervals is set to greater than one), both the upper and lower frequency boundaries must also be provided. The minimum frequencies of interest must be specified; ABAQUS/Standard will extract Eigenvalues until either the requested number of Eigenvalues has been extracted in the given range or all the frequencies in the given range have been extracted. If the parallel Lanczos Eigenvalue extraction method is invoked, the minimum and maximum frequencies of interest must be specified. As a result, the Lanczos Eigensolver option was used for the pole natural frequencies analysis.

2.4.2 Automatic Multi-level Substructuring (AMS) Eigensolver

For the AMS method, the maximum frequency of interest (the global frequency) is needed, and ABAQUS/Standard will extract all the modes up to this frequency. The minimum frequencies of interest and/or the number of requested modes must also be specified. However, specifying these values will not affect the number of modes extracted by the Eigensolver; it will only affect the number of modes that are stored for output or for a subsequent model analysis.

2.4.3 Subspace Iteration Method

For the subspace iteration procedure, the number of Eigenvalues required should be given; ABAQUS/Standard chooses a suitable number of vectors for the iteration. If

the subspace iteration technique is requested, the maximum frequency of interest is needed; ABAQUS/Standard extracts Eigenvalues until either the requested number of Eigenvalues has been extracted, or the last frequency extracted exceeds the maximum frequency of interest.

The Eigenvalue problem for the natural frequencies of an un-damped finite element model is:

$$(-\omega^2 \mathbf{M}^{MN} + \mathbf{K}^{MN})\phi^N = 0$$

Where $\boldsymbol{M}^{MN}$ is the mass matrix (which is symmetric and positive definite),

$\boldsymbol{K}^{MN}$ is the stiffness matrix (which includes initial stiffness effects if the base state includes the effects of nonlinear geometry),

ϕ^N is the Eigenvector (the mode of vibration), and

M and N are degrees of freedom.

When $\boldsymbol{K}^{MN}$ is positive definite, all Eigenvalues are positive. Rigid body modes and instabilities cause $\boldsymbol{K}^{MN}$ to be indefinite. Rigid body modes produce zero Eigen values. Instabilities produce negative Eigenvalues and occur when you include initial stress effects. ABAQUS/Standard solves the Eigen frequency problem only for symmetric matrices.

CHAPTER 3

PARAMETRIC STUDY

3.1 Introduction

The verified and converged FEM developed in Chapter 2 was used to conduct a parametric study of poles with different combinations of the geometric parameters used by the Texas Department of Transportation (TxDOT) as reported by Jung et al. (2006) and Jung (2005).

The dependent variables consisted of the first, the second and the third modes of frequency, and the independent variables were defined as the pole geometric variables (pole length, plate thickness, thickness at the top of pole, thickness at the bottom of pole, diameter of bolt, diameter of pole at the bottom, diameter of pole at the top, clearance distance, diameter of the bolt circle, plate dimension, and pre-tension load). Prediction equations for dependent variable (frequency) versus independent variable (geometry) were developed for both circular and octagonal tapered poles. A sensitivity study on the validity of the equations was conducted by varying the independent variables one at a time, from low-to-intermediate-to-high values while keeping other independent variables at their intermediate values. This provided information with regard to the effect of each independent variable on the dependent variables.

Finally, the values of predicted dependent variables were compared with the FEA for additional prediction equation verification.

3.2 Selection of Test Cases

The 80 test cases for circular and octagonal poles selected by Jung (2005) and Jung et al. (2006) which were identified in TxDOT Project 0-4470 were used as the basis for the selection of parametric study cases. The definitions of the independent variables are:

- l = pole length
- t_p = plate thickness
- $t_{pole\text{-}top}$ = thickness at the top of pole
- $t_{pole\text{-}btm}$ = thickness at the bottom of pole
- d_b = diameter of bolt
- d_{btm} = diameter of pole at the bottom
- d_{top} = diameter of pole at the top
- c_d = clearance distance
- b_c = diameter of the bolt circle
- p_d = plate dimension
- F_p = pre-tension load
- F_y = yield stress
- E = elastic modulus
- e = 2.718

The definitions of the dependent variables are: the natural frequency of the first, second, and the third mode.

The following procedure was adopted to select the test matrix:

1) Pole height (l) was varied from 30 ft (6.1 m) to 60 ft (18.3 m) based on the practical design. Generally, less than 30 ft (6.1 m) high pole is installed by a direct burial. The height was increased by 5 ft (1.5 m).
2) Plate thickness (t_p) was varied from 0.5 in. (12.7 mm) to 1.75 in. (44.5 mm).
3) The pole thickness at the top ($t_{pole\text{-}top}$) and the bottom ($t_{pole\text{-}btm}$) of the pole was varied from 0.1 in. (2.5 mm) to 0.5 in. (12.7 mm).
4) Bolt diameter (d_b) sizes were adopted from the LRFD codes (AISC, 1999) which were varied between 0.75 in. (19.1 mm) and 2 in. (50.8 mm).
5) The pole's bottom and top diameters were varied from 7 in. (17.8 mm) to 18 in. (45.7 mm), and 4 in. (10.2 mm) to 10 in. (25.4 mm), respectively.
6) Installation gap was used to give adequate space for leveling. This gap was selected to be greater than or equal to the nut thickness due to the double nut configuration.
7) The tensile strength for steel (F_y) was limited to $F_y \leq 58$ ksi (400 MPa) and $F_y \leq 105$ ksi (724 MPa) for the pole and the bolt, respectively.
8) The edge distance between the centers of the bolt hole on the end-plate to the edge of the end-plate was selected to be 1.5 d_b per LRFD codes (AISC, 1999), as shown in Figure 3.1, to avoid the end-plate rupture.

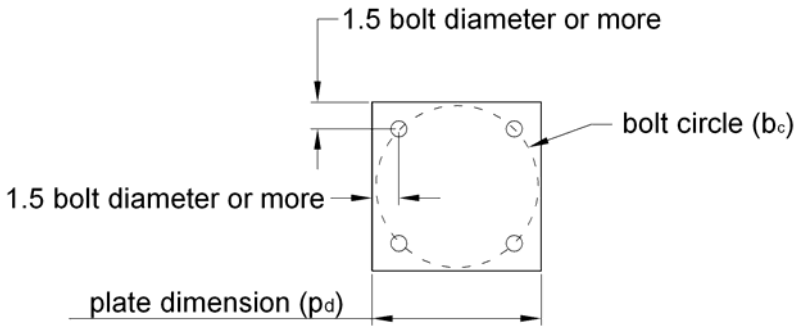

Figure 3.1 Pole end-plate.

9) The bolt minimum of bolt pre-tension load depends on the bolt diameter (AISC, 1999), which is shown in Table 3.1.

Table 3.1 Pre-tension Load Was Used.

Bolt Diameter (in)	0.5	0.75	1	1.25	1.5	1.75	2
Pre-tension Load (kips)	12	28	51	71	103	152	198

Tables 3.2 shows the selected test case based on the aforementioned variation of variables for circular steel poles.

Table 3.2 Independent Parameters Used for Circular Steel Poles.

Test Case	l ft	t_p in.	$t_{pole\text{-}top}$ in.	$t_{pole\text{-}btm}$ in.	d_b in.	d_{btm} in.	d_{top} in.	c_d in.	F_y ksi	b_c in.	p_d in.	F_p kips
1	40	1	0.2	0.3	1.25	11	7	3	50	15.5	14	71
2	40	1	0.3	0.2	1.5	12	6	3.75	50	17	17	103
3	40	1.25	0.2	0.2	1.25	11	6	3.5	50	16	15	71
4	40	1.25	0.2	0.25	1.5	14	8	3.5	50	19	18	103
5	40	1.5	0.2	0.25	1.75	12	6	3.75	50	18	18	152
6	40	1.5	0.25	0.25	1.5	16	9	3.25	50	22	20	103
7	40	1.5	0.25	0.3	1.25	12	7	2.75	50	16.5	16	71
8	45	1	0.2	0.25	1.25	12	5	3	50	16.5	14.5	71
9	45	1	0.25	0.25	1.5	12	5	3.25	50	17	17.5	103
10	45	1	0.3	0.3	1.5	12	5	3.5	50	17	19	103
11	45	1.25	0.2	0.2	1.25	11	4	2.75	50	16	16	71
12	45	1.25	0.2	0.3	1.5	12	6	3.5	50	17	17	103
13	45	1.25	0.3	0.2	1.25	11	8	3	50	15.5	14.5	71
14	45	1.5	0.2	0.2	1.25	11	8	3	50	15.5	15	71
15	45	1.5	0.3	0.3	1.75	13	8	4	50	19	18	152
16	45	1.5	0.3	0.4	1.25	11	6	3.75	50	16	14	71
17	45	1.75	0.2	0.2	1.5	14	7	3.5	50	19	17	103
18	50	1	0.2	0.25	1.5	14	7	3.5	50	19	17.5	103
19	50	1.25	0.15	0.2	1.5	12	7	3.25	50	17	15	103
20	50	1.25	0.2	0.2	1.25	11	6	3.5	50	15.5	15	71
21	50	1.25	0.3	0.4	1	11	6	3	50	15	14	51
22	50	1.5	0.25	0.25	2	18	9	4.25	50	26	26	198
23	50	1.5	0.3	0.3	2	18	10	4.5	50	26	26	198
24	50	1.75	0.3	0.3	1	7	5	3	50	10.5	9.5	51
25	50	1.75	0.3	0.2	1.75	14	7	4	50	20	18	152
26	55	1.25	0.3	0.2	1.25	11	5	3	50	15.5	14	71
27	55	1.5	0.2	0.2	1.5	12	8	3.5	50	17	16	103
28	55	1.75	0.25	0.25	2	15	9	4.5	50	22	21	198
29	60	1.25	0.2	0.25	1.5	16	9	3.25	50	22	19.5	103
30	60	1.5	0.2	0.3	1	7	5	3.5	50	10.5	10.5	51
31	60	1.5	0.3	0.3	1.75	14	8	3.5	50	20	18	152
32	60	1.75	0.25	0.25	1.5	16	8	3.5	50	22	19	103
33	60	1.75	0.3	0.3	1.5	12	8	3.5	50	17	15.5	103

Table 3.2 - *Continued*

Test Case	l ft	t_p in.	$t_{pole\text{-}top}$ in.	$t_{pole\text{-}btm}$ in.	d_b in.	d_{btm} in.	d_{top} in.	c_d in.	F_y ksi	b_c in.	p_d in.	F_p kips
34	60	1.75	0.3	0.3	1.75	16	8	3.5	50	23	21	152
35	60	0.75	0.5	0.5	0.5	16	9	3.25	50	22	19.5	12
36	60	0.75	0.5	0.5	0.5	16	9	3.25	50	22	19.5	12
37	60	0.75	0.5	0.5	0.75	16	9	3.25	50	22	19.5	28
38	60	0.75	0.5	0.5	1	16	9	3.25	50	22	19.5	51
39	60	0.75	0.5	0.5	1.25	16	9	3.25	50	22	19.5	71
40	60	0.5	0.5	0.5	0.75	16	9	3.25	50	22	19.5	28
41	60	0.75	0.5	0.5	0.75	16	9	3.25	50	22	19.5	28
42	60	1	0.5	0.5	0.75	16	9	3.25	50	22	19.5	28
43	60	1.25	0.5	0.5	0.75	16	9	3.25	50	22	19.5	28
44	60	0.75	0.25	0.25	0.75	16	9	3.25	50	22	19.5	28
45	60	0.75	0.5	0.5	0.75	16	9	3.25	50	22	19.5	28
46	60	0.75	0.75	0.75	0.75	16	9	3.25	50	22	19.5	28

Table 3.3 shows the selected test case based on the aforementioned variation of variables for octagonal steel poles.

Table 3.3 Independent Parameters Used for Octagonal Steel Poles.

Test Case	l ft	t_p in.	$t_{pole\text{-}top}$ in.	$t_{pole\text{-}btm}$ in.	d_b in.	d_{btm} in.	d_{top} in.	c_d in.	F_y ksi	b_c in.	p_d in.	F_p kips
1	40	1	0.2	0.3	1.25	11	7	3	50	15.5	14	71
2	40	1	0.3	0.2	1.5	12	6	3.75	50	17	17	103
3	40	1.25	0.2	0.2	1.25	11	6	3.5	50	16	15	71
4	40	1.25	0.2	0.25	1.5	14	8	3.5	50	19	18	103
5	40	1.5	0.2	0.25	1.75	12	6	3.75	50	18	18	152
6	40	1.5	0.25	0.25	1.5	16	9	3.25	50	22	20	103
7	40	1.5	0.25	0.3	1.25	12	7	2.75	50	16.5	16	71
8	45	1	0.2	0.25	1.25	12	5	3	50	16.5	14.5	71
9	45	1	0.25	0.25	1.5	12	5	3.25	50	17	17.5	103
10	45	1	0.3	0.3	1.5	12	5	3.5	50	17	19	103
11	45	1.25	0.2	0.2	1.25	11	4	2.75	50	16	16	71

Table 3.3 - *Continued*

Test	l	t_p	$t_{pole\text{-}top}$	$t_{pole\text{-}btm}$	d_b	d_{btm}	d_{top}	c_d	F_y	b_c	p_d	F_p
Case	ft	in.	in.	in.	in.	in.	in.	in.	ksi	in.	in.	kips
12	45	1.25	0.2	0.3	1.5	12	6	3.5	50	17	17	103
13	45	1.25	0.3	0.2	1.25	11	8	3	50	15.5	14.5	71
14	45	1.5	0.2	0.2	1.25	11	8	3	50	15.5	15	71
15	45	1.5	0.3	0.3	1.75	13	8	4	50	19	18	152
16	45	1.5	0.3	0.4	1.25	11	6	3.75	50	16	14	71
17	45	1.75	0.2	0.2	1.5	14	7	3.5	50	19	17	103
18	50	1	0.2	0.25	1.5	14	7	3.5	50	19	17.5	103
19	50	1.25	0.15	0.2	1.5	12	7	3.25	50	17	15	103
20	50	1.25	0.2	0.2	1.25	11	6	3.5	50	15.5	15	71
21	50	1.25	0.3	0.4	1	11	6	3	50	15	14	51
22	50	1.5	0.25	0.25	2	18	9	4.25	50	26	26	198
23	50	1.5	0.3	0.3	2	18	10	4.5	50	26	26	198
24	50	1.75	0.3	0.3	1	7	5	3	50	10.5	9.5	51
25	50	1.75	0.3	0.2	1.75	14	7	4	50	20	18	152
26	55	1.25	0.3	0.2	1.25	11	5	3	50	15.5	14	71
27	55	1.5	0.2	0.2	1.5	12	8	3.5	50	17	16	103
28	55	1.75	0.25	0.25	2	15	9	4.5	50	22	21	198
29	60	1.25	0.2	0.25	1.5	16	9	3.25	50	22	19.5	103
30	60	1.5	0.2	0.3	1	7	5	3.5	50	10.5	10.5	51
31	60	1.5	0.3	0.3	1.75	14	8	3.5	50	20	18	152
32	60	1.75	0.25	0.25	1.5	16	8	3.5	50	22	19	103
33	60	1.75	0.3	0.3	1.5	12	8	3.5	50	17	15.5	103
34	60	1.75	0.3	0.3	1.75	16	8	3.5	50	23	21	152

3.3 Development of the Frequency Equations

3.3.1 Basis of Regression Analysis

Regression equations are developed from sample data collected from numerous experiments conducted, to determine the values of the dependent parameters for predetermined values of independent parameters. However, the finite element analysis

is not a physical experiment in true sense; it is an analytical process for experiments. This is because the results for each case are completely deterministic and reproducible.

To perform the regression analysis, it is common procedure to represent the response of dependent parameter as a function of the independent parameters. In the parametric study, the three parameters of the pole are the response measured as functions of the independent parameters. These independent parameters for the 46 and 34 cases selected, as described in Tables 3.2 and 3.3, were the input data to the computer program, ABAQUS, which eventually were solved for the natural frequencies. Thus, the objective of the regression analysis was to develop equations for the parameters defining natural frequencies of the pole as functions of geometric parameters of the pole. For example, the following would be the form of the equation which is a function of certain parameters:

$$f = f(l, t_p, t_{pole-top}, t_{pole-btm}, d_b, d_{btm}, d_{top}, c_d, b_c, p_d) \tag{3.1}$$

Determination of the function f_1 is discussed in general terms as follows. Let

$$x = f(X_1, X_2, X_3, \ldots\ldots\ldots\ldots X_n) \tag{3.2}$$

be a function of n independent parameters, intended to fit data collected from a study. A linear (or summation) regression model for the function is written as

$$\begin{aligned} x = {} & C_0 + C_1X_1 + C_2\ X_2 + C_3X_3 + \ldots\ldots\ldots\ldots\ldots\ldots + C_nX_n + C_{12}X_1X_2 \\ & + C_{23}X_2X_3 + \ldots\ldots\ldots\ldots + C_{n1}X_nX_1 + C_{123}X_1X_2X_3 + \ldots\ldots\ldots\ldots \\ & + C_{123\ldots\ldots n}(X_1X_2X_3\ldots\ldots\ldots\ldots\ldots\ldots X_n) \end{aligned} \tag{3.3}$$

These techniques yield information on the relative significance of not only the main parameters $X_1, X_2, ..., X_n$, but also the interactions between the same parameters $X_1X_2X_3, ..., (X_1X_2...X_n)$. However, in most practical problems, such as the one studied, many of the higher-order interactions may be eliminated on the basis of physical and intuitive considerations. Probable interactions must, however, be included in the model. The behavior of the pole seems to be a simple solution considering the cantilever profile of the member, but there are many more parameters that can be considered in an analytical study and regression analysis. For example, bolt diameter, base diameter, base condition and connection, yield stress, plate thickness, and tapering can be factors contributing to the outcome. This possibility makes this type of an analytical study and regression analysis a complex and interesting study, but does not facilitate the complete defining of all the interactions.

If a linear regression model is not found satisfactory, an alternative method is the product regression model of the form:

$$x = C_0 X_1^{C_1} X_2^{C_2} ... X_n^{C_n} \tag{3.4}$$

This nonlinear regression method was used in this project because of the complexity of the interactions involved. This may be reduced to a linear regression model if the logarithms are taken off from both sides as shown below:

$$\ln x = \ln C_0 + C_1 \ln X_1 + C_2 X_2 + ... + C_n \ln X_n \tag{3.5}$$

Denoting the logarithms of the various parameters by prime superscripts, Equation 3.5 becomes:

$$x' = C_0' + C_1X_1' + C_2X_2' + ... + C_nX_n' \tag{3.6}$$

This is similar to the first group of terms in Equation 3.2. It should be noted that in Equation 3.6, product terms of the form X_1', X_2', X_3', etc., do not occur, so no interactions are present.

In this study, the coefficient C_0' and the exponents $C_1, C_2, ..., C_n$ in Equation 3.5 are determined by multiple regression analysis, so as to obtain the best least square fit to the data. With this method, the best fit regression equation is taken as the one which minimizes the sum of the squares of the deviations of the data points from the equation fit to the data. To demonstrate the basic principles, say that the value of the dependent variable predicted from the best fit equation is x_i', for any particular set of values, $X_{1i}', X_{2i}', X_{3i}', ..., X_{ni}'$, while it is measured (or directly determined) that the value is $\overline{x}_i$. Deviation of the predicted value from the measured value is given by:

$$\overline{x}_i - x_i' = \overline{x}_i - \left(C_0' + C_1x_{1i}' + C_2x_{2i}' + ... + C_nx_{ni}'\right) \tag{3.7}$$

The sum of the squares, S for m number of data is given by:

$$S = \sum_{i=1}^{m} \left(\overline{x}_i' - x_i'\right)^2 \tag{3.8}$$

The unknown coefficients $C_0', C_1, C_2, ..., C_n$ are determined by minimizing the quality S with respect to each coefficient; in other words, by setting it equal to zero, as shown below.

$$\frac{\partial S}{\partial C_0'} = \frac{\partial S}{\partial C_1} = \frac{\partial S}{\partial C_2} = ... = \frac{\partial S}{\partial C_n} = 0 \tag{3.9}$$

This will result in $(n+1)$ linear simultaneous equations from which the coefficients $C_0^{'}, C_1, C_2, ..., C_n$ can be determined. To determine C_0, the anti-logarithm of C_0' must be found.

A "goodness of fit" of the prediction equation is a comparison of S, the sum of the squares, and the deviations for the constant term C_0 above. The constant term model is:

$$S = C_0^{'} \tag{3.10}$$

and the sum of the squares of this model can be written as

$$S_0 = \sum_{i=1}^{m} \left(\bar{x}_i^{'} - x_0^{'}\right)^2 \tag{3.11}$$

in which $x_0^{'}$ is the mean. The difference between S_0 and S is called as the "sum of squares due to regression" and the ratio $\frac{(S_0 - S)}{S_0}$ is called as the "coefficient of multiple determination," R^2 which can also be written:

$$R^2 = 1 - \frac{S}{S_0} \tag{3.12}$$

A value of $R^2 = 1$ implies that S is zero and the regression prediction equation passes through all the data points. A value of $R^2 = 0.90$ means that 90 % of the sum of squares of the deviations of the observed (or directly determined) $\bar{x}_i^{'}$ values about their $x_0^{'}$ can be explained by the prediction equation obtained.

In the parametric study conducted, all the cases considered had the independent parameters inputted into the finite element computer program, ABAQUS, and the output was the response of the dependent parameters. Therefore, a rerun of the same case would have the same quantitative response, thus, not providing any information regarding the realistic variance in the response. The coefficient of multiple determination R^2 was the unique criterion used to measure the accuracy of the prediction equations to characterize the behavior of the typical pole.

3.3.2 Equations of Pole's Natural Frequency

Three empirical equations are obtained for the first, second, and third mode frequencies by conducting regression analyses. This is accomplished by multiplication of the undetermined powers for all the geometric parameters. It simply implies that the changes in these geometric parameters are independent to each other (independent variables), thus, they are independent variables. The aforementioned empirical equations for the first, second, and third frequency modes as well as the coefficients of determination (R^2) are presented in Equations 3.13 through 3.15 for the circular poles and Equations 3.16 through 3.18 for the octagonal poles.

The prediction equations for circular poles are:

<u>1st Mode:</u> <u>R^2=0.987</u>

$$f = e^{10.2439} \cdot l^{-1.8914} \cdot t_p^{0.1846} \cdot t_{pole-top}^{-0.3361} \cdot t_{pole-btm}^{0.2278} \cdot d_b^{0.1918} \cdot d_{btm}^{1.4904} \cdot d_{top}^{-0.1997} \cdot c_d^{-0.1734} \cdot b_c^{-0.5289} \cdot p_d^{0.0797} \quad (3.13)$$

<u>2nd Mode:</u> <u>R^2=0.983</u>

$$f = e^{11.2437} \cdot l^{-1.8289} \cdot t_p^{0.0574} \cdot t_{pole-top}^{-0.1552} \cdot t_{pole-btm}^{0.0456} \cdot d_b^{0.0783} \cdot d_{btm}^{0.6863} \cdot d_{top}^{0.2483} \cdot c_d^{-0.1641} \cdot b_c^{0.0258} \cdot p_d^{0.0258} \quad (3.14)$$

<u>3rd Mode:</u> <u>R^2=0.977</u>

$$f = e^{11.9885} \cdot l^{-1.8084} \cdot t_p^{0.0116} \cdot t_{pole-top}^{-0.1063} \cdot t_{pole-btm}^{0.0004} \cdot d_b^{0.0399} \cdot d_{btm}^{0.4497} \cdot d_{top}^{0.3905} \cdot c_d^{-0.1680} \cdot b_c^{0.2009} \cdot p_d^{0.0061} \quad (3.15)$$

The prediction equations for octagonal poles are:

<u>1st Mode:</u> <u>R^2=0.998</u>

$$f = e^{11.0081} \cdot l^{-2.0086} \cdot t_p^{0.1102} \cdot t_{pole-top}^{-0.2880} \cdot t_{pole-btm}^{0.2325} \cdot d_b^{0.1813} \cdot d_{btm}^{1.2842} \cdot d_{top}^{-0.1966} \cdot c_d^{-0.0483} \cdot b_c^{-0.3110} \cdot p_d^{0.0248} \quad (3.16)$$

<u>2nd Mode:</u> <u>R^2=0.999</u>

$$f = e^{12.5319} \cdot l^{-1.9854} \cdot t_p^{0.0929} \cdot t_{pole-top}^{-0.1115} \cdot t_{pole-btm}^{0.0368} \cdot d_b^{0.1160} \cdot d_{btm}^{0.8855} \cdot d_{top}^{0.1987} \cdot c_d^{-0.0266} \cdot b_c^{-0.2609} \cdot p_d^{0.0273} \quad (3.17)$$

<u>3rd Mode:</u> <u>R^2=0.997</u>

$$f = e^{13.3695} \cdot l^{-1.9520} \cdot t_p^{0.0657} \cdot t_{pole-top}^{-0.0637} \cdot t_{pole-btm}^{-0.0123} \cdot d_b^{0.1170} \cdot d_{btm}^{0.7732} \cdot d_{top}^{0.3149} \cdot c_d^{-0.0029} \cdot b_c^{-0.2726} \cdot p_d^{0.0193} \quad (3.18)$$

By utilizing Equations 3.13 through 3.18, a sensitivity study was conducted for 46 circular pole cases and 34 octagonal pole cases to identify the effect of the total pole assembly geometric variables on its first three natural frequencies. This was done by varying one variable at a time, from its low-to-medium-to-high values while keeping other variables at their intermediate values. The sensitivity plots identify the effect of each independent variable (pole geometric variable) on the behavior of the dependent variable (frequency). For example, a steep slope on such a graph indicates that the effect

of that independent variable is significant. On the other hand, if the effect of variation of the independent variable is insignificant, the graph would have a flat slope.

For example, the effects of the pole's length and the bottom diameter, with the steepest slopes as shown in Figures 3.2 (a) and 3.2 (b), respectively, are the highest on the natural frequency. On the other hand, the effect of the gap distance between the pole's end-plate and the concrete base is insignificant on the pole's natural frequency, as shown in Figures 3.2(c) and 3.2 (d).

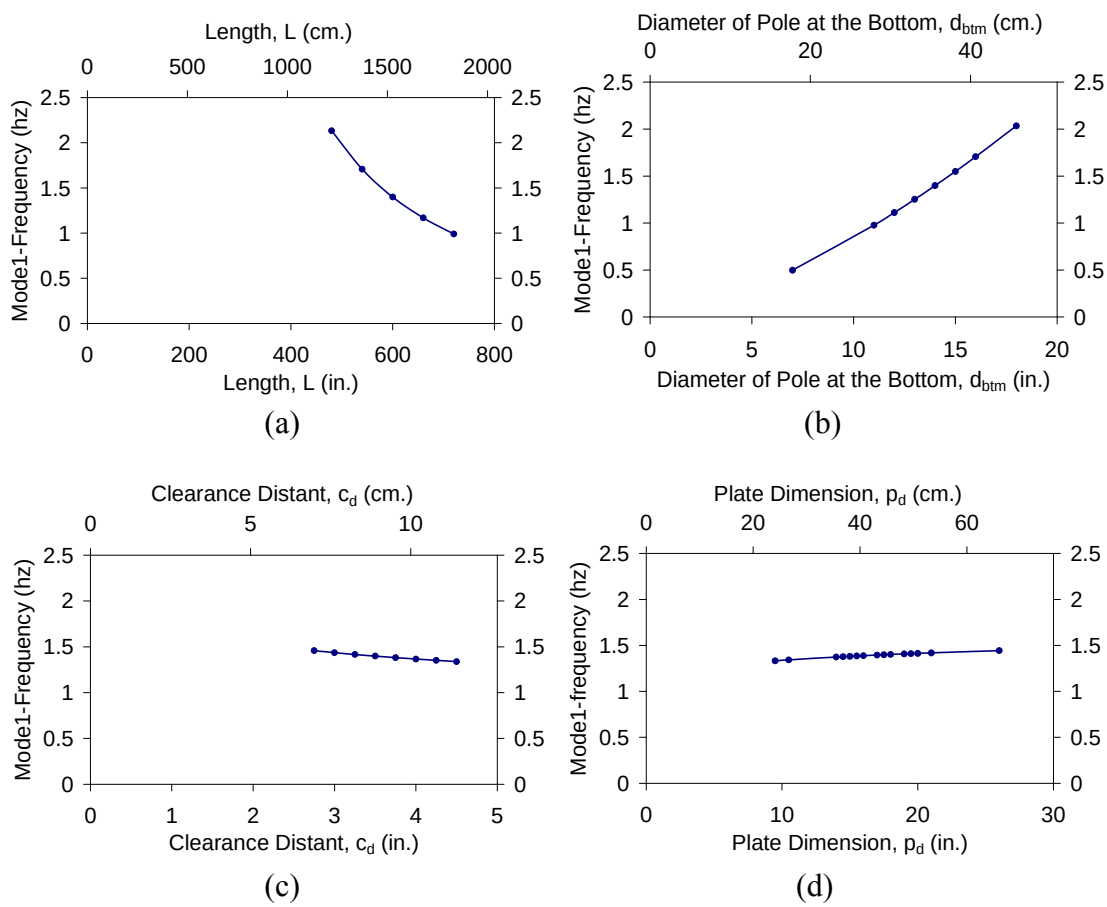

Figure 3.2 Sensitivity analyses for the first mode of octagonal pole with the changing in: (a) Length, (b) Pole diameter at bottom, (c) Clearance distance, (d) Plate dimension.

Furthermore, study on the sensitivity of independent variables is shown in Appendix C, which shows the effect of each independent variable on the pole's frequency for the first, second and third mode of the circular and octagonal poles, respectively. The results of natural frequencies and deformation mode shape of the circular and octagonal pole are shown in Appendices A and B, respectively.

3.4 Comparison Between Predicted and Experimental Vibrational Frequencies

The developed equations (Equations 3.13 through 3.18) for the first, second, and third frequency modes of the circular and octagonal poles were compared to those obtained from the finite element analyses. Figure 3.3 shows a plot comparing the predicted and FEM frequency results, which shows a close correlation. Tables 3.4 and 3.5 present the percentage error between the FEM and the predicted results, the mean square error of the predicted results for the cases studied. The prediction equations are accutely predict the first two important natural frequency of the pole since they obtained the low mean square error.

It should be noted that Figure 3.3 can be used as an envelope defining a range of frequency values for the three vibrational modes (from 0.56 Hz to 33.68 Hz). The information from Figure 3.3 was used to develop the mechanical device, which is presented in Chapter 4.

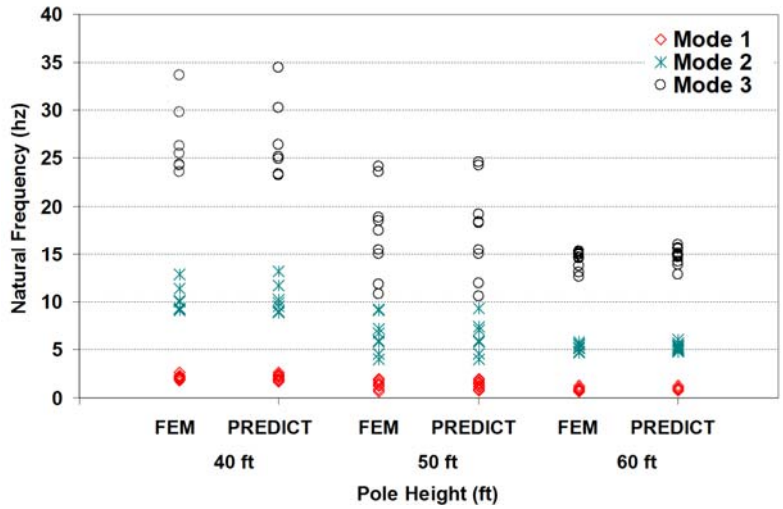

Figure 3.3 Comparison between predicted and FEM results.

Table 3.4 Error Comparisons Between the Predicted and the FEM Results of Circular Poles

Case	Mode 1			Mode 2			Mode 3		
No.	Predicted (Hz)	FEM (Hz)	Error (%)	Predicted (Hz)	FEM (Hz)	Error (%)	Predicted (Hz)	FEM (Hz)	Error (%)
1	1.88	1.91	-1.23	9.50	9.30	2.12	25.12	24.42	2.80
2	1.69	1.78	-5.19	8.82	9.19	-4.19	23.31	24.30	-4.24
3	1.78	1.84	-3.12	8.91	9.05	-1.57	23.27	23.59	-1.35
4	2.43	2.26	7.19	11.67	11.35	2.74	30.29	29.85	1.47
5	2.21	2.20	0.34	9.86	10.02	-1.65	24.90	25.46	-2.27
6	2.64	2.56	2.86	13.11	12.83	2.17	34.40	33.68	2.11
7	2.13	2.08	2.30	10.18	10.12	0.53	26.36	26.31	0.19
8	1.72	1.69	1.77	7.46	7.29	2.27	18.76	18.34	2.29
9	1.61	1.64	-1.50	7.23	7.27	-0.58	18.32	18.39	-0.35
10	1.56	1.60	-2.48	7.00	7.14	-2.04	17.75	18.12	-2.06
11	1.61	1.58	2.20	6.75	6.69	0.90	16.72	16.60	0.69
12	1.80	1.80	0.03	7.90	7.91	-0.09	19.95	19.97	-0.08
13	1.23	1.25	-1.76	7.41	7.46	-0.68	20.55	20.60	-0.27
14	1.45	1.44	1.17	7.98	7.89	1.05	21.50	21.24	1.20
15	1.65	1.69	-2.44	8.47	8.67	-2.29	22.36	22.89	-2.36

Table 3.4 - *Continued*

Case	Mode 1			Mode 2			Mode 3		
No.	Predicted (Hz)	FEM (Hz)	Error (%)	Predicted (Hz)	FEM (Hz)	Error (%)	Predicted (Hz)	FEM (Hz)	Error (%)
16	1.49	1.55	-3.75	6.95	7.21	-3.65	17.85	18.51	-3.71
17	2.02	1.93	4.71	9.18	9.16	0.31	23.33	23.52	-0.84
18	1.57	1.56	0.77	7.41	7.18	3.10	19.16	18.44	3.73
19	1.45	1.41	2.92	7.03	6.74	4.24	18.28	17.40	4.82
20	1.19	1.20	-0.96	5.91	5.90	0.16	15.44	15.37	0.46
21	1.21	1.24	-2.63	5.76	5.81	-0.75	14.95	14.95	-0.01
22	1.93	1.90	1.42	9.33	9.10	2.43	24.25	23.57	2.81
23	1.84	1.83	0.38	9.30	9.15	1.66	24.55	24.08	1.91
24	0.75	0.73	2.50	3.99	4.02	-0.66	10.59	10.80	-1.94
25	1.42	1.40	1.85	7.06	7.16	-1.35	18.36	18.80	-2.39
26	0.92	0.91	1.35	4.57	4.51	1.28	11.90	11.74	1.31
27	1.09	1.07	2.53	5.83	5.68	2.60	15.56	15.13	2.79
28	1.35	1.34	0.81	6.85	6.82	0.49	18.03	17.93	0.54
29	1.28	1.46	-13.9	6.40	7.87	-23.08	16.89	21.38	-26.5
30	0.58	0.56	1.87	2.94	2.91	1.15	7.73	7.66	0.91
31	1.07	1.04	2.96	5.40	5.21	3.43	14.20	13.66	3.83
32	1.28	1.21	5.13	6.05	5.78	4.45	15.62	14.91	4.54
33	0.91	0.88	3.28	4.80	4.72	1.72	12.76	12.57	1.48
34	1.26	1.21	4.39	6.01	5.76	4.26	15.55	14.85	4.53
35	0.81	0.79	2.07	5.10	5.12	-0.27	14.58	14.57	0.05
36	0.88	0.87	0.51	5.27	5.26	0.10	14.82	14.87	-0.37
37	0.93	0.95	-2.30	5.39	5.41	-0.38	14.99	15.08	-0.59
38	0.97	1.01	-4.74	5.48	5.55	-1.28	15.12	15.28	-1.05
39	0.81	0.72	11.0	5.15	5.05	1.98	14.75	14.62	0.90
40	0.88	0.87	0.51	5.27	5.26	0.10	14.82	14.87	-0.37
41	0.92	0.96	-4.29	5.36	5.44	-1.49	14.87	15.09	-1.48
42	0.96	1.04	-7.96	5.43	5.60	-3.15	14.91	15.31	-2.68
43	0.94	0.92	2.74	5.68	5.41	4.78	15.95	15.21	4.60
44	0.88	0.87	0.51	5.27	5.26	0.10	14.82	14.87	-0.37
45	0.84	0.83	0.55	5.04	5.13	-1.88	14.19	14.56	-2.58
46	0.81	0.74	8.55	4.88	4.59	5.99	13.77	12.99	5.66
	Mean square error = 0.37			**Mean square error = 1.85**			**Mean square error = 5.41**		

Table 3.5 Error Comparisons Between the Predicted and the FEM Results of Octagonal Poles

Case	Mode 1			Mode 2			Mode 3		
No.	Predicted (Hz)	FEM (Hz)	Error (%)	Predicted (Hz)	FEM (Hz)	Error (%)	Predicted (Hz)	FEM (Hz)	Error (%)
1	1.99	1.98	0.74	9.71	9.63	0.87	25.25	25.20	0.20
2	1.85	1.84	0.63	9.54	9.48	0.71	25.18	25.00	0.71
3	1.89	1.88	0.40	9.39	9.46	-0.80	24.37	24.84	-1.93
4	2.52	2.49	1.34	12.18	12.24	-0.51	31.36	31.82	-1.46
5	2.32	2.39	-2.94	10.50	10.72	-2.09	26.56	27.06	-1.88
6	2.69	2.66	1.16	13.48	13.26	1.64	34.70	32.48	6.39
7	2.16	2.15	0.22	10.52	10.46	0.64	26.97	27.13	-0.56
8	1.77	1.77	0.23	7.62	7.59	0.41	19.08	19.02	0.34
9	1.70	1.69	0.56	7.52	7.52	0.09	19.07	18.99	0.39
10	1.67	1.66	0.93	7.41	7.39	0.25	18.80	18.71	0.51
11	1.63	1.63	0.23	6.90	6.90	0.00	17.06	17.10	-0.27
12	1.86	1.86	0.18	8.21	8.17	0.46	20.73	20.60	0.66
13	1.27	1.29	-1.32	7.61	7.71	-1.30	20.84	21.24	-1.94
14	1.46	1.48	-1.23	8.10	8.12	-0.31	21.64	21.83	-0.88
15	1.75	1.75	0.17	8.96	8.94	0.24	23.57	23.58	-0.04
16	1.58	1.59	-0.39	7.40	7.40	0.01	18.93	19.00	-0.35
17	2.01	1.97	1.99	9.60	9.55	0.61	24.49	24.65	-0.62
18	1.61	1.63	-1.38	7.46	7.49	-0.38	19.17	19.14	0.13
19	1.45	1.46	-0.54	7.00	6.96	0.54	18.14	17.96	1.02
20	1.22	1.24	-1.54	6.07	6.08	-0.11	15.89	15.83	0.43
21	1.24	1.27	-2.55	5.87	5.95	-1.38	15.09	15.33	-1.57
22	1.98	1.98	0.33	9.48	9.43	0.58	24.36	24.32	0.15
23	1.92	1.91	0.49	9.54	9.50	0.43	24.83	24.88	-0.22
24	0.77	0.75	3.00	4.21	4.13	1.95	11.28	11.09	1.68
25	1.46	1.44	1.43	7.46	7.37	1.32	19.52	19.33	0.98
26	0.93	0.94	-0.40	4.65	4.65	0.03	12.15	12.10	0.40
27	1.09	1.10	-0.94	5.84	5.85	-0.15	15.60	15.58	0.18
28	1.38	1.38	-0.23	7.03	7.03	0.00	18.50	18.47	0.21
29	1.25	1.19	4.59	6.07	5.96	1.89	15.76	15.66	0.62
30	0.59	0.58	1.13	3.01	2.99	0.58	8.03	7.89	1.74
31	1.07	1.07	-0.24	5.36	5.38	-0.39	14.06	14.09	-0.21
32	1.24	1.25	-1.04	5.96	5.96	0.04	15.30	15.35	-0.32
33	0.91	0.91	-0.08	4.84	4.86	-0.35	12.90	12.93	-0.28
34	1.24	1.25	-0.53	5.92	5.95	-0.44	15.19	15.32	-0.84
	Mean square error = 0.13			**Mean square error = 0.43**			**Mean square error = 2.48**		

CHAPTER 4

ENNERGY DISSIPATION CHARACTERISTIC OF POLES

4.1 Introduction

In this chapter, cyclic loads were applied to 34 selected cases of circular poles to study the hysteresis loop of the poles with respect to a variety of the poles' geometrical parameters. The displacement control algorithm was used in ABAQUS to apply the displacement at the tip of the pole (Figure 4.1). The amplitude of the displacement followed the current criteria in FEMA-350 (FEMA 2000a) and the AISC LRFD Seismic Provisions (AISC 2002). The FEMA 2000a criteria are based on Ricles et al. (2000).

The finite element study involved modeling the circular poles to evaluate the effect of variety geometrical parameters on poles' behavior. These included: the pole size, the pole thickness, the pole height, the bolt diameter, and the end plate thickness. The ABAQUS Standard (ABAQUS 2006) was used to develop three-dimensional nonlinear finite element models of the circular poles as shown in Table 4.1

Geometric nonlinearities were accounted by using the small strain, large displacement formulation. A von Mises material with strain-hardening was used to account for material nonlinearities.

Table 4.1 Independent Parameters of Circular Steel Poles Used for Cyclic Study.

Test Case	l ft	t_p in.	$t_{pole\text{-}top}$ in.	$t_{pole\text{-}btm}$ in.	d_b in.	d_{btm} in.	d_{top} in.	c_d in.	F_y ksi	b_c in.	p_d in.	F_p kips
1	40	1	0.2	0.3	1.25	11	7	3	50	15.5	14	71
2	40	1	0.3	0.2	1.5	12	6	3.75	50	17	17	103
3	40	1.25	0.2	0.2	1.25	11	6	3.5	50	16	15	71
4	40	1.25	0.2	0.25	1.5	14	8	3.5	50	19	18	103
5	40	1.5	0.2	0.25	1.75	12	6	3.75	50	18	18	152
6	40	1.5	0.25	0.25	1.5	16	9	3.25	50	22	20	103
7	40	1.5	0.25	0.3	1.25	12	7	2.75	50	16.5	16	71
8	45	1	0.2	0.25	1.25	12	5	3	50	16.5	14.5	71
9	45	1	0.25	0.25	1.5	12	5	3.25	50	17	17.5	103
10	45	1	0.3	0.3	1.5	12	5	3.5	50	17	19	103
11	45	1.25	0.2	0.2	1.25	11	4	2.75	50	16	16	71
12	45	1.25	0.2	0.3	1.5	12	6	3.5	50	17	17	103
13	45	1.25	0.3	0.2	1.25	11	8	3	50	15.5	14.5	71
14	45	1.5	0.2	0.2	1.25	11	8	3	50	15.5	15	71
15	45	1.5	0.3	0.3	1.75	13	8	4	50	19	18	152
16	45	1.5	0.3	0.4	1.25	11	6	3.75	50	16	14	71
17	45	1.75	0.2	0.2	1.5	14	7	3.5	50	19	17	103
18	50	1	0.2	0.25	1.5	14	7	3.5	50	19	17.5	103
19	50	1.25	0.15	0.2	1.5	12	7	3.25	50	17	15	103
20	50	1.25	0.2	0.2	1.25	11	6	3.5	50	15.5	15	71
21	50	1.25	0.3	0.4	1	11	6	3	50	15	14	51
22	50	1.5	0.25	0.25	2	18	9	4.25	50	26	26	198
23	50	1.5	0.3	0.3	2	18	10	4.5	50	26	26	198
24	50	1.75	0.3	0.3	1	7	5	3	50	10.5	9.5	51
25	50	1.75	0.3	0.2	1.75	14	7	4	50	20	18	152
26	55	1.25	0.3	0.2	1.25	11	5	3	50	15.5	14	71
27	55	1.5	0.2	0.2	1.5	12	8	3.5	50	17	16	103
28	55	1.75	0.25	0.25	2	15	9	4.5	50	22	21	198
29	60	1.25	0.2	0.25	1.5	16	9	3.25	50	22	19.5	103
30	60	1.5	0.2	0.3	1	7	5	3.5	50	10.5	10.5	51
31	60	1.5	0.3	0.3	1.75	14	8	3.5	50	20	18	152
32	60	1.75	0.25	0.25	1.5	16	8	3.5	50	22	19	103
33	60	1.75	0.3	0.3	1.5	12	8	3.5	50	17	15.5	103
34	60	1.75	0.3	0.3	1.75	16	8	3.5	50	23	21	152

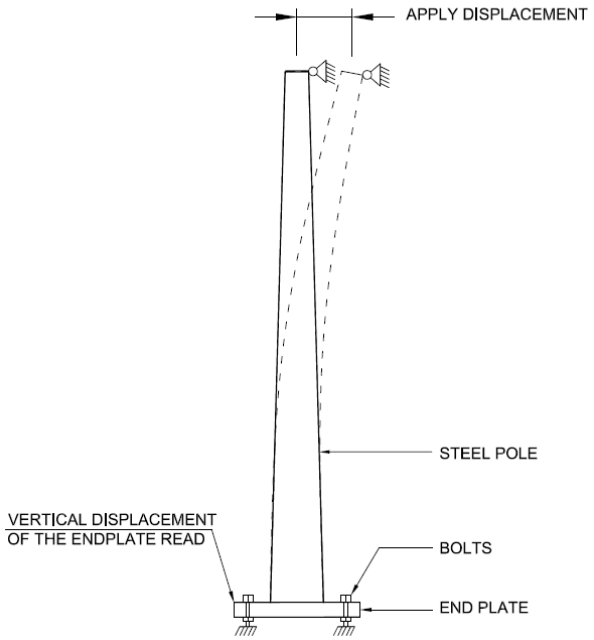

Figure 4.1 The schematic of displacement control for cyclic study

A typical three-dimensional finite element model of end-plate connection is shown in Figure 4.2

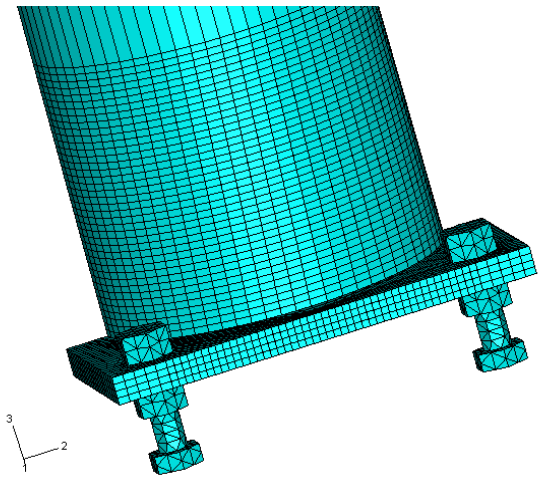

Figure 4.2 Typical 3-D model of pole end-plate

The brick C3D8 element was employed to model the pole; the number of elements used for the circular pole ranged from 5682 elements to 13789 elements, and 9761 to 21048 nodes, which results in 29283 to 63144 degrees of freedom. A convergence study of the model was described in Chapter 3.

4.2 Material model

A linear kinematic hardening model (ABAQUS, 2006) was used in ABAQUS to simulate the behavior of the materials of the poles subjected to cyclic loading. The evolution law in these models consists of a kinematic hardening component, which describes the translation of the yield surface in stress space. The Bauschinger effect was employed by ABAQUS as shown in Figure 4.3.

4.2.1 Elastic response

The ABAQUS plasticity models also require an elasticity definition to deal with the recoverable part of the strain. In ABAQUS the elasticity is defined by including linear elastic behavior or, if relevant for some plasticity models, porous elastic behavior in the same material definition. In the case of the von Mises and Johnson-Cook plasticity models in ABAQUS the elasticity can alternatively be defined by using an equation of state with associated deviatoric behavior. When performing an elastic-plastic analysis at finite strains, ABAQUS assumes that the plastic strains dominate the deformation and that the elastic strains are small. This restriction is imposed by the elasticity models that ABAQUS uses. It is justified because most materials have a well-defined yield point that is a very small percentage of their Young's modulus; for example, the yield stress of metals is typically less than 1% of the Young's modulus of

the material. Therefore, the elastic strains will also be less than this percentage, and the elastic response of the material can be modeled accurately as being linear.

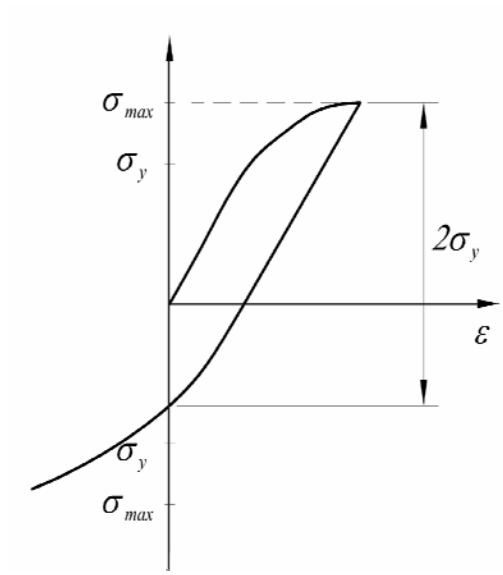

Figure 4.3 The Bauschinger effect

In ABAQUS the elastic strain energy reported is updated incrementally. The incremental change in elastic strain energy (ΔE_s) is computed as

$$\Delta E_s = \Delta E_t - \Delta E_p \qquad (4.1)$$

where ΔE_t is the incremental change in total strain energy and ΔE_p is the incremental change in plastic energy dissipation.

The incremental change in elastic strain energy (ΔE_s) is much smaller than ΔE_t and ΔE_p for increments in which the deformation is almost all plastic. Approximations in the calculations of ΔE_t and ΔE_p result in deviations from the true solutions that are insignificant compared to ΔE_t and ΔE_p but can be significant relative to ΔE_s. Typically, the elastic strain energy solution is quite accurate, but in some rare

cases the approximations in the calculations of ΔE_t and ΔE_p can lead to a negative value reported for the elastic strain energy. These negative values are most likely to occur in an analysis that uses rate-dependent plasticity. As long as the absolute value of the elastic strain energy is very small compared to the total strain energy, a negative value for the elastic strain energy should not be considered an indication of a serious solution problem (ABAQUS, 2006).

4.2.2 Plasticity theories

Most materials of engineering interest initially respond elastically. Elastic behavior means that the deformation is fully recoverable. When the load is removed, the specimen returns to its original shape. If the load exceeds the yield load, the deformation is no longer fully recoverable. Some part of the deformation will remain when the load is removed.

Plasticity theories model the material's mechanical response as it undergoes such non-recoverable deformation in a ductile fashion. The theories have been developed most intensively for metals, but they are also applied to soils, concrete, rock, ice, crushable foam, and so on. These materials behave in very different ways. For example, large values of pure hydrostatic pressure cause very little inelastic deformation in metals, but quite small hydrostatic pressure values may cause a significant, non-recoverable volume change in a soil sample. Nonetheless, the fundamental concepts of plasticity theories are sufficiently general that models based on these concepts have been developed successfully for a wide range of materials.

Most of the plasticity models in ABAQUS are "incremental" theories in which the mechanical strain rate is decomposed into an elastic part and a plastic part. Incremental plasticity models are usually formulated in terms of a yield surface, which generalizes the concept of "yield load" into a test function that can be used to determine if the material responds purely elastically at a particular state of stress, temperature, etc; a flow rule, which defines the inelastic deformation that occurs if the material point is no longer responding purely elastically; and evolution laws that define the hardening - the way in which the yield and/or flow definitions change as inelastic deformation occurs.

4.2.3 Stress-strain relationship

The stress-strain relationship was used in conjunction with the assumption that the material is a von Mises material and associated the flow rule. The hardening model used in the analysis included combined nonlinear isotropic and kinematic strain. The relationship of stress and strain of the material as shown below:

$$\sigma_{true} = \sigma_{eng}(1 + \varepsilon_{eng})$$

$$\varepsilon_{true}^{pl} = \ln(1 + \varepsilon_{eng}) - \frac{\sigma_{true}}{E}$$

where: σ_{true} and ε_{true}^{pl} are the true stress and true plastic strain respectively.

σ_{eng} and ε_{eng} are the engineering stress and strain, respectively.

E: Young's modulus.

The material model is show in Figures 4.3a and 4.3b.

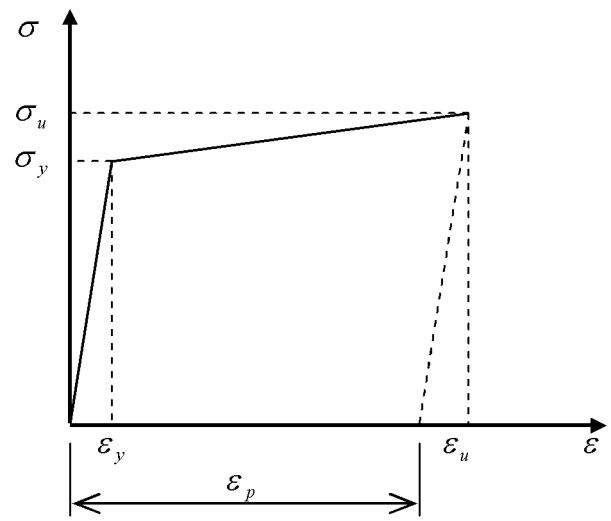

Figure 4.4 Stress-strain hardening curve of material

For the bolts, the first yield occurs at 81 ksi (558 MPa). The material then hardens to 105 ksi (724 MPa) at 20 percent strain (ASTM A325). Assuming that the Young's modulus is 29,000 ksi (200 GPa), the plastic strain at the 20 percent strain point is $\varepsilon_p = 0.144$. For the pole and end-plate, first yield occurs at 36 ksi (248 MPa). The material then hardens to 58 ksi (400 MPa) at 20 percent strain (ASTM A36). Assuming that the Young's modulus is 29,000 ksi (200 GPa), the plastic strain at the 20 percent strain point is $\varepsilon_p = 0.175$.

4.3 Loading protocol

The analyses were conducted by applying the increasing cyclic variable amplitude displacement at the top of the pole. The cyclic displacement amplitude followed the loading protocol in the AISC Seismic Provisions (AISC 2002), which is

identical to the SAC loading protocol (1997). The loading protocol composed of the following steps was incorporated in ABAQUS:

- Step 1: 6 cycles with peak drift angle of 0.00375 rad
- Step 2: 6 cycles with peak drift angle of 0.005 rad
- Step 3: 6 cycles with peak drift angle of 0.0075 rad
- Step 4: 4 cycles with peak drift angle of 0.01 rad
- Step 5: 2 cycles with peak drift angle of 0.015 rad
- Step 6: 2 cycles with peak drift angle of 0.02 rad
- Step 7: 2 cycles with peak drift angle of 0.03 rad
- Step 8 and further steps will be repeated with the drift angle of 0.01 rad for each 2 cycles until the pole reaches inelastic mode. The loading protocol is shown in Figure 4.5.

The amplitude of pole displacement varies, depending on the pole height, which is shown in Figures 4.6 to 4.10

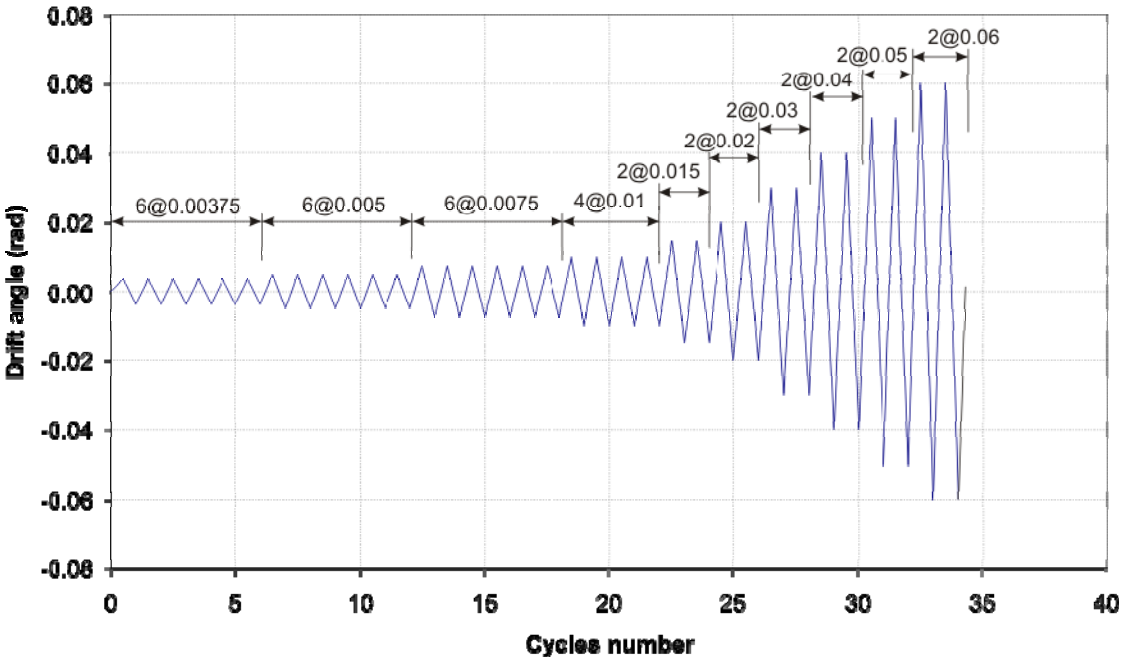

Figure 4.5 Loading protocol (AISC, 2002)

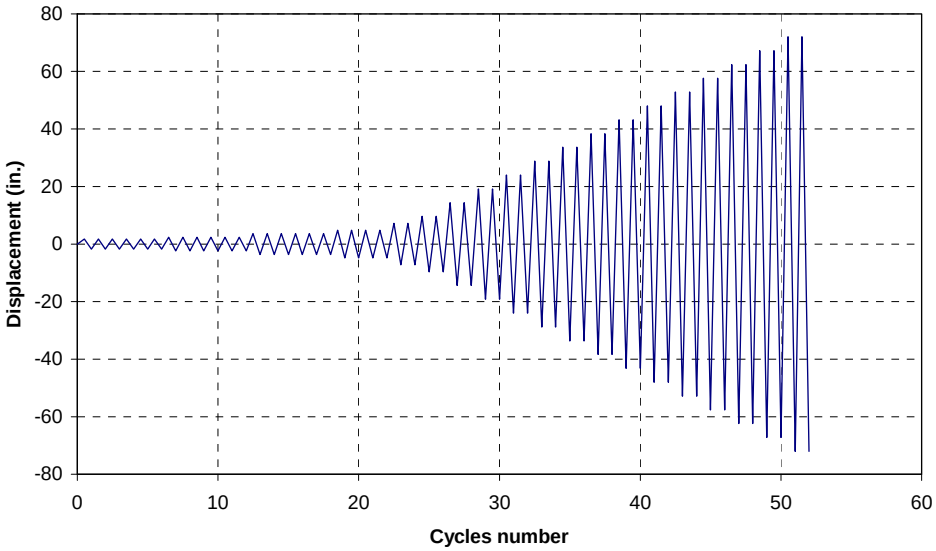

Figure 4.6 Loading protocol for 40 ft pole

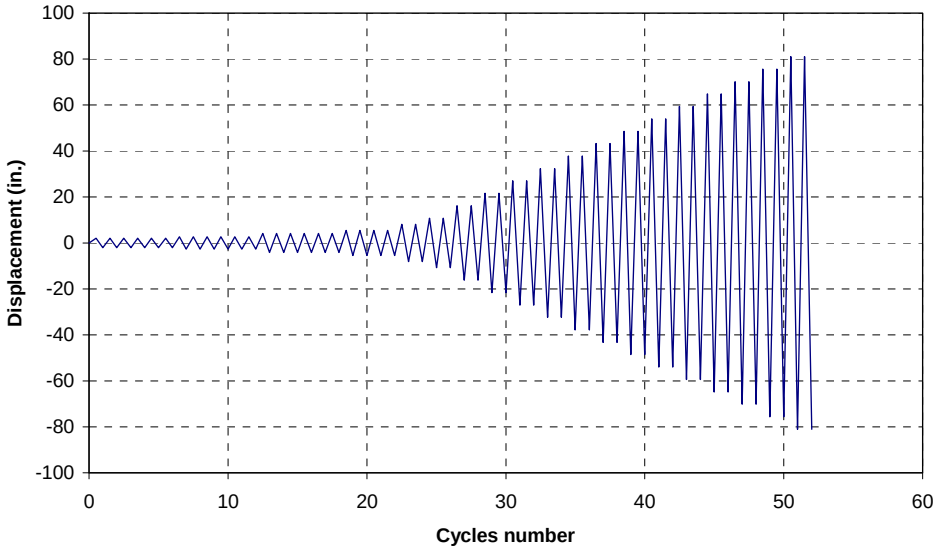

Figure 4.7 Loading protocol for 45 ft pole

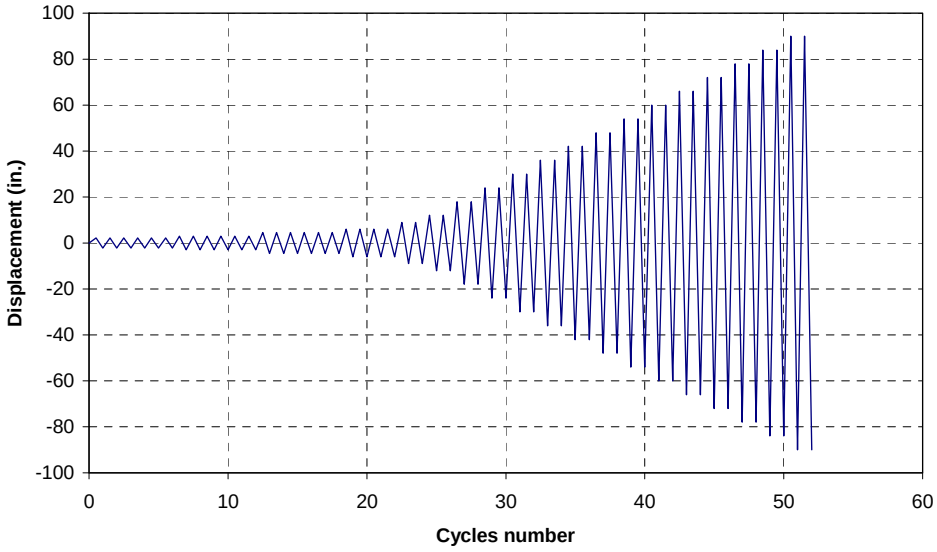

Figure 4.8 Loading protocol for 50 ft pole

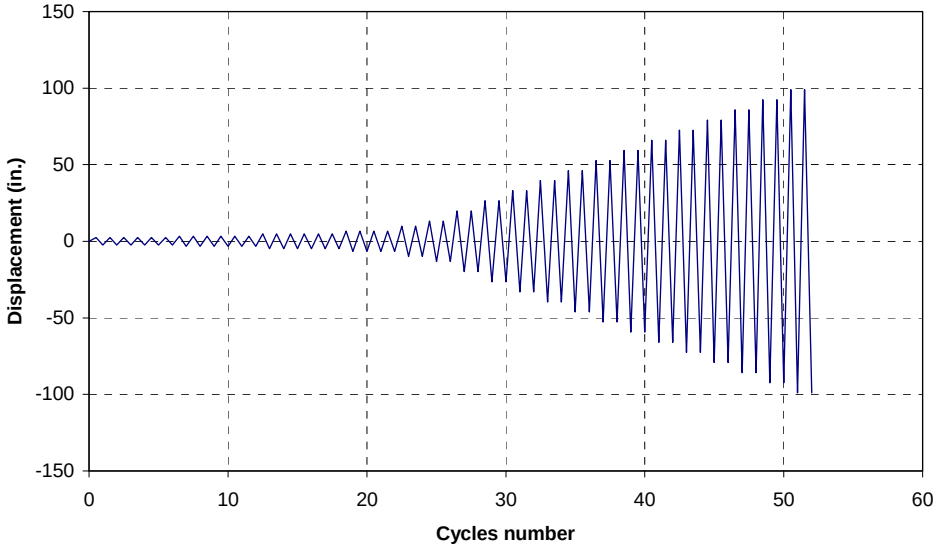

Figure 4.9 Loading protocol for 55 ft pole

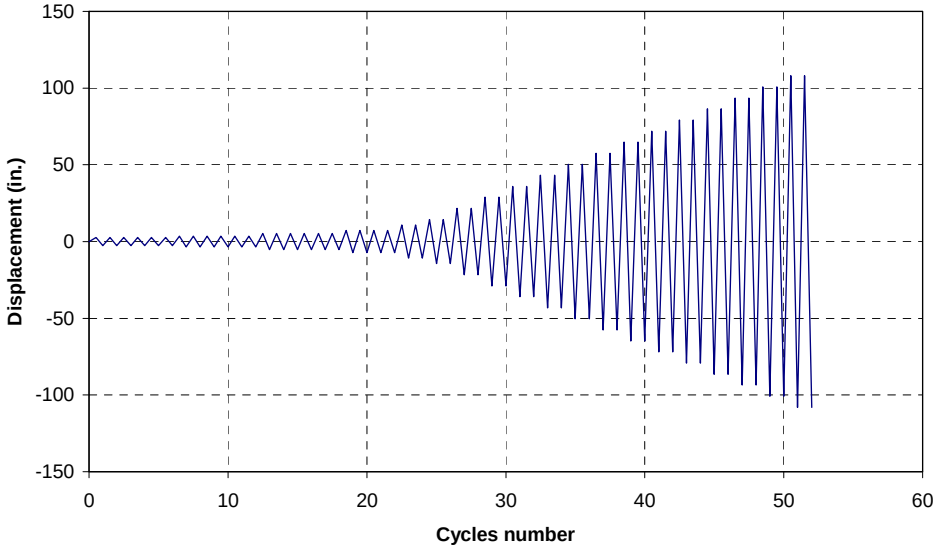

Figure 4.10 Loading protocol for 60 ft pole

4.4 Result Discussion

The dissipation energy of different steel poles geometry is summarized in the Table 4.2. The range of dissipated energy is from 22 kip-ft-rad (30 kN-m-rad) of case 30th to 2,253,049 kip-ft-rad (3,055,148 kN-m-rad) of case 29th. Figures 4.11-4.14 are the dot plot of dissipated energy in the categorizing of pole height, pole thickness, bolt diameter, and the end-plate thickness. The normalized hysteresis loop of all cases was plot in Appendix D.

Table 4.2 Result of Hysteresis Analysis

Test No.	Normalized Moment	Normalized Moment	Normalized Rotation	Dissipated Energy	Dissipated Energy
	Kip-ft	kN-m		Kip-ft-Rad	kN-m-Rad
1	600	814	333	909,469	1,233,240
2	600	814	500	57,780	78,350
3	500	678	667	20,588	27,917
4	800	1085	333	1,073,131	1,455,166
5	600	814	1000	59,447	80,610
6	1000	1356	250	1,126,963	1,528,162
7	600	814	250	280,871	380,861
8	300	407	1000	53,072	71,966
9	300	407	1000	5,802	7,868
10	500	678	333	43,205	58,586
11	450	610	500	2,555	3,465
12	600	814	400	43,232	58,623
13	400	542	1000	40,227	54,548
14	400	542	1000	34,907	47,334
15	500	678	1000	29,822	40,439
16	600	814	1000	34,602	46,920
17	500	678	1000	51,346	69,625
18	450	610	667	172,561	233,993
19	400	542	1000	74,987	101,682
20	250	339	1333	2,375	3,221
21	400	542	500	186,661	253,112
22	850	1153	667	80,868	109,657
23	1000	1356	286	1,318,662	1,788,106
24	200	271	10000	132	179
25	600	814	2000	10,346	14,029
26	300	407	1000	4,266	5,785
27	400	542	2000	5,726	7,764
28	800	1085	1000	17,840	24,191
29	700	949	333	2,253,059	3,055,148
30	200	271	5000	22	30
31	600	814	667	50,315	68,227
32	600	814	1000	155,450	210,790
33	600	814	1000	6,252	8,478
34	1000	1356	500	73,106	99,132

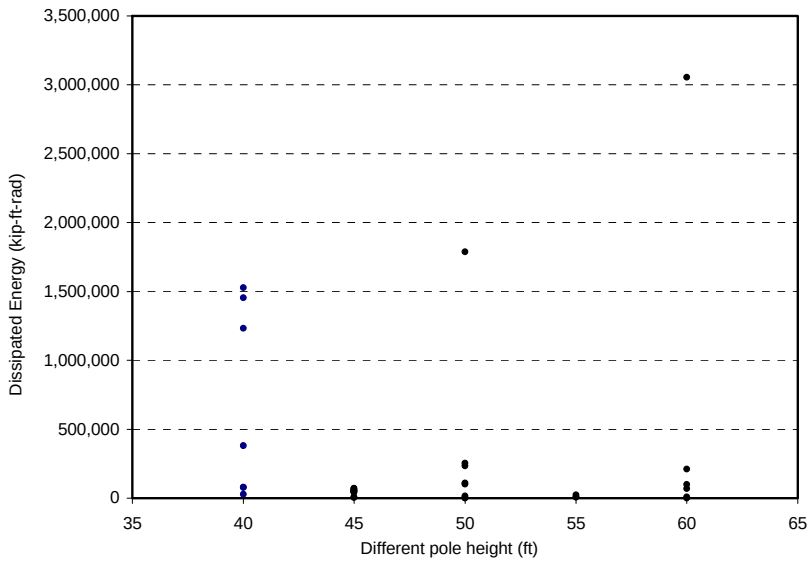

Figure 4.11 Dissipated energy vs. pole height

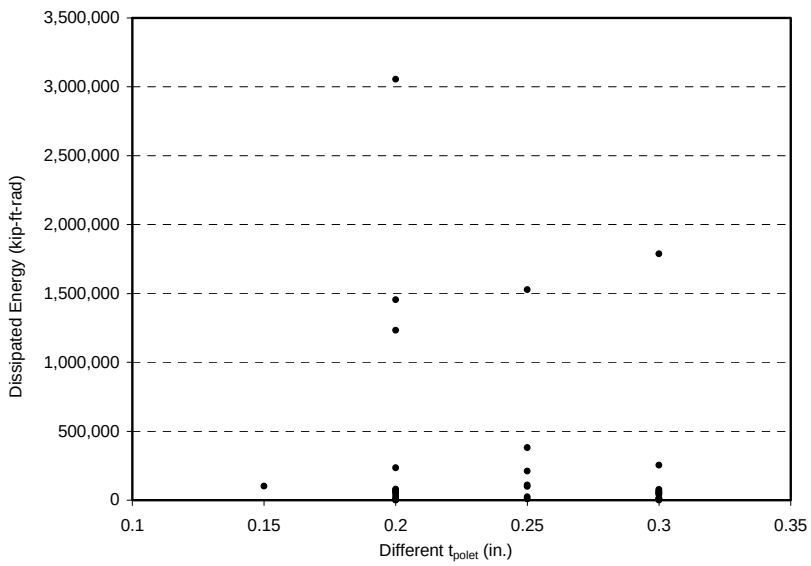

Figure 4.12 Dissipated energy vs. pole thickness

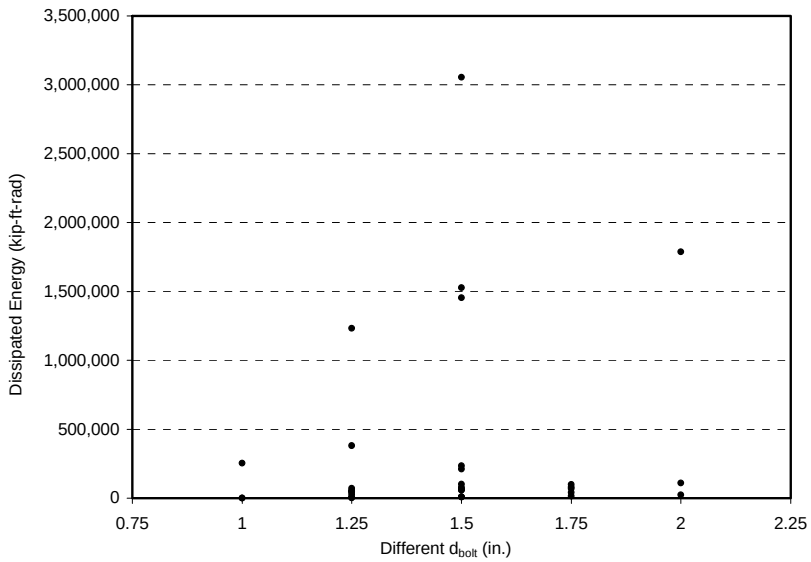

Figure 4.13 Dissipated energy vs. bolt diameter

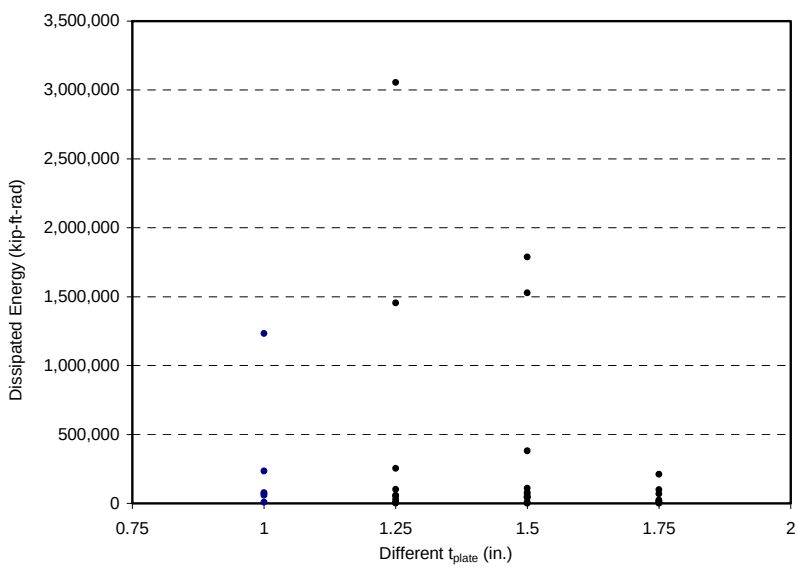

Figure 4.14 Dissipated energy vs. end-plate thickness

CHAPTER 5

DEVELOPMENT OF MECHANICAL VIBRATION ISOLATOR

5.1 Introduction

This chapter describes the engineering analysis, development and testing of a low-cost, biaxial mechanical vibration isolator specifically aimed at high-frequency motion abatement in pole mounted camera applications and similarly conditioned supports. The device works on the principle of force and displacement transmissibility reduction via the use of a lightly damped sprung interface with a tuned natural frequency. The isolator is inserted between the top of the pole and the seat of the camera, and operates by rejecting undesirable high-frequency modal vibrations experienced by the main support. This has the effect of diminishing high-acceleration ground inputs which are principally responsible for image distortion. By design, the isolator trades its high-frequency performance for a low-frequency heave, which does not induce blur but causes limited horizon shift. This characteristic is complementary to that of electronic image stabilization technology, whose performance suffers when significant motion is present in the incoming video feed. For this reason, the proposed mechanical solution is prescribed as an ancillary technique to image processing in installations where high-frequency or displacement conditions prevail at the camera support.

5.2 Theoretical Isolator Design

The fundamental principle of a passive, spring-mass isolator is to introduce tuned amounts of energy storage (inertia, springs) and dissipation (damping) between two mechanically connected bodies in order to reduce the transmission of high-frequency forces and displacements at their interface. In practice, one of the bodies is responsible for the undesirable high-energy "input" motions from which a second body is to be isolated. A standard CCTV installation described above represents such a case, where the dominant pole dynamics are directly transmitted to the camera through a bolted flange. Figure 5.1 depicts the passive isolator principle that replaces a rigid connection.

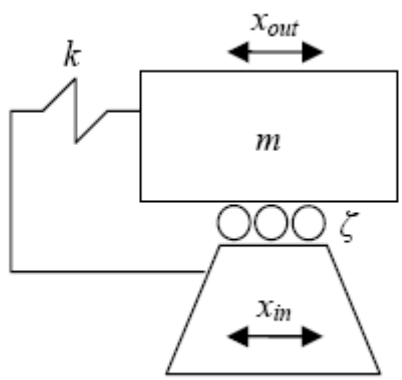

Figure 5.1 Passive mechanical isolation.

Our principal objective becomes to insert a mechanism at the seat of the camera with engineered mass, spring, and damper such that a minimum of pole vibration (x_{in}) is experienced by the camera (x_{out}). However, a second and equally important design constraint is imposed by the fact that once isolated, the spring-mass is subject to wind loading which must evidently be taken into account. These two problems will be

considered in turn. Absent disturbance forces acting on the spring-mass, the figure of merit in isolator design is the transmissibility ratio (TR), which describes the proportion of input displacement reproduced at the output. This figure identically describes the transmitted force, and it is a function of the isolator dynamics and the excitation frequency. Equations 5.1 (a) and 5.1 (b) concisely expresses this relationship in terms of damping ratio ζ and the ratio of input frequency to spring-mass natural frequency r_ω:

$$TR = \sqrt{\frac{1 + (2\zeta r_\omega)^2}{(1 - r_\omega^2)^2 + (2\zeta r_\omega)^2}} \tag{5.1 a}$$

Where

$$r_\omega = \frac{\omega_{in}}{\omega_n} = \frac{\omega_{in}}{\sqrt{\left(\frac{k}{m}\right)_{sprung}}} \tag{5.1 b}$$

The plots in Figure 5.2 describe the value of transmissibility as a function of its two non-dimensional parameters ζ and r_ω; the horizontal line of 100% transmissibility represents direct motion transfer (as if rigidly attached), while values below represent isolation.

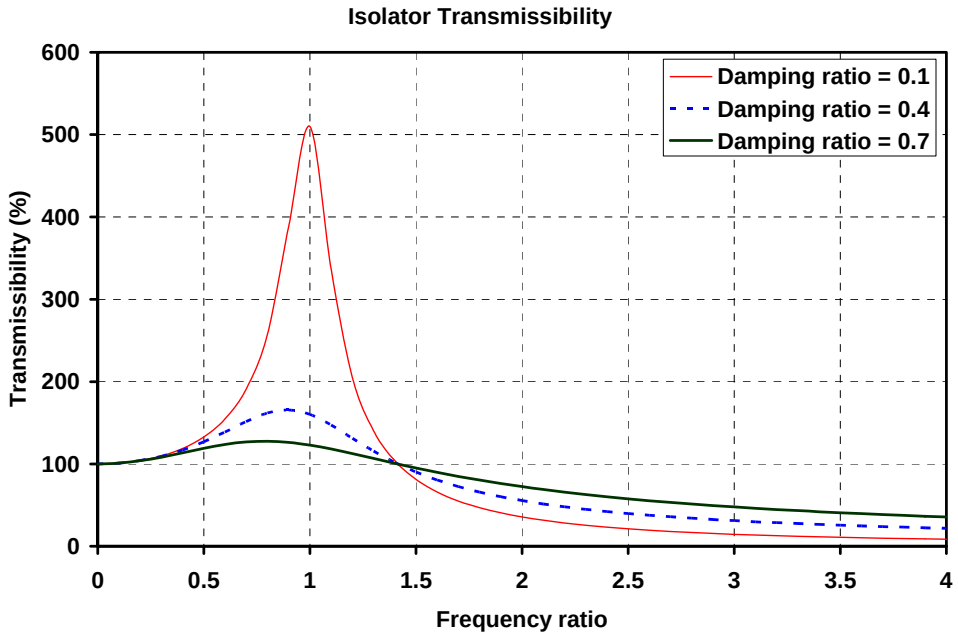

Figure 5.2 Non-dimensional isolation performances.

Several characteristics are immediately apparent. First, the isolator is effective at high input frequencies specifically above ratios to the spring-mass frequency of approximately 1.4, to the right of which an isolation region is defined. Second, the isolator actually amplifies, or at best directly transfers, input signals in the low-frequency (non-isolation) region. Third, the damping ratio has a substantial influence in isolation performance, particularly in the non-isolation region where a resonant input frequency would cause theoretically infinite displacements at the spring-mass. Finally, total isolation is approached asymptotically, but never actually achieved. This ideal state is realized only in the trivial case of zero damping and spring forces; i.e., a perfect bearing. As described in the previous section, the pole input dynamics have superimposed vibratory displacements at discrete modal frequencies, with the highest

energy content typically found in the first and second modes (1-2 Hz and 5-10 Hz for high-altitude poles). Taking 1 Hz as a worst case, an ideal isolator design appears that by setting the natural sprung-mass frequency below 0.7 Hz (1/1.4) as practical. For example, given a set of bearings with ζ =0.1, an isolator with a resonant frequency of 0.6 Hz would decrease the first two modal displacements to 58% and 3% of their input value. Conveniently, the isolator performs best where it matters most, since image quality rapidly degrades in proportion to frequency. A relatively slow (1 Hz) heave may be tolerable or easily stabilized electronically, whereas a 5 Hz shake is liable to render the image unusable.

The matter of fabricating a "0.6 Hz isolator" with a suitably low damping ratio is, however, constrained by both equipment limitations and wind loading effects. Attaining a low isolator frequency requires a combination of soft springs and heavy suspended mass within practical range. Frictional values affecting the damping ratio are important to a lesser extent, and depend upon the design and quality of the bearings. These and other design implementation matters are addressed in the following sections.

5.3 Practical Isolator Design

We first consider spring-mass selection. The weight of a typical camera plus positioner unit used by TxDOT as of this writing (Cohu Manual, 2002), is about 28 lb, with newer models weighing half as much. Even with the heaviest equipment, the sought-after 0.6 Hz isolator would require a spring with a stiffness as low as 0.7 lb/in. Though commercially available, the use of such light springs would be impractical for two reasons. First, any amount of static (non-linear) friction present at the bearings

would easily overpower the weak centering force provided by such a spring, creating stick-slip behavior and reducing the effective range of travel in the slide due to off-center settling of the camera. Second, and most importantly, the spring alone react wind forces directly impinging on the camera; weak springs would result in undue camera displacements which, in addition to unintended panning, would force the isolator against its mechanical limits where its effectiveness is lost. Inevitably, wind considerations alone demand that a sufficiently stiff spring be chosen first. In order to obtain a working estimate of the aerodynamic force F_d acting on the camera, we use a wind drag (Munson et al., 1994) model given by:

$$F_d = \frac{1}{2} C_d \rho A u^2 \tag{5.2}$$

In the above formula, ρ is the density of air, u is the design wind speed, A is the maximum projected area, and C_d is the drag coefficient. C_d is approximated as 0.9; this is a working value between the theoretical drag of a flat plate and that of a cylinder considering that the camera casing has smooth rounded edges. This estimate applies for Reynolds numbers in excess of 100,000, which holds true for the wind loads and characteristic lengths under consideration. The area A for the camera in our example comes from its lateral (largest) projection, shown in Figure 5.3; its value is estimated from CAD models as 0.74 ft^2.

Figure 5.3 Side view of typical CCTV camera for aerodynamic loading estimates.

A static force balanced against wind drag may be used to arrive at an appropriate, first-order spring stiffness value; resonant gusts may occasionally occur, but are not a prevailing condition and thus not a design consideration. In the equation below, y_{max} represents the limiting spring-mass displacement.

$$ky_{\max} = F_d \tag{5.3}$$

The matter of selecting y_{max} raises the question of whether any amount of camera motion would pan or otherwise degrade the image. It happens, as a fortunate artifice of optics, that small transverse camera motions (axial or lateral) cause virtually imperceptible shifts in image horizon in panoramic views. Laboratory and field tests have shown that image quality is not compromised by camera displacements as large as ±1.5 in. even though such motions become increasingly noticeable as the image comes under heavy magnification. For design purposes, the value of y_{max} is thus selected as 1.5 in. based on experimental knowledge. To complete the solution of Equations 5.2

and 5.3, we must finally select an arbitrary design wind speed where the isolator would be at the limit of its functional range. A working value of 60 mph is offered based on three considerations. First, this threshold is far in excess of the 10-14 mph Texas average, as reported by the National Climatic Data Center (www.ncdc.noaa.gov/oa/climate/online/ccd/avgwind.html) from records kept over 48 years. Second, it lies at the high end of the state average wind gust strength (40-60 mph, according to data collected by the National Institute of Standards and Technology (www.itl.nist.gov/div898/winds/data/NISTTTU/wind_speed_data.txt)), given that we have applied conservative area and drag coefficient models. Third, gusts exceeding this value will only cause a momentary disturbance in the isolator performance, and designing for the highest conceivable wind speed requires an impractically heavy suspended mass. In light of these factors, we arrive at a spring rate of 4 lb/in. for our case study; the velocity square relation to displacement is shown in Figure 5.4. It is clear, in any case that a camera design with a low aerodynamic profile (e.g., dome enclosure, no sun visor), is of interest in order to minimize its susceptibility to wind.

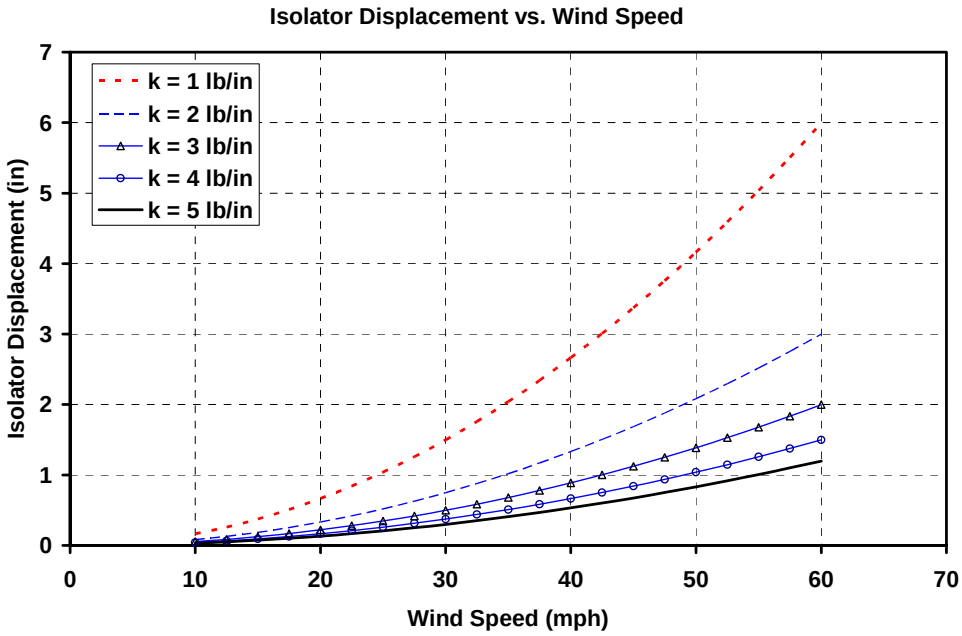

Figure 5.4 Wind speed vs. deflection characteristics for case study.

With a spring stiffness value established, we can now solve for the required inertia of the spring-mass in order to achieve a 0.6 Hz isolation frequency. Using a spring rate of 4 lb/in. in Equations 5.1 (a) and (b), we find that we would need to add approximately 100 lb ballast to the camera.

5.4 Isolator Operational Envelopes

Going beyond the example provided above, we may solve Equations 5.1 (a) and (b) through Equation 5.3 to produce a set of performance envelopes that generalize the passive isolator design for pole-mounted cameras. Since there is a large set of parameters which could feasibly be varied, we selected as input parameters the three most important (and often conflicting) ones: transmissibility ratio, wind speed, and spring-mass. We held constant, using values from the previous example, the camera

aerodynamic properties (drag coefficient and characteristic length), slide damping ratio, and maximum slide displacement. To generate the graphs, we used representative pole frequencies of interest, which included the first and second modes for 50 ft (1.8 / 8.5 Hz) and 60 ft (0.9 / 4.7 Hz). Figure 5.5 below shows the relationship between wind speed and spring-mass for varying pole frequencies, assuming a nominal transmissibility of 50%. This plot shows the confluence high wind loads and low input frequencies, both of which contribute nonlinearly and adversely to the need for heavy spring-masses. As in subsequent graphs, we find that the lowest pole frequencies are problematic for a passive isolator, while higher frequencies result in values that are both reasonable and easy to implement.

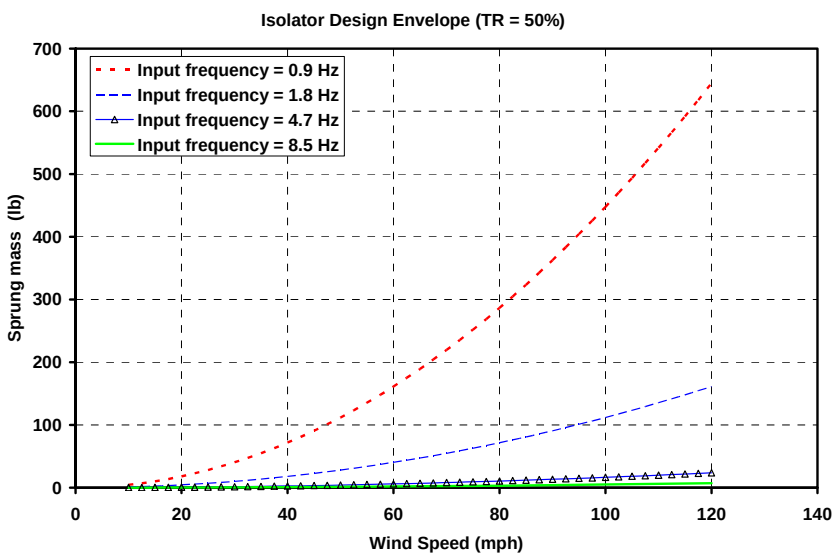

Figure 5.5 Wind speed vs. spring-mass assuming 50% transmissibility for different pole frequencies.

Figure 5.6 illustrates the equally critical and acute effect of low transmissibility ratios, showing that even away from the worst frequency and wind loading scenarios (1.8 Hz and 60 mph), wholly impractical spring-mass values become necessary when trying to reach high vibration isolation levels. This is an artifact of the asymptotic trend toward complete isolation mentioned previously, and the result is that passive isolators should not be used for transmissibility ratios below 10-15% due to a precipitous loss of effectiveness.

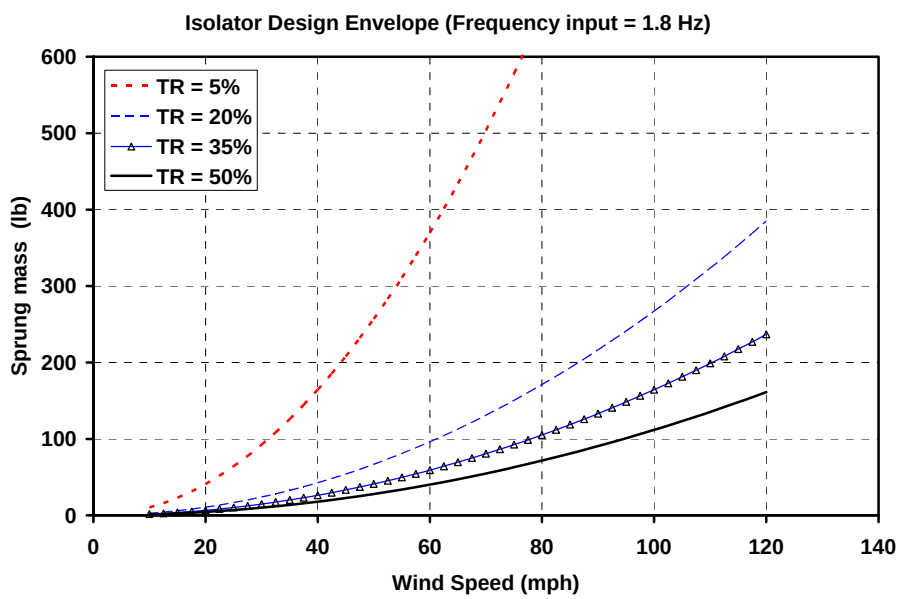

Figure 5.6 Wind speed vs. spring-mass assuming 1.8 Hz pole frequency for different transmissibility ratios.

Figure 5.7 further illustrates the sensitivity of the passive isolator design to transmissibility ratio and frequency. These graphs apply to the second and third lowest vibration frequency cases; of note is the substantially lower spring-mass requirement when the isolator is targeted at the second mode rather than the first mode vibratory

modes for the poles under consideration (the spring-mass axis scale has been kept the same to accentuate this fact).

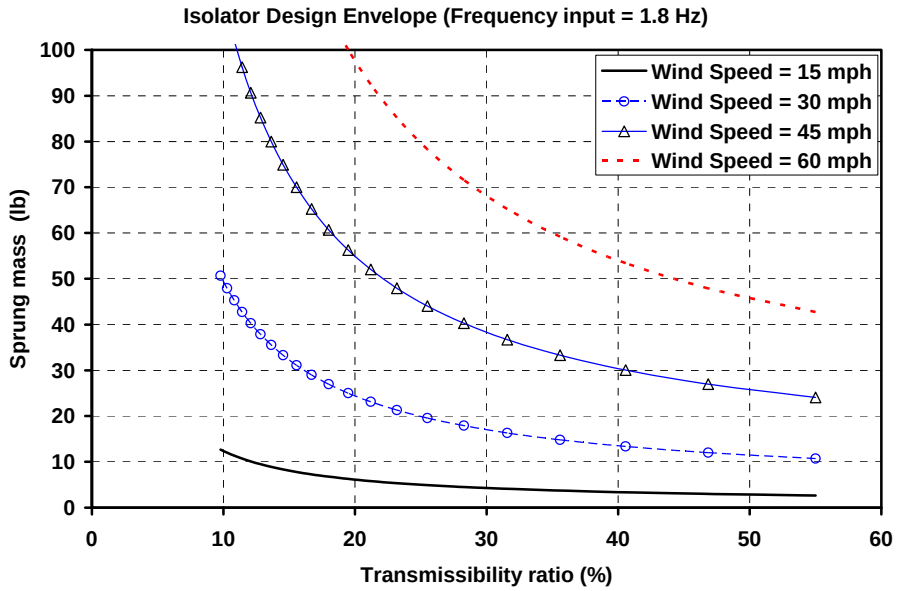

Figure 5.7 Transmissibility ratios vs. spring-mass assuming 1.8 Hz pole frequency for different wind speeds.

While the performance envelopes (Figure 5.8) make it clear that passive isolation is best suited to abate high pole dynamics, the fundamental mode will always be present and must be properly accounted for in isolators whose natural frequency exceeds that of the fundamental mode. In such cases, the low-frequency component in fact operates in the non-isolation region and is amplified. This compromise is acceptable when other means are available to cope with low-frequency heave (e.g., electronic image stabilization). Isolators which exercise this compromise must verify that the amplification of the low-frequency heave is kept within acceptable bounds (15-25%), by making sure that the fundamental frequency is sufficiently higher than the isolator natural frequency to avoid resonance.

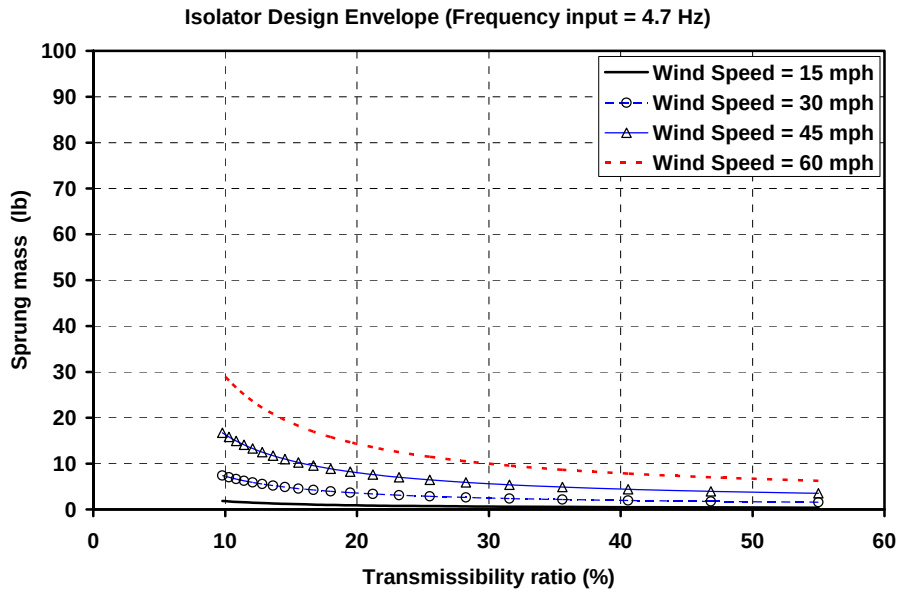

Figure 5.8 Transmissibility ratios vs. spring-mass assuming 4.7 Hz pole frequency for different wind speeds.

In a typical case, good transmissibility reductions may be achieved for the second mode (TR<0.3) at the penalty of a moderately amplified first mode (TR<1.25); for this to occur, ratios of input frequency to isolator frequency must be below 0.5. As an example of this important point, let us return to the 60 ft pole initially considered (0.9 / 4.7 Hz modal frequencies) and target only the second modal frequency for abatement. From Equations 5.1 (a) and (b) and Figure 5.4, an isolator frequency of 2 Hz will provide input to isolator frequency ratios of 0.45 and 2.45. The corresponding transmissibility ratios for these values are 1.25 and 0.24, meaning that the isolator will amplify 0.9 Hz pole heave by 25%, but in doing so it will suppress 4.7 Hz amplitudes that cause severe image distortion by over 75% (ζ=0.1). If this exchange is acceptable, a 2 Hz isolator may be easily implemented, for a camera weight of 28 lb, through the use

of 11.6 lb/in. springs without adding any ballast. Figure 5.9 below illustrates the operating points for each pole frequency.

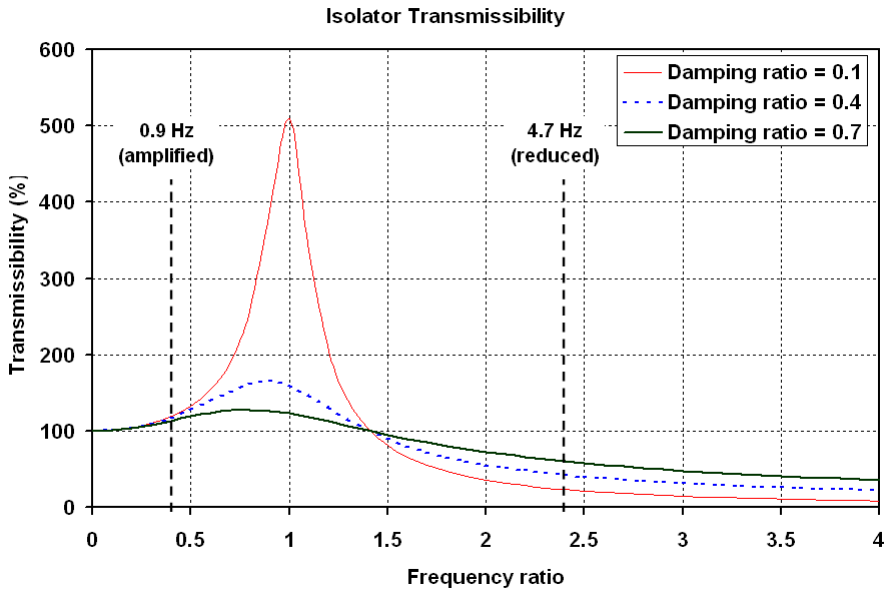

Figure 5.9 Transmissibility ratios vs. spring-mass assuming 4.7 Hz pole frequency for different wind speeds.

5.5 Mechanical Configuration

In order to achieve omni-directional isolation for the camera on the X-Y (horizontal) plane, we must at minimum provide for free motion of the spring-mass along said axes. It was observed in the previous section that transverse camera motions are both necessary and acceptable; by contrast, camera rotation about the vertical axis does result in significant image panning, owing to the geometry of angular displacement magnified over distance. In consequence, the bearing configuration requires the exclusive use of two orthogonal translational stages; such that rotational motion is fully constrained (this is somewhat regrettable, since X-Y-θ isolation turns out to have an easier and more compact mechanical solution than the needed X-Y configuration). The

resulting lack of rotational isolation is not of concern, since the pole does not normally experience loads which excite torsional dynamics. Of the available options to enforce transverse X-Y constraints, the most straightforward is to clock two linear slides at 90° with respect to one another. There is a large selection of linear bearings in the market from which to choose; as a practical matter, because the camera tether issues out of its bottom (Figure 5.10), parallel slide models where a clearance center hole can be machined provide the most compact and convenient packaging. The initial field prototype used in this work uses a commercial, instrument-grade XY table customized similar to that shown in Figure 5.11.

Figure 5.10 Pigtail connector for typical CCTV cameras.

Figure 5.11 XY table with parallel slides and center clearance.

An interface plate is required to mate the seat of the camera to the top slide, and this provides a convenient means to increase the inertia of the spring-mass to the required value where needed. Figure 5.12 shows the major design elements for a passive mechanical isolator pole interface plate, biaxial sprung slides, and tuned ballast mass rendered in CAD (not shown are the springs and end-of-travel cushioning elements).

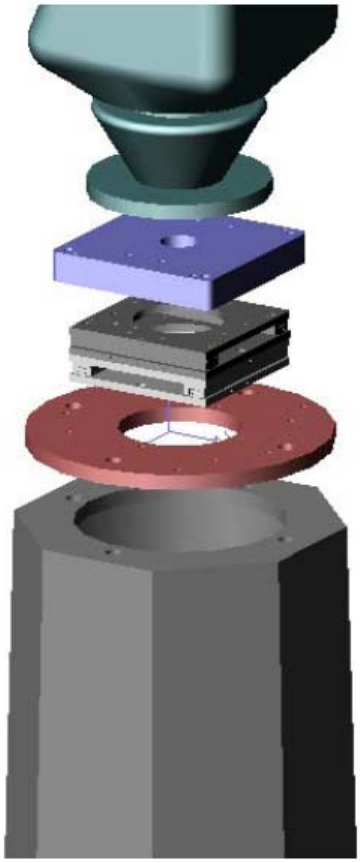

Figure 5.12 Exploded CAD view of main components in a pole-mounted passive isolator design.

5.6 Prototype Implementation and Test

In order to test the theory presented above, both a computer-controlled vibration simulator and physical prototypes were constructed. The simulator has a linear slide to provide the main vibrational input with programmable amplitudes and frequencies; a motorized rotational platform was included to test for isolation performance at arbitrary directions on the horizontal plane. An initial physical prototype was built to verify high-frequency isolation performance on a single axis, later expanded to two axes, and eventually reconfigured to be mounted on an actual pole for field testing. Figure 5.14

shows the most current simulator and prototype isolation device. A battery of simulator tests was conducted with rigid mount versus mechanical isolator at different frequency and amplitude input conditions. Direct camera video feedback was used for a qualitative evaluation of isolator performance. It was found that heavy image distortion occurred at vibratory frequencies in the 4-6 Hz range, even at smaller 0.04-0.06 in. (1-1.5 mm) input amplitudes; at higher amplitudes 0.08-0.12 in. (2-3 mm), a whiplash effect due to high accelerations would cause the camera tilt axis step motor to lose registration. Under these input conditions, regardless of amplitude, the mechanical isolator was able to stabilize the image and render it usable even under heavy magnification (23x optical zoom). At low input frequencies, the simulator showed the expected increase in camera heave with isolator natural frequencies in excess of the input frequency. A series of proof-of-concept field tests have been performed with the above prototype, which has been mounted atop standard 50 ft and 60 ft poles in Texas Department of Transportation installations (Fort Worth, Amarillo, and Dallas Districts). The field observations align well with both the analytical predictions and simulator results. It has been confirmed, both qualitatively in live image feeds and quantitatively through accelerometer data, that the second mode (5 Hz) image distortion present in 60 ft poles is effectively cancelled by mechanical means. These tests have also confirmed that the low-frequency heave characteristic of mechanical isolation, even when operating the device in the amplification regime has essentially unnoticeable effects in panoramic views. Under higher magnification, transverse camera motions do eventually introduce some degree of horizon shift in the image; although the slow rate of motion and lack of blur allows

useful information to still be extracted from these images, it would be, in practice, desirable to have it completely eliminated. For this reason, and particularly in installations where slow fundamental frequencies are present (<2 Hz), the mechanical isolator technique is seen as complementary to electronic image stabilization. The following steps summarize the design roadmap and tuning process of a passive mechanical isolator for the cases under study:

1. Establish the input frequencies with relevant energy content present at the camera support which is to be suppressed (FEM analysis or direct measurement).

2. If the lowest frequency present is well in excess of 2 Hz, the passive isolator may provide a complete solution. If there is a low fundamental frequency below 2 Hz, but also higher frequencies which are of interest to suppress, a passive isolator design may apply in conjunction with electronic image stabilization.

3. Based on the aerodynamic profile of the camera, establish minimum acceptable support stiffness values for the spring-mass to react wind loads (eq. 5.3).

4. Establish transmissibility reduction targets for the problematic frequencies (20-50%) and calculate spring-mass requirement using $\zeta \approx 0.1\text{-}0.2$ and the design envelopes provided in Figures 5.7 and 5.8. In the case, where a low fundamental frequency is present, ensure that the resulting amplification is kept to acceptable levels (Figure 5.9).

5. Build isolator as two orthogonal linear slides of adequate load capacity, frictional quality, and nominal travel of at least ±1.5 in.. Add external weight at the camera seat interface to reach the computed spring-mass value.

5.7 Lab Testing

The device was developed and tested in the Process Automation Laboratory at the Texas Manufacturing Assistance Center, Automation and Robotics Research Institute (ARRI).

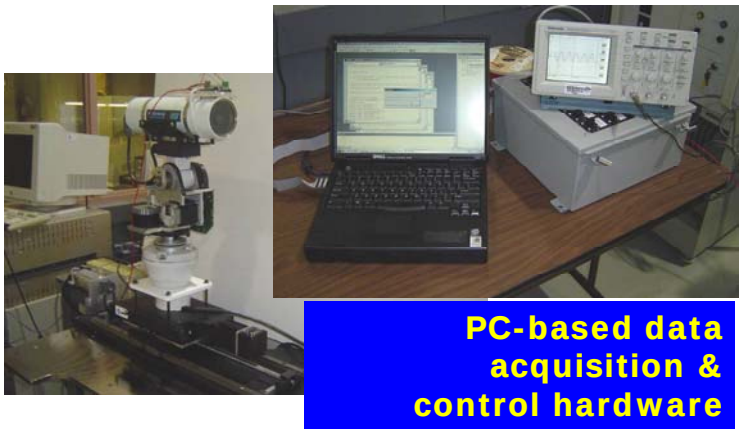

(a)

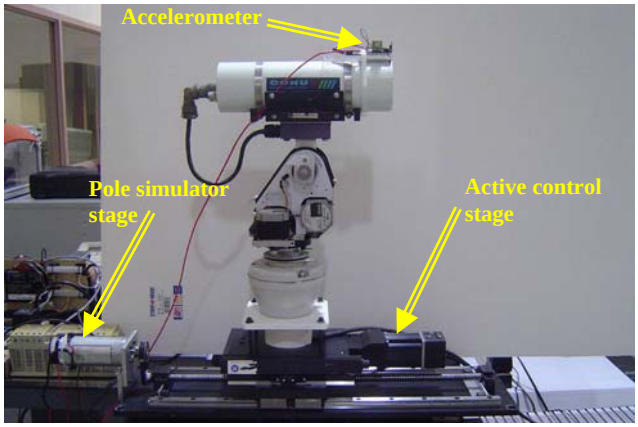

(b)

Figure 5.13 Test setup for the mechanical device testing at ARRI laboratory;
(a) PC-based data acquisition & control hardware, (b) Close view of the test setup at ARRI Laboratory

5.8 Field Testing

With the support of TxDOT in Fort Worth, Amarillo and Dallas, bucket trucks were provided for the mechanical device installation. All the instruments were brought to the top of the camera pole by using a bucket truck (Figure 5.14), while live video images were simultaneously recorded from the camera controller at the pole base.

Testing procedure:

1- Commission a bucket truck from the transportation control center.

2- Install the accelerometer (Figure 5.15) on the top of the pole and on the camera, as shown in Figures 5.16 to 5.17.

3- Record the acceleration of the pole and camera under quiescent, natural wind-induced loads.

4- Record the acceleration of the pole and camera in response to a broadband step input, provided by hand-striking the pole.

5- Install the isolator, as shown in Figures 5.18 to 5.20.

6- Repeat steps 3 and 4.

7- While performing steps 3, 4, and 6, record live video images from the camera controller.

8- Remove all of the instruments; return the camera pole to its original state.

(a)

(b)

Figure 5.14 Field instrumentation in Fort Worth; (a) Rosedale-I35W, (b) Loop 280-I35W.

(a)

(b)

Figure 5.15 Field instrumentation in Amarillo; (a) Soncy-I40W, (b) Bell-I40W

Figure 5.16 Field instrumentation in Dallas (Hampton-I20 East).

Figure 5.17 Tri-Axis serial accelerometer.

(a)

(b)

Figure 5.18 Installation of accelerometers on the poles and cameras;
(a) in Fort Worth, (b) in Amarillo.

(a)

(b)

Figure 5.19 Field measurements; (a) Accelerometers installed on the pole and camera in Dallas, (b) Mechanical device installed on the pole in Fort Worth.

(a)

(b)

Figure 5.20 Field measurements; (a) Mechanical device installed on the pole in Amarillo, (b) Mechanical device installed on the pole in Dallas

The mechanical isolator device was tested in the Fort Worth, Amarillo and Dallas Districts to evaluate its image enhancement ability. For the field testing, camera image videos and pole acceleration data were recorded. The induced load sources are wind load and the load applied by striking the pole by hand. Accelerometer data were collected from two sensors mounted orthogonally in the horizontal plane; these showed consistent frequency content along North-South (NS) and East-West (EW) directions, as would be expected due to axial symmetry. The measured frequency values, clustered around 1 Hz and 5 Hz, were also consistent with analytical and FEM predictions for the 60 ft pole. Very low spectral content was found above 5 Hz. Figure 5.21 is the result from Forth Worth that was used to verify the FEM analysis of pole vibrational frequency.

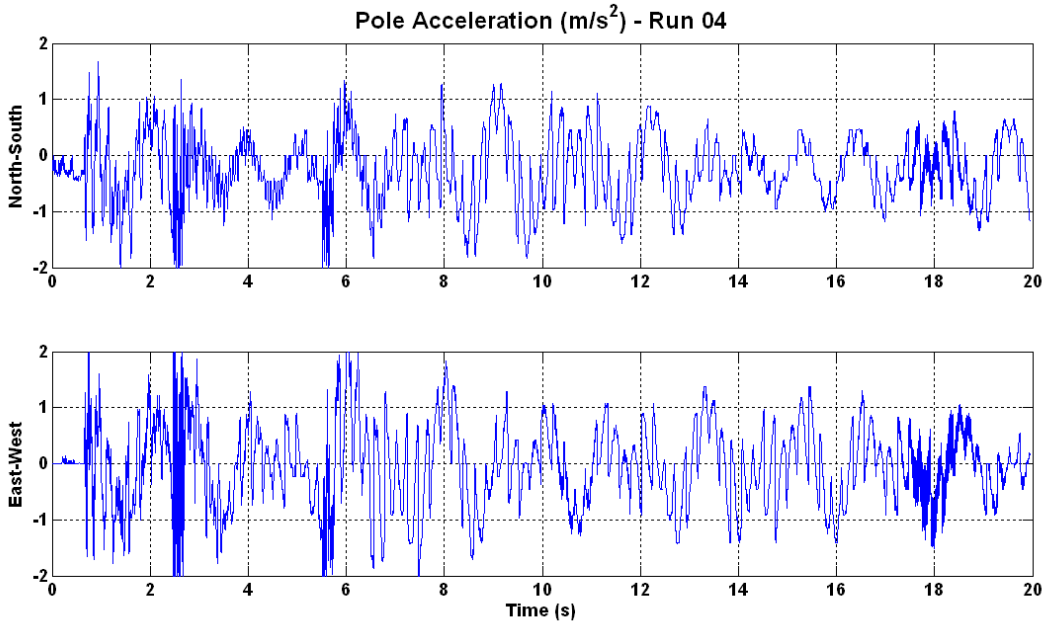

(a)

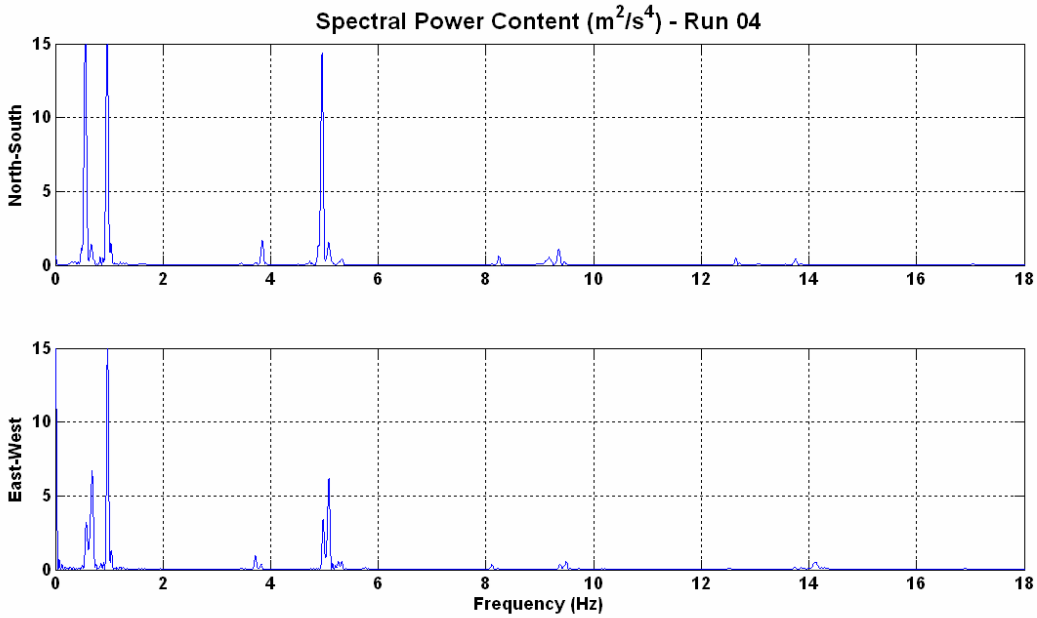

(b)

Figure 5.21 Data analysis of the pole at Rosedale-I35W, Fort Worth; (a) acceleration result, (b) vibrational frequency result.

CHAPTER 6

ELECTRONIC IMAGE STABILIZATION FOR TRAFFIC CAMERAS

6.1 Introduction

The aim of the electronic digital image stabilization is to remove the unwanted motion (jitter) from an image sequence. The undesired motion between consecutive frames can be the result of the camera translation, camera rotation, image scaling (zoom), or perspective transformation. An electronic image stabilization system achieves its task by finding correlation between consecutive frames and compensating for the undesired motion. Finding the correlation between consecutive frames for static scenery is a straightforward and simple mathematical operation. However, for dynamic sequences, the challenge is to distinguish between the background and other moving objects in order to be able to compensate only for the undesired camera motion. In general an electronic image stabilization system is divided into two major components:

- **Motion Estimation:**

The task of the motion estimation component is to determine the amount of motion (motion vector) between successive frames which is the result of the camera vibration. A perfect motion estimation component should distinguish between moving objects, intentional camera motion (such as panning and tilting), and unintentional motion such as high-frequency vibration and jitter.

- **Motion Compensation:**

The motion compensation component uses the estimated motion vector from the motion estimation component in order to stabilize the image sequence. Motion compensation may include corrective actions such as scaling, translating, rotating, and/or un-warping the image sequence. The block diagram of the image stabilization system is shown in Figure 6.1.

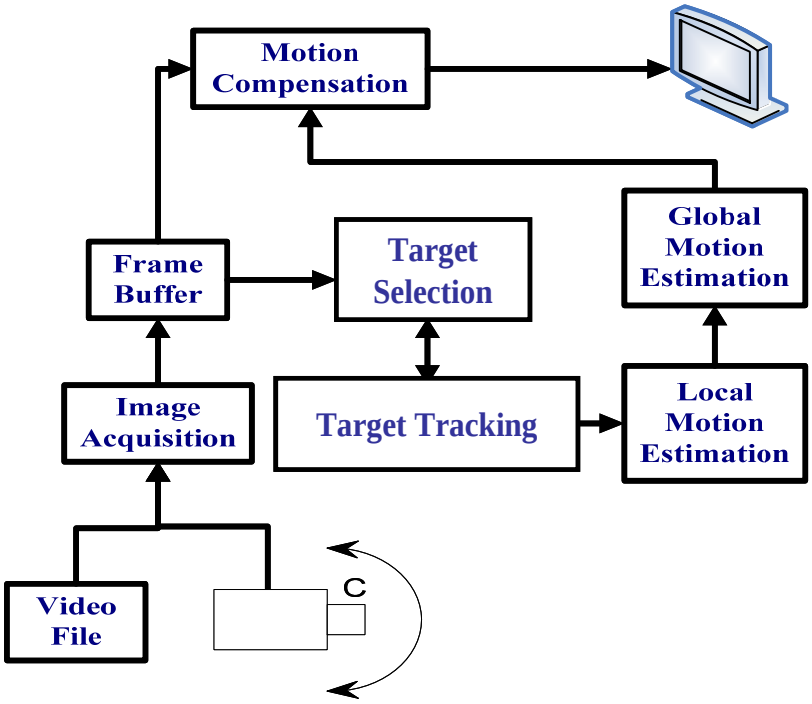

Figure 6.1 Block diagram of the image stabilization system.

6.2 Program Algorithm

6.2.1 Image Stabilization for Traffic Cameras

Traffic cameras typically display the images of distant objects such as buildings, cars, and roads. This means that the perspective effects are negligible. In addition, jitter in the traffic cameras is usually caused by the vibration of the camera around the

vertical axis with minimal or no rotation around the optical axis. It may be assumed that traffic cameras are looking at planar scenes with translational motion between frames with no rotation, scaling or perspective effects.

The most straightforward approach to motion estimation is to find the cross correlation between successive frames. This can be accomplished by calculating the Mean Squared Error (MSE) or Mean of Absolute Difference (MAD) between the successive frames. The maximum point on the cross correlation function (or the minimum point on MSE / MAD) determines the estimated motion vector. However, the calculation of the cross-correlation function is computationally very expensive which reduces the throughput of the system. In addition the existence of independently moving objects in the image sequence (such as cars that are moving against the background) may reduce the accuracy of the motion estimation system. Different techniques have been proposed to increase the accuracy of the motion estimation vector and reduce the computational load of the system. One such technique is to divide the image frame into blocks (sub-images) and estimate the local motion of each sub-image independently. The global motion vector can be calculated from the set of the local motion vectors based on a predefined algorithm.

6.2.2 Blocks (Sub-images)

Consider the sequence $f_{1,} f_{2,} ..., f_i, ...$. In each frame, f_i, N blocks $B_1^i, B_2^i, ..., B_N^i$ (sub-images) are defined. These blocks are not necessarily the same size and may or may not be overlapping. In addition, some regions of the image may not be covered by any blocks, as shown in Figure 6.2.

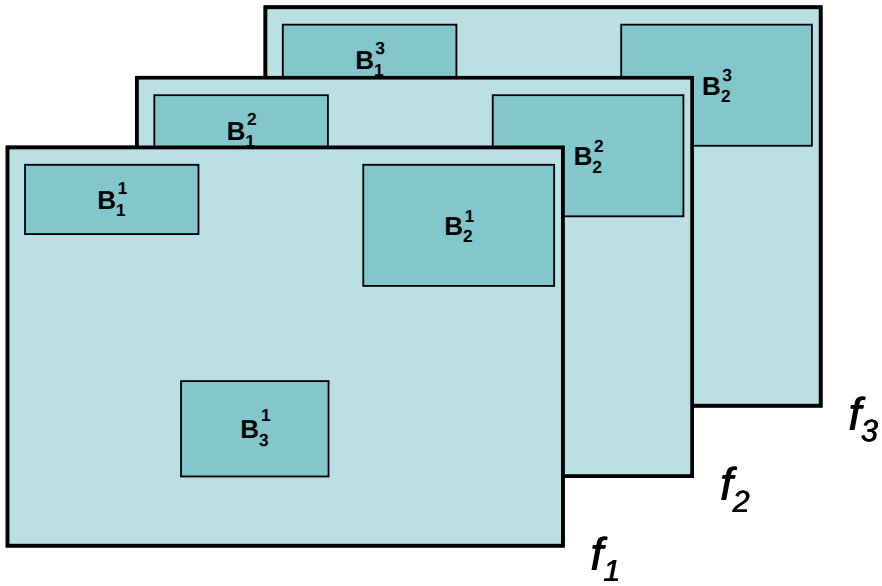

Figure 6.2 Image sequence with selected blocks.

Each block (sub-image) is considered to be an independent region within the image.

6.2.3 Target Selection

To compute a local motion vector, a target (feature) must be acquired and tracked within the boundaries of each block.

The upper left location of the selected target in the B_j^i (jth block in the ith frame) is given as $T_j^i = \begin{bmatrix} x_j^i \\ y_j^i \\ 1 \end{bmatrix}$ where $\begin{bmatrix} x_j^i \\ y_j^i \\ 1 \end{bmatrix}$ is the homogeneous coordinates of the target with respect to the complete image frame as, shown in Figure 6.3.

The following criteria must be considered for target selection:

- A target must be as unique as possible. Selecting a target that has multiple instances in the scene may reduce the accuracy of the motion estimation process. For

example, selecting a texture (or part of a texture) as a target is not a good practice because a texture can easily be repeated in a different part of the image.

- If possible, it is best to select those targets that belong to distant scene points in the background. These targets reduce the perspective projection effects and support the assumption that the camera is looking at a planar image.
- Targets with constant average pixel intensity will improve the tracking process. For example, selecting a blinking light as a target complicates the tracking process.

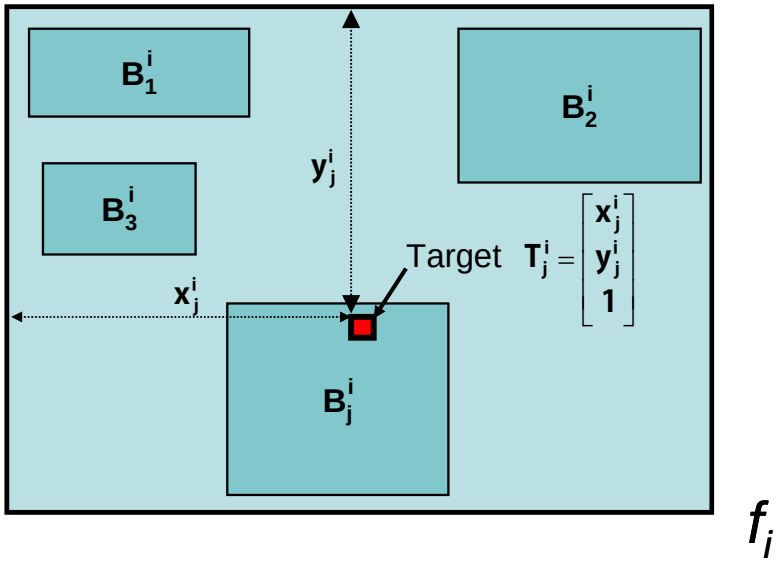

Figure 6.3 Selected target in block j and frame i

In order to be able to compare the performance and robustness of different target selection algorithms, four different methods have been implemented:

- Method 1:

- Select the largest possible block in the center of each block as the target. Notice that the entire block cannot be selected as the target because to track a target it must be able to move within the block, as shown in Figure 6.4.

Figure 6.4 Selected targets with largest possible block.

- Method 2:

- Select the central region of each block as the target. The height and width of the target is set by the user (Figure 6.5).

Figure 6.5 Selected targets at the center of each block.

■ Method 3:

- Convert an image to gray image. The conversion to gray scale image is necessary since the color information is not used in the edge detection algorithm.
- Find edges in the gray image.
- Select the region with maximum standard deviation as the target. If the second step is omitted (only the region with maximum standard deviation is selected without edge detection), the system may select a texture as a target, as shown in Figure 6.6.

Figure 6.6 Selected targets with maximum standard deviation in each block.

- Method 4:

- Select the region with maximum entropy as the target. Selecting a target with maximum entropy ensures that flat areas of the image are not selected as a target (Figure 6.7).

Figure 6.7 Selected targets with maximum entropy in each block.

6.2.4 Target Tracking

Once a target is selected, it can be tracked in the successive frames by defining a window around the previous location of the target and performing a local search. The search algorithm is based on calculating a dissimilarity measure while the target in the previous frame is sliding over the current search window. The dissimilarity measure for each location of the target is defined as the Mean of Absolute Differences (MAD) between the target and the search window. Given the location of the target in block k of frame t-1

$T_k^{t-1} = \begin{bmatrix} x_k^{t-1} \\ y_k^{t-1} \\ 1 \end{bmatrix}$ the MAD for this target in frame t is calculated as:

$$MAD(u,v) = \frac{\sum_{m=1}^{Ht}\sum_{n=1}^{Vt}\left| f_t\left(x_k^{t-1}+u+m, y_k^{t-1}+v+n\right) - f_{t-1}\left(x_k^{t-1}+m, y_k^{t-1}+n\right)\right|}{Ht * Vt}$$

Where Ht and Vt are the horizontal and vertical size of the target.

The new location of the target is calculated by finding the minimum of the MAD over the search window. The target is assumed to be lost if the minimum MAD is larger than a specified threshold.

Notes:

The width and height of the target (in pixels) can be interactively set by the user from the GUI. Both width and height of the target must be odd.

The width and height of the search window can be interactively set by the user.

6.2.5 Estimation of Global Motion

Theoretically, for a static scene, all the motion vectors for two successive frames are the result of the camera motion and should be similar. In this case, the global motion vector can be estimated by averaging all the motion vectors from sub-images. However, the motion vectors from sub-images with independently moving objects may not be reliable and should be excluded from the global motion vector calculation. Different methods have been suggested to estimate the global motion vector from a given set of the local motion vector, as follows:

- Method 1:

- The simplest approach for estimating the global motion vector is to assume that the smallest local motion vector is representative of the true background motion and select it as the estimate of the global motion. The advantage of this method is its simplicity. However, if an independently moving object in the scene is selected as a target and it is moving in the same direction as the camera

vibration, then the resulting local motion vector may have smaller magnitude than the other local motion vectors (which may be indicators of the true camera motion).

$\vec{G}^t = \min\left(\vec{V}_1^t, \vec{V}_2^t, ..., \vec{V}_N^t\right)$ where $\vec{G}^t$ is the global motion vector for frame t, and N is number of blocks (sub-images) in a frame.

- Method 2:

- Select the average of all the local motion vectors as the estimate of the global motion vector.

  $\vec{G}^t = average\left(\vec{V}_1^t, \vec{V}_2^t, ..., \vec{V}_N^t\right)$ where $\vec{G}^t$ is the global motion vector for frame t and N is number of blocks (sub-images) in a frame.

- Method 3:

- Select the median of the local motion vectors as the estimate of the global motion vector.

  $\vec{G}^t = median\left(\vec{V}_1^t, \vec{V}_2^t, ..., \vec{V}_N^t\right)$

- Method 4:

- Reject those local motion vectors that do not agree with dominant motion vectors and then estimate the global motion vector by the least squared error fit of the remaining local motion vectors.

- Given the coordinates of the targets in the ith frame $\left\{T_1^i, T_2^i ..., T_N^i\right\}$ and the location of the corresponding targets in the previous frame $\left\{T_1^{i-1}, T_2^{i-1} ..., T_N^{i-1}\right\}$

then the corresponding targets in successive frames are related to each other by a linear transformation matrix M:

$$T_j^i = [M] * T_j^{i-1}$$

where

$$[M] = \begin{bmatrix} m_{11} & m_{12} & m_{13} \\ m_{21} & m_{22} & m_{23} \\ m_{31} & m_{32} & 1 \end{bmatrix}$$

- For a traffic camera the motion between successive frames is assumed to be only translational and the matrix M reduces to:

$$[M] = \begin{bmatrix} 1 & 0 & m_{13} \\ 0 & 1 & m_{23} \\ 0 & 0 & 1 \end{bmatrix}$$

- The motion vector for the ith frame is defined as:

$$\vec{V}_j^i = T_j^i - T_j^{i-1} = ([M] - [I]) * T_j^{i-1}$$

Where $\vec{V}_j^i$ is the local motion vector for the jth block in the ith frame and M is the translation matrix. Given two corresponding targets T_j^i and T_j^{i-1}, two linear equations can be established to solve the two parameters m_{13} and m_{23}. Considering that there are N targets in each frame (one target per block), an over-constraint system of 2N linear equations can be established to find the global translation matrix. The set of 2N equations with two unknowns m_{13} and m_{23} can be solved by pseudo-inverse method to find the best estimate for the global motion vector with the least square error.

$T_j^i \cong \left[\widetilde{M}\right] * T_j^{i-1}$ for j=1,2,…N

Where $\left[\widetilde{M}\right]$ is the estimate of the translation matrix M with the least square error.

It should be noted that in the calculation of $\left[\widetilde{M}\right]$ all local motion vectors are considered (even the outliers).

- To identify the local motion vectors that do not agree with others (outliers) the residual (error) of each local motion vector is calculated:

  $\varepsilon_j = Magnitude\left(T_j^i - \left[\widetilde{M}\right] * T_j^{i-1}\right)$

Where ε_j is the residue (error) of the target j.

If the absolute difference between the residue of a target and the average residue is greater than a given threshold then that target is considered an outlier and it is discarded. Once the outliers are identified the matrix $\left[\widetilde{M}\right]$ is recalculated using the remaining targets.

6.2.6 Motion Compensation

The motion compensation module utilizes the estimated global motion vector to compensate for the camera motion. In practice, the motion compensation module keeps a history of the estimated global motion vector between successive frames and compensation is performed by translating each frame relative to a reference frame. Given the current frame f_t and the reference frame f_{t-i}, the translation for the current frame can be calculated as

$$\vec{U}^t = \varphi\left(\vec{G}^{t-i}, \vec{G}^{t-i+1}, ..., \vec{G}^t\right)$$

Where $\vec{U}^t$ is the effective motion compensation vector for frame t and $\vec{G}^t$ is the global motion vector for frame t. φ is a function defining the dependency of $\vec{U}^t$ on the current and previous $\vec{G}^i$. In practice, the stabilized image is displayed by translating the reference frame by $-\vec{U}^t$. It should be noted that translating a frame creates a blank band around the resulting image. For example, translating a frame by 10 pixels to the right creates a 10-pixel-wide blank area on the left of the image. A problem associated with using a reference frame for calculating the effective motion compensation vector is that if the camera continuously moves in one direction (such as panning) eventually the magnitude of the effective motion compensation vector $\vec{U}^t$ can grow in such a way that the current frame might not have anything in common with the reference frame. To avoid this problem $\vec{U}^t$ is reinitialized if it exceeds given thresholds in horizontal or vertical directions.

In the simplest form $\vec{U}^t$ can be set equal to the global motion vector for the current frame; i.e.,

$$\vec{U}^t = \vec{G}^t$$

This approach will be ineffective when the frequency of the camera vibration is less than the frame frequency.

Another method is to define the effective motion compensation vector as the accumulation of previous global motion vectors; i.e.,

$$\vec{U}^t = \sum_{j=0}^{i} \vec{G}^{t-i}$$

The problem with the simple accumulation approach is that the overall image stabilization system will be very sensitive to the motion vector for the current frame and it will follow every sudden jump in the direction or magnitude of the estimated global motion vector. To overcome this problem a nonlinear exponential filter is used for the calculation of total motion between the current frame and reference frame.

$$\vec{U}^t = \alpha\vec{G}^t + (1-\alpha)\vec{G}^{t-1}$$

Where α is the exponential time coefficient. This coefficient controls the agility of the system to respond to sudden changes in direction and magnitude of the motion. For example if α is set equal to 1, then the system only responds to the motion vector between the current and previous frame and completely ignores the history of the direction and magnitude of the previous motion vectors. On the other hand, if α is set near zero, the change of the motion vector for the current frame has a small effect on the effective motion compensation vector. $\vec{U}^t$, and the image stabilization system resists sudden changes in magnitude and direction of the motion vector.

Figures F.1 through F.4 of Appendix F present the image correction results by using the developed electrical device. As can be seen from these figures the electrical device is most effective at low vibrational frequencies such as those presented in Figures F.1 and F.2 for frequency values of 0.94 Hz and 1.35 Hz, respectively. At high frequencies, however, the image processing algorithm is not effective, as shown in Figures F.3 and F.4 for frequency values of 3.57 Hz and 6.94 Hz, respectively. Thus,

the combination of the electrical device for low frequencies (1.5 Hz and less) and the mechanical device for high frequency (1.5 Hz and greater) will eliminate the image distortion completely. It should be noted that even though Figures F.1 and F. 2 do show a difference in the corrected and uncorrected images, the dynamic view during the video presentation clearly shows the effect of large period of vibration is eliminated. This means that the images with low vibrational frequencies are not disturbed when they are viewed; however, the images are isolating back and forth with high periods of vibration, which is eliminated by the developed electrical device.

CHAPTER 7

SUMMARY, CONCLUSIONS, AND RECOMMENDATIONS

7.1 Summary

This study, which used the results from TxDOT Project 0-4470, aimed at developing algorithms to correct the disturbed images received from the typical TxDOT CCTV due to pole vibration. A comprehensive literature review is presented in Chapter 1, which includes identification of different TxDOT pole sizes and heights, a complete literature review on the experimental and analytical studies on the tapered poles and their connection assembly, and a complete literature search on the passive and active damping devices used for structural systems (poles, buildings, and bridges).

In Chapter 2, several complete nonlinear inelastic three-dimensional finite element models of the poles were developed and compared with several field and experimental results. The full-scale experimental load deformation data obtained from TxDOT Project 0-4470 was used for the initial verification of the FEM analyses. From this result the initial optimized models for both circular and octagonal poles were developed. The analyses included frequency calculations for the poles by considering nonlinear contact, nonlinear geometric and inelastic material behavior. The FEM models were further verified with the field experimental data obtained from the accelerometers installed on a 60 ft pole in Fort Worth and by consulting the TxDOT

officials. Also, due to the multiple nonlinear effects in the analysis, an energy based convergence was adopted in which the error between the external work done and the strain energy was compared with the increasing mesh density. Finally, the FEM solution for the pole with fixed support was compared with the classical solution for a multi-degree of freedom system, which showed an almost exact correlation.

Chapter 3 discussed comprehensive parametric and sensitivity studies that were conducted for 80 test cases of circular and octagonal poles. The test cases were selected by consulting TxDOT Project 0-4470 based on the current variation of geometric variables used in the TxDOT pole design. The FEM frequency analyses for the first, second, and third modes were conducted for the 80 test cases, and the results are presented in Appendices A and B which include deformed geometry and the associated mode shapes and frequency values. Regression equations for the dependent variables (Modes 1, 2, and 3 frequencies) were developed as functions of the independent variables (poles geometric and force related variables). A complete sensitivity analysis was conducted to identify the effect of each independent variable on the dependent variables. This was done by varying one independent variable at a time and keeping all other independent variables at their intermediate values when calculating the dependent variables. Also, the predicted values for the frequencies were compared against the verified FEM, which showed very close correlation with maximum error in the range of 0% to 5.66%. Finally, the range of frequency for all the existing and possible future TxDOT poles was identified to assist in developing the electrical and mechanical devices.

In Chapter 4, there were 34 cases of the circular hollow tapered steel poles were studied. The hysteresis loop of the poles with different geometrical parameters were obtained by using non-linear The energy dissipation calculations are presented for each geometric parameter by calculating the area under the outer hysteresis.

In Chapters 5 and 6, mechanical and electrical devices were developed based on the information obtained from the aforementioned experimental, field, and finite element analyses. The mechanical device was developed based on the range of the frequencies obtained in the parametric study which is a multidirectional mass-sprung system. The developed device was tested both in the field and the laboratory. Two field tests and 35 laboratory tests were conducted to evaluate and optimize the mechanical device. The electrical algorithm was developed for digital image stabilization in order to remove the unwanted motion from an image sequence. The undesired motion between consecutive frames is the result of the camera translation, camera rotation, image scaling (zoom), or perspective transformation. Thus, an effective correlation between consecutive frames and compensating for the undesired motion is found by developing an algorithm and optimizing it by several image stabilization tests.

7.2 Conclusions

The following are the forefronts of the major conclusions of this study:

- A complete three-dimensional nonlinear FEM of the pole and its connection assembly was developed and verified against field and experimental tests. The error between the field test and FEM was 6.42 % and 7.02 % for the first and second vibrational mode, respectively. The

maximum error between the experimental load-deformation (TxDOT Project 0-4470) and the FEM were between 0% and 5.2 %.

- The developed prediction equations for the first, second, and third frequencies had R^2 = 0.987; 0.983; and 0.977, respectively, for the circular pole. For the octagonal pole, the R^2 of the first, second, and third frequencies equal: 0.998; 0.999; and 0.997, respectively.
- The absolute value of error in the developed prediction equations for the first, second, and third modes were between 0% and 5.66% for all 80 test cases of circular and octagonal poles.
- The range of the first, second, and third natural frequencies obtained from the 80 cases selected (based on the TxDOT pole design) were from 0.56 Hz to 33.68 Hz for circular and from 0.58 Hz to 32.48 Hz for octagonal poles.
- The sensitivity analyses for all 80 tests cases showed that the effects of pole length and diameter of pole at the bottom are significant on the pole's frequency.
- The sensitivity analysis indicated that the effect of the plate thickness, thickness at the top of pole, thickness at the bottom of pole, diameter of bolt, diameter of pole at the top, clearance distance, diameter of the bolt circle, plate dimension, and pre-tension load are insignificant on the pole's frequency.
- With the drift angle of 6% was used, not all of the pole reach the inelastic behavior, thus the hysteresis loop of those cases is linear. The range of

energy dissipation is from 22 kip-ft-rad to 2,253,059 kipt-ft-rad for studied circular poles.

- The laboratory test and field results showed that the image processing algorithm is highly effective on low vibration frequencies (1.5 Hz and less).
- The field and laboratory studies showed that the developed mechanical device is highly effective in stabilizing the image distortion and in most cases eliminating them (refer to Appendix E). It is shown that at high pole frequencies (4.8 Hz and higher) the images are corrected by up to 90.6 %.
- The videos obtained for the images before and after stabilization by using the developed mechanical device indicate that the distorted images are significantly corrected, and the distortions are completely eliminated when viewed by human eyes.

7.3 Recommendations

It is recommended that the hysteresis loop of the octagonal poles should be studied; more parametric study of the poles and end-plate connection geometrical parameters should be done to develop the equations for predicting the hysteresis loop.

It is also recommended that the result of this study be implemented and integrated for both electrical and mechanical devices developed for TxDOT. The developed mechanical device has multi-degrees of freedom vibration elimination capability which includes rotational Degrees of Freedom (D.O.F.). During the implementation, it is proposed that an inventory of all the pole sizes within the state of Texas be conducted. The weight of the device is optimized for different pole sizes.

Thus, the pole height sizes will be categorized for implementing the proposed device weight. The device will be installed such that it resists the harsh weather conditions. An integration system between the electrical device (for low frequency) and the mechanical device (for high frequency) is developed and will be implemented in the field. It is recommended that the implementation phase include but not be limited to the following:

- An inventory of all TxDOT poles with different heights will be conducted. This will assist the investigators in obtaining information with regard to the pole top configuration, which is necessary for device installation detail.
- The device-to-pole connection detail will be presented. Depending on the configuration of a pole's top, different connection detail will be presented.
- The device will be installed on the selected poles with different device-pole-connection detail, and their performances will be monitored long-term. It is anticipated that the device will be implemented in different regions of Texas with different weather conditions such as Amarillo, Galveston, Dallas, and other selected regions.
- An integration algorithm between the electrical and mechanical devices is developed and will be tested and monitored in the field on the identified poles.

APPENDIX A

CIRCULAR POLES

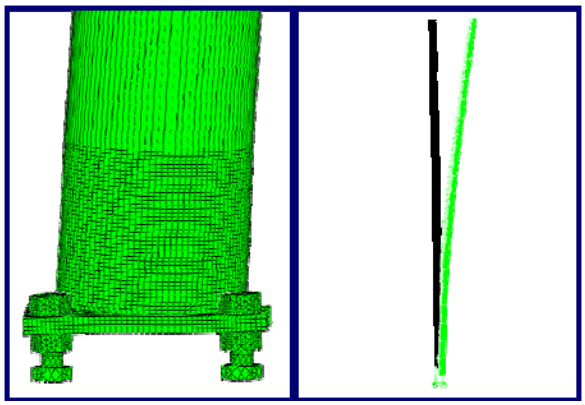

(a)

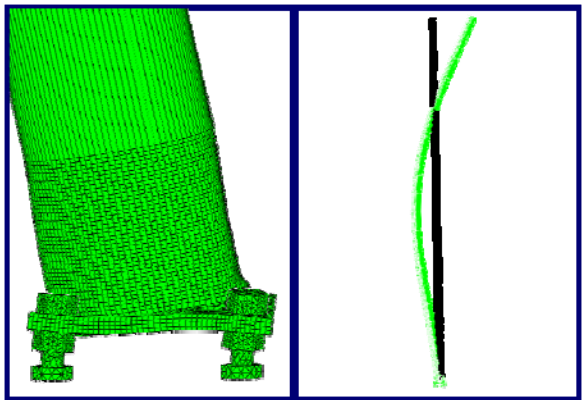

(b)

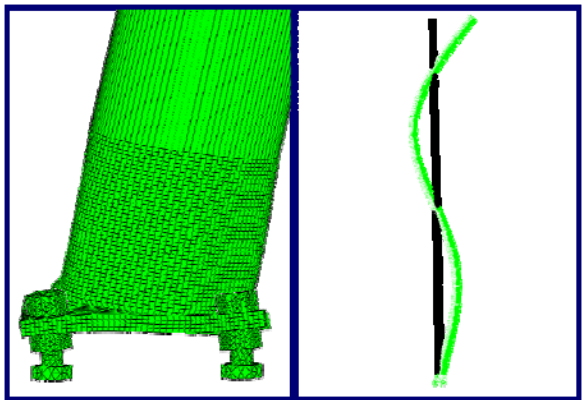

(c)

Figure A.1 Case 01 circular pole mode shape deformation
(a) Mode 1, f = 1.905 Hz; (b) Mode 2, f = 9.302 Hz; (c) Mode 3, f = 24.418 Hz.

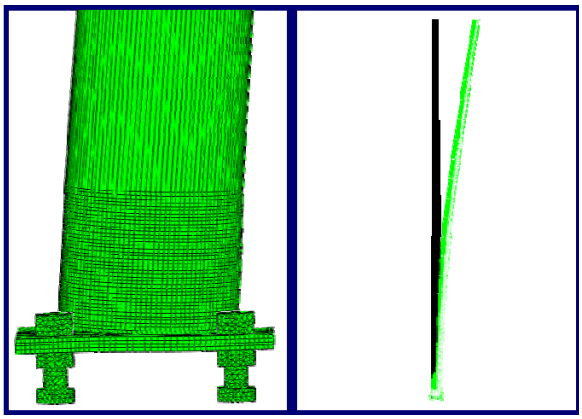

(a)

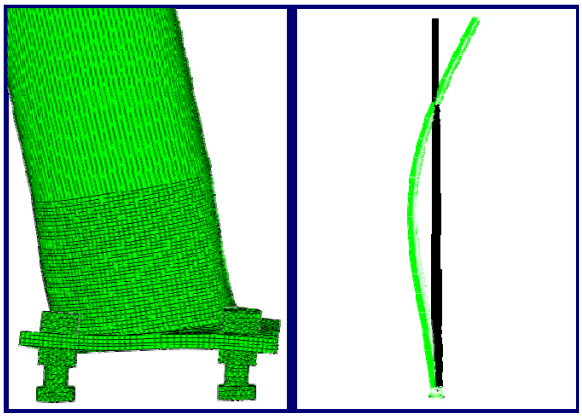

(b)

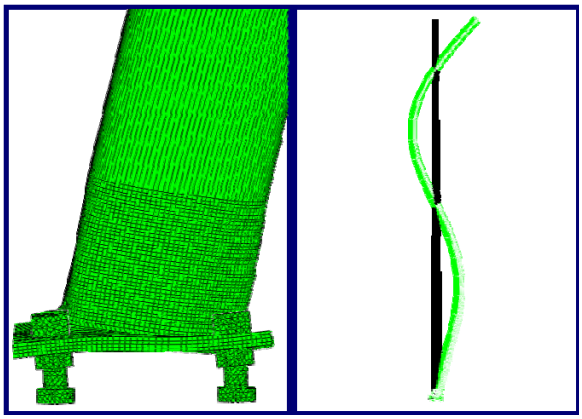

(c)

Figure A.2 Case 02 circular pole mode shape deformation
(a) Mode 1, f = 1.782 Hz; (b) Mode 2, f = 9.187 Hz; (c) Mode 3, f = 24.299 Hz.

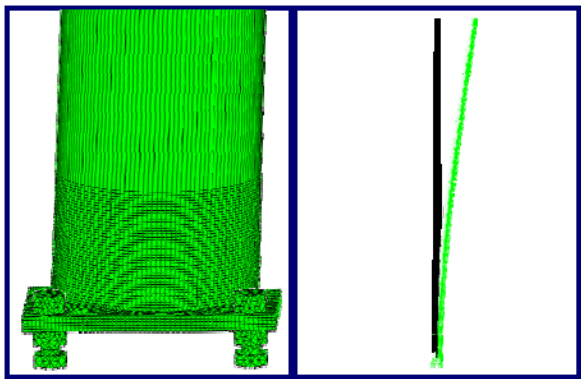

(a)

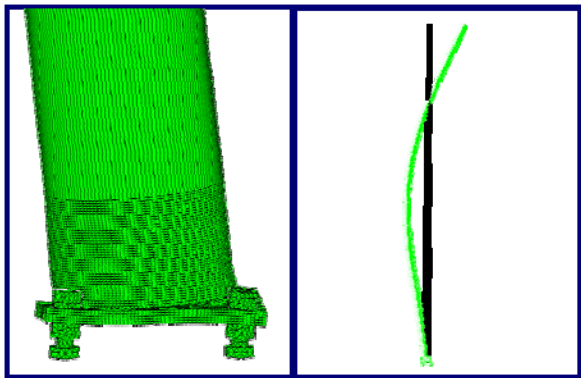

(b)

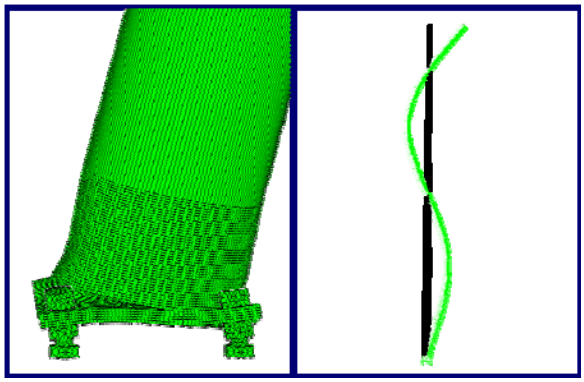

(c)

Figure A.3 Case 03 circular pole mode shape deformation
(a) Mode 1, f = 1.46 Hz; (b) Mode 2, f = 7.87 Hz; (c) Mode 3, f = 21.38 Hz.

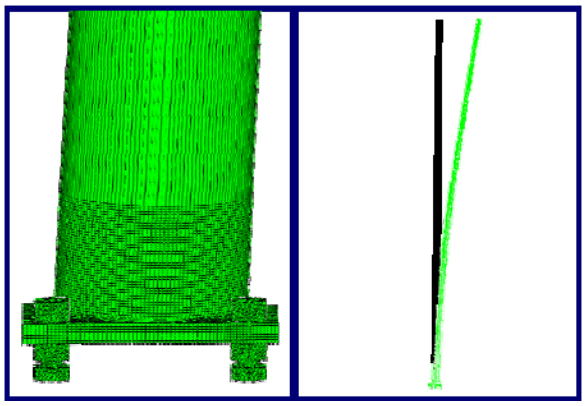

(a)

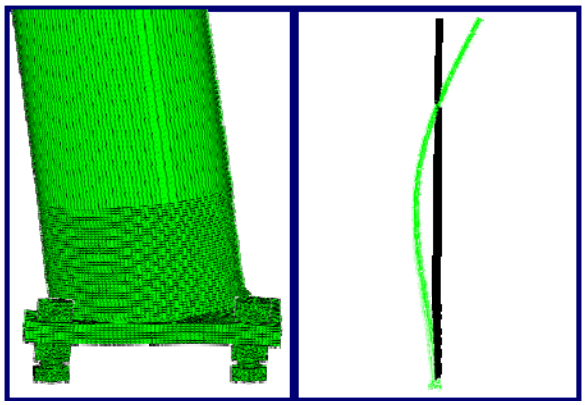

(b)

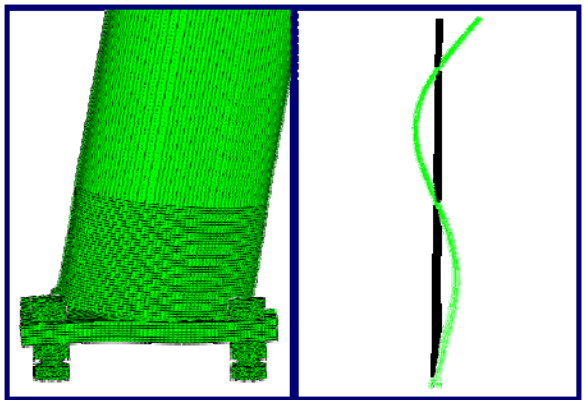

(c)

Figure A.4 Case 04 circular pole mode shape deformation
(a) Mode 1, f = 2.26 Hz; (b) Mode 2, f = 11.35 Hz; (c) Mode 3, f = 29.85 Hz.

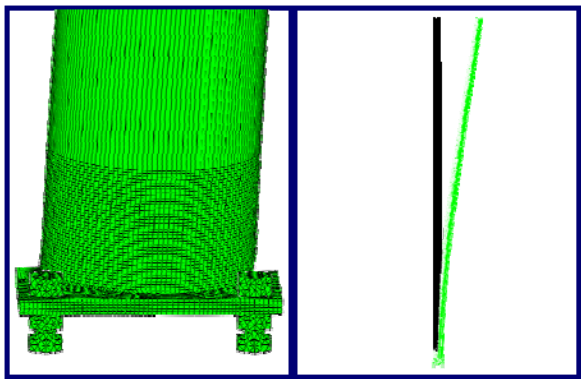

(a)

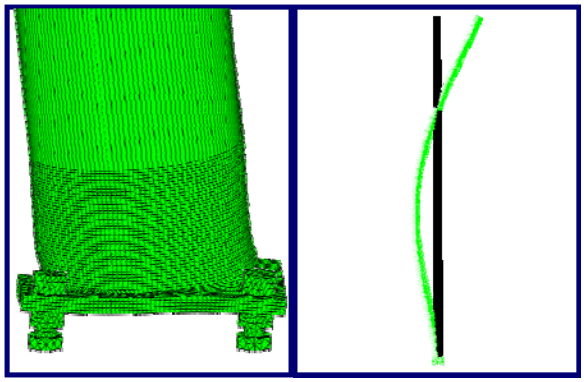

(b)

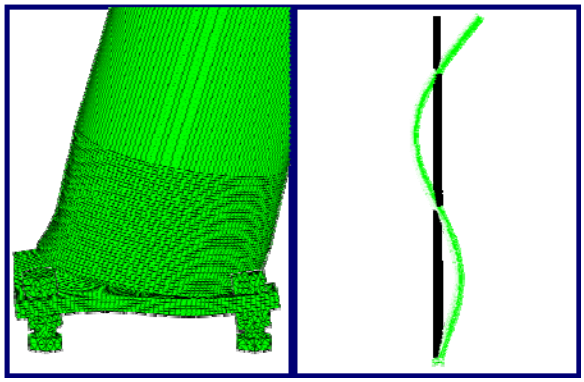

(c)

Figure A.5 Case 05 circular pole mode shape deformation
(a) Mode 1, f = 1.456 Hz; (b) Mode 2, f = 7.875 Hz; (c) Mode 3, f = 21.376 Hz.

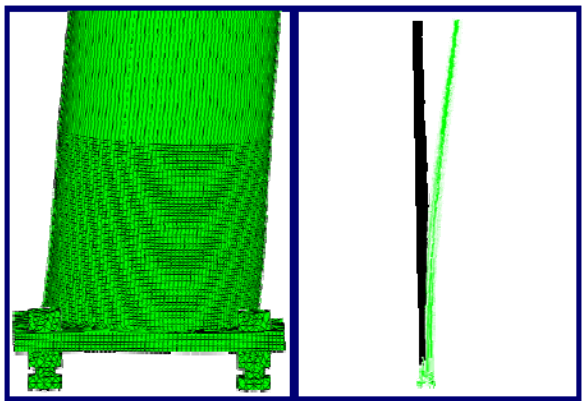

(a)

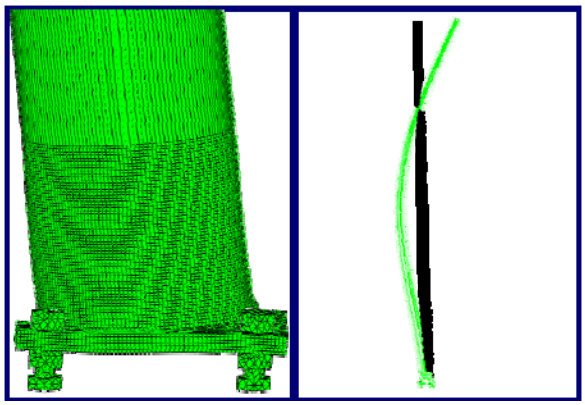

(b)

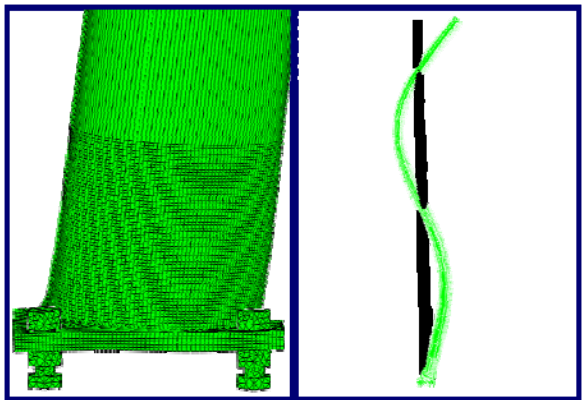

(c)

Figure A.6 Case 06 circular pole mode shape deformation
(a) Mode 1, f = 2.564 Hz; (b) Mode 2, f = 12.826 Hz; (c) Mode 3, f = 33.679 Hz.

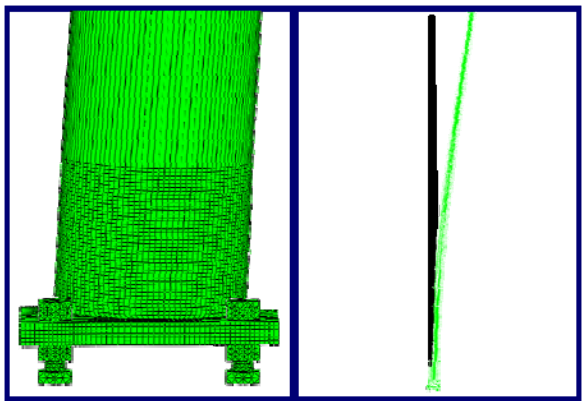

(a)

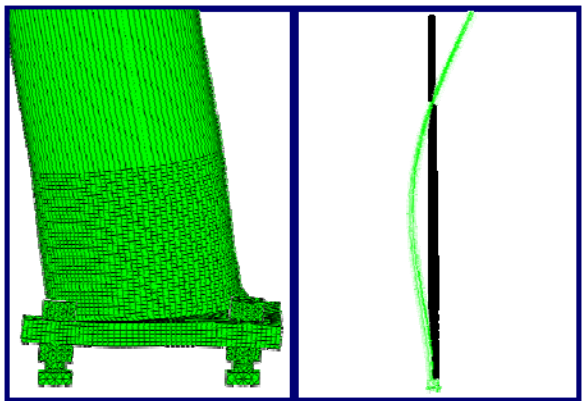

(b)

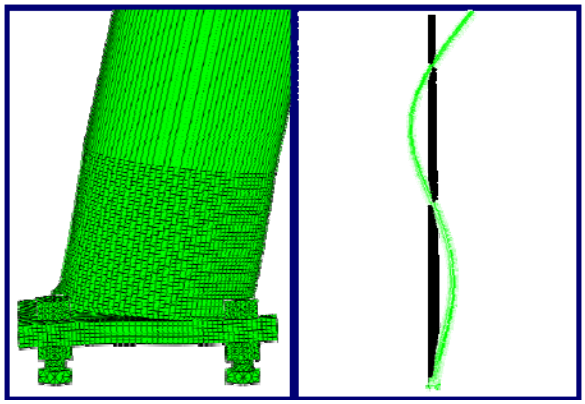

(c)

Figure A.7 Case 07 circular pole mode shape deformation
(a) Mode 1, f = 2.083 Hz; (b) Mode 2, f = 10.123 Hz; (c) Mode 3, f = 26.314 Hz.

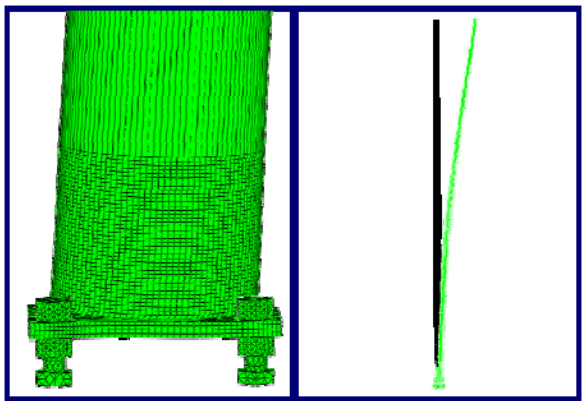

(a)

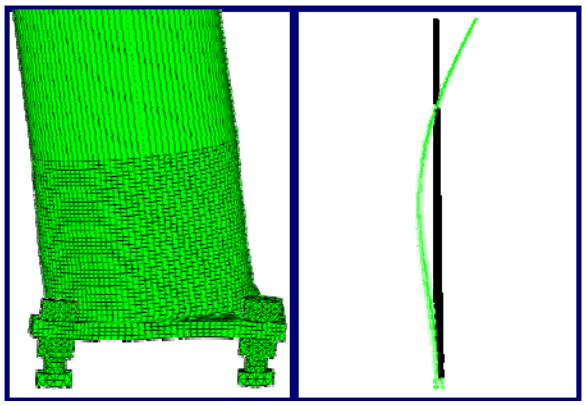

(b)

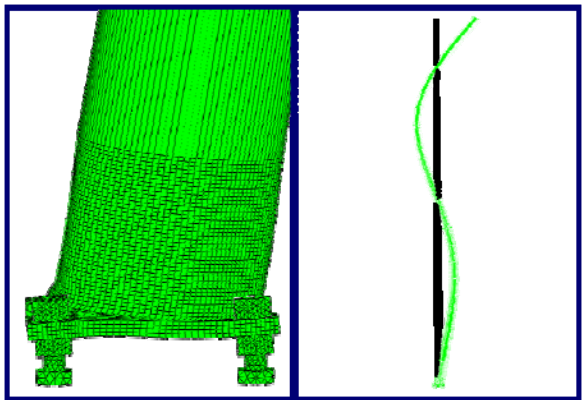

(c)

Figure A.8 Case 08 circular pole mode shape deformation
(a) Mode 1, f = 1.694 Hz; (b) Mode 2, f = 7.294 Hz; (c) Mode 3, f = 18.335 Hz.

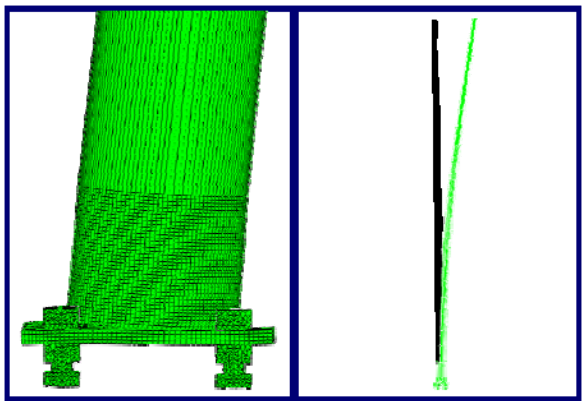

(a)

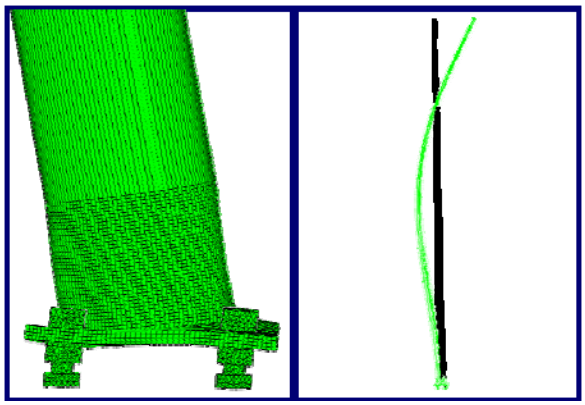

(b)

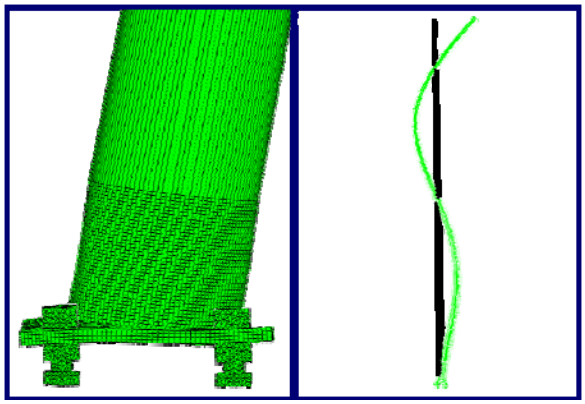

(c)

Figure A.9 Case 09 circular pole mode shape deformation
(a) Mode 1, f = 1.636 Hz; (b) Mode 2, f = 7.270 Hz; (c) Mode 3, f = 18.389 Hz.

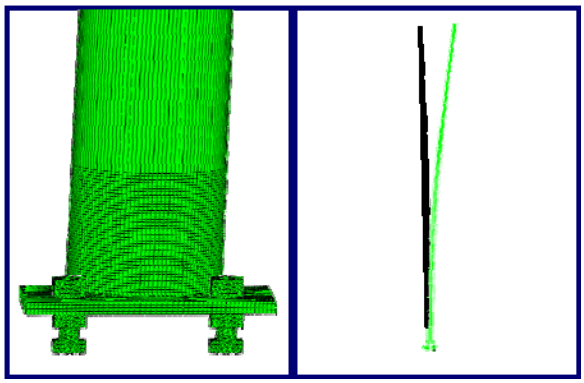

(a)

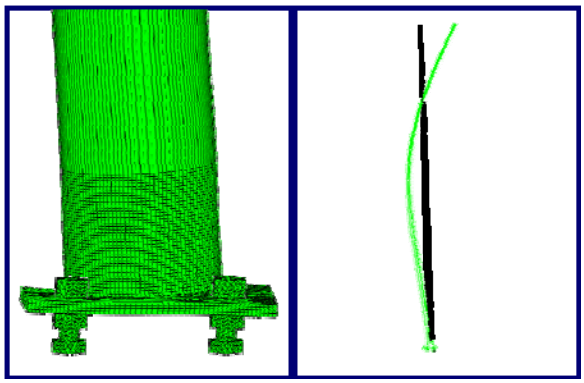

(b)

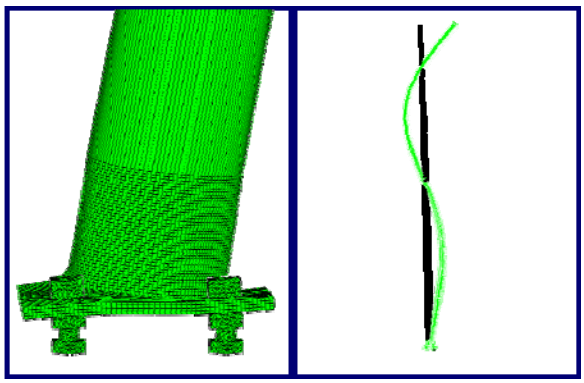

(c)

Figure A.10 Case 10 circular pole mode shape deformation
(a) Mode 1, f = 1.599 Hz; (b) Mode 2, f = 7.143 Hz; (c) Mode 3, f = 18.117 Hz.

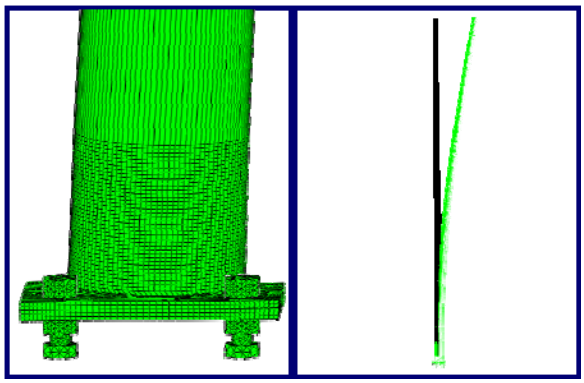

(a)

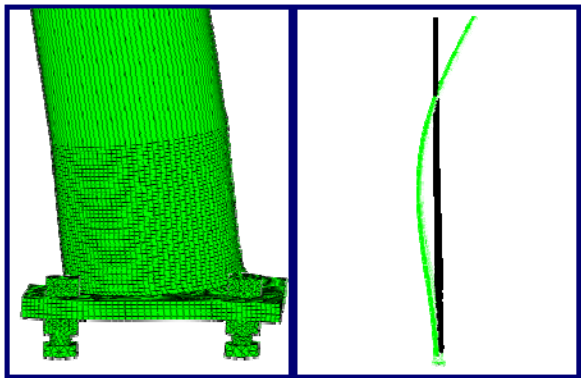

(b)

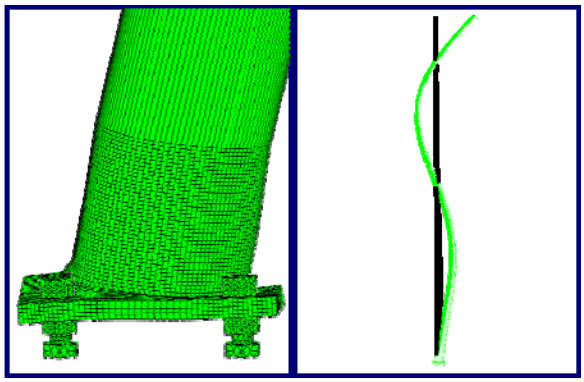

(c)

Figure A.11 Case 11 circular pole mode shape deformation
(a) Mode 1, f = 1.579 Hz; (b) Mode 2, f = 6.694 Hz; (c) Mode 3, f = 16.601 Hz.

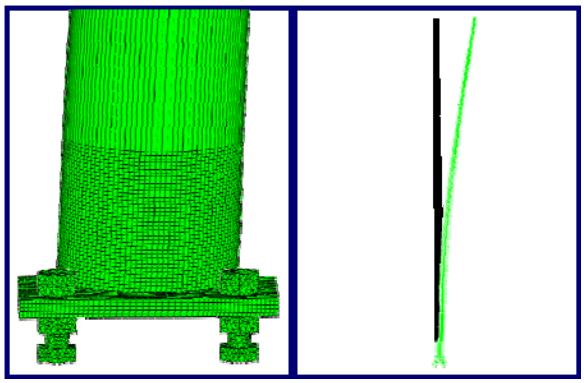

(a)

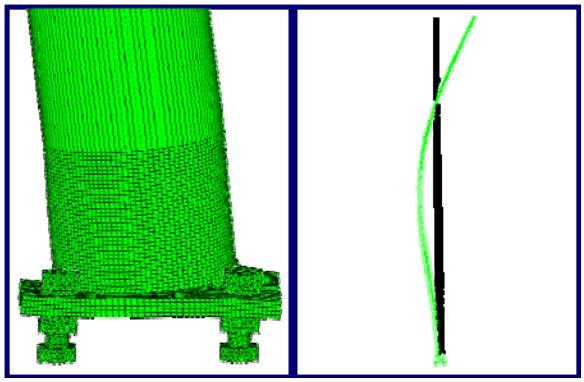

(b)

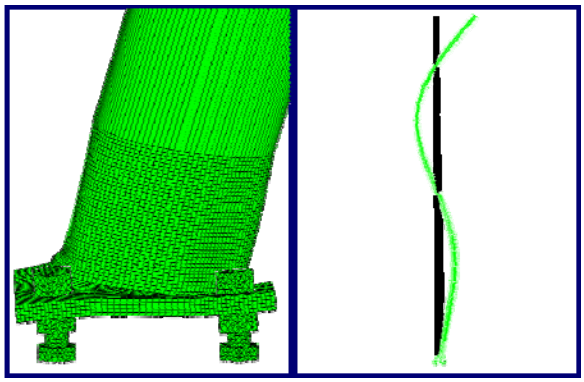

(c)

Figure A.12 Case 12 circular pole mode shape deformation
(a) Mode 1, f = 1.796 Hz; (b) Mode 2, f = 7.907 Hz; (c) Mode 3, f = 19.969 Hz.

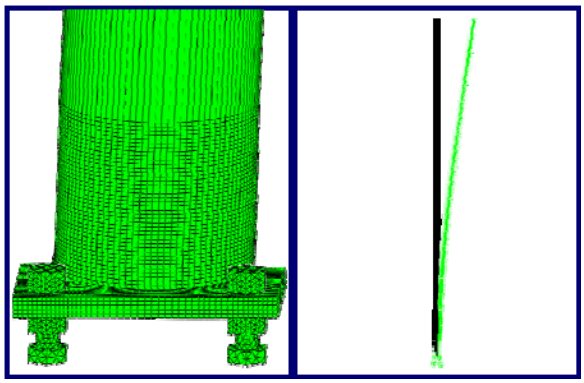

(a)

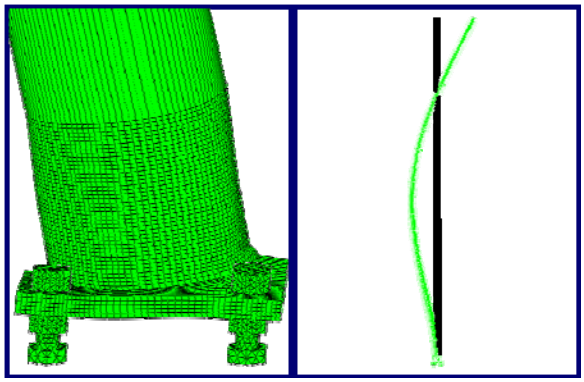

(b)

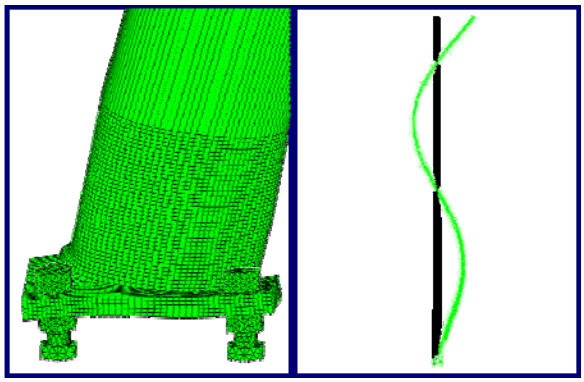

(c)

Figure A.13 Case 13 circular pole mode shape deformation
(a) Mode 1, f = 1.247 Hz; (b) Mode 2, f = 7.465 Hz; (c) Mode 3, f = 20.604 Hz.

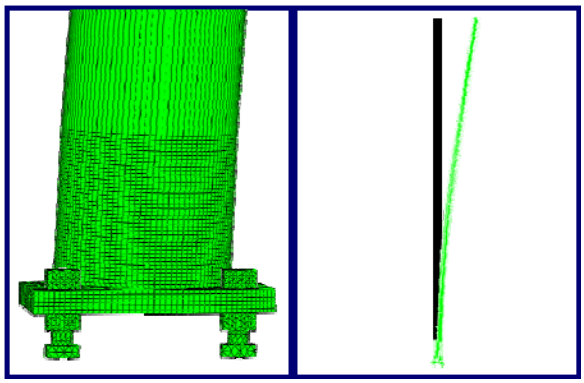

(a)

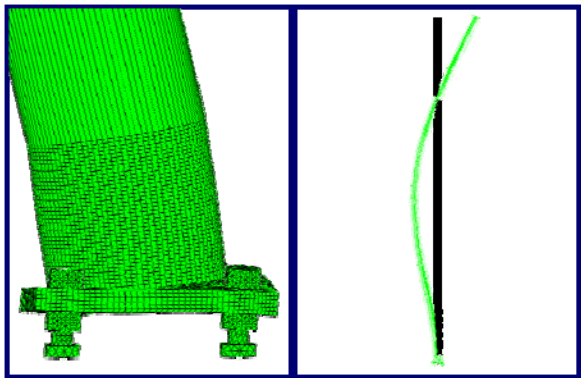

(b)

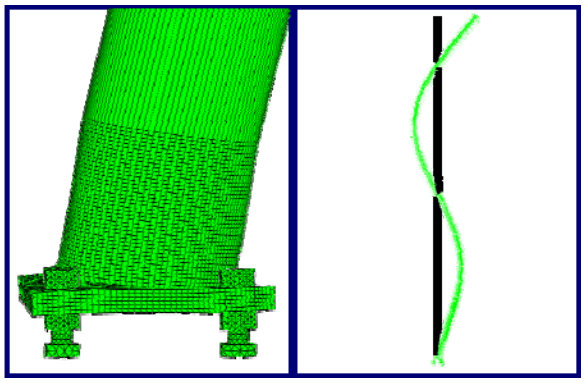

(c)

Figure A.14 Case 14 circular pole mode shape deformation
(a) Mode 1, f = 1.436 Hz; (b) Mode 2, f = 7.895 Hz; (c) Mode 3, f = 21.241 Hz.

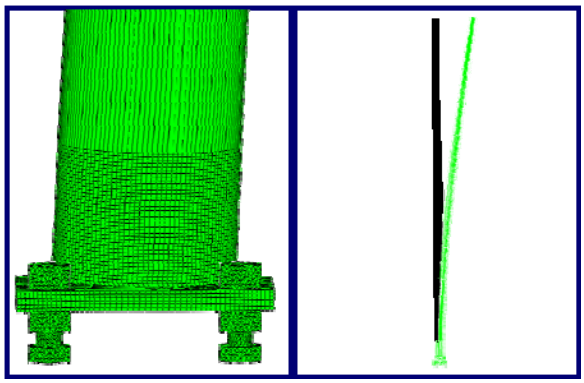

(a)

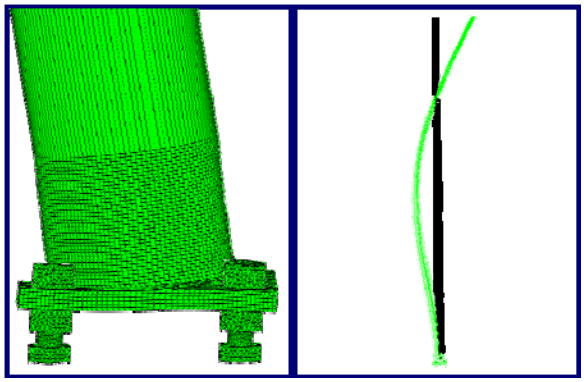

(b)

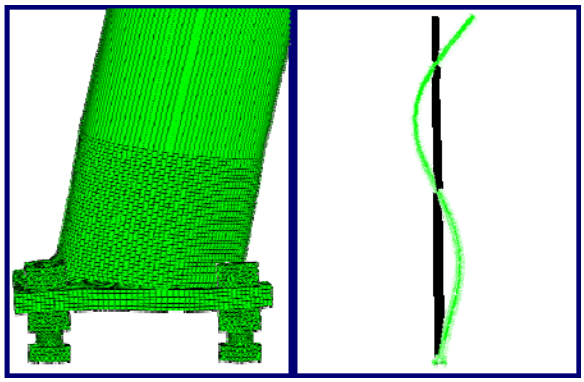

(c)

Figure A.15 Case 15 circular pole mode shape deformation
(a) Mode 1, f = 1.692 Hz; (b) Mode 2, f = 8.666 Hz; (c) Mode 3, f = 22.891 Hz.

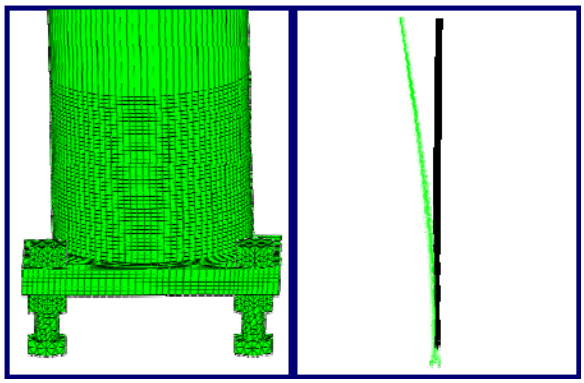

(a)

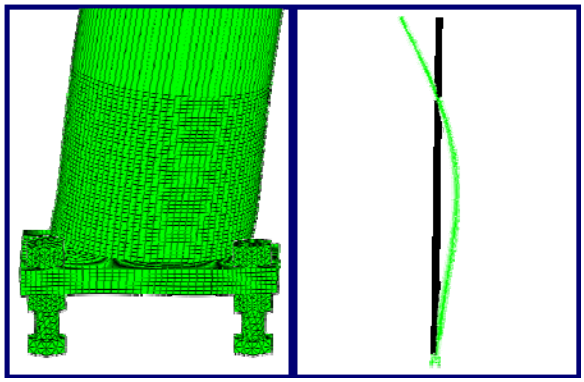

(b)

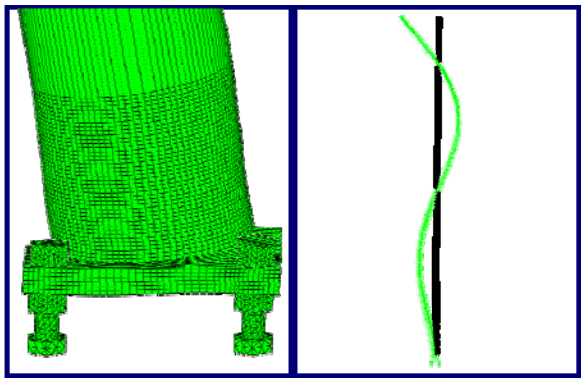

(c)

Figure A.16 Case 16 circular pole mode shape deformation
(a) Mode 1, f = 1.547 Hz; (b) Mode 2, f = 7.206 Hz; (c) Mode 3, f = 18.510 Hz.

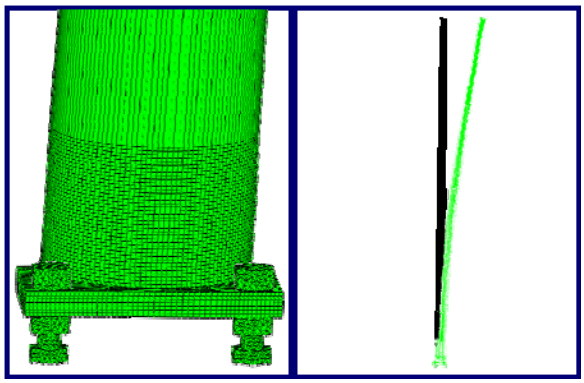

(a)

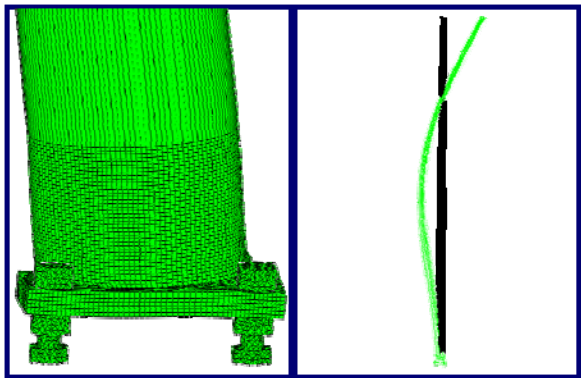

(b)

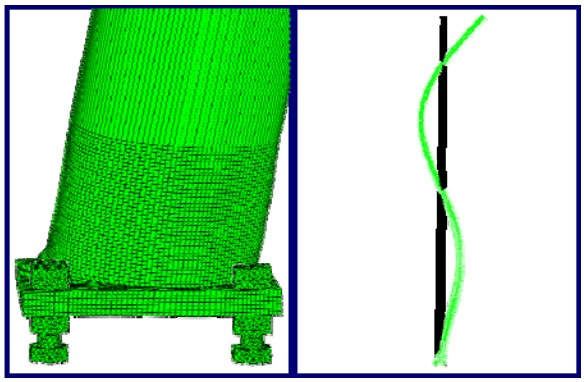

(c)

Figure A.17 Case 17 circular pole mode shape deformation
(a) Mode 1, f = 1.928 Hz; (b) Mode 2, f = 9.156 Hz; (c) Mode 3, f = 23.524 Hz.

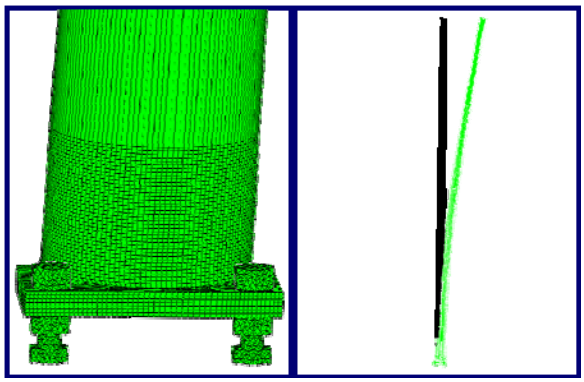

(a)

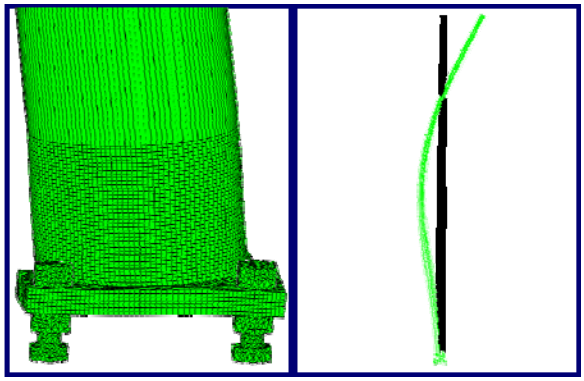

(b)

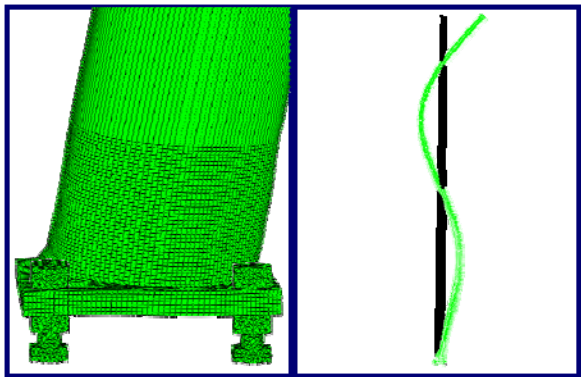

(c)

Figure A.18 Case 18 circular pole mode shape deformation
(a) Mode 1, f = 1.561 Hz; (b) Mode 2, f = 7.180 Hz; (c) Mode 3, f = 18.443 Hz.

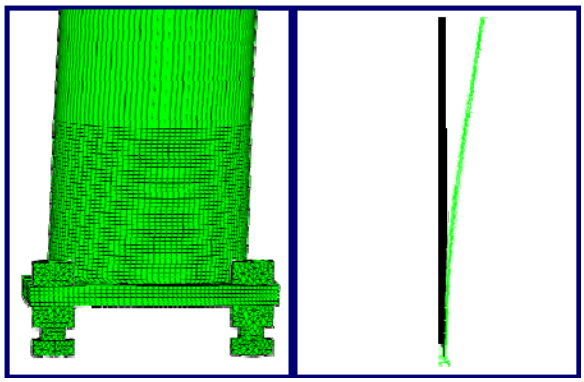

(a)

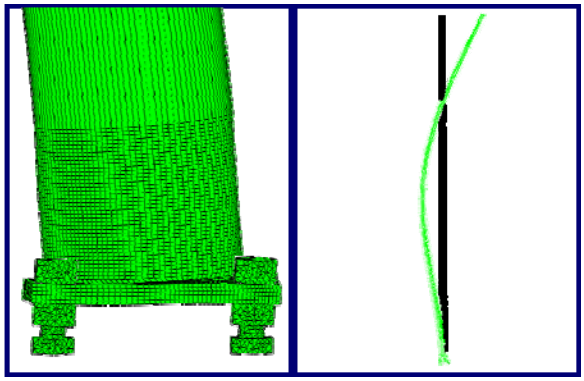

(b)

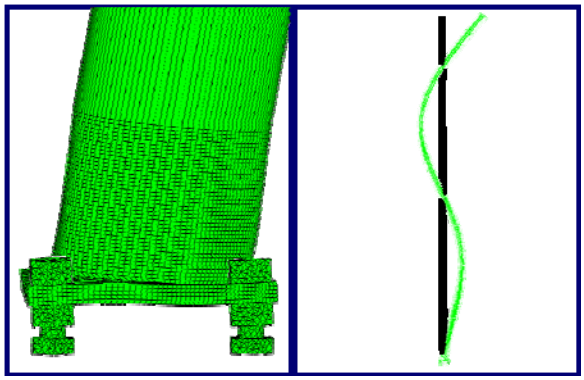

(c)

Figure A.19 Case 19 circular pole mode shape deformation
(a) Mode 1, f = 1.410 Hz; (b) Mode 2, f = 6.736 Hz; (c) Mode 3, f = 17.400 Hz.

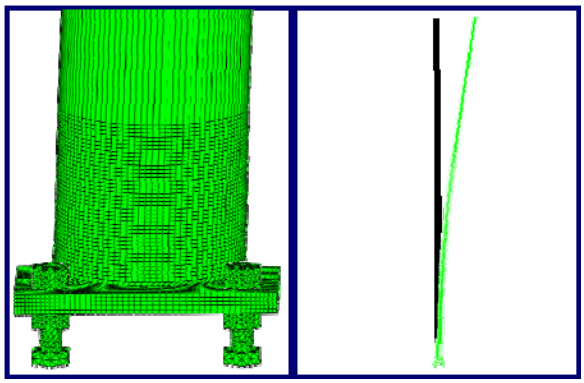

(a)

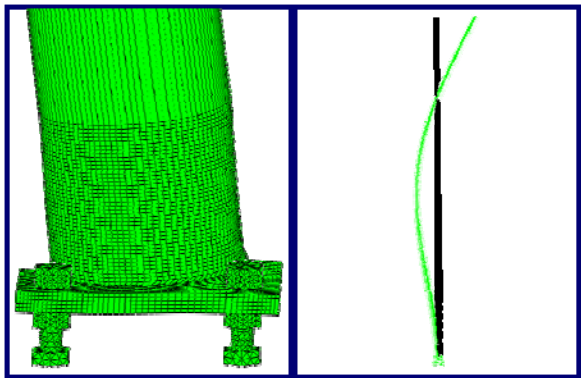

(b)

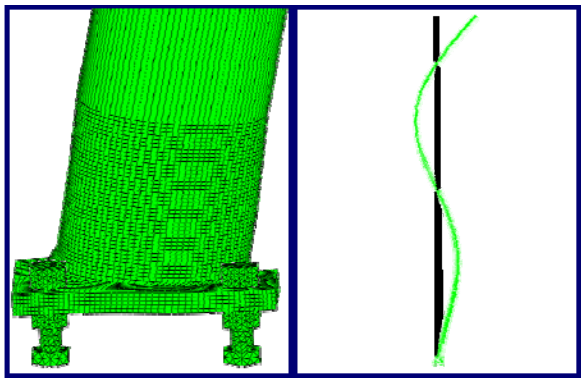

(c)

Figure A.20 Case 20 circular pole mode shape deformation
(a) Mode 1, f = 1.198 Hz; (b) Mode 2, f = 5.902 Hz; (c) Mode 3, f = 15.371 Hz.

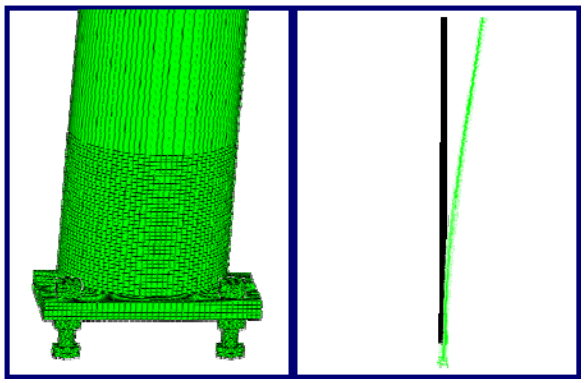

(a)

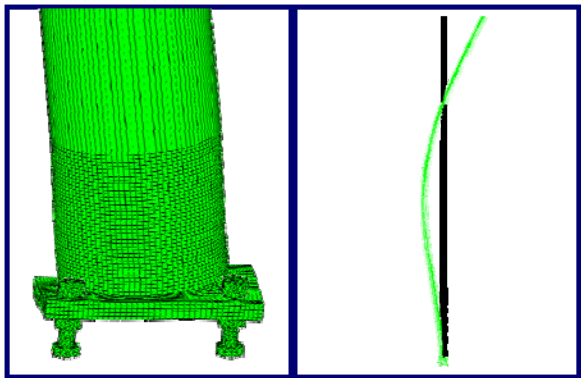

(b)

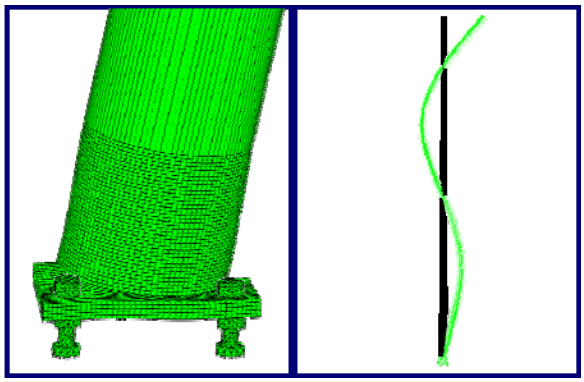

(c)

Figure A.21 Case 21 circular pole mode shape deformation
(a) Mode 1, f = 1.243 Hz; (b) Mode 2, f = 5.808 Hz; (c) Mode 3, f = 14.948 Hz.

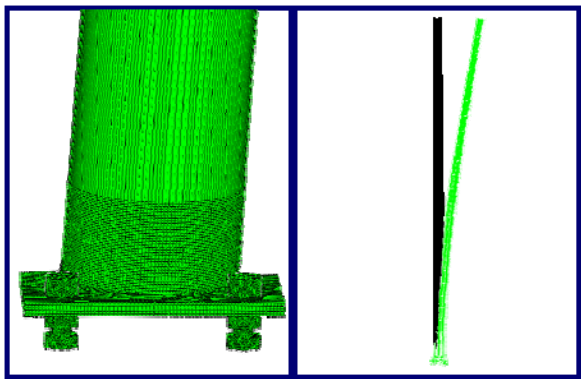

(a)

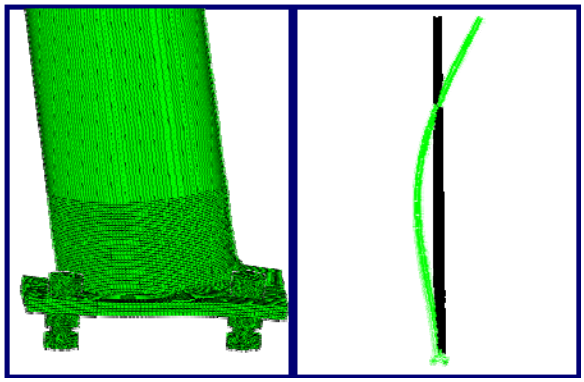

(b)

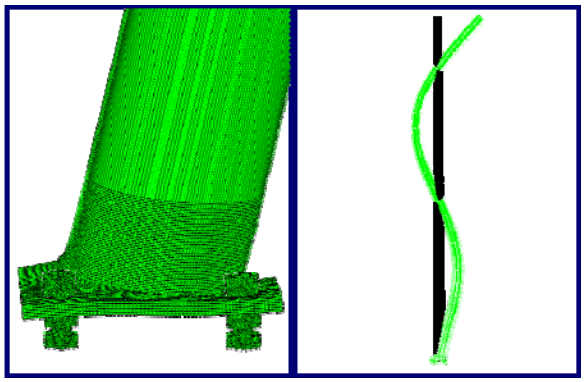

(c)

Figure A.22 Case 22 circular pole mode shape deformation
(a) Mode 1, f = 1.903 Hz; (b) Mode 2, f = 9.104 Hz; (c) Mode 3, f = 23.573 Hz.

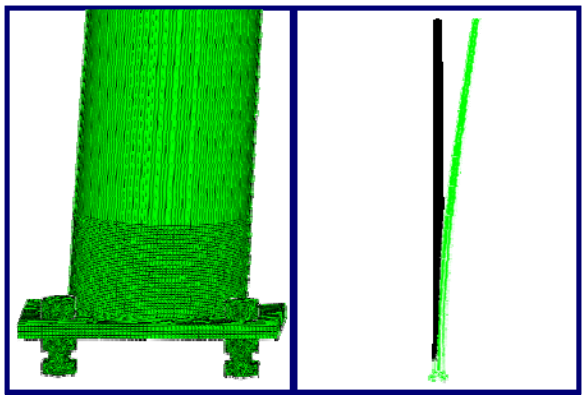

(a)

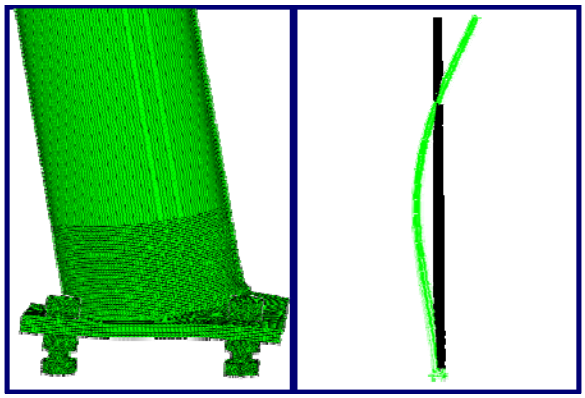

(b)

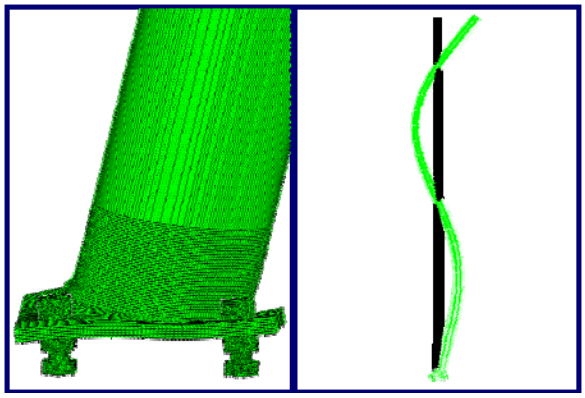

(c)

Figure A.23 Case 23 circular pole mode shape deformation
(a) Mode 1, f = 1.828 Hz; (b) Mode 2, f = 9.147 Hz; (c) Mode 3, f = 24.084 Hz.

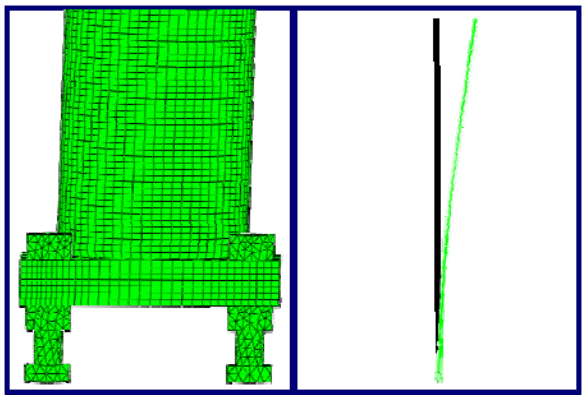

(a)

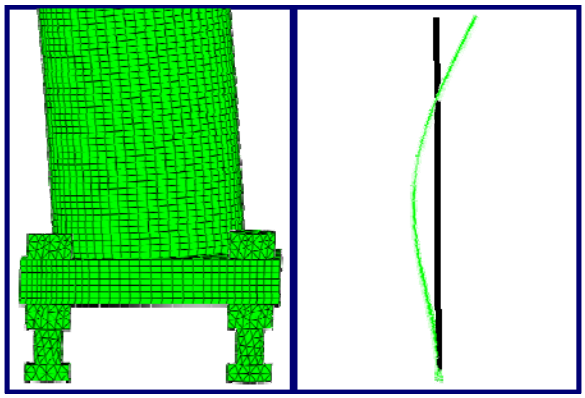

(b)

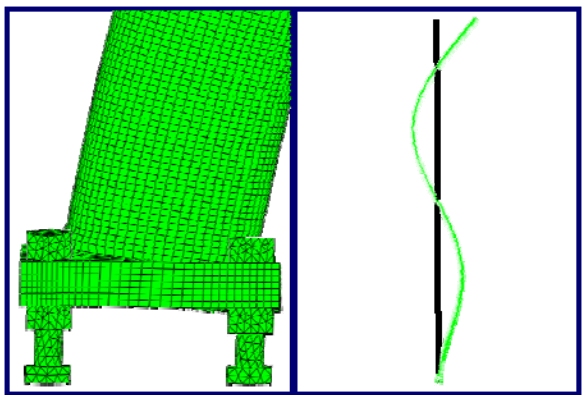

(c)

Figure A.24 Case 24 circular pole mode shape deformation
(a) Mode 1, f = 0.730 Hz; (b) Mode 2, f = 4.018 Hz; (c) Mode 3, f = 10.796 Hz.

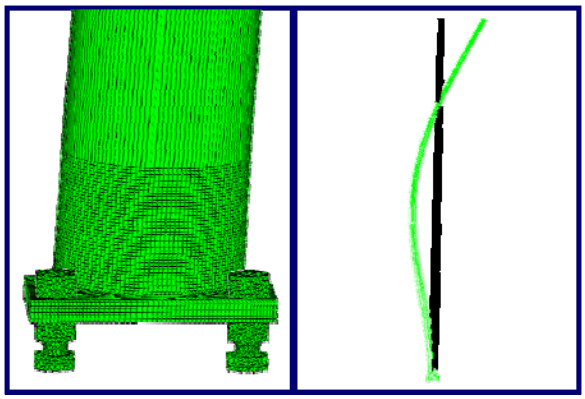

(a)

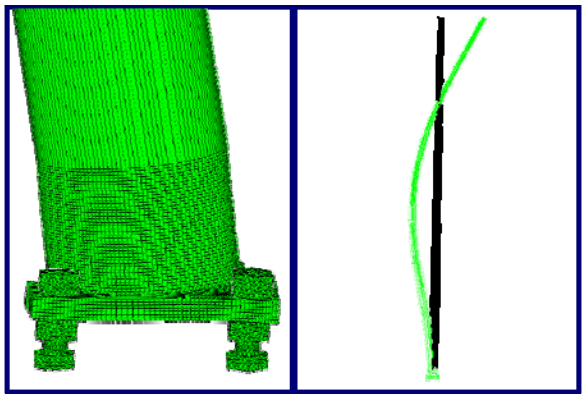

(b)

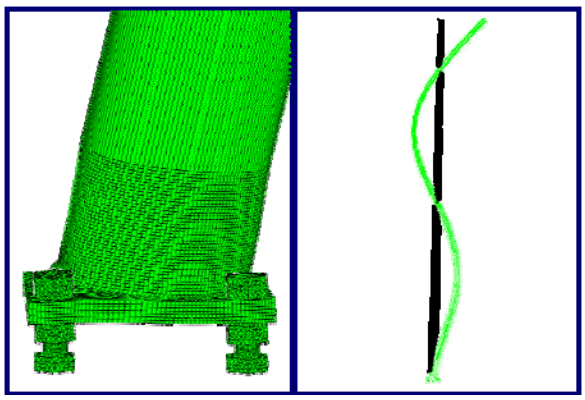

(c)

Figure A.25 Case 25 circular pole mode shape deformation
(a) Mode 1, f = 1.396 Hz; (b) Mode 2, f = 7.158 Hz; (c) Mode 3, f = 18.802 Hz.

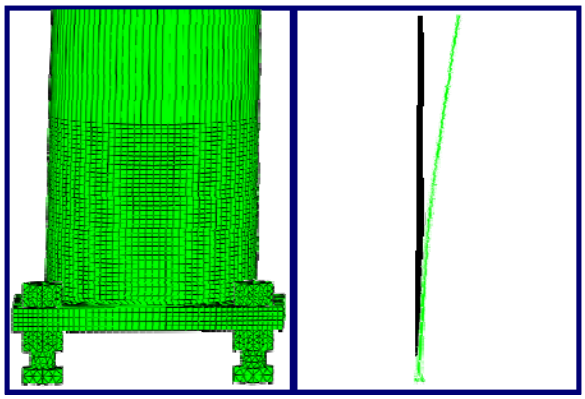

(a)

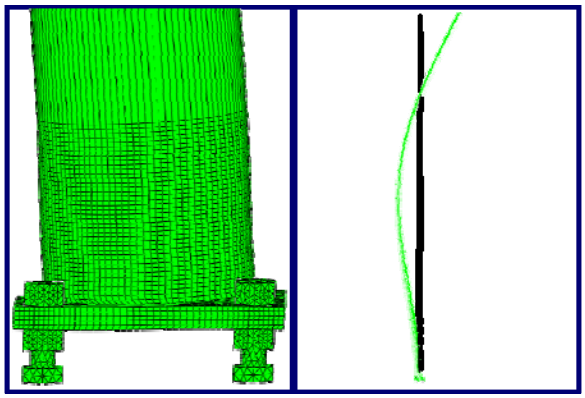

(b)

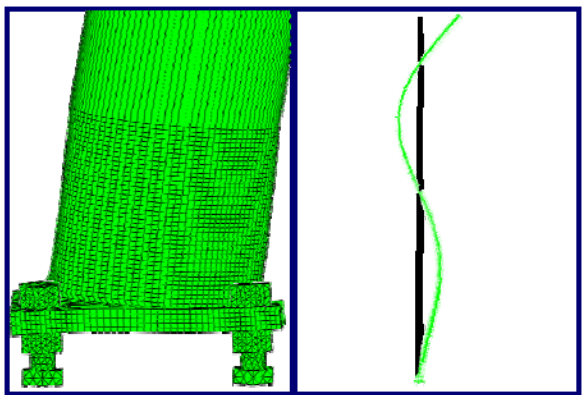

(c)

Figure A.26 Case 26 circular pole mode shape deformation
(a) Mode 1, f = 0.909 Hz; (b) Mode 2, f = 4.512 Hz; (c) Mode 3, f = 11.742 Hz.

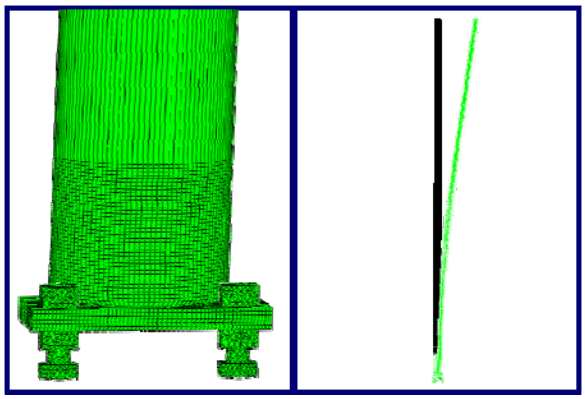

(a)

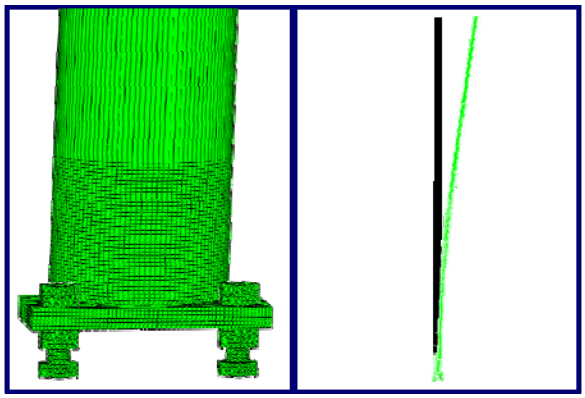

(b)

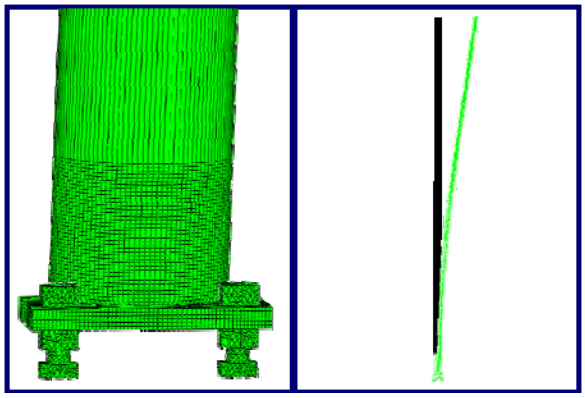

(c)

Figure A.27 Case 27 circular pole mode shape deformation
(a) Mode 1, f = 1.067 Hz; (b) Mode 2, f = 5.680 Hz; (c) Mode 3, f = 15.127 Hz.

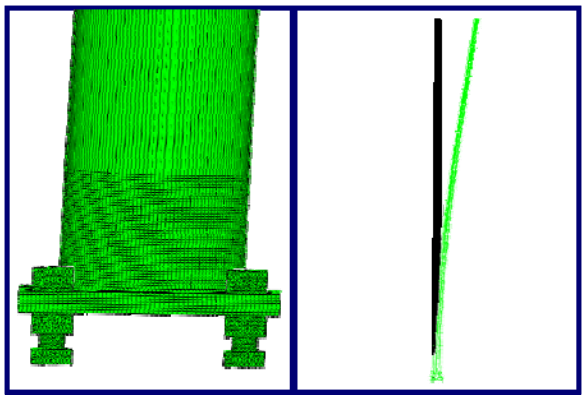

(a)

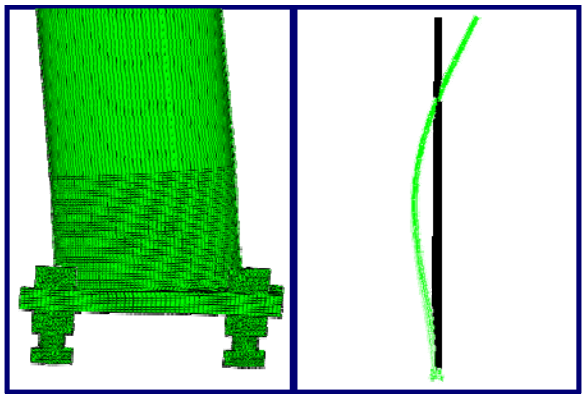

(b)

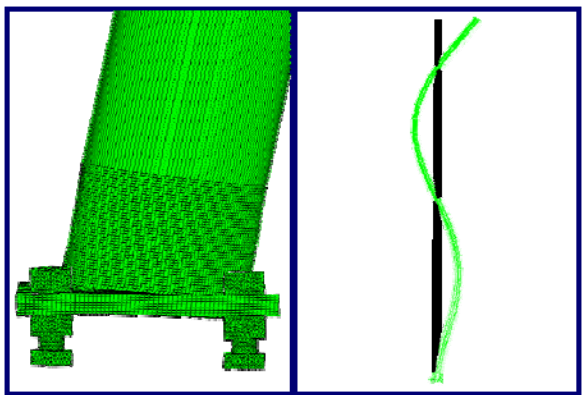

(c)

Figure A.28 Case 28 circular pole mode shape deformation
(a) Mode 1, f = 1.338 Hz; (b) Mode 2, f = 6.820 Hz; (c) Mode 3, f = 17.932 Hz.

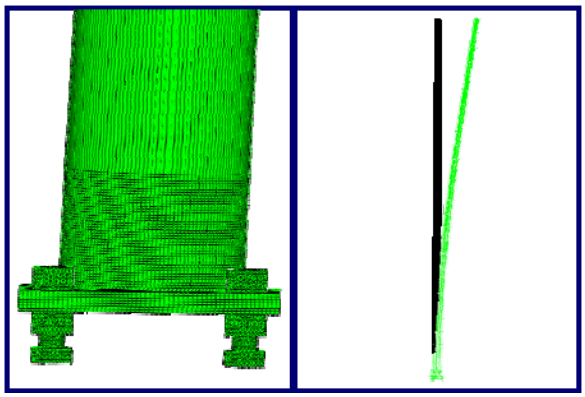

(a)

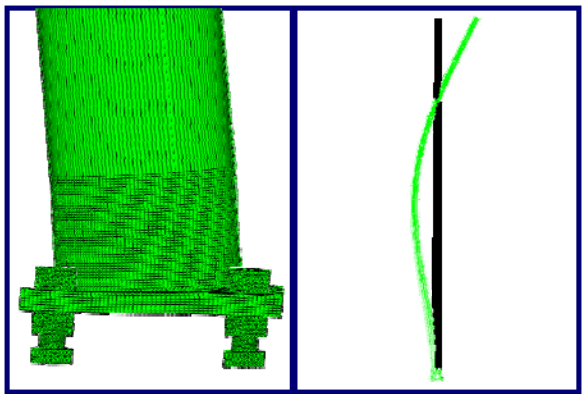

(b)

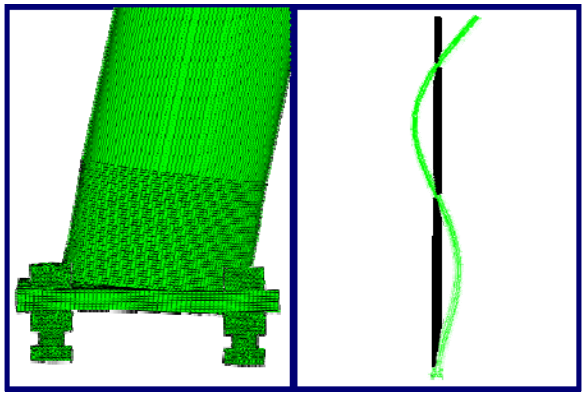

(c)

Figure A.29 Case 29 circular pole mode shape deformation
(a) Mode 1, f = 1.338 Hz; (b) Mode 2, f = 6.820 Hz; (c) Mode 3, f = 17.932 Hz.

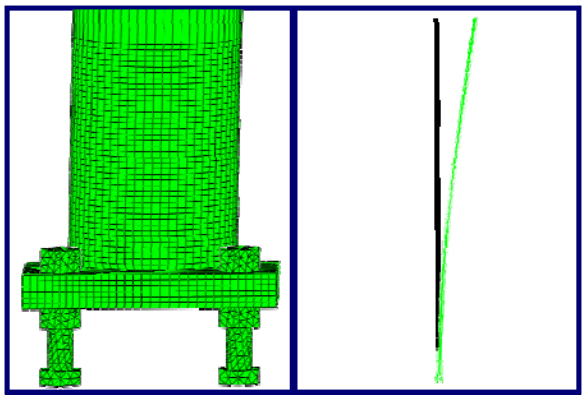

(a)

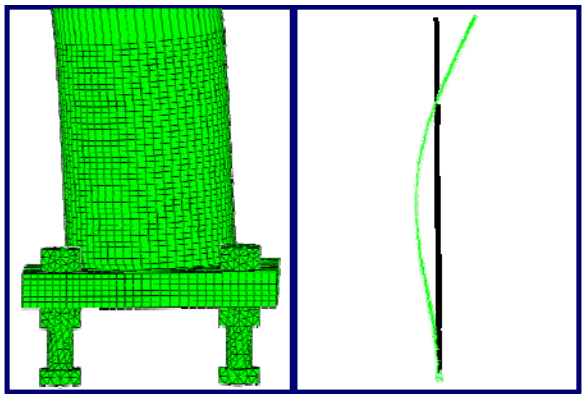

(b)

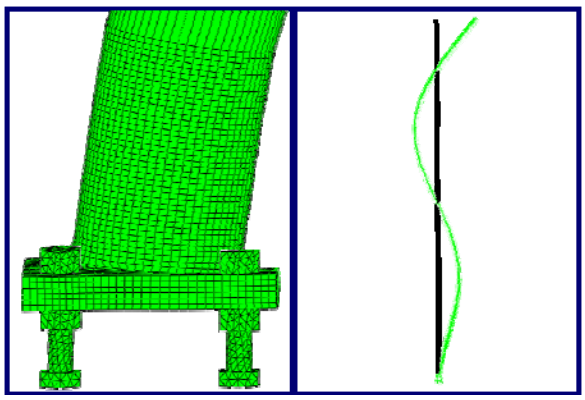

(c)

Figure A.30 Case 30 circular pole mode shape deformation
(a) Mode 1, f = 0.565 Hz; (b) Mode 2, f = 2.909 Hz; (c) Mode 3, f = 7.664 Hz.

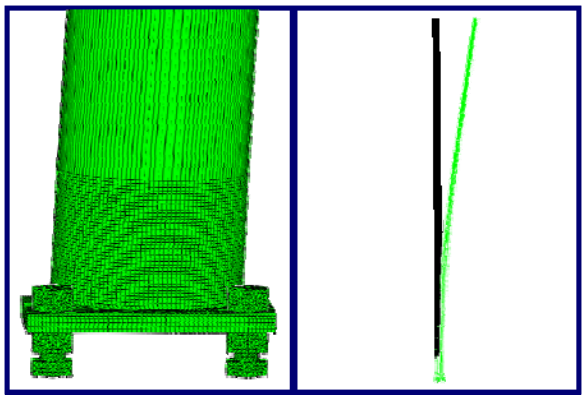

(a)

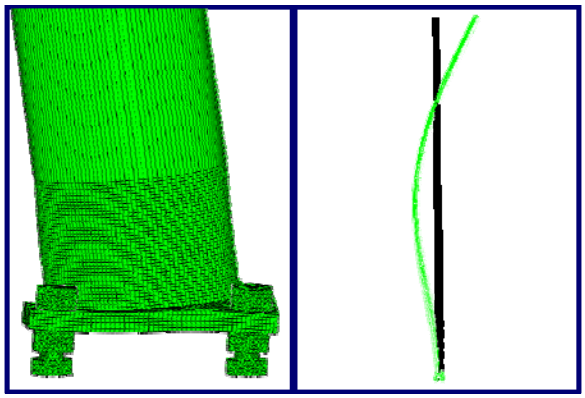

(b)

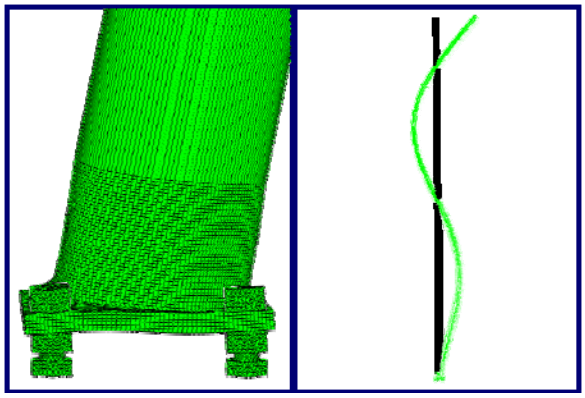

(c)

Figure A.31 Case 31 circular pole mode shape deformation
(a) Mode 1, f = 1.039 Hz; (b) Mode 2, f = 5.213 Hz; (c) Mode 3, f = 13.661 Hz.

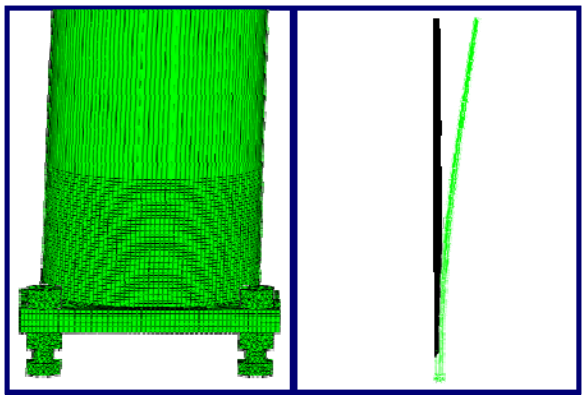

(a)

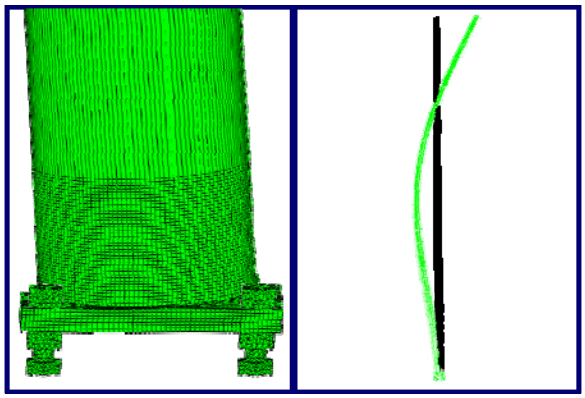

(b)

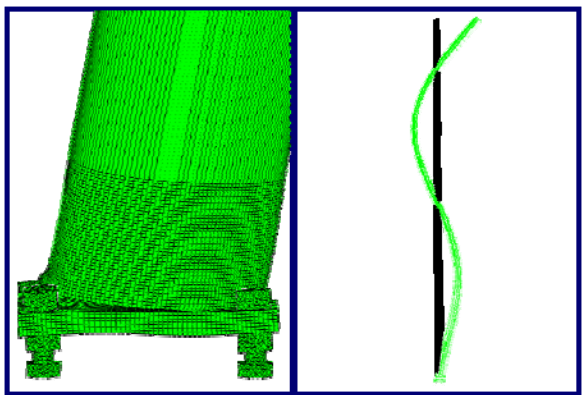

(c)

Figure A.32 Case 32 circular pole mode shape deformation
(a) Mode 1, f = 1.219 Hz; (b) Mode 2, f = 5.785 Hz; (c) Mode 3, f = 14.916 Hz.

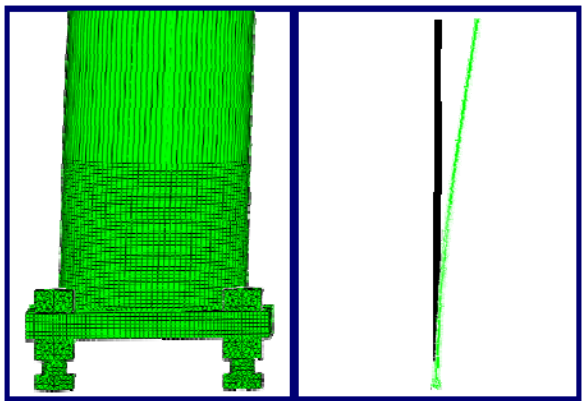

(a)

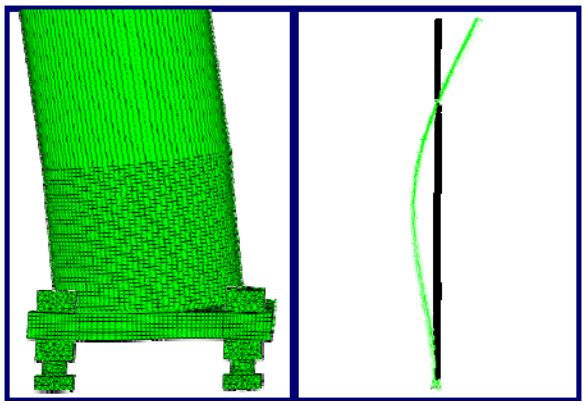

(b)

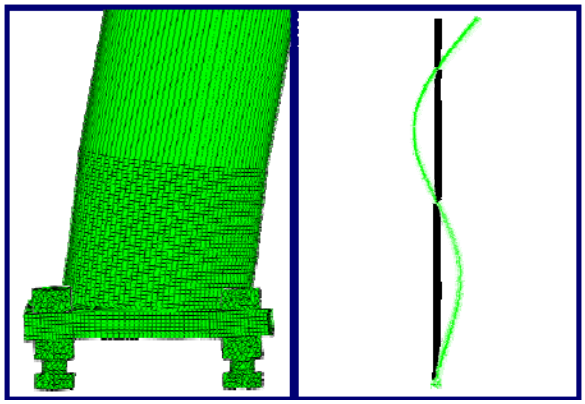

(c)

Figure A.33 Case 33 circular pole mode shape deformation
(a) Mode 1, f = 0.884 Hz; (b) Mode 2, f = 4.717 Hz; (c) Mode 3, f = 12.570 Hz.

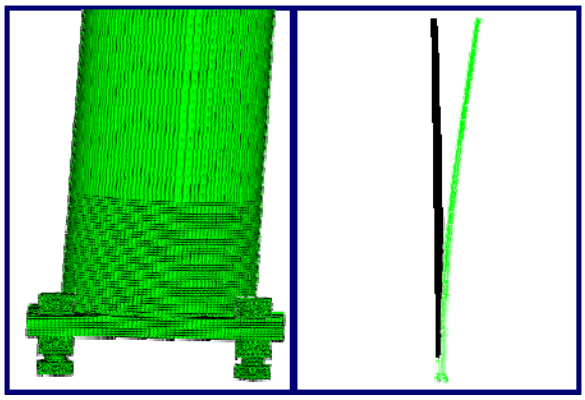

(a)

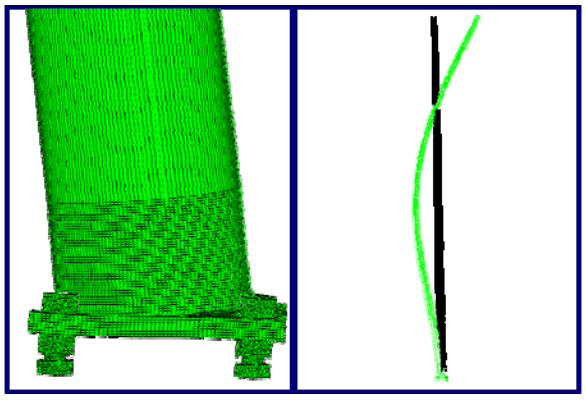

(b)

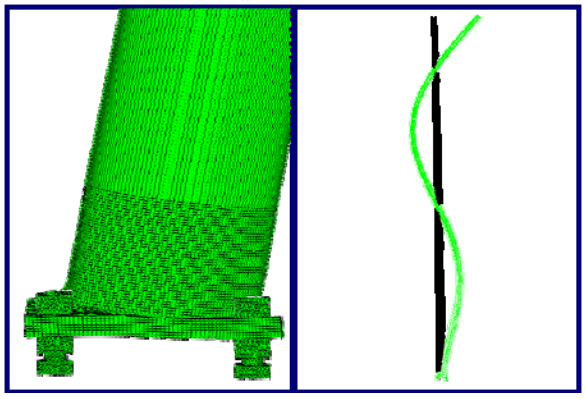

(c)

Figure A.34 Case 34 circular pole mode shape deformation
(a) Mode 1, f = 1.207 Hz; (b) Mode 2, f = 5.756 Hz; (c) Mode 3, f = 14.849 Hz.

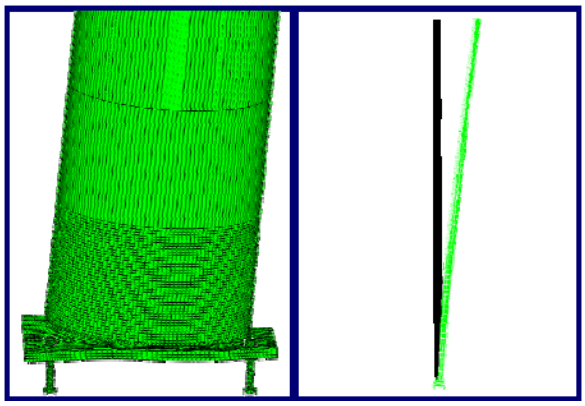

(a)

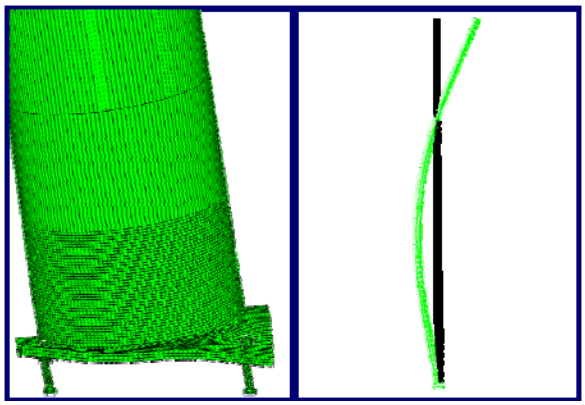

(b)

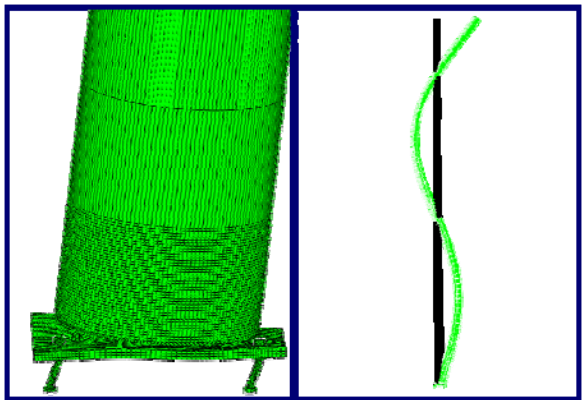

(c)

Figure A.35 Case 35 circular pole mode shape deformation
(a) Mode 1, f = 0.794 Hz; (b) Mode 2, f = 5.118 Hz; (c) Mode 3, f = 14.573 Hz.

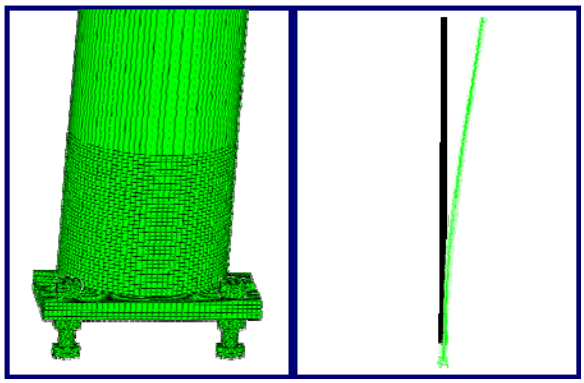

(a)

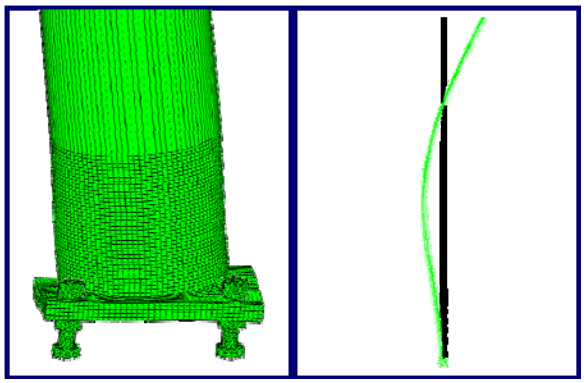

(b)

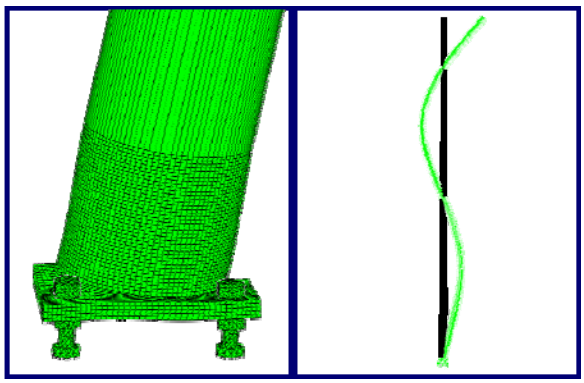

(c)

Figure A.36 Case 36 circular pole mode shape deformation
(a) Mode 1, f =0.872 Hz; (b) Mode 2, f = 5.264 Hz; (c) Mode 3, f = 14.873 Hz.

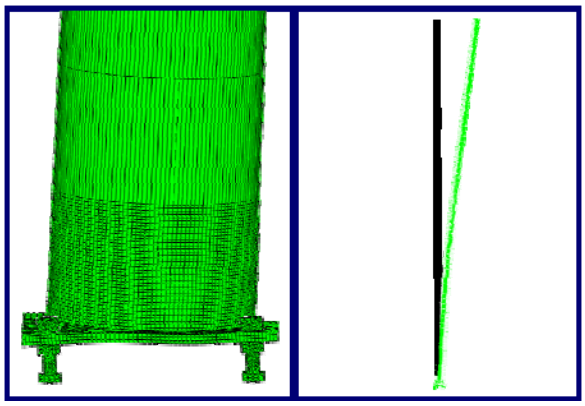

(a)

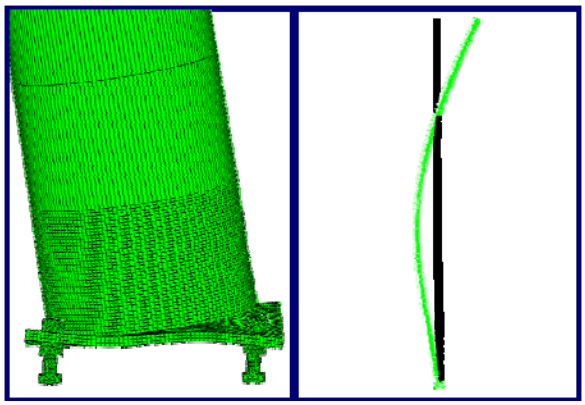

(b)

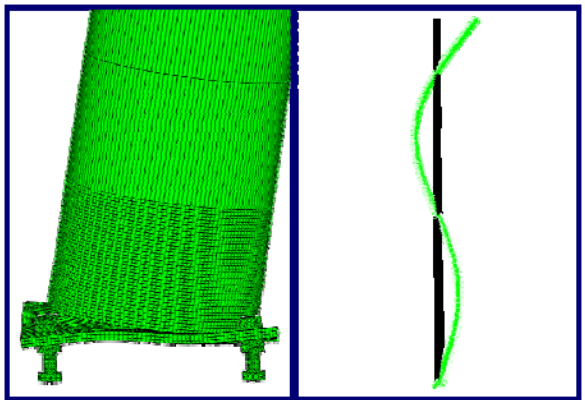

(c)

Figure A.37 Case 37 circular pole mode shape deformation
(a) Mode 1, f = 0.947 Hz; (b) Mode 2, f = 5.409 Hz; (c) Mode 3, f = 15.077 Hz.

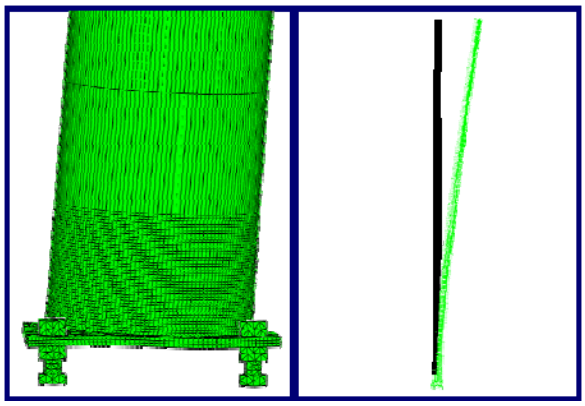

(a)

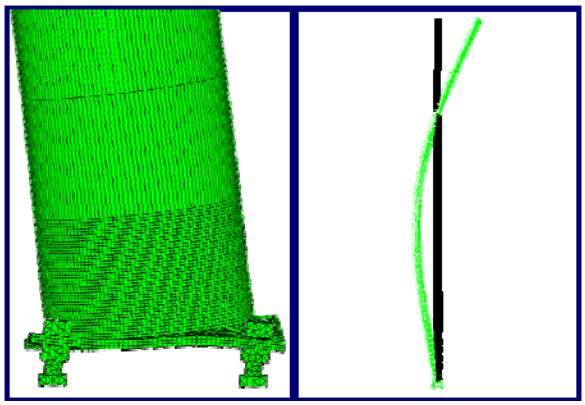

(b)

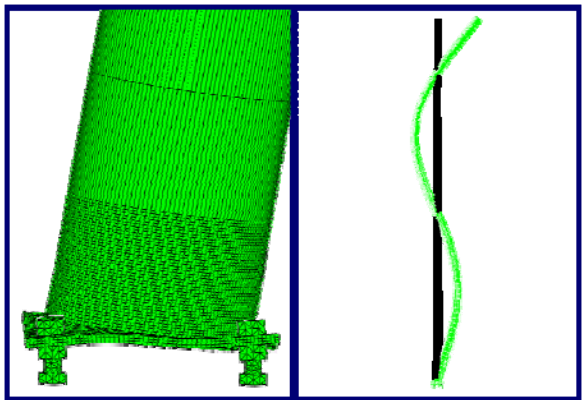

(c)

Figure A.38 Case 38 circular pole mode shape deformation
(a) Mode 1, f = 1.012 Hz; (b) Mode 2, f = 5.554 Hz; (c) Mode 3, f = 15.281 Hz.

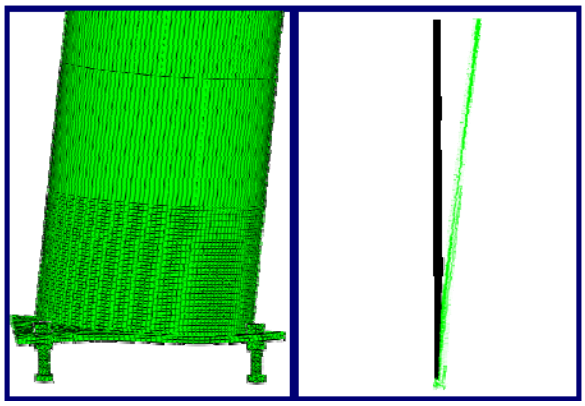

(a)

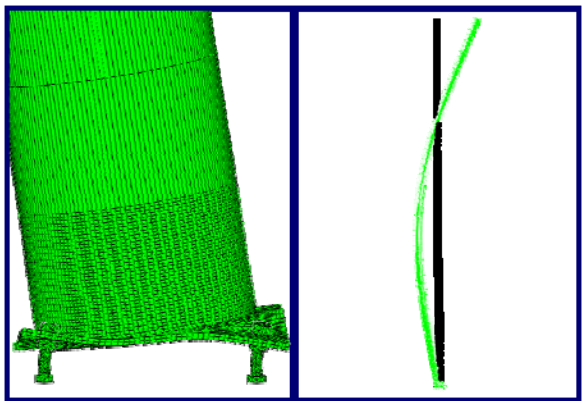

(b)

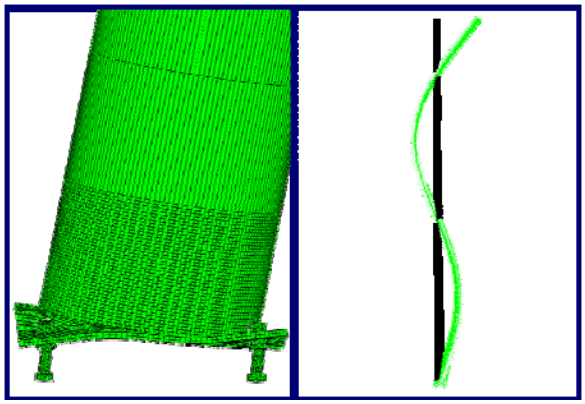

(c)

Figure A.39 Case 39 circular pole mode shape deformation
(a) Mode 1, f = 0.723 Hz; (b) Mode 2, f = 5.046 Hz; (c) Mode 3, f = 14.616 Hz.

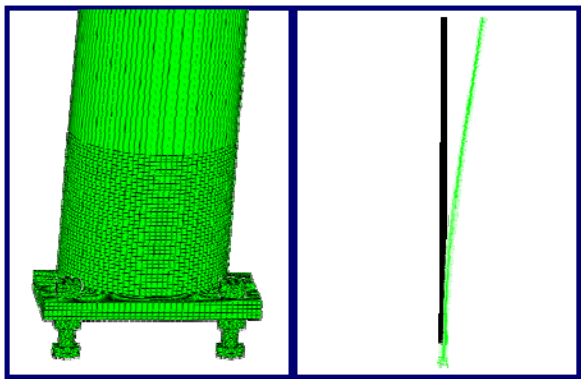

(a)

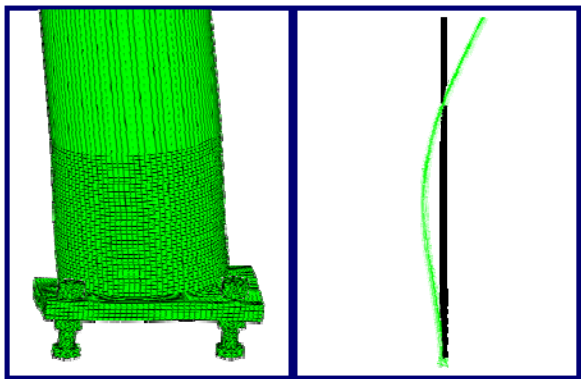

(b)

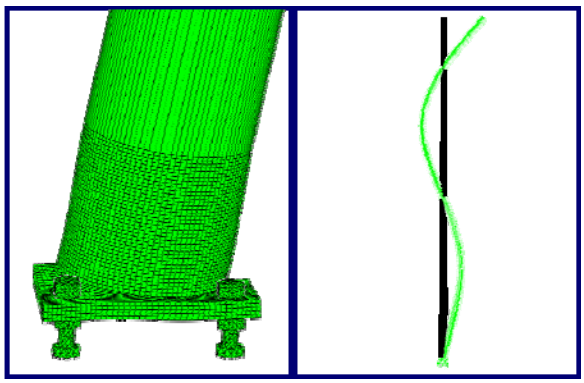

(c)

Figure A.40 Case 40 circular pole mode shape deformation
(a) Mode 1, f =0.872 Hz; (b) Mode 2, f = 5.264 Hz; (c) Mode 3, f = 14.873 Hz.

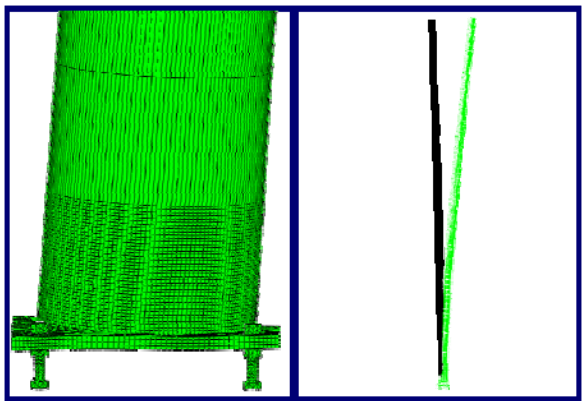

(a)

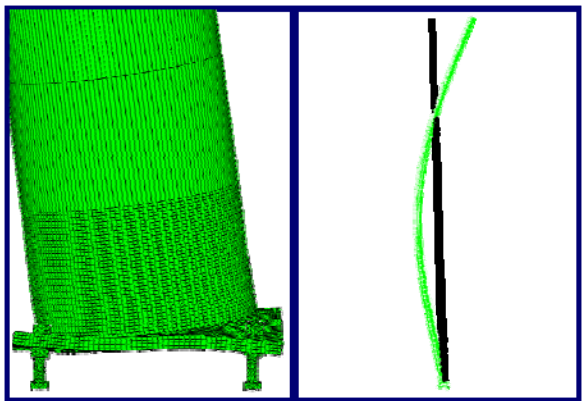

(b)

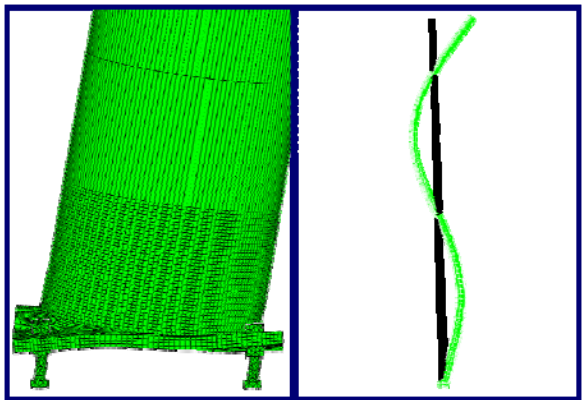

(c)

Figure A.41 Case 41 circular pole mode shape deformation
(a) Mode 1, f = 0.964 Hz; (b) Mode 2, f = 5.436 Hz; (c) Mode 3, f = 15.087 Hz.

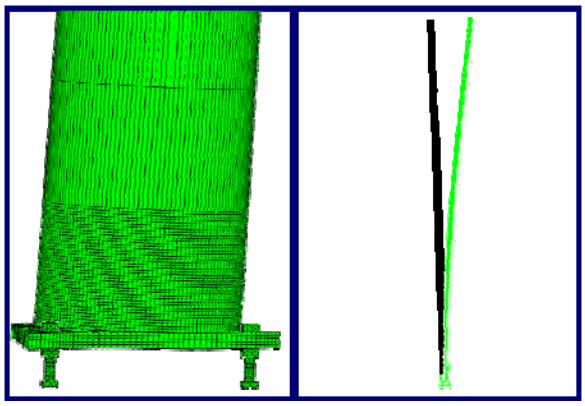

(a)

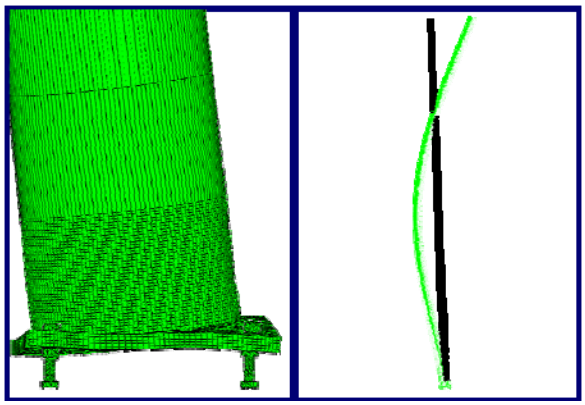

(b)

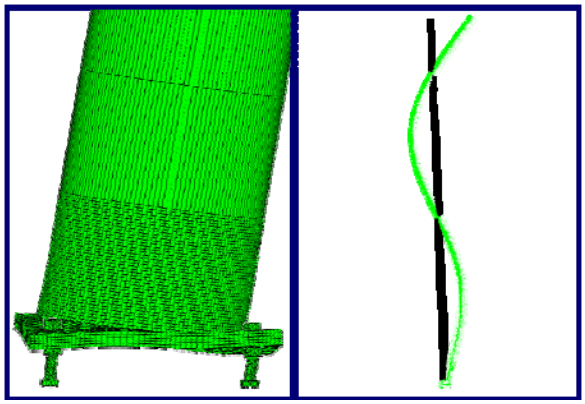

(c)

Figure A.42 Case 42 circular pole mode shape deformation
(a) Mode 1, f = 1.039 Hz; (b) Mode 2, f = 5.596 Hz; (c) Mode 3, f = 15.305 Hz.

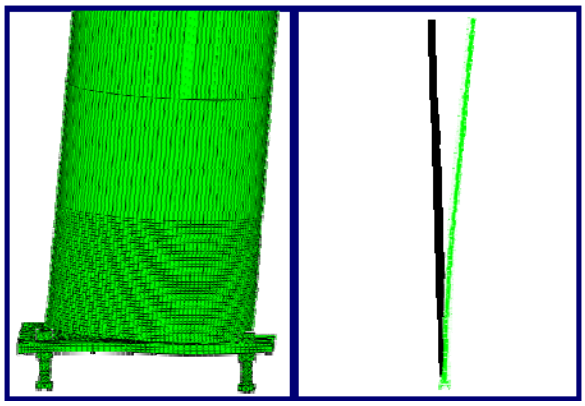

(a)

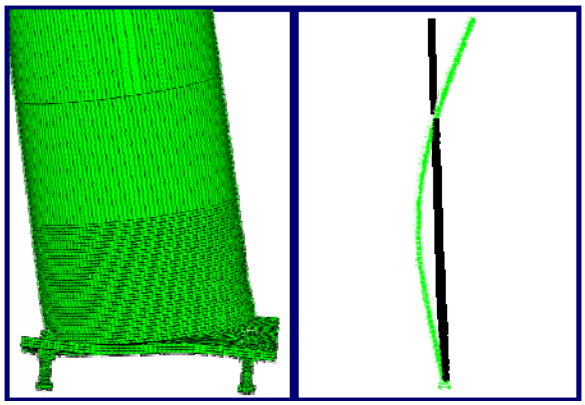

(b)

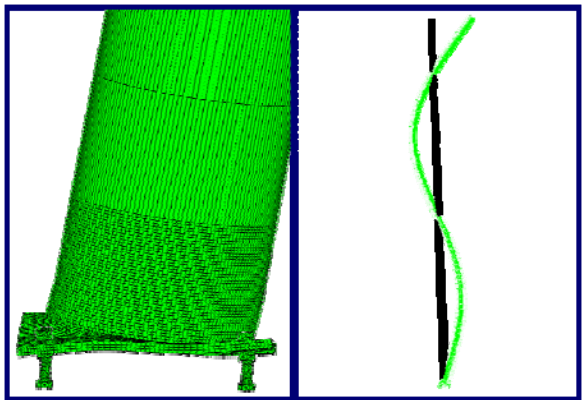

(c)

Figure A.43 Case 43 circular pole mode shape deformation
(a) Mode 1, f = 0.919 Hz; (b) Mode 2, f = 5.413 Hz; (c) Mode 3, f = 15.214 Hz.

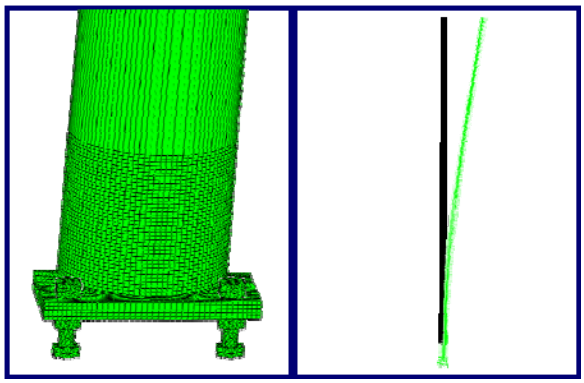

(a)

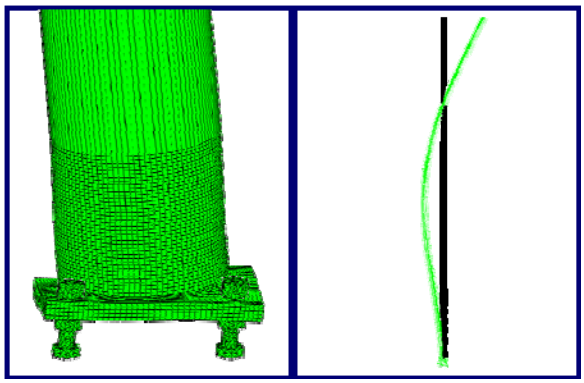

(b)

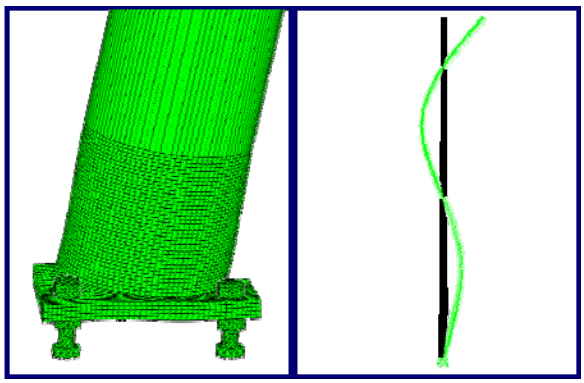

(c)

Figure A.44 Case 44 circular pole mode shape deformation
(a) Mode 1, f =0.872 Hz; (b) Mode 2, f = 5.264 Hz; (c) Mode 3, f = 14.873 Hz.

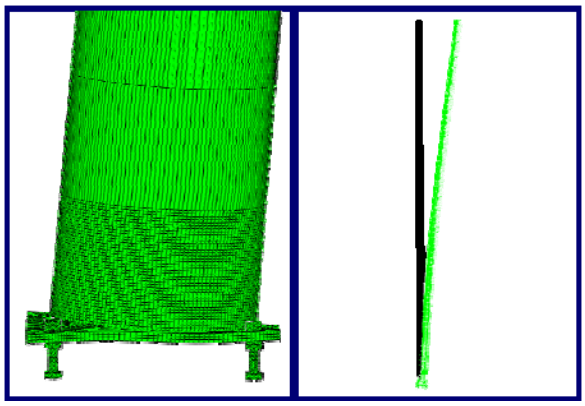

(a)

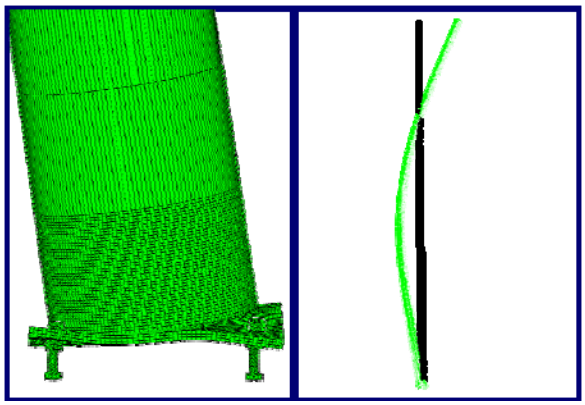

(b)

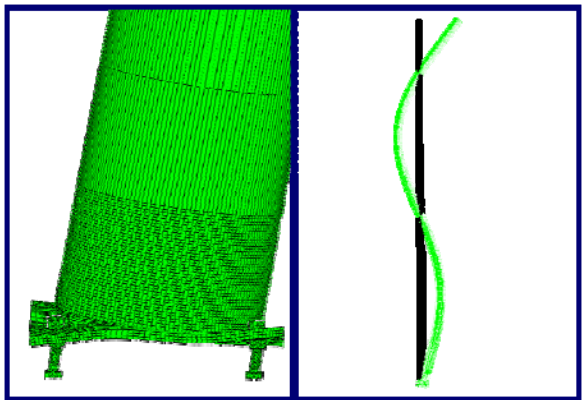

(c)

Figure A.45 Case 45 circular pole mode shape deformation
(a) Mode 1, f = 0.834 Hz; (b) Mode 2, f = 5.135 Hz; (c) Mode 3, f = 14.560 Hz.

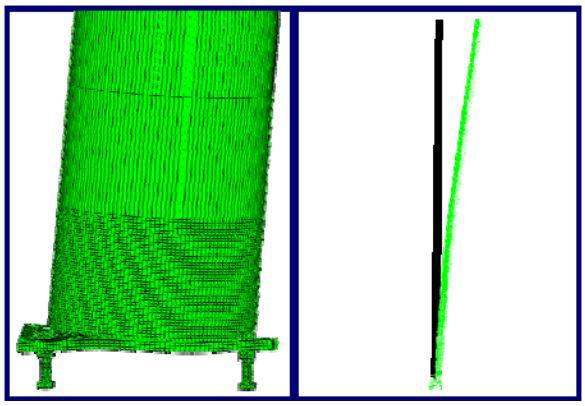

(a)

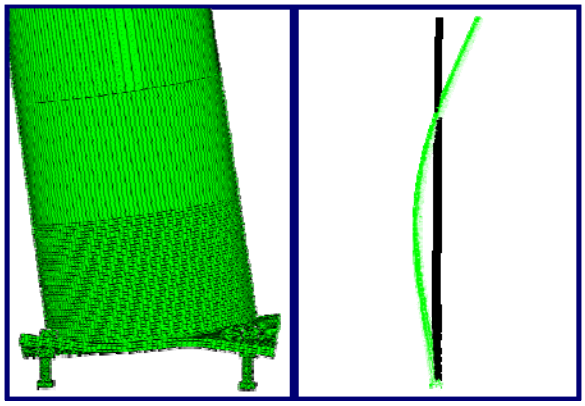

(b)

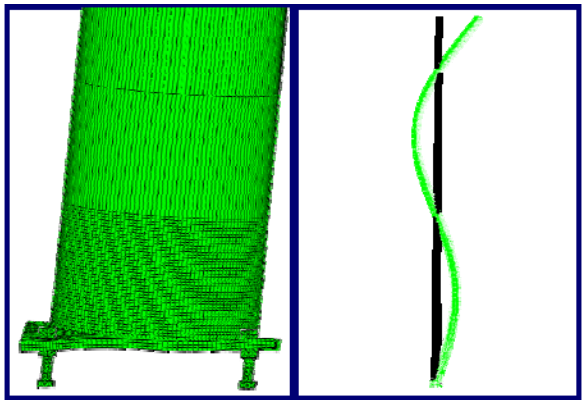

(c)

Figure A.46 Case 46 circular pole mode shape deformation
(a) Mode 1, f = 0.743 Hz; (b) Mode 2, f = 4.591 Hz; (c) Mode 3, f = 12.989 Hz.

APPENDIX B

OCTAGONAL POLES

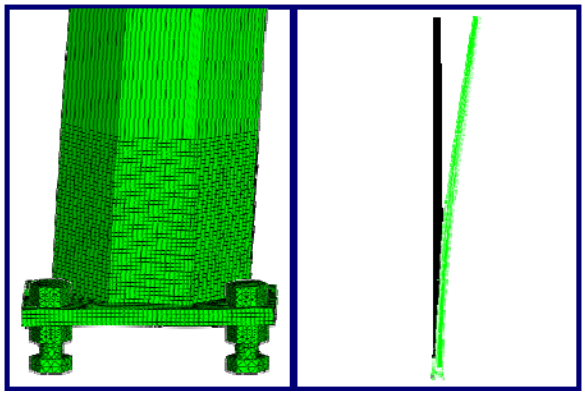

(a)

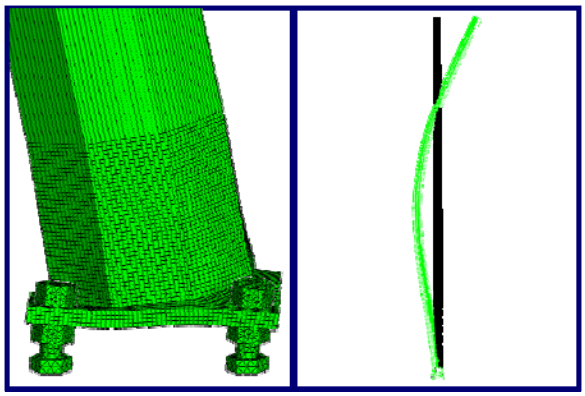

(b)

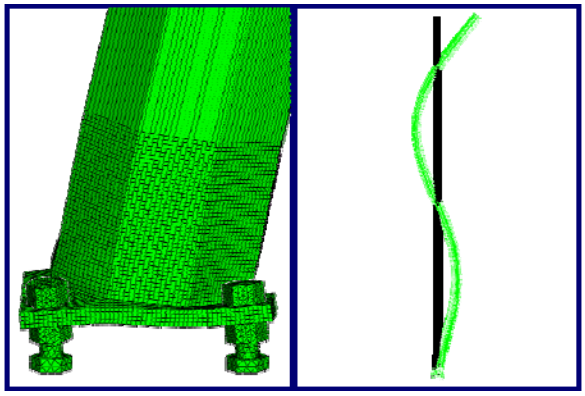

(c)

Figure B.1 Case 01 octagonal pole mode shape deformation
(a) Mode 1, f = 1.976 Hz; (b) Mode 2, f = 9.626 Hz; (c) Mode 3, f = 25.199 Hz.

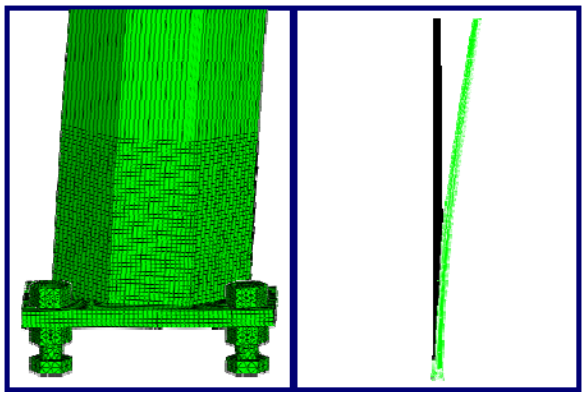

(a)

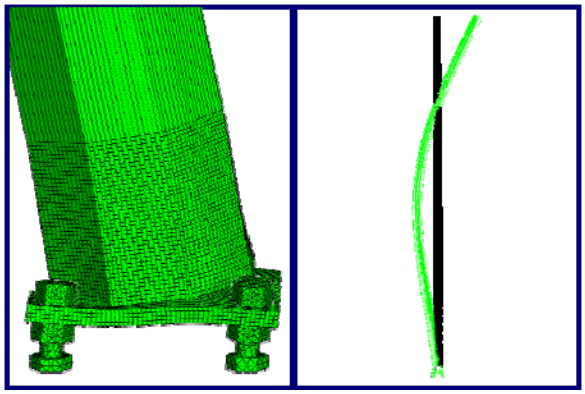

(b)

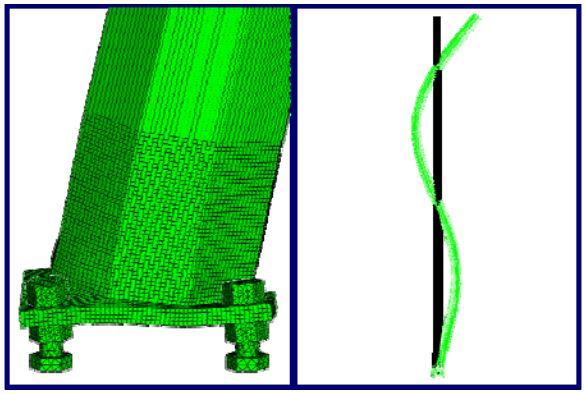

(c)

Figure B.2 Case 02 octagonal pole mode shape deformation
(a) Mode 1, f = 1.843 Hz; (b) Mode 2, f = 9.477 Hz; (c) Mode 3, f = 25.001 Hz.

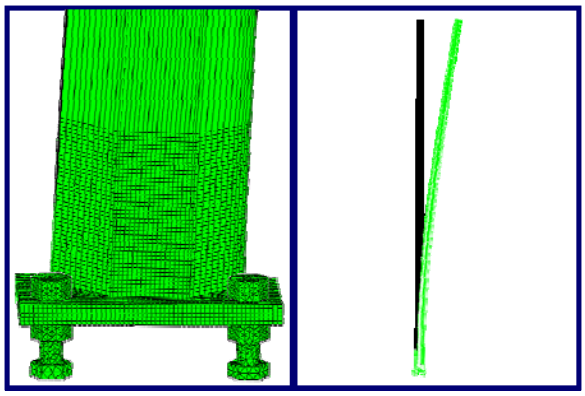

(a)

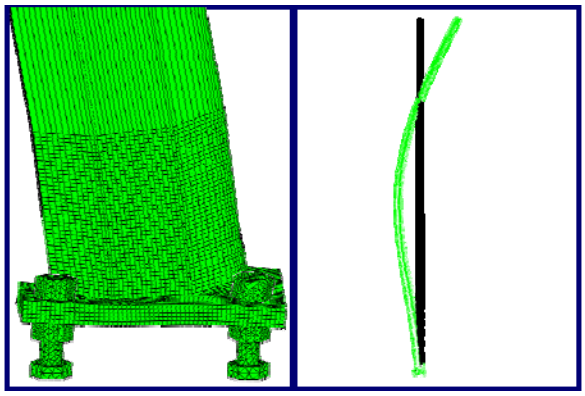

(b)

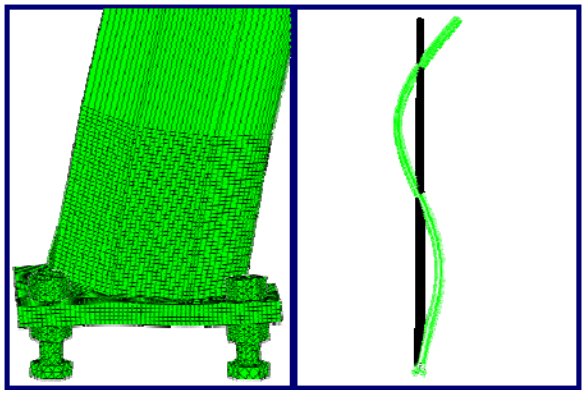

(c)

Figure B.3 Case 03 octagonal pole mode shape deformation
(a) Mode 1, f = 1.879 Hz; (b) Mode 2, f = 9.465 Hz; (c) Mode 3, f = 24.841 Hz.

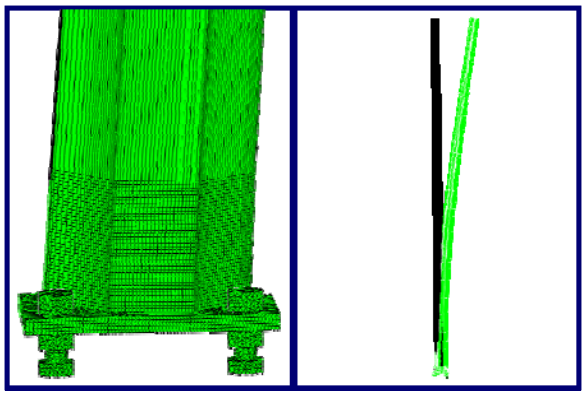

(a)

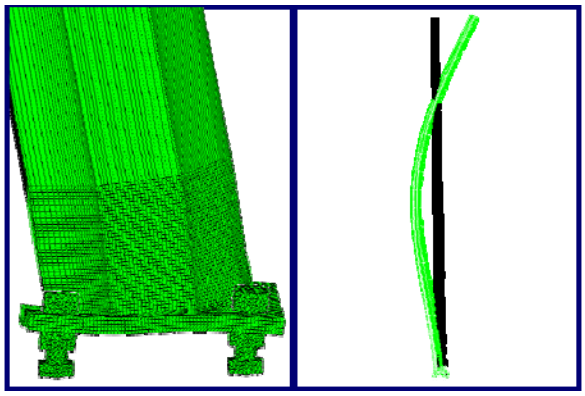

(b)

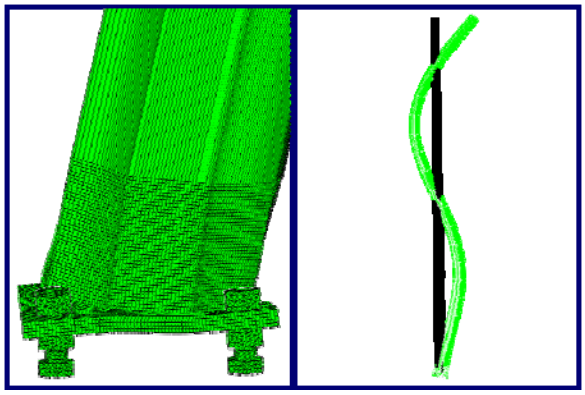

(c)

Figure B.4 Case 04 octagonal pole mode shape deformation
(a) Mode 1, f = 2.485 Hz; (b) Mode 2, f = 12.239 Hz; (c) Mode 3, f = 31.817 Hz.

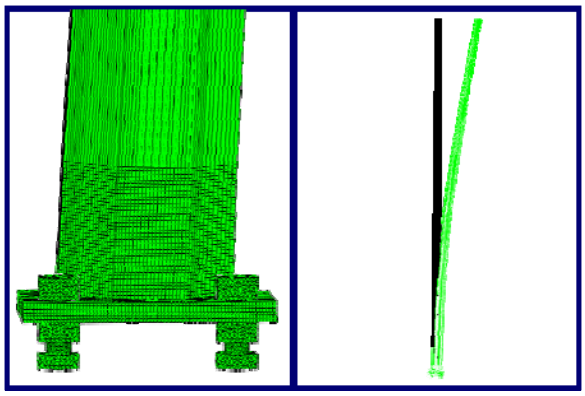

(a)

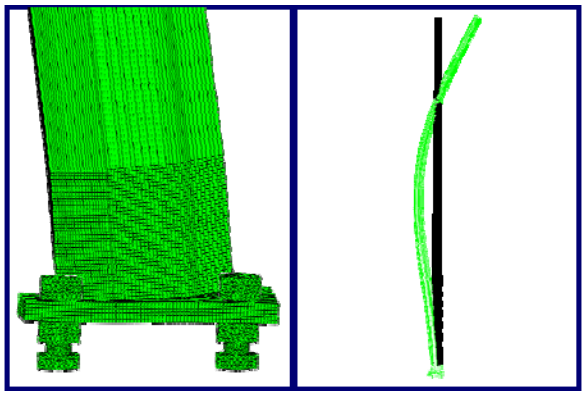

(b)

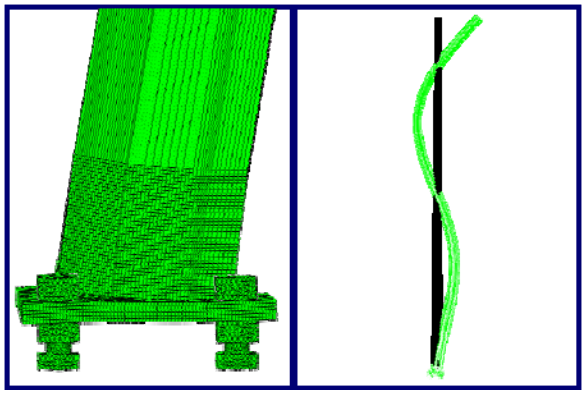

(c)

Figure B.5 Case 05 octagonal pole mode shape deformation
(a) Mode 1, f = 2.391 Hz; (b) Mode 2, f = 10.721 Hz; (c) Mode 3, f = 27.056 Hz.

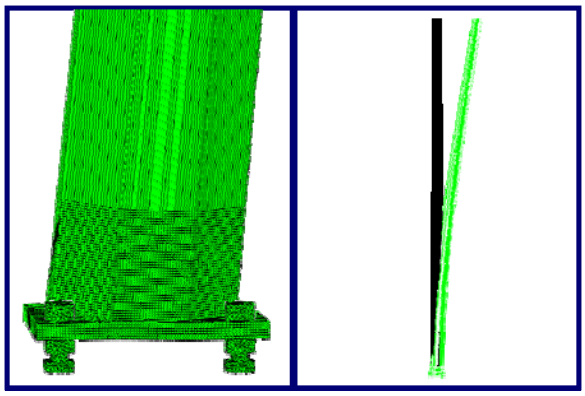

(a)

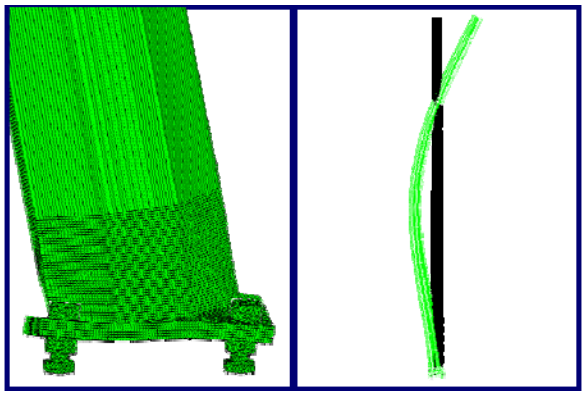

(b)

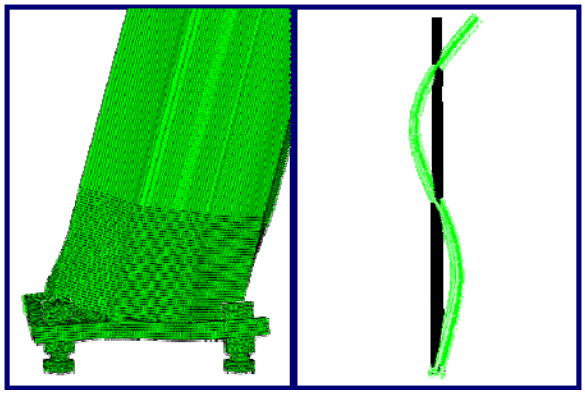

(c)

Figure B.6 Case 06 octagonal pole mode shape deformation
(a) Mode 1, f = 2.659 Hz; (b) Mode 2, f = 13.257 Hz; (c) Mode 3, f = 34.655 Hz.

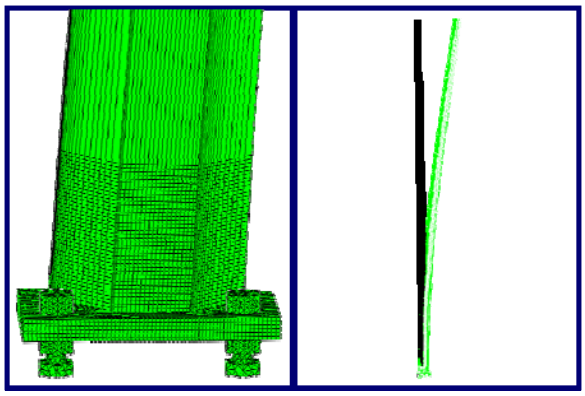

(a)

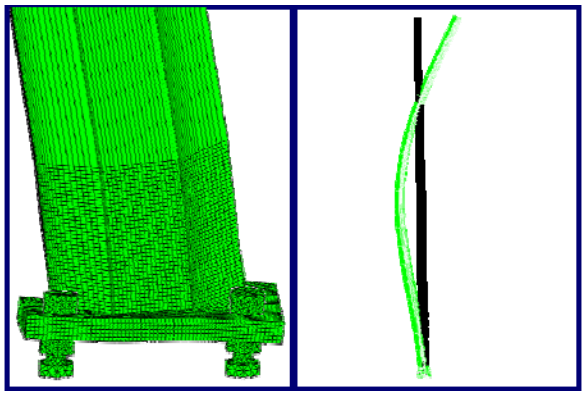

(b)

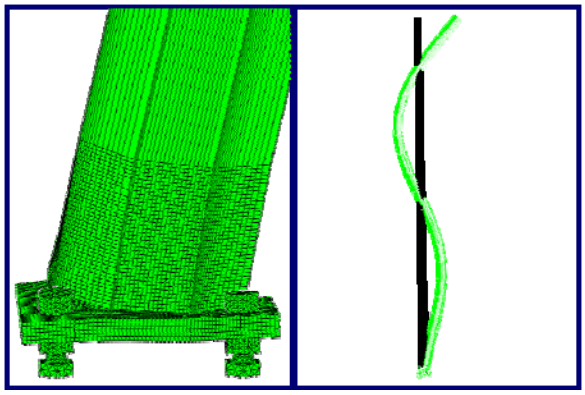

(c)

Figure B.7 Case 07 octagonal pole mode shape deformation
(a) Mode 1, f = 2.154 Hz; (b) Mode 2, f = 10.455 Hz; (c) Mode 3, f = 27.127 Hz.

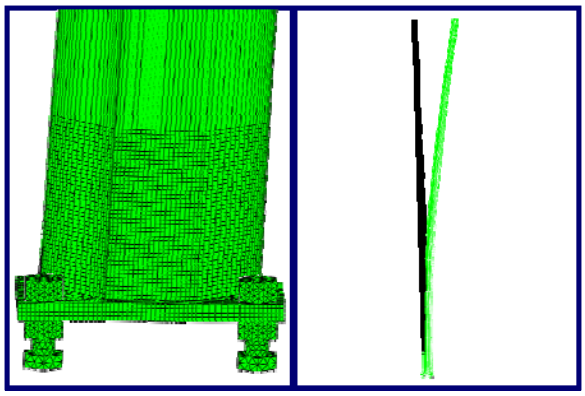

(a)

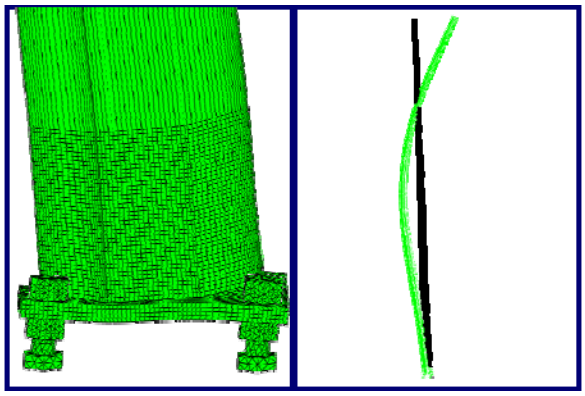

(b)

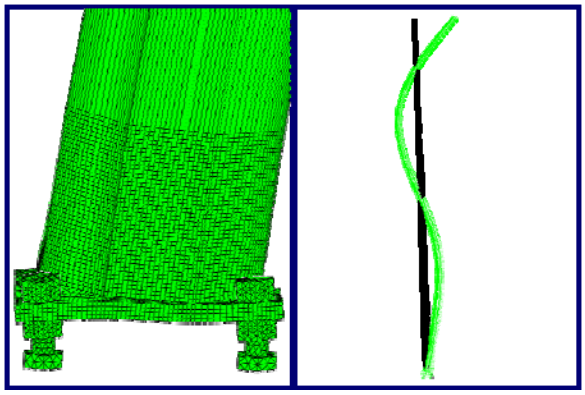

(c)

Figure B.8 Case 08 octagonal pole mode shape deformation
(a) Mode 1, f = 1.768 Hz; (b) Mode 2, f = 7.591 Hz; (c) Mode 3, f = 19.015 Hz.

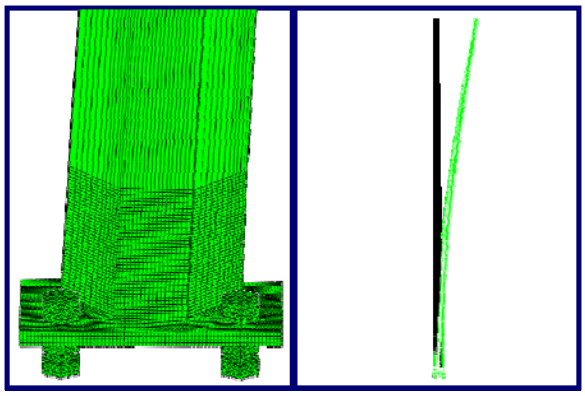

(a)

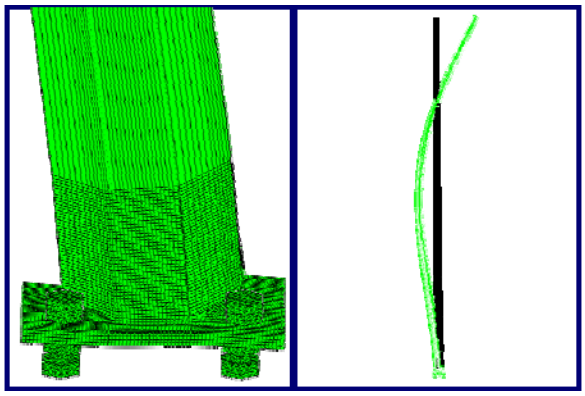

(b)

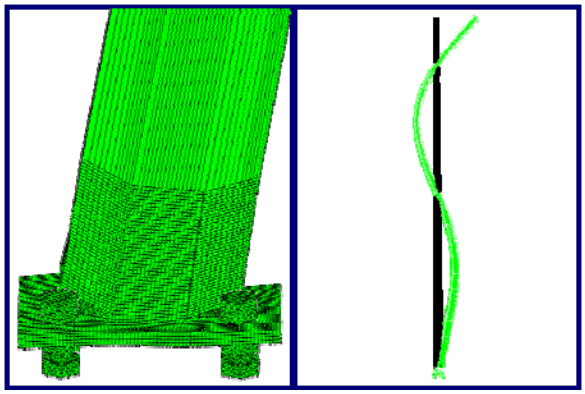

(c)

Figure B.9 Case 09 octagonal pole mode shape deformation
(a) Mode 1, f = 1.686 Hz; (b) Mode 2, f = 7.518 Hz; (c) Mode 3, f = 18.993 Hz.

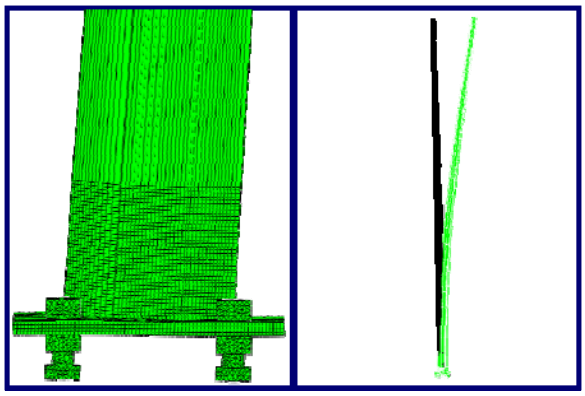

(a)

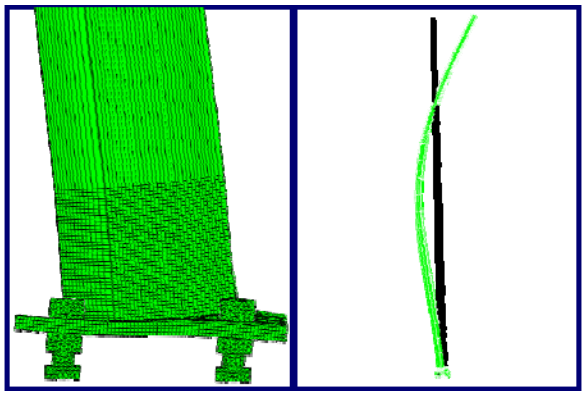

(b)

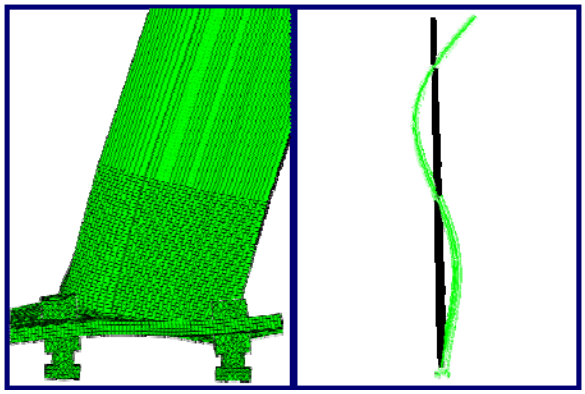

(c)

Figure B.10 Case 10 octagonal pole mode shape deformation
(a) Mode 1, f = 1.657 Hz; (b) Mode 2, f = 7.390 Hz; (c) Mode 3, f = 18.705 Hz.

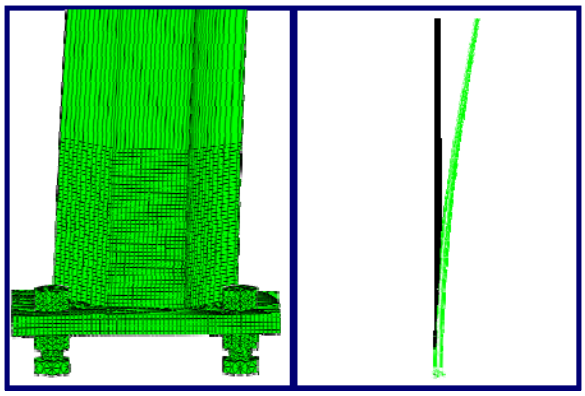

(a)

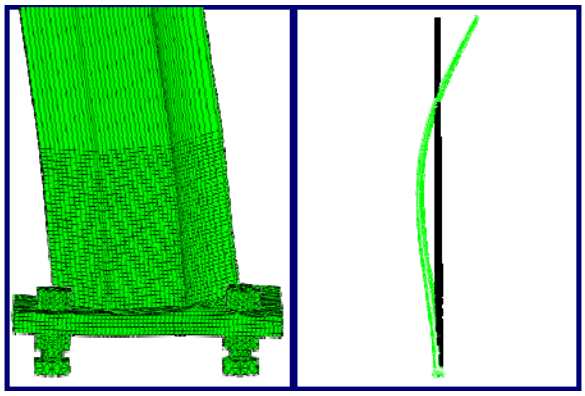

(b)

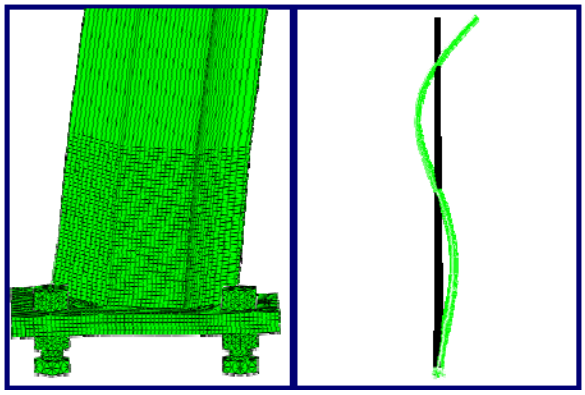

(c)

Figure B.11 Case 11 octagonal pole mode shape deformation
(a) Mode 1, f = 1.628 Hz; (b) Mode 2, f = 6.901 Hz; (c) Mode 3, f = 17.102 Hz.

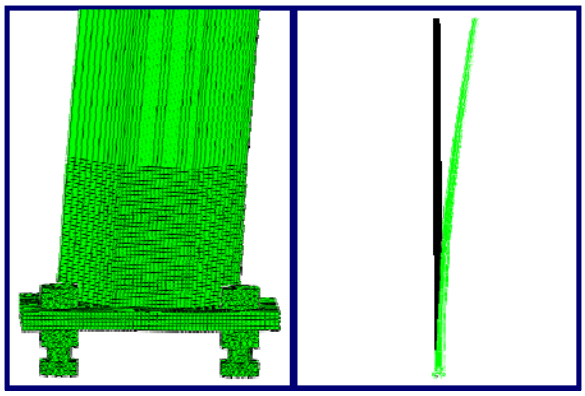

(a)

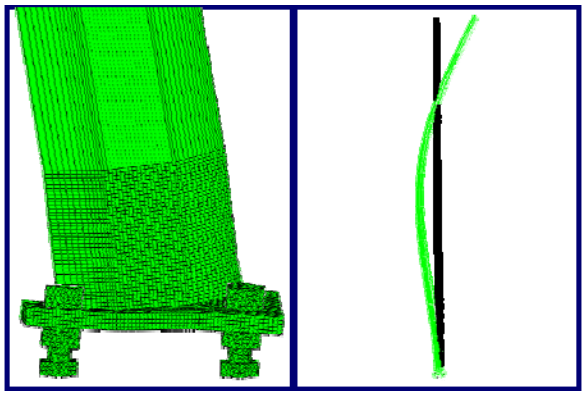

(b)

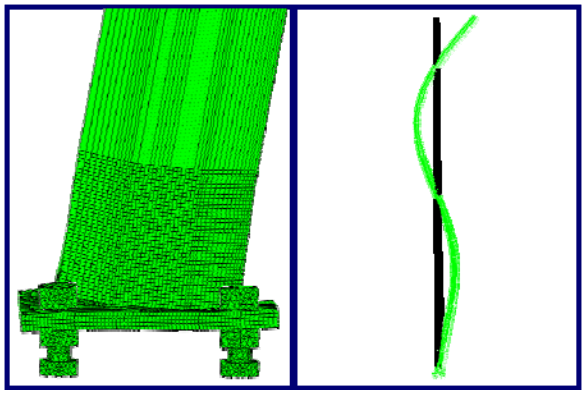

(c)

Figure B.12 Case 12 octagonal pole mode shape deformation
(a) Mode 1, f = 1.856 Hz; (b) Mode 2, f = 8.167 Hz; (c) Mode 3, f = 20.597 Hz.

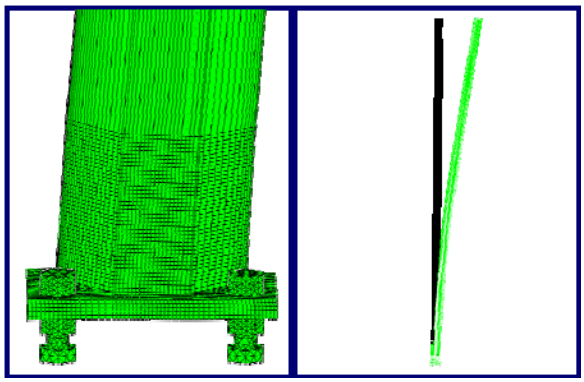

(a)

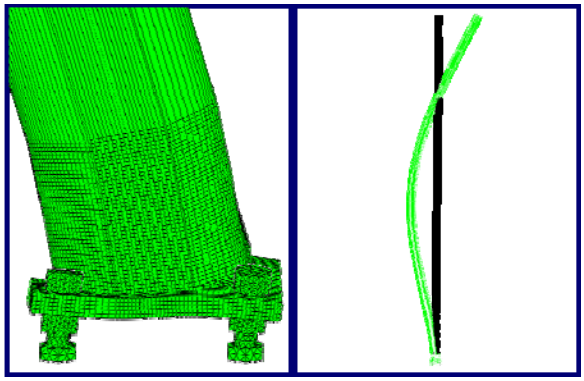

(b)

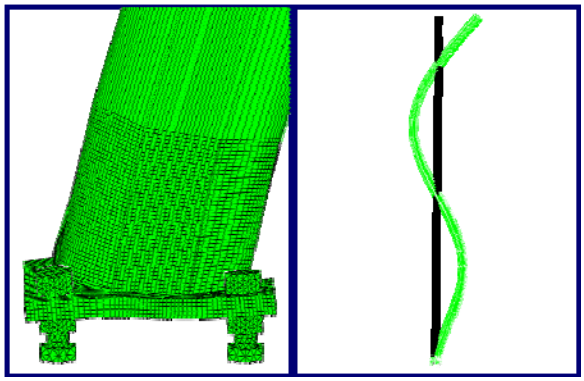

(c)

Figure B.13 Case 13 octagonal pole mode shape deformation
(a) Mode 1, f = 1.290 Hz; (b) Mode 2, f = 7.708 Hz; (c) Mode 3, f = 21.242 Hz.

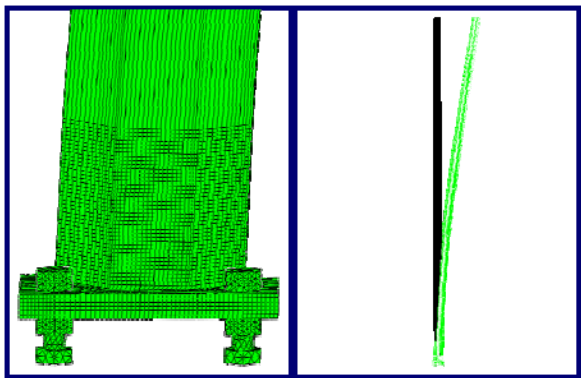

(a)

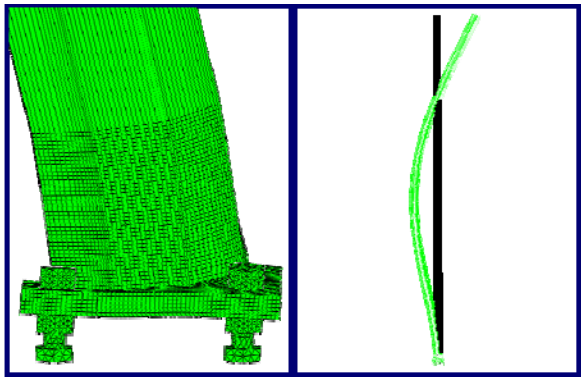

(b)

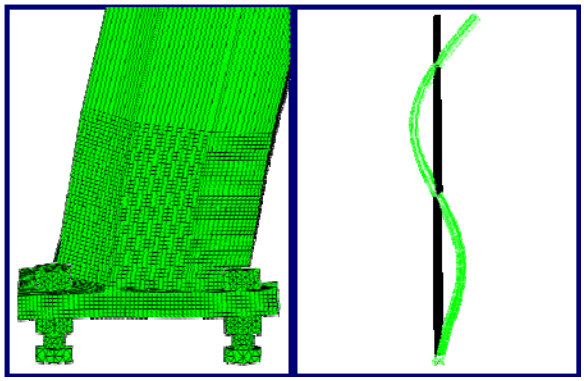

(c)

Figure B.14 Case 14 octagonal pole mode shape deformation
(a) Mode 1, f = 1.478 Hz; (b) Mode 2, f = 8.121 Hz; (c) Mode 3, f = 21.830 Hz.

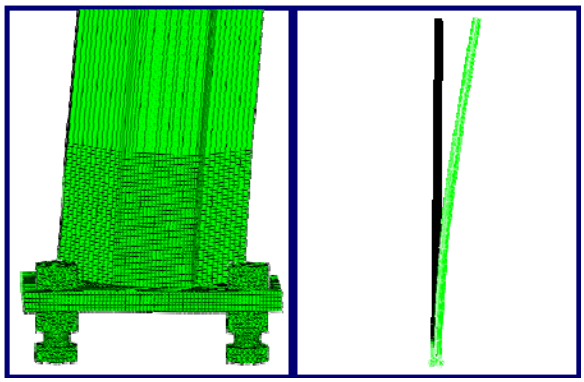

(a)

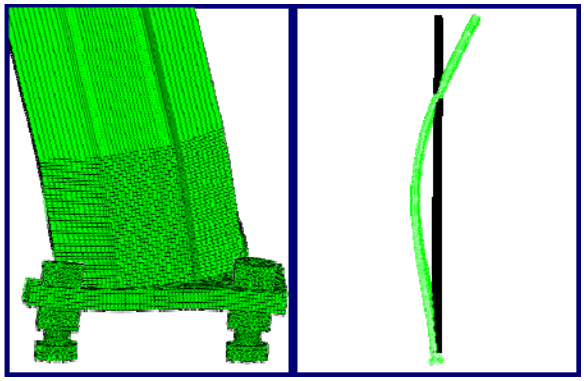

(b)

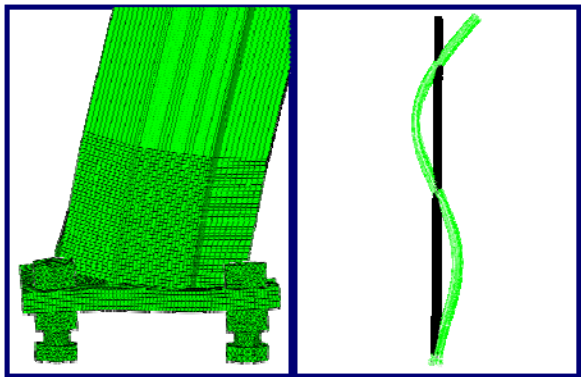

(c)

Figure B.15 Case 15 octagonal pole mode shape deformation
(a) Mode 1, f = 1.747 Hz; (b) Mode 2, f = 8.940 Hz; (c) Mode 3, f = 23.577 Hz.

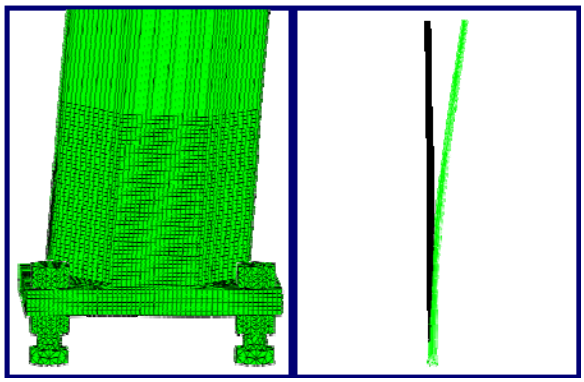

(a)

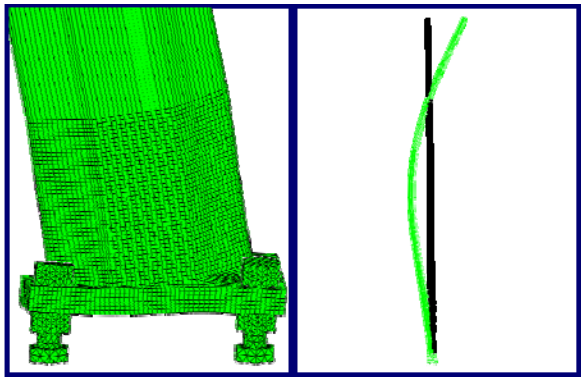

(b)

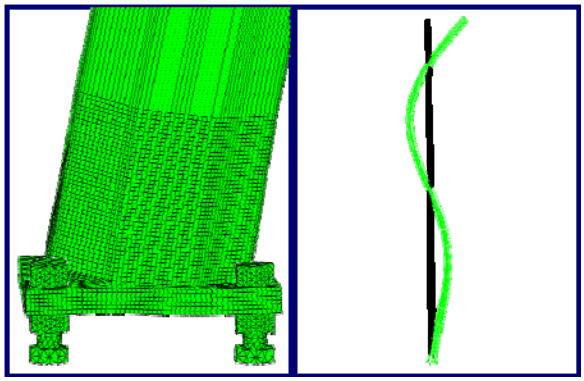

(c)

Figure B.16 Case 16 octagonal pole mode shape deformation
(a) Mode 1, f = 1.589 Hz; (b) Mode 2, f = 7.398 Hz; (c) Mode 3, f = 18.999 Hz.

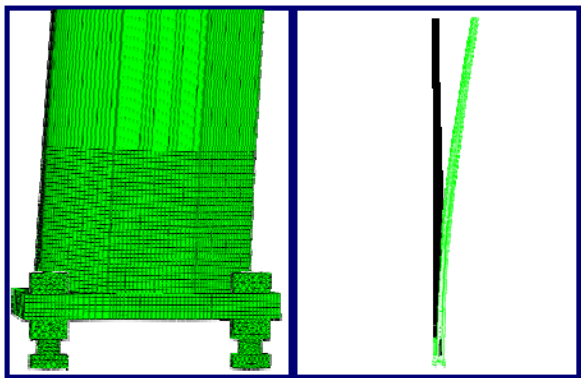

(a)

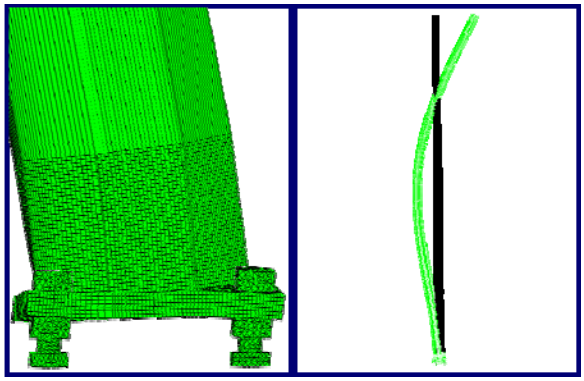

(b)

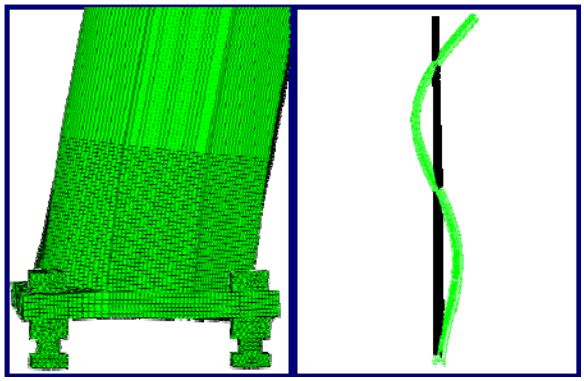

(c)

Figure B.17 Case 17 octagonal pole mode shape deformation
(a) Mode 1, f = 1.971 Hz; (b) Mode 2, f = 9.547 Hz; (c) Mode 3, f = 24.645 Hz.

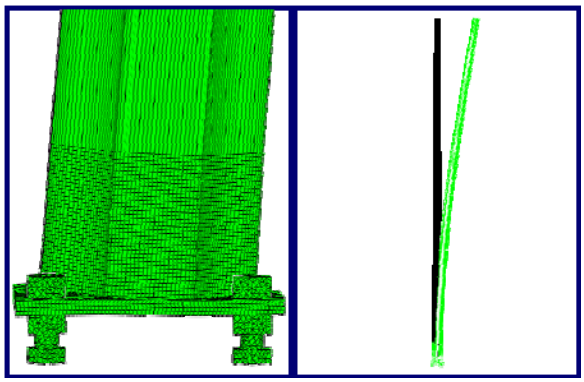

(a)

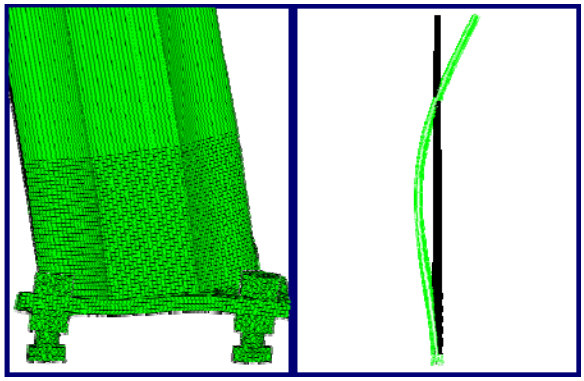

(b)

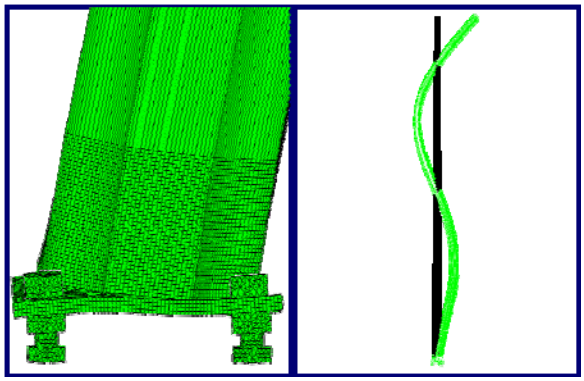

(c)

Figure B.18 Case 18 octagonal pole mode shape deformation
(a) Mode 1, f = 1.634 Hz; (b) Mode 2, f = 7.486 Hz; (c) Mode 3, f = 19.143 Hz.

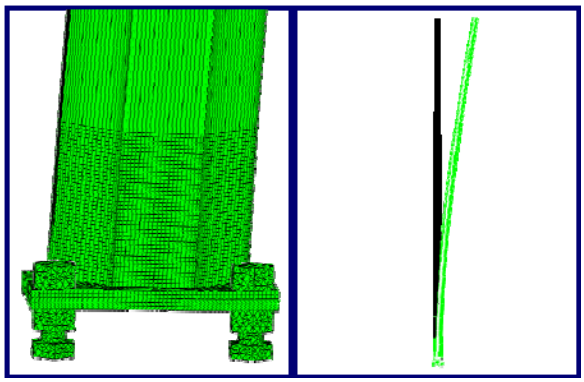

(a)

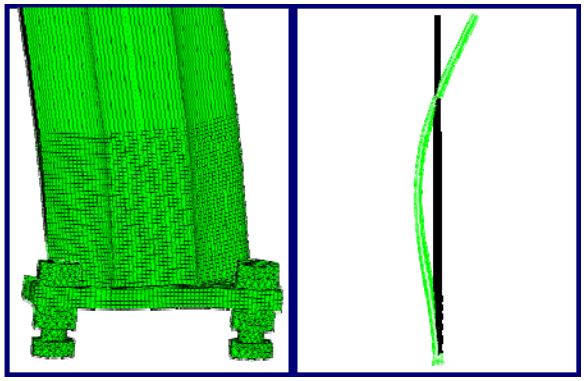

(b)

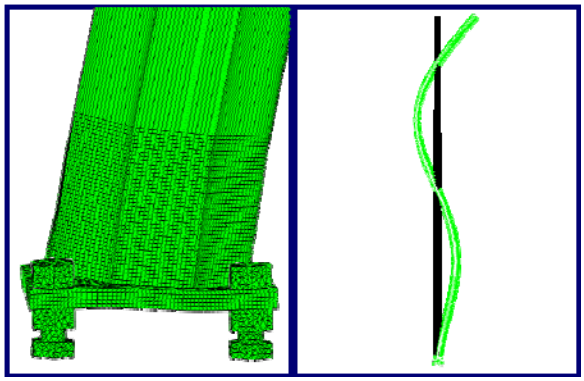

(c)

Figure B.19 Case 19 octagonal pole mode shape deformation
(a) Mode 1, f = 1.456 Hz; (b) Mode 2, f = 6.958 Hz; (c) Mode 3, f = 17.955 Hz.

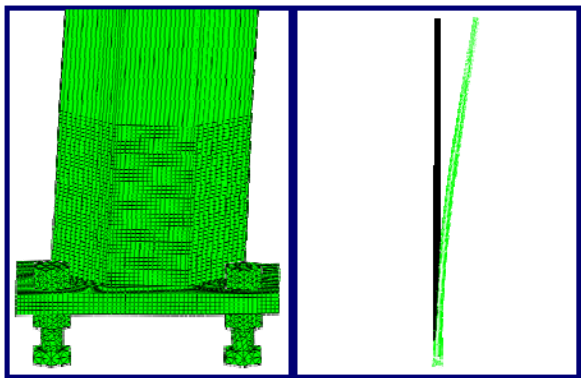

(a)

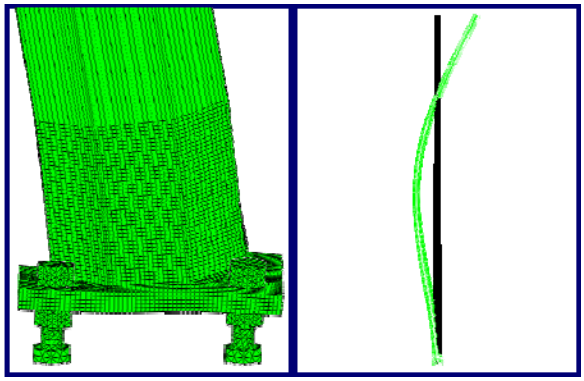

(b)

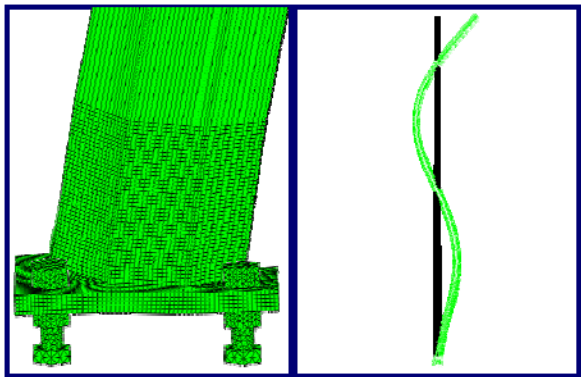

(c)

Figure B.20 Case 20 octagonal pole mode shape deformation
(a) Mode 1, f = 1.235 Hz; (b) Mode 2, f = 6.081 Hz; (c) Mode 3, f = 15.825 Hz.

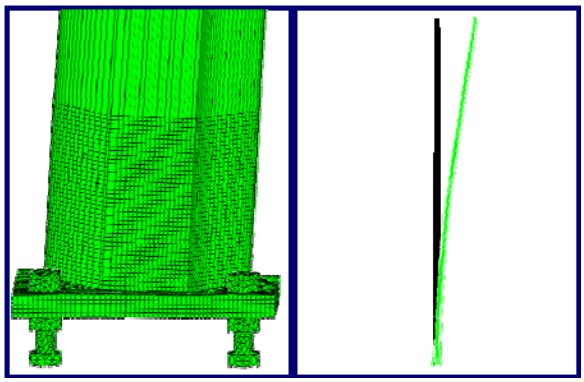

(a)

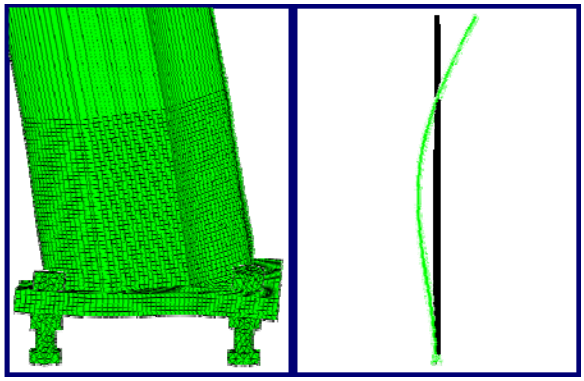

(b)

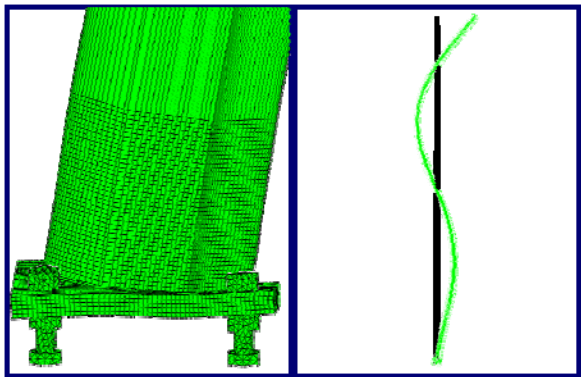

(c)

Figure B.21 Case 21 octagonal pole mode shape deformation
(a) Mode 1, f = 1.274 Hz; (b) Mode 2, f = 5.953 Hz; (c) Mode 3, f = 15.329 Hz.

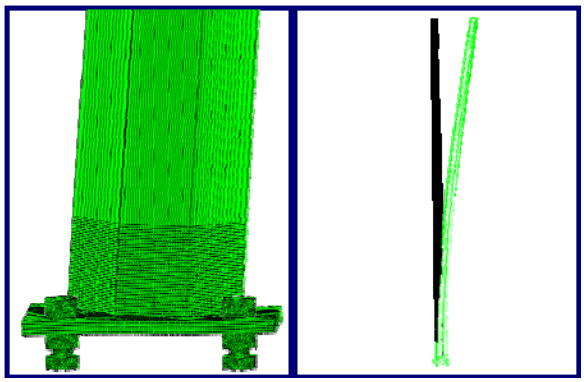

(a)

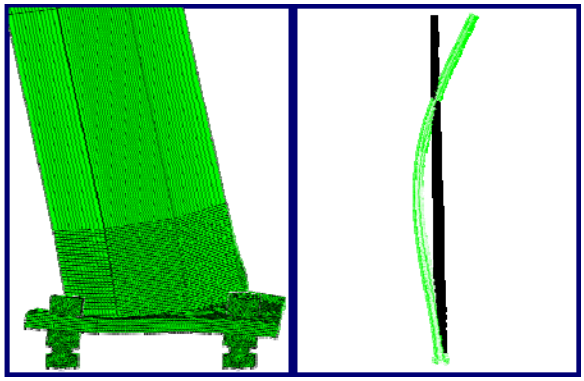

(b)

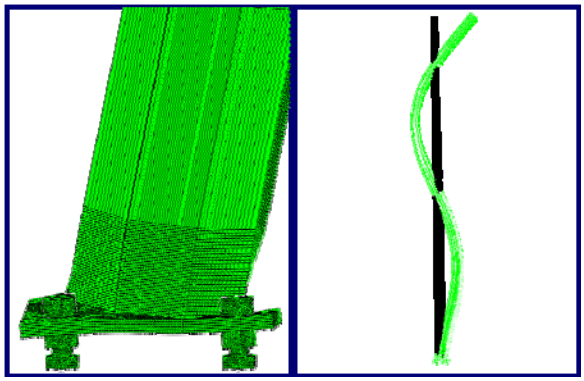

(c)

Figure B.22 Case 22 octagonal pole mode shape deformation
(a) Mode 1, f = 1.975 Hz; (b) Mode 2, f = 9.428 Hz; (c) Mode 3, f = 24.320 Hz.

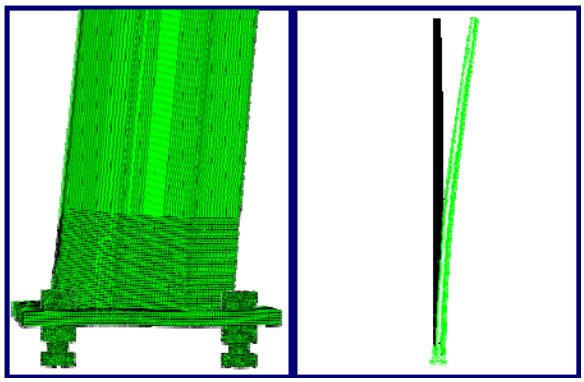

(a)

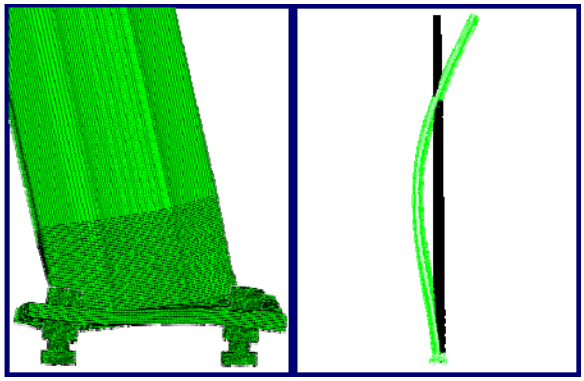

(b)

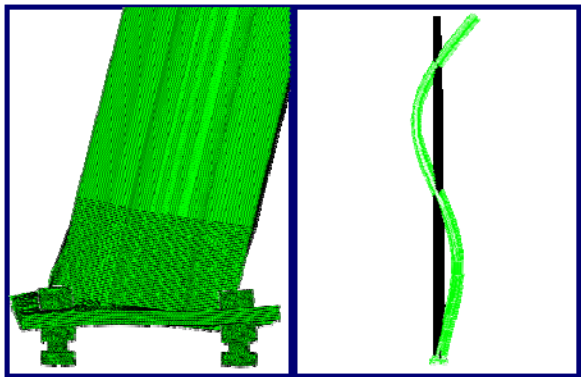

(c)

Figure B.23 Case 23 octagonal pole mode shape deformation
(a) Mode 1, f = 1.907 Hz; (b) Mode 2, f = 9.497 Hz; (c) Mode 3, f = 24.880 Hz.

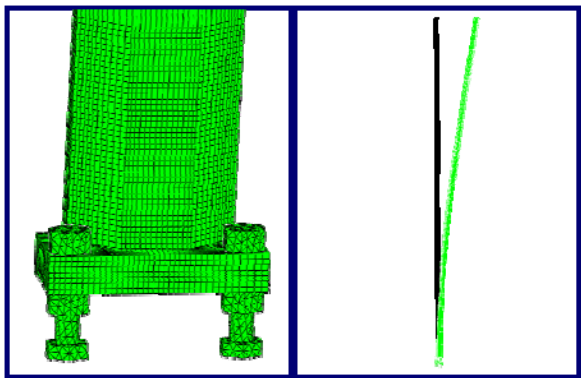

(a)

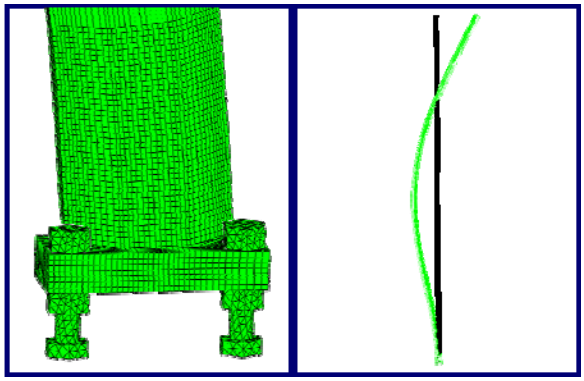

(b)

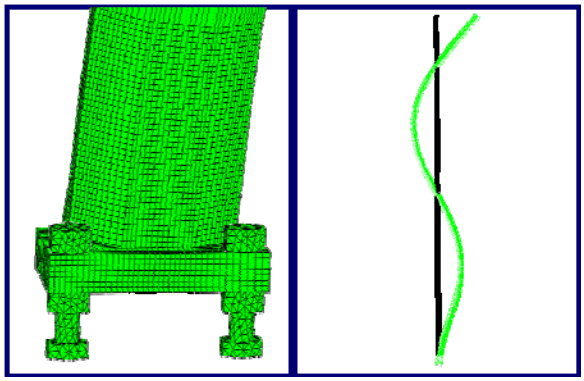

(c)

Figure B.24 Case 24 octagonal pole mode shape deformation
(a) Mode 1, f = 0.751 Hz; (b) Mode 2, f = 4.129 Hz; (c) Mode 3, f = 11.093 Hz.

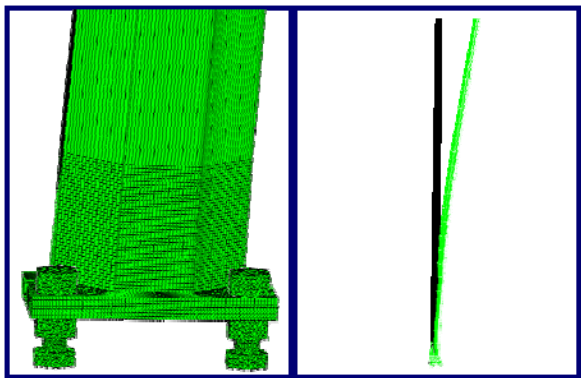

(a)

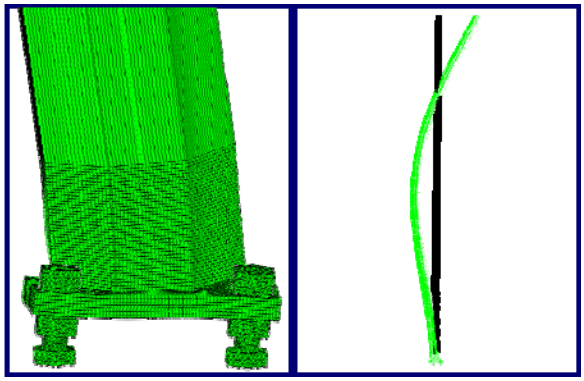

(b)

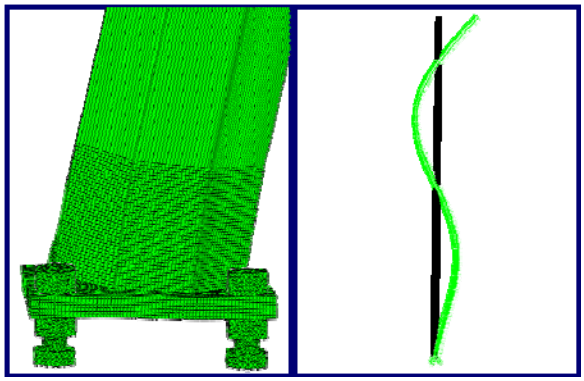

(c)

Figure B.25 Case 25 octagonal pole mode shape deformation
(a) Mode 1, f = 1.437 Hz; (b) Mode 2, f = 7.367 Hz; (c) Mode 3, f = 19.332 Hz.

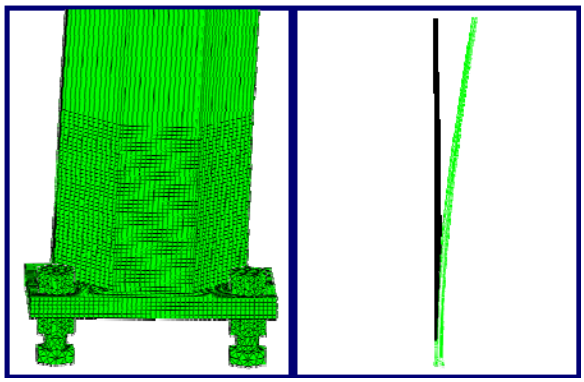

(a)

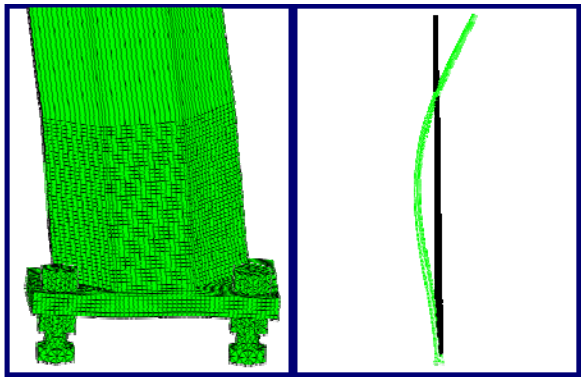

(b)

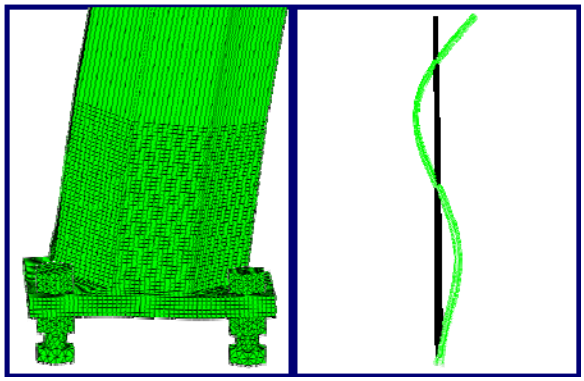

(c)

Figure B.26 Case 26 octagonal pole mode shape deformation
(a) Mode 1, f = 0.937 Hz; (b) Mode 2, f = 4.651 Hz; (c) Mode 3, f = 12.098 Hz.

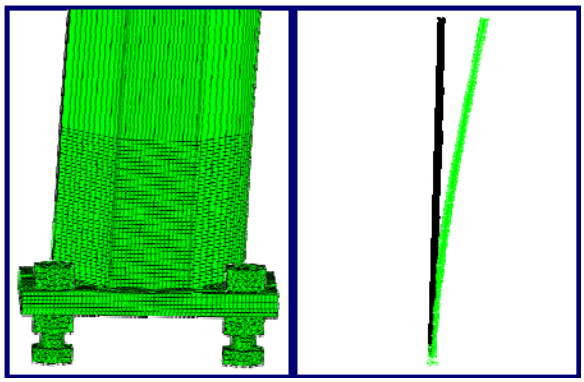

(a)

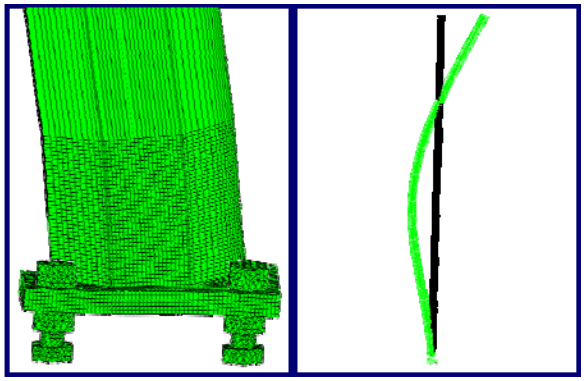

(b)

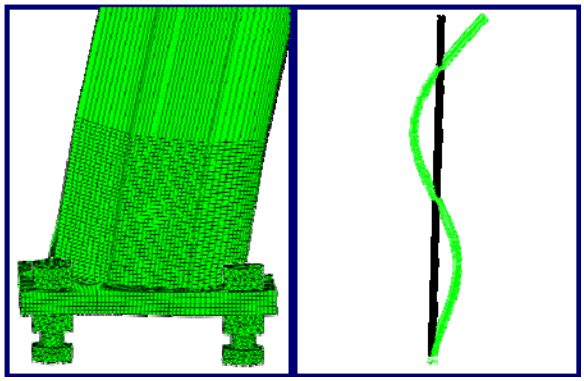

(c)

Figure B.27 Case 27 octagonal pole mode shape deformation
(a) Mode 1, f = 1.100 Hz; (b) Mode 2, f = 5.854 Hz; (c) Mode 3, f = 15.577 Hz.

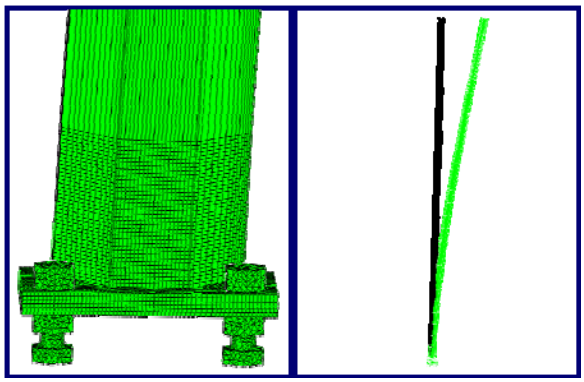

(a)

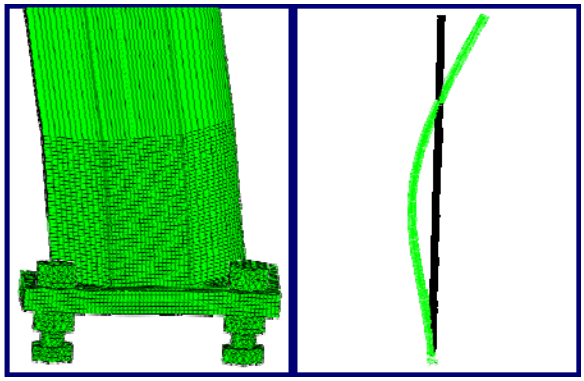

(b)

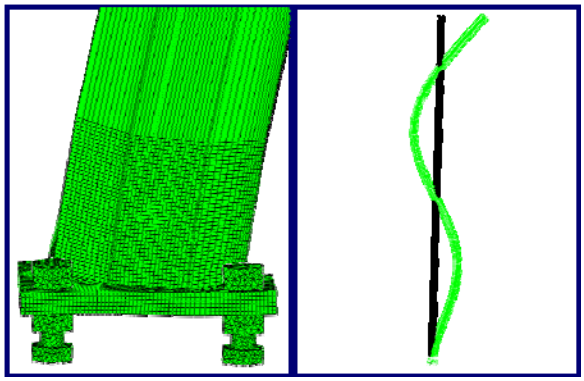

(c)

Figure B.28 Case 28 octagonal pole mode shape deformation
(a) Mode 1, f = 1.381 Hz; (b) Mode 2, f = 7.033 Hz; (c) Mode 3, f = 18.466 Hz.

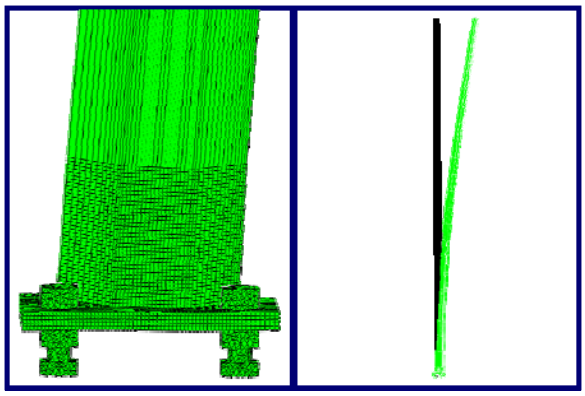

(a)

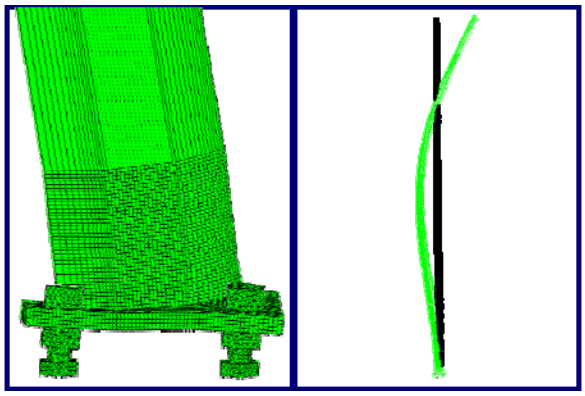

(b)

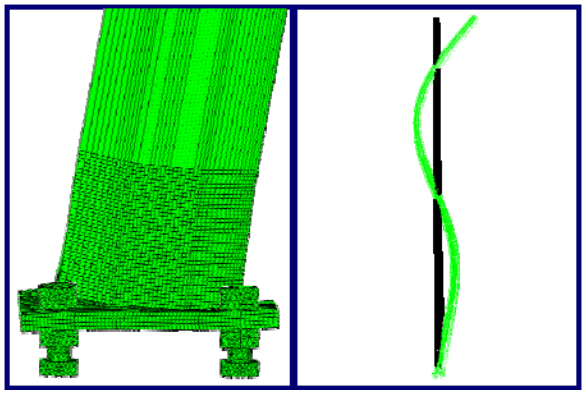

(c)

Figure B.29 Case 29 octagonal pole mode shape deformation
(a) Mode 1, f = 1.188 Hz; (b) Mode 2, f = 5.959 Hz; (c) Mode 3, f = 15.662 Hz.

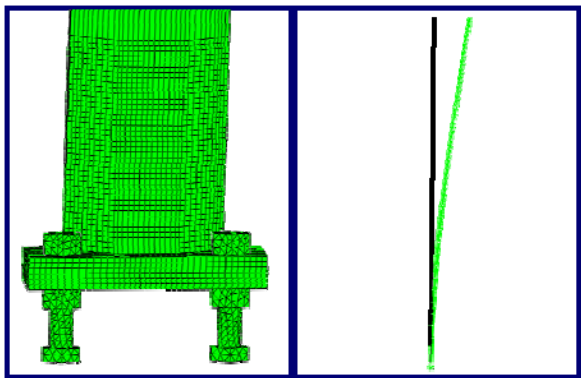

(a)

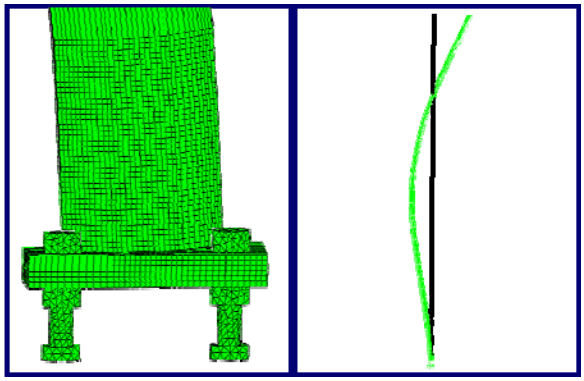

(b)

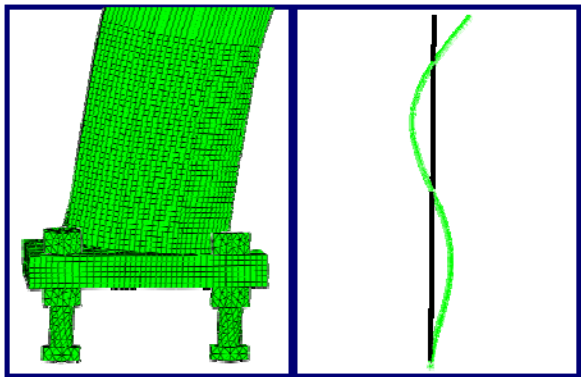

(c)

Figure B.30 Case 30 octagonal pole mode shape deformation
(a) Mode 1, f = 0.582 Hz; (b) Mode 2, f = 2.994 Hz; (c) Mode 3, f = 7.886 Hz.

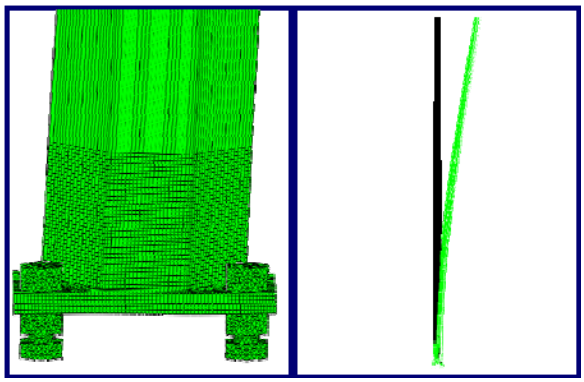

(a)

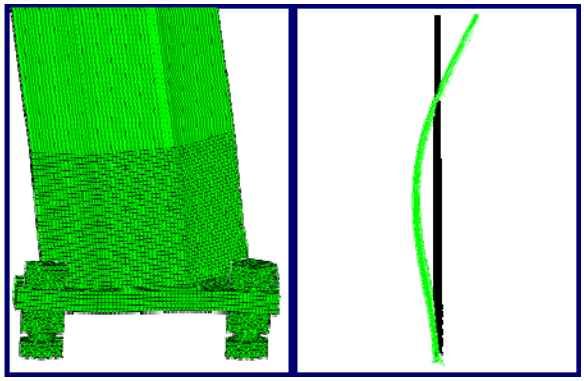

(b)

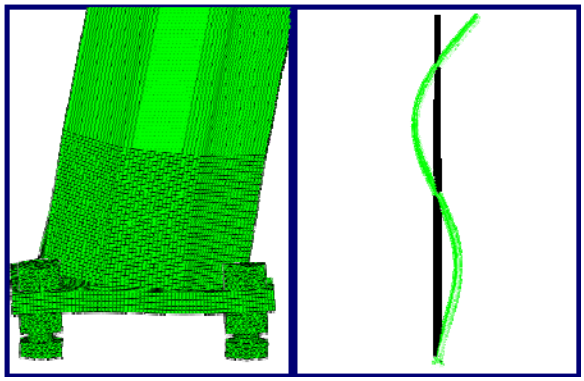

(c)

Figure B.31 Case 31 octagonal pole mode shape deformation
(a) Mode 1, f = 1.073 Hz; (b) Mode 2, f = 5.381 Hz; (c) Mode 3, f = 14.085 Hz.

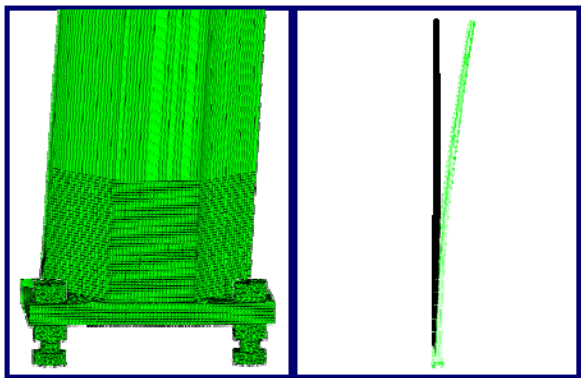

(a)

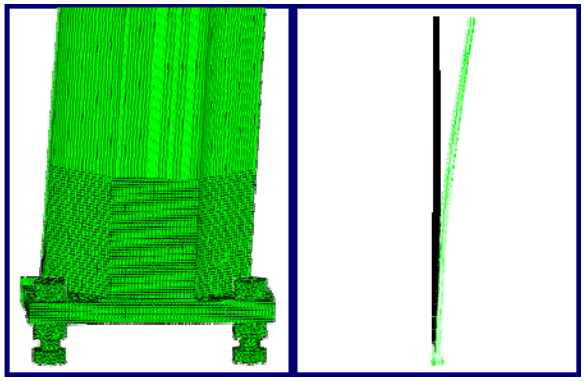

(b)

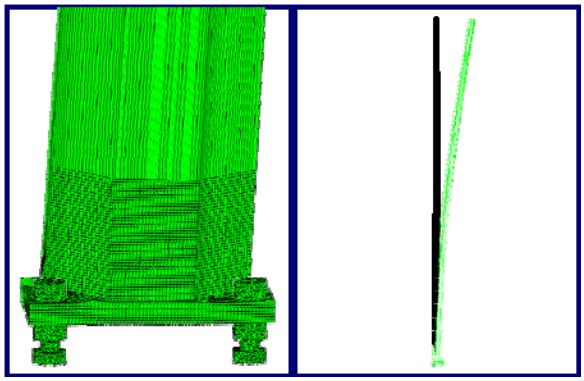

(c)

Figure B.32 Case 32 octagonal pole mode shape deformation
(a) Mode 1, f = 1.249 Hz; (b) Mode 2, f = 5.957 Hz; (c) Mode 3, f = 15.352 Hz.

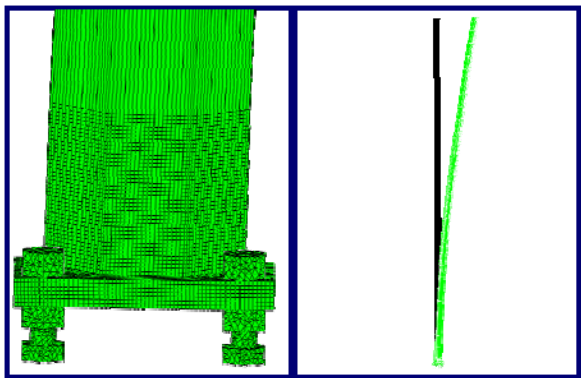

(a)

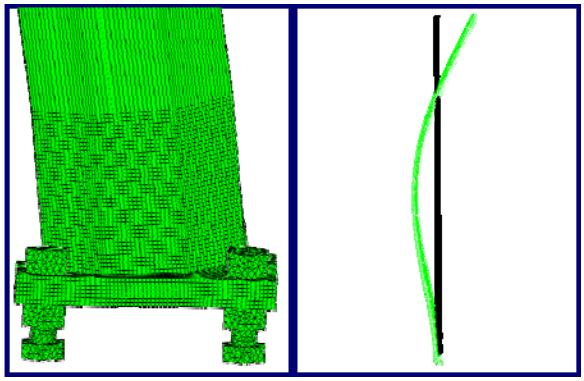

(b)

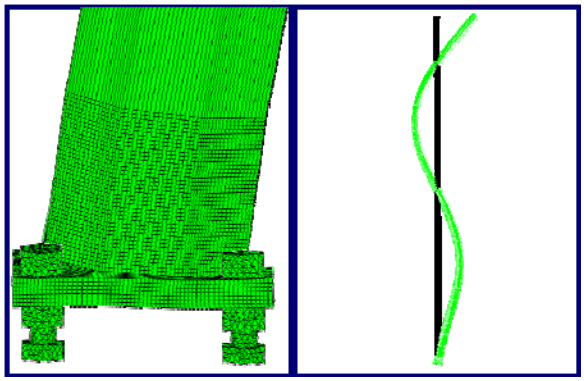

(c)

Figure B.33 Case 33 octagonal pole mode shape deformation
(a) Mode 1, f = 0.911 Hz; (b) Mode 2, f = 4.856 Hz; (c) Mode 3, f = 12.934 Hz.

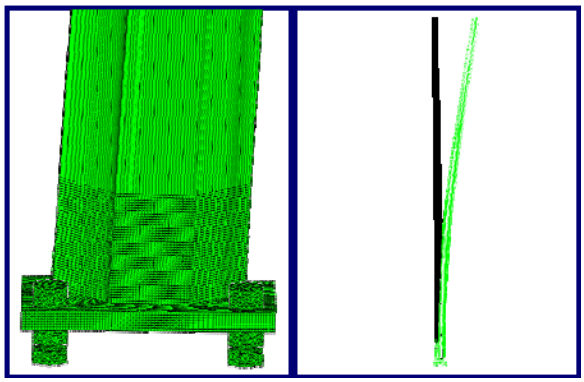

(a)

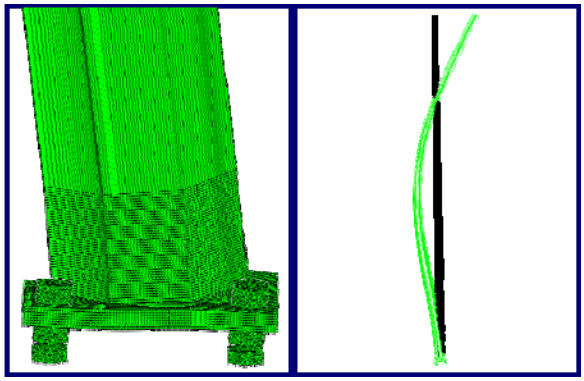

(b)

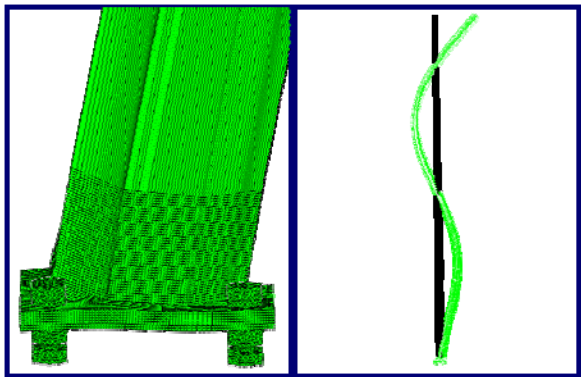

(c)

Figure B.34 Case 34 octagonal pole mode shape deformation
(a) Mode 1, f = 1.249 Hz; (b) Mode 2, f = 5.949 Hz; (c) Mode 3, f = 15.323 Hz.

APPENDIX C

NATURAL FREQUENCY SENSITIVITY STUDIES OF CIRCULAR AND OCTAGONAL POLES

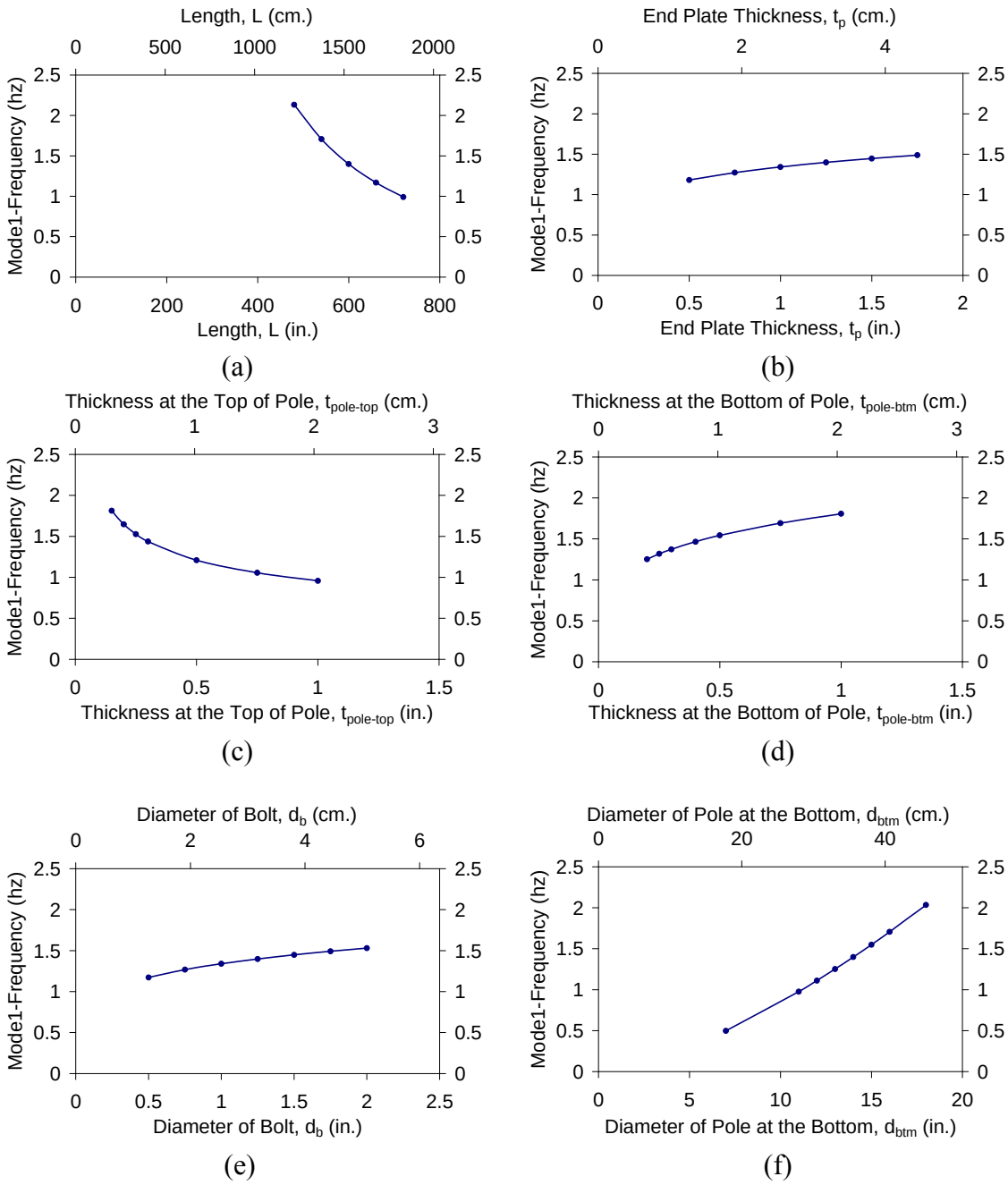

Figure C.1 Sensitivity plots of the first mode of the circular poles with the changing in: (a) Length, (b) End plate thickness, (c) Thickness at the top of pole, (d) Thickness at bottom of pole, (e) Diameter of bolt, (f) Diameter of pole at bottom.

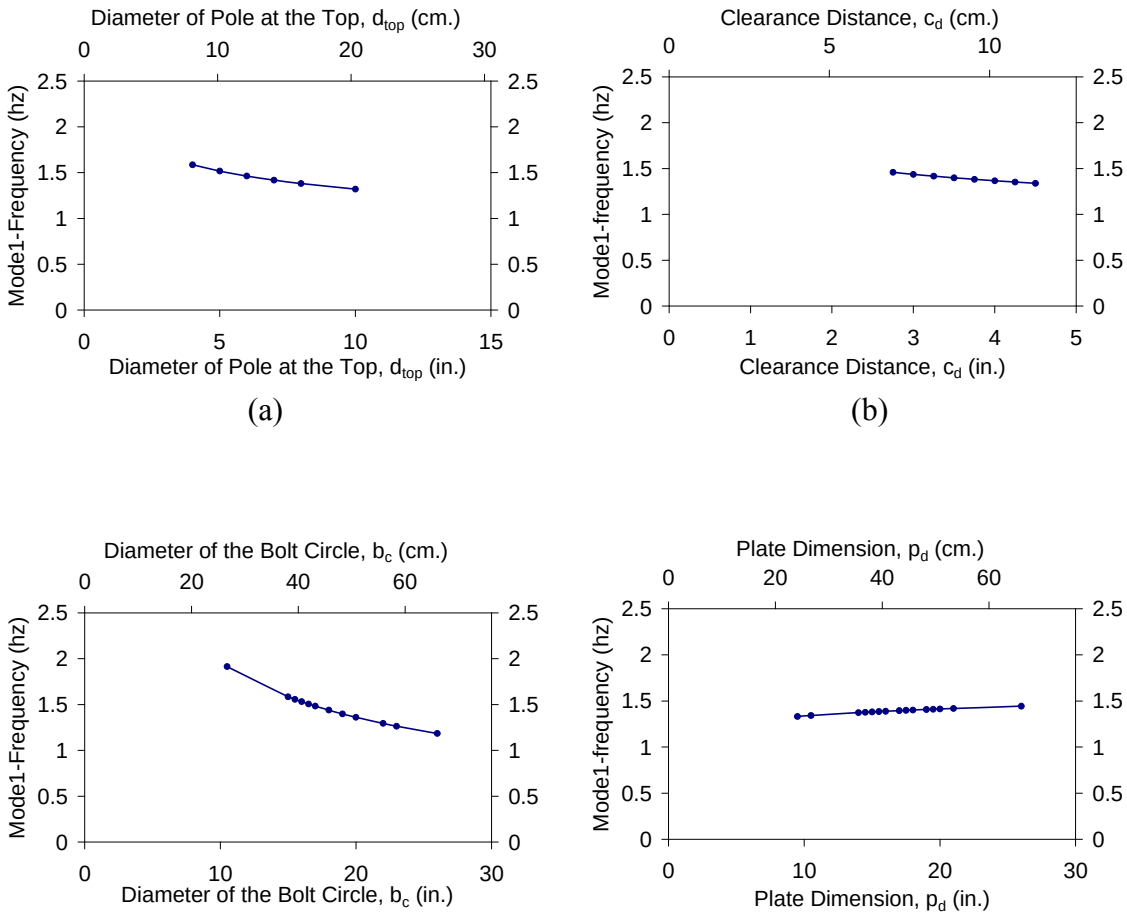

Figure C.2 Sensitivity plots of the first mode of the circular poles with the changing in: (a) Diameter of pole at top, (b) Clearance distance, (c) Diameter of bolt circle, (d) Plate dimension.

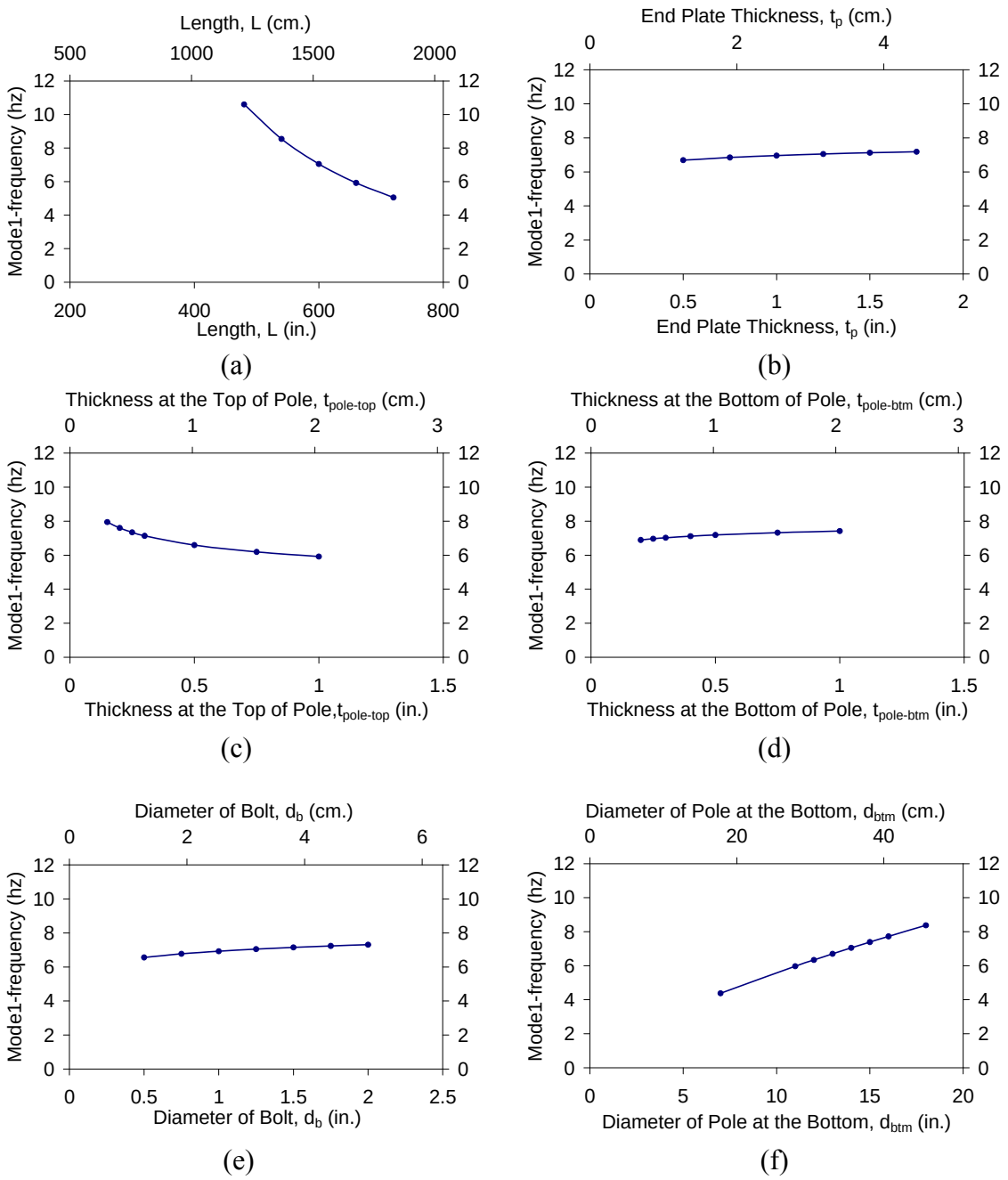

Figure C.3 Sensitivity plots of the second mode of the circular poles with the changing in: (a) Length, (b) End plate thickness, (c) Thickness at the top of pole, (d) Thickness at bottom of pole, (e) Diameter of bolt, (f) Diameter of pole at bottom.

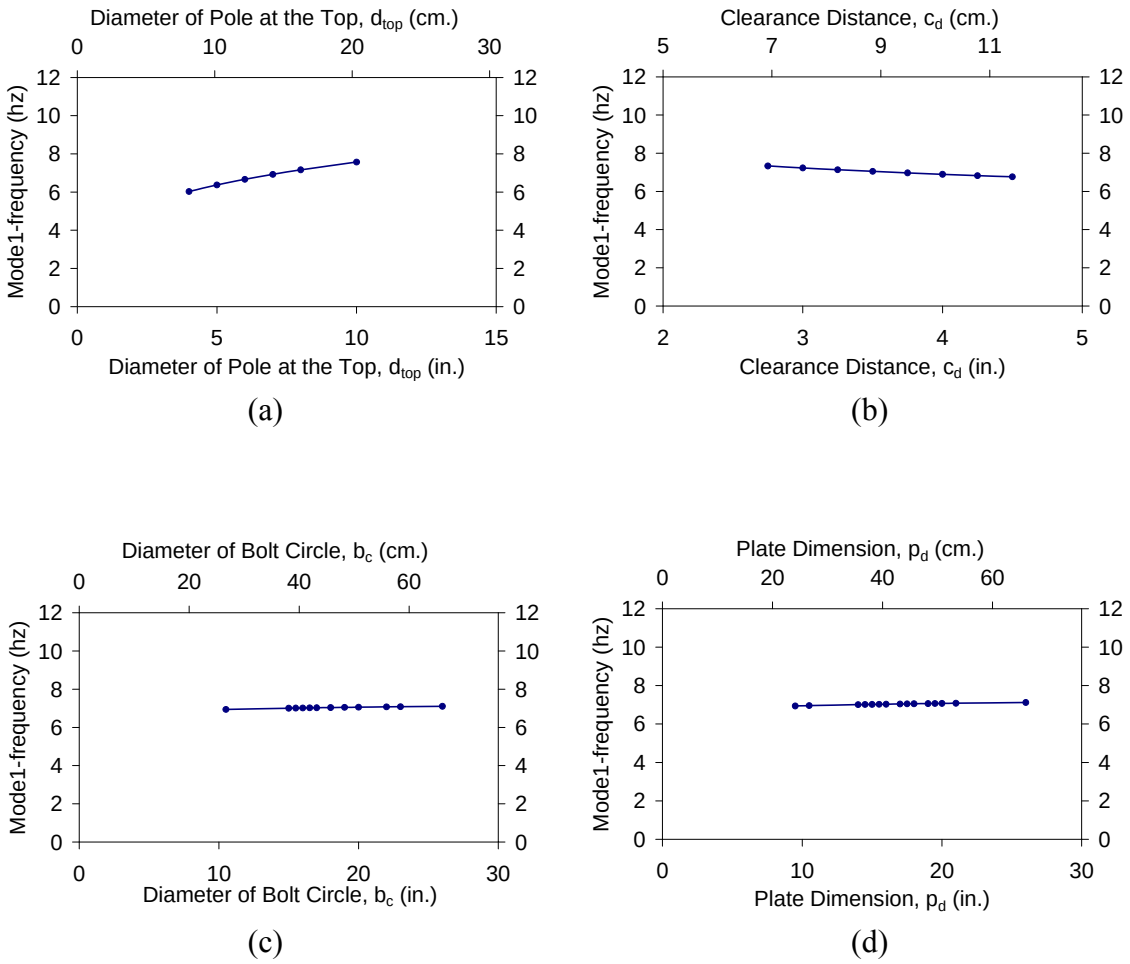

Figure C.4 Sensitivity plots of the second mode of the circular poles with the changing in: (a) Diameter of pole at top, (b) Clearance distance, (c) Diameter of bolt circle, (d) Plate dimension.

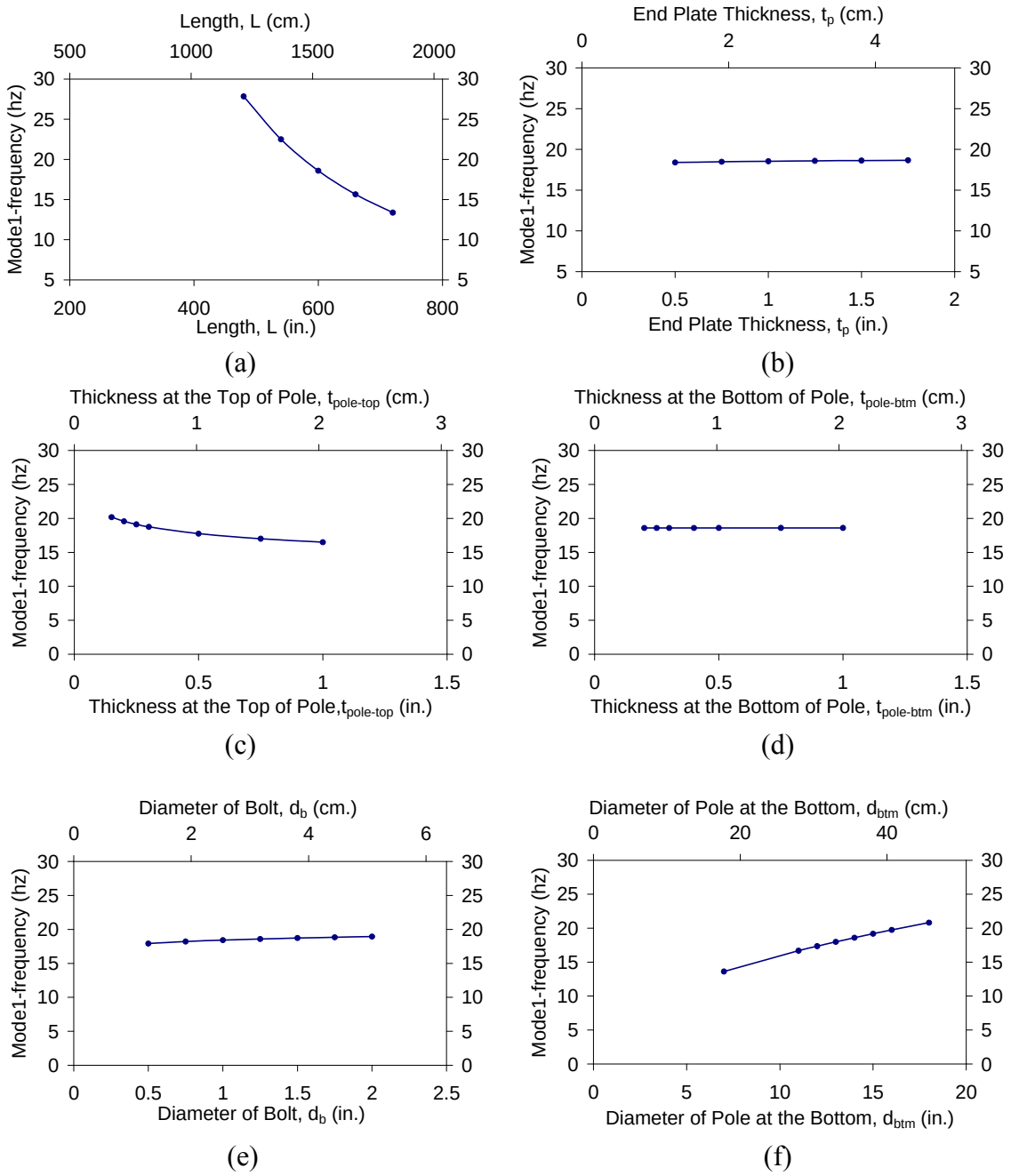

Figure C.5 Sensitivity plots of the third mode of the circular poles with the changing in: (a) Length, (b) End plate thickness, (c) Thickness at the top of pole, (d) Thickness at bottom of pole, (e) Diameter of bolt, (f) Diameter of pole at bottom.

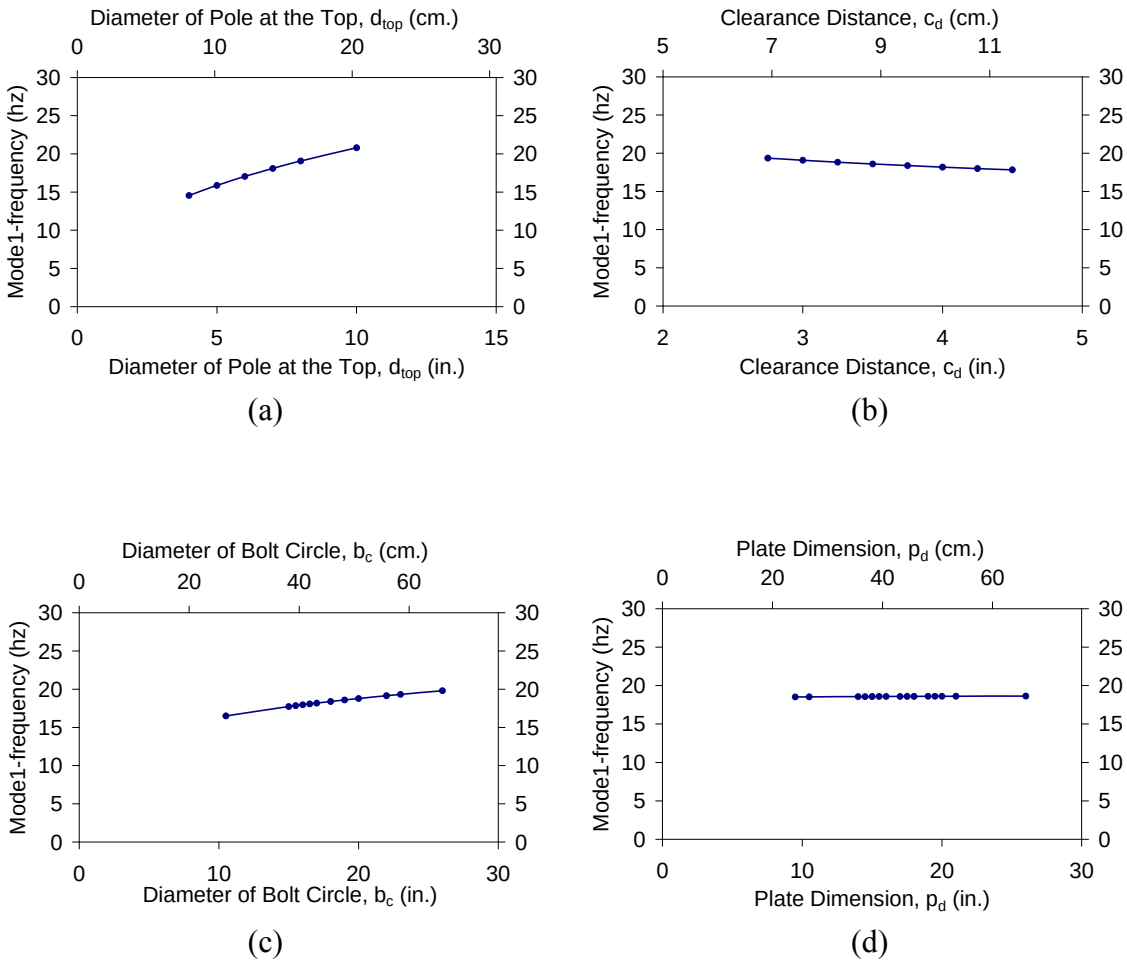

Figure C.6 Sensitivity plots of the third mode of the circular poles with the changing in: (a) Diameter of pole at top, (b) Clearance distance, (c) Diameter of bolt circle, (d) Plate dimension.

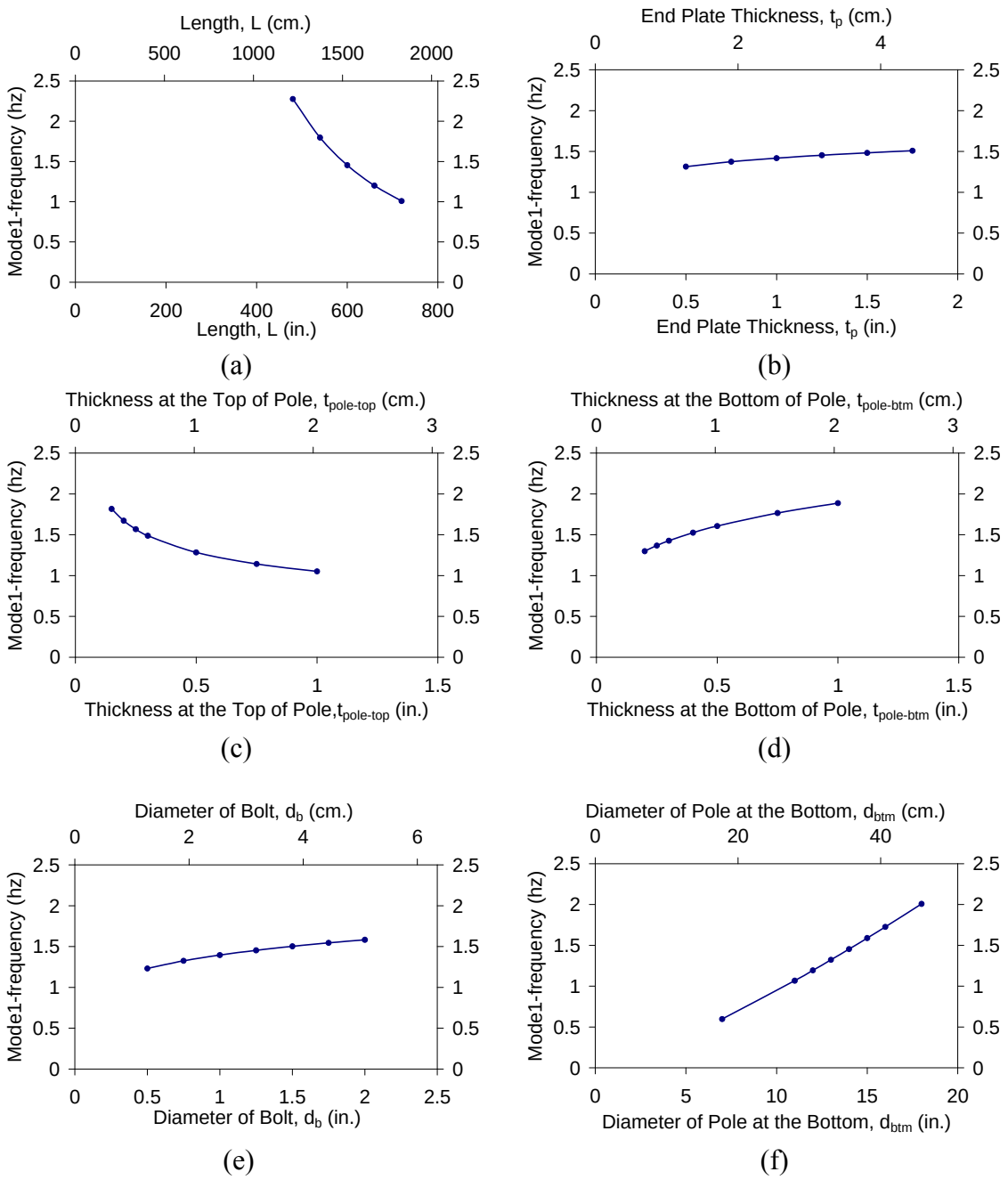

Figure C.7 Sensitivity plots of the first mode of the octagonal poles with the changing in: (a) Length, (b) End plate thickness, (c) Thickness at the top of pole, (d) Thickness at bottom of pole, (e) Diameter of bolt, (f) Diameter of pole at bottom.

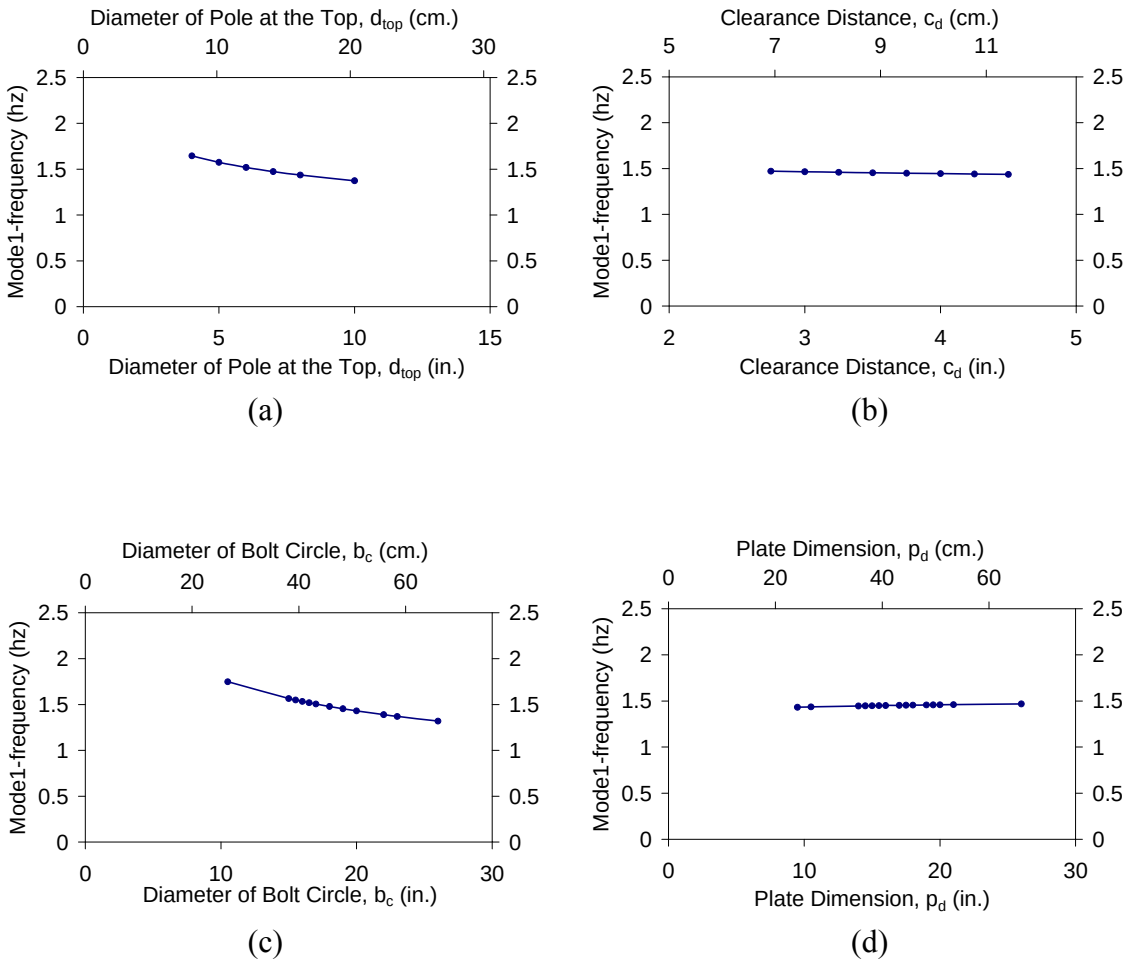

Figure C.8 Sensitivity plots of the first mode of the octagonal poles with the changing in: (a) Diameter of pole at top, (b) Clearance distance, (c) Diameter of bolt circle, (d) Plate dimension.

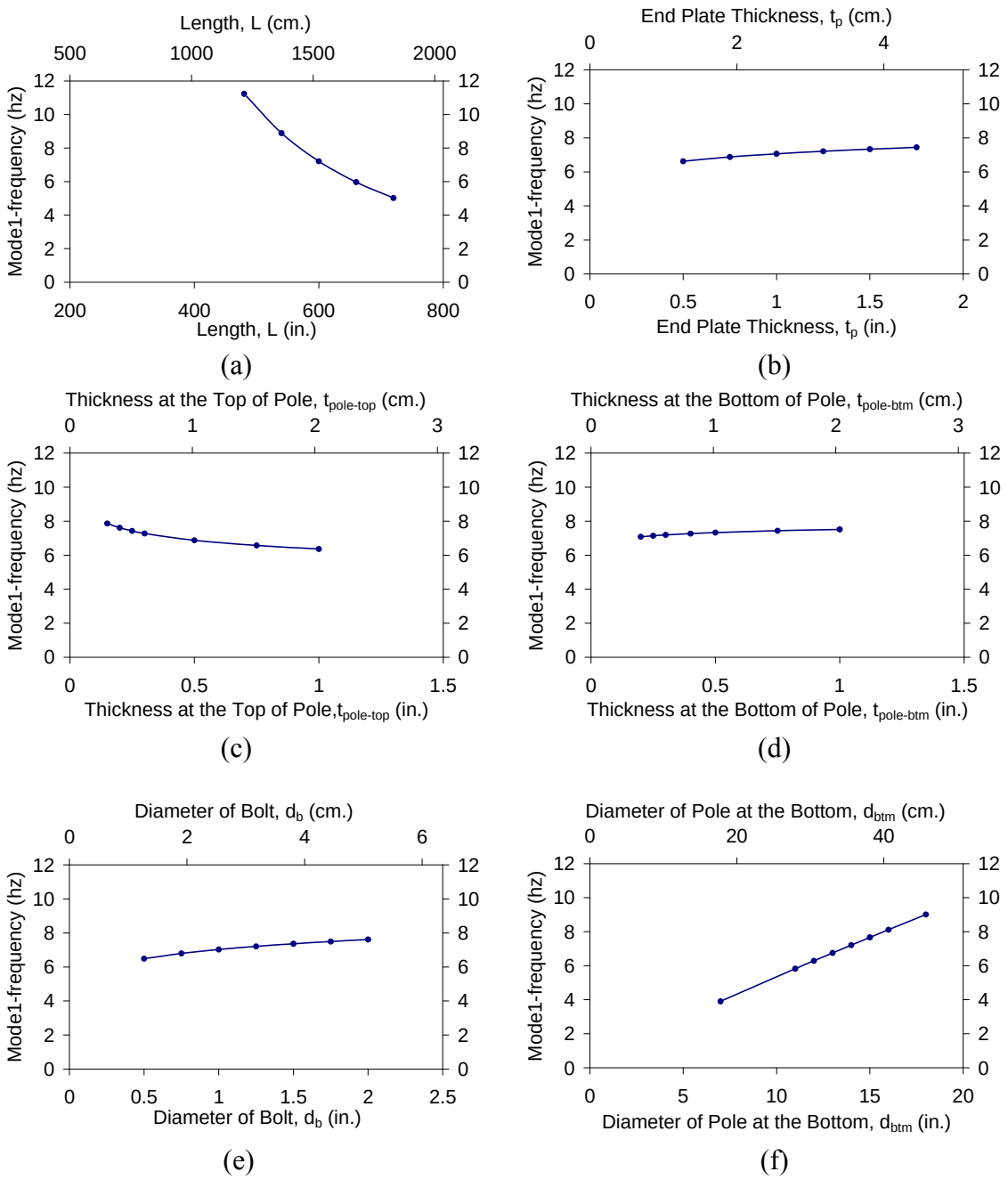

Figure C.9 Sensitivity plots of the second mode of the octagonal poles with the changing in: (a) Length, (b) End plate thickness, (c) Thickness at the top of pole, (d) Thickness at bottom of pole, (e) Diameter of bolt, (f) Diameter of pole at bottom.

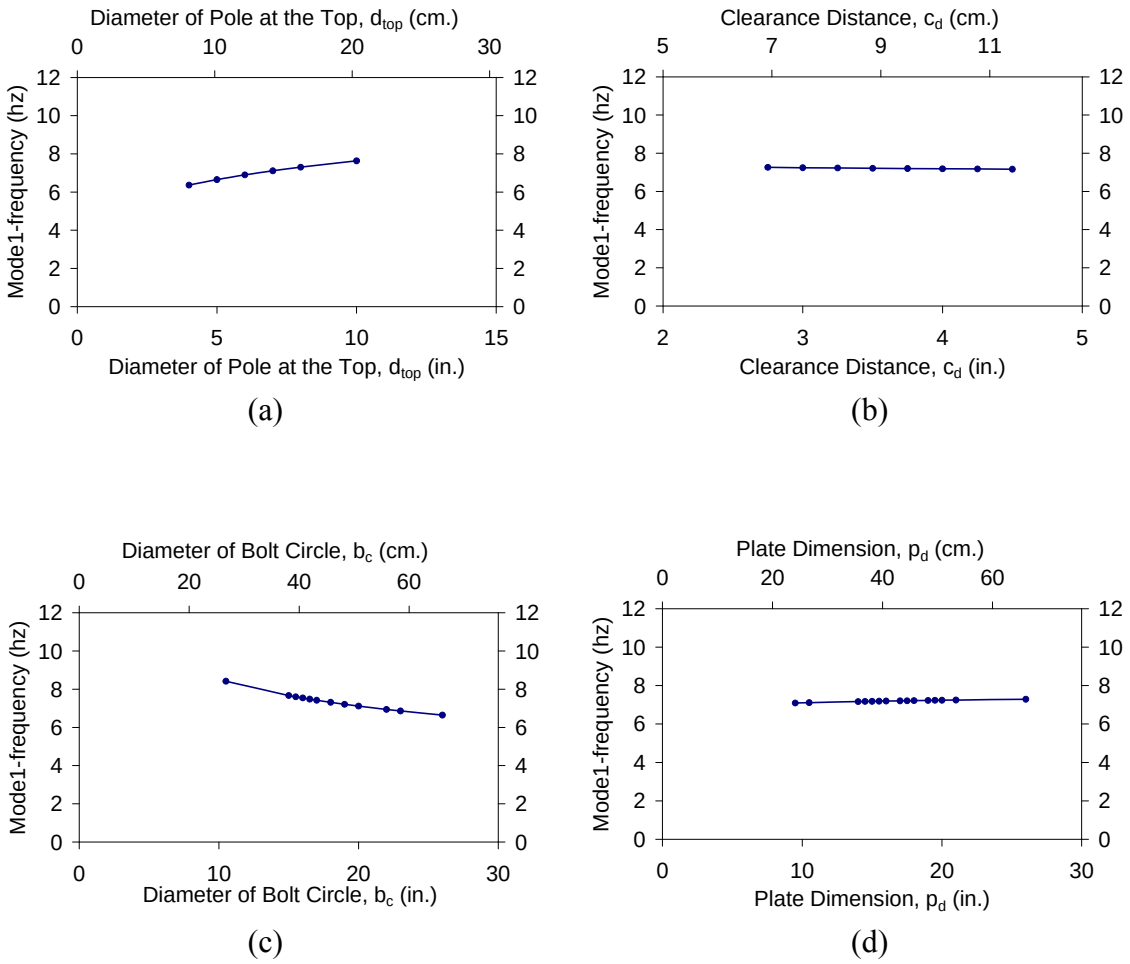

Figure C.10 Sensitivity plots of the second mode of the octagonal poles with the changing in: (a) Diameter of pole at top, (b) Clearance distance, (c) Diameter of bolt circle, (d) Plate dimension.

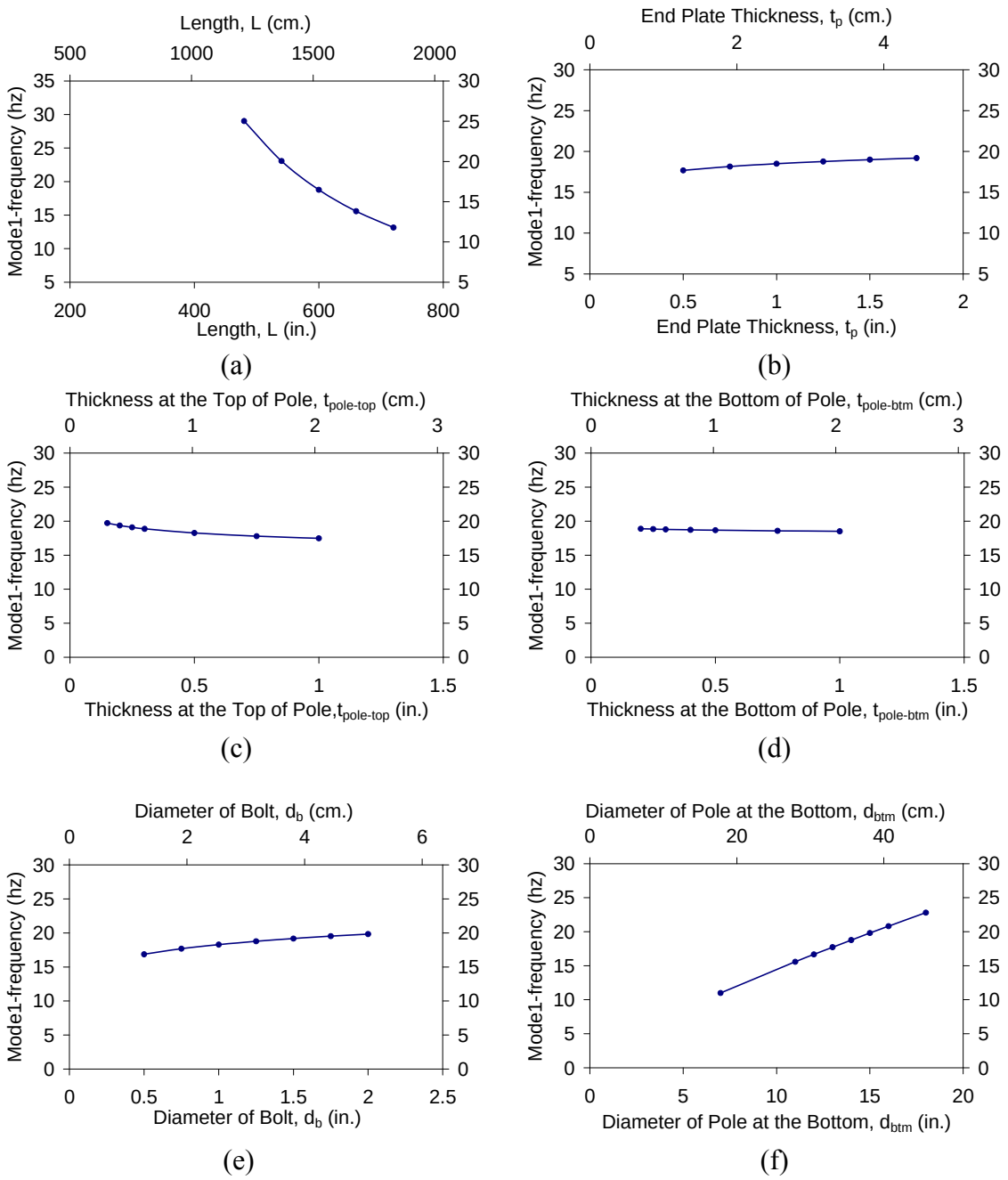

Figure C.11 Sensitivity plots of the third mode of the octagonal poles with the changing in: (a) Length, (b) End plate thickness, (c) Thickness at the top of pole, (d) Thickness at bottom of pole, (e) Diameter of bolt, (f) Diameter of pole at bottom.

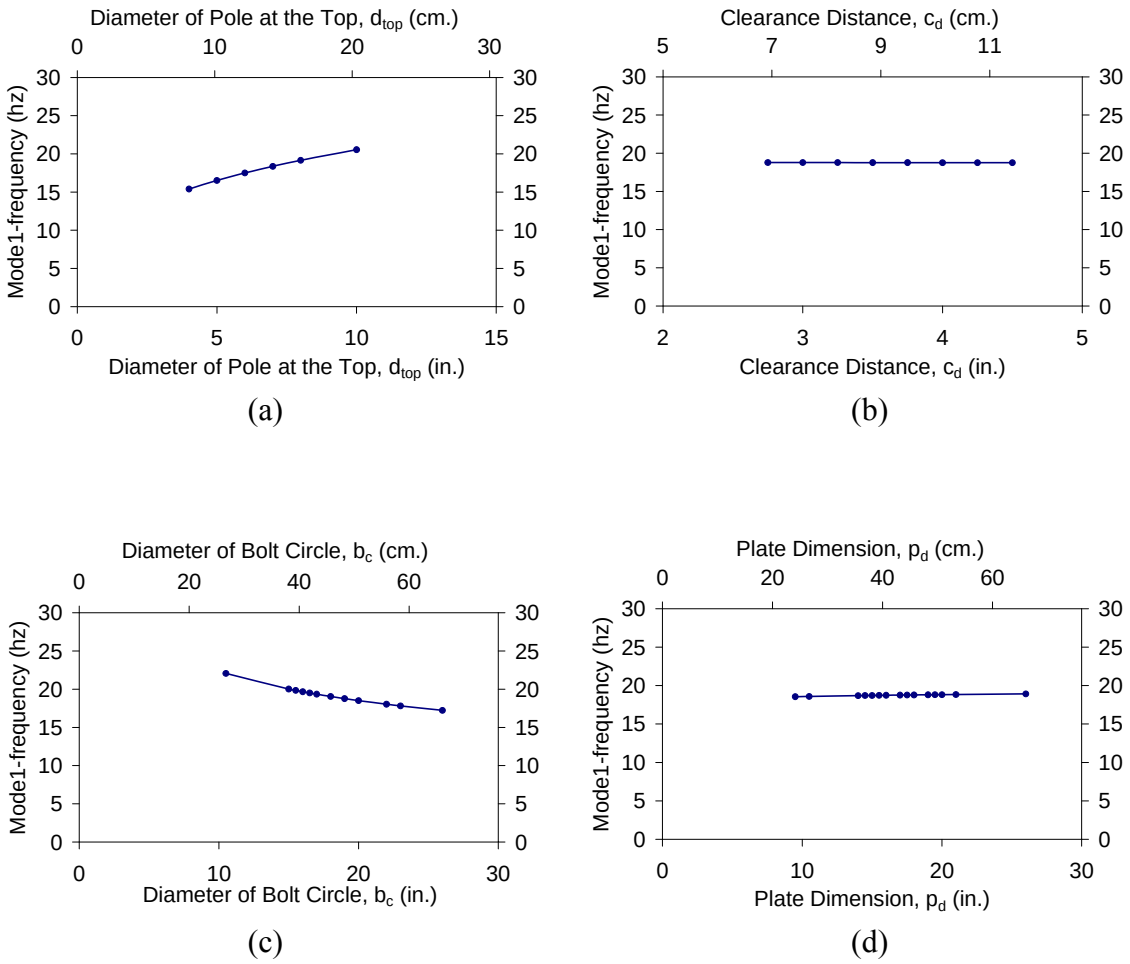

Figure C.12 Sensitivity plots of the third mode of the octagonal poles with the changing in: (a) Diameter of pole at top, (b) Clearance distance, (c) Diameter of bolt circle, (d) Plate dimension.

APPENDIX D

HYSTERESIS PLOT

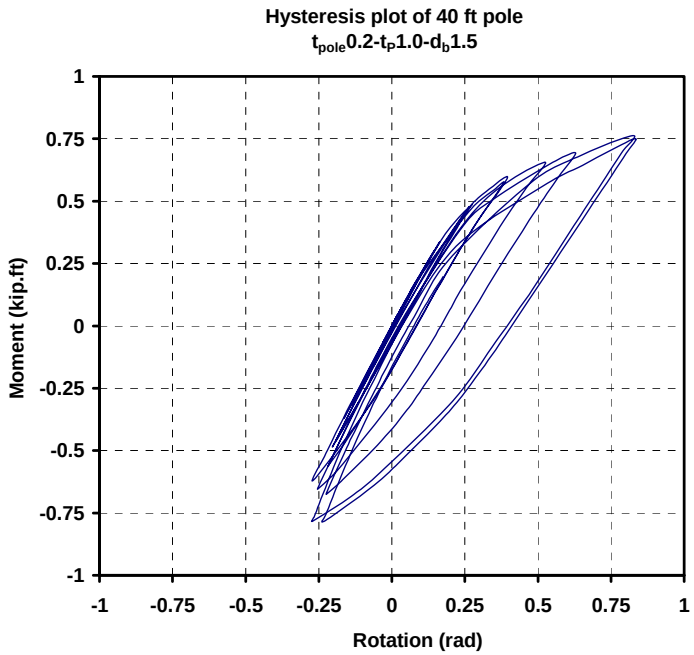

Figure D.1 Hysteresis plot of case 01

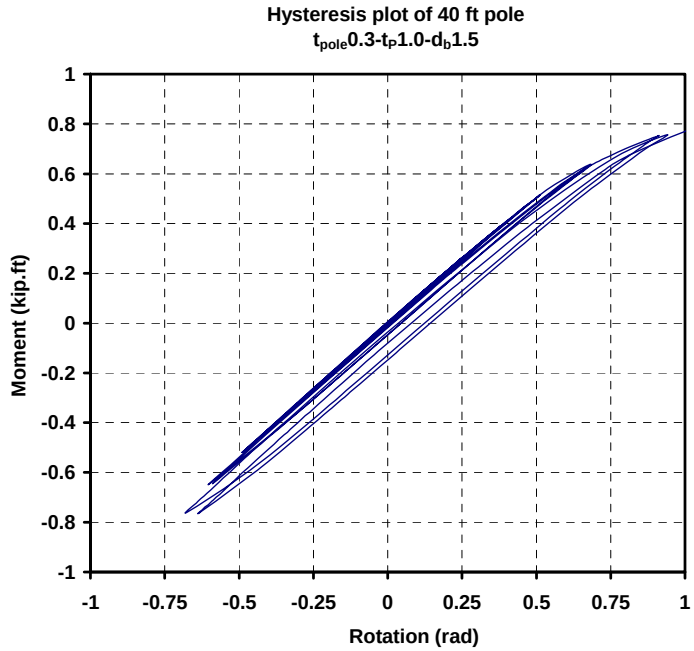

Figure D.2 Hysteresis plot of case 02

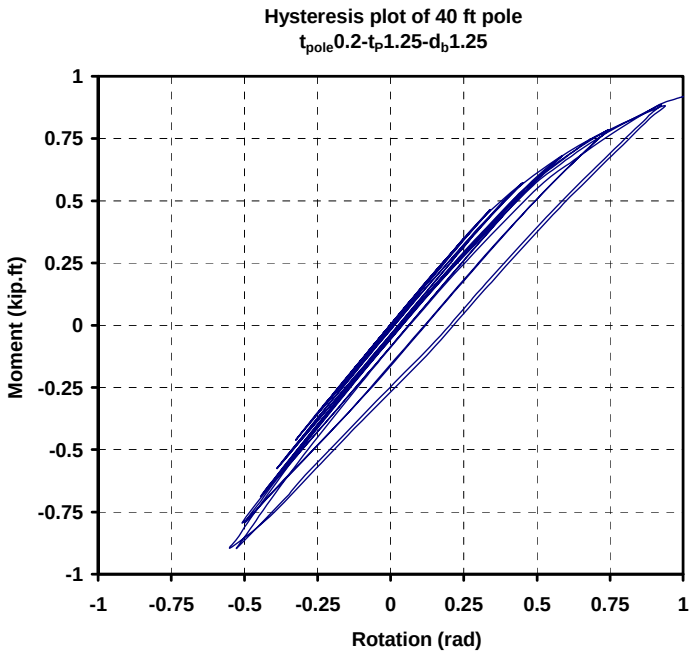

Figure D.3 Hysteresis plot of case 03

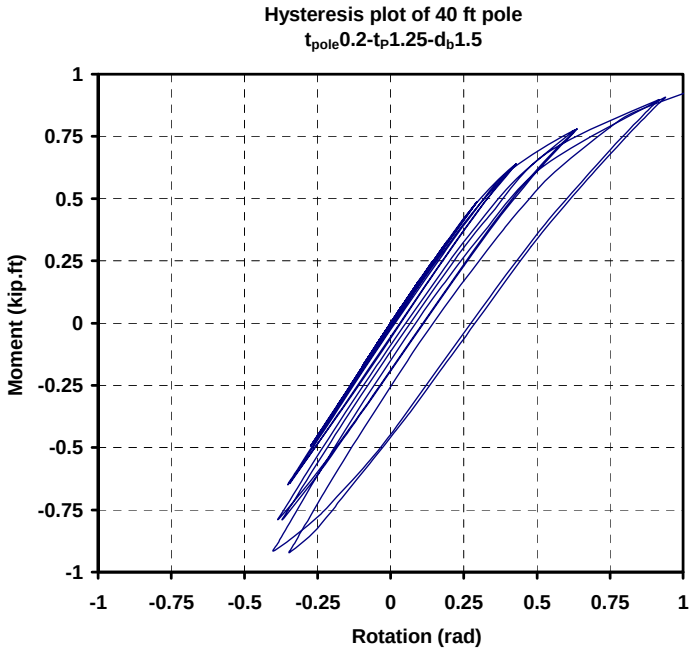

Figure D.4 Hysteresis plot of case 04

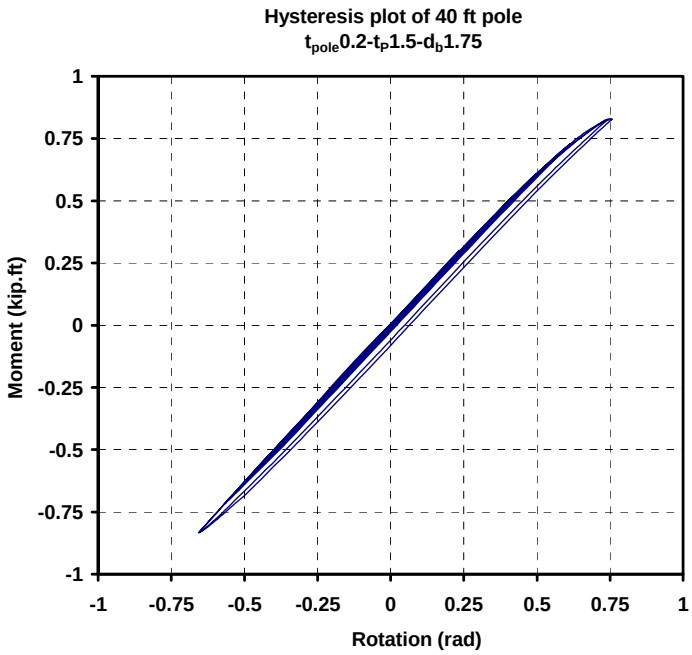

Figure D.5 Hysteresis plot of case 05

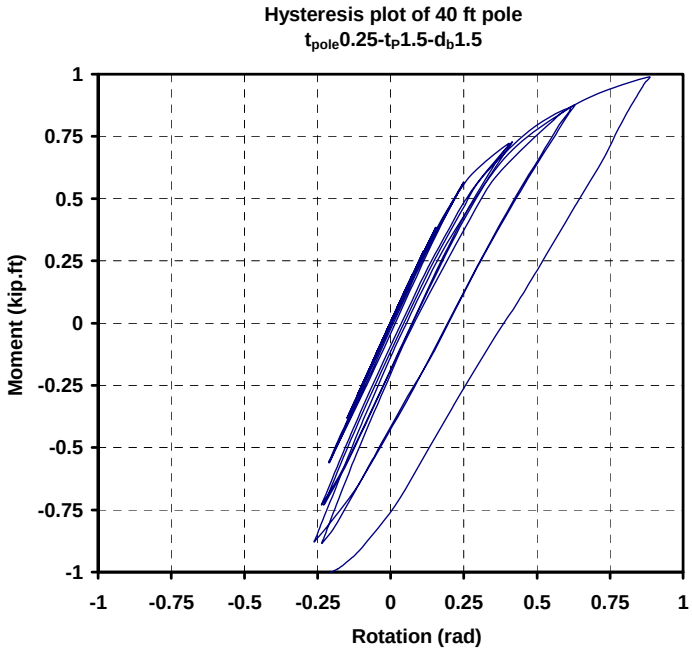

Figure D.6 Hysteresis plot of case 06

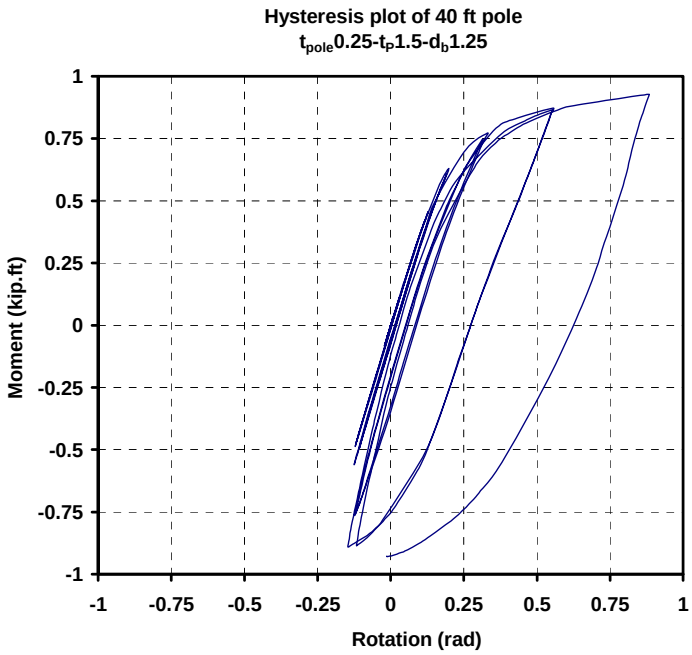

Figure D.7 Hysteresis plot of case 07

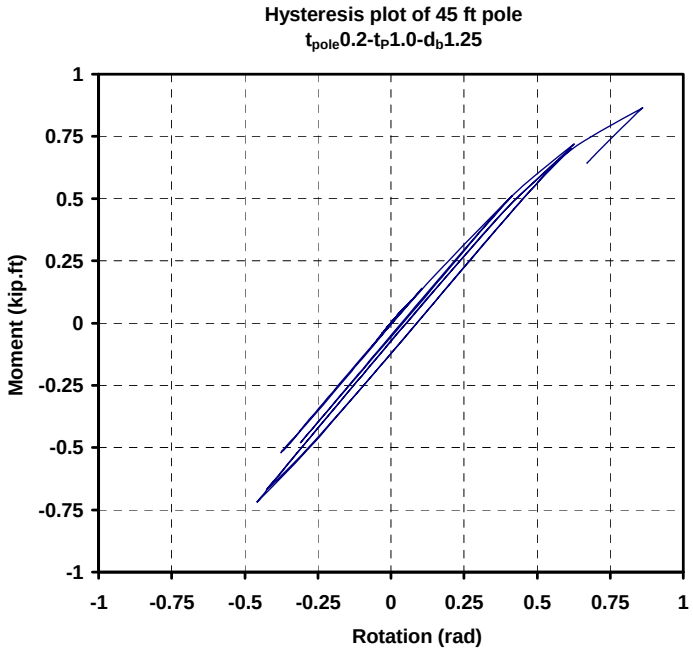

Figure D.8 Hysteresis plot of case 08

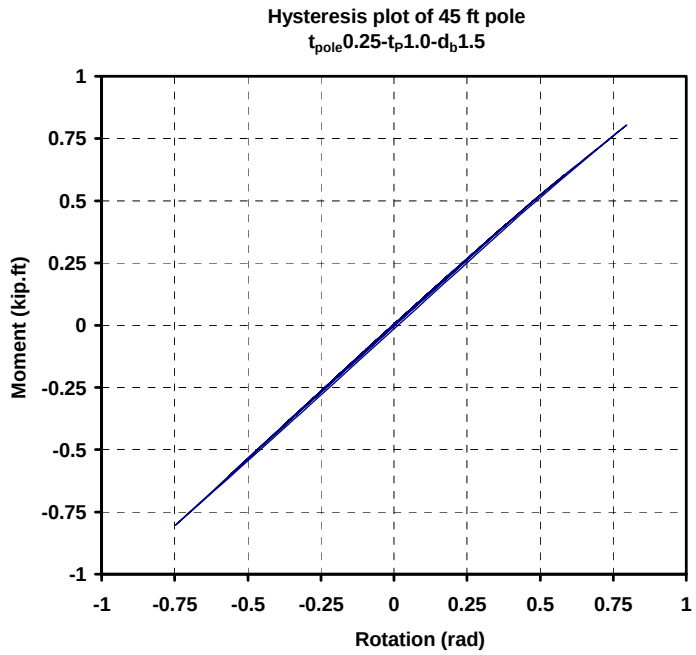

Figure D.9 Hysteresis plot of case 09

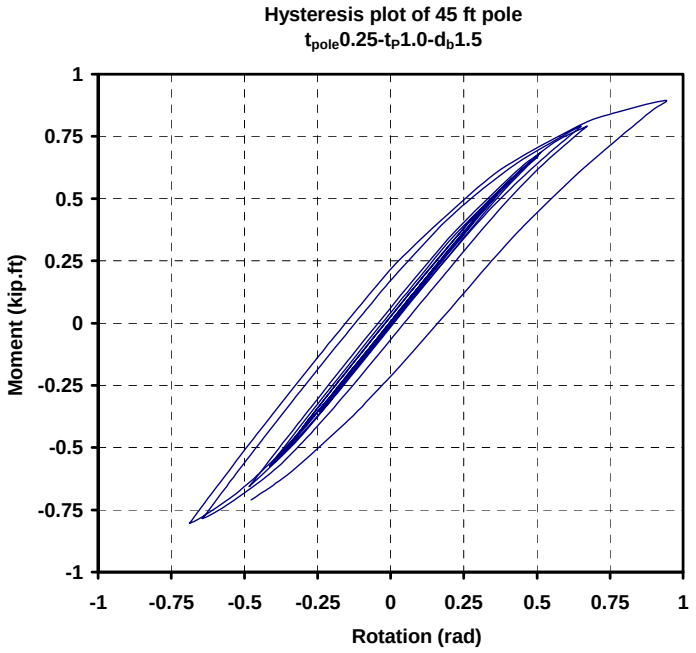

Figure D.10 Hysteresis plot of case 10

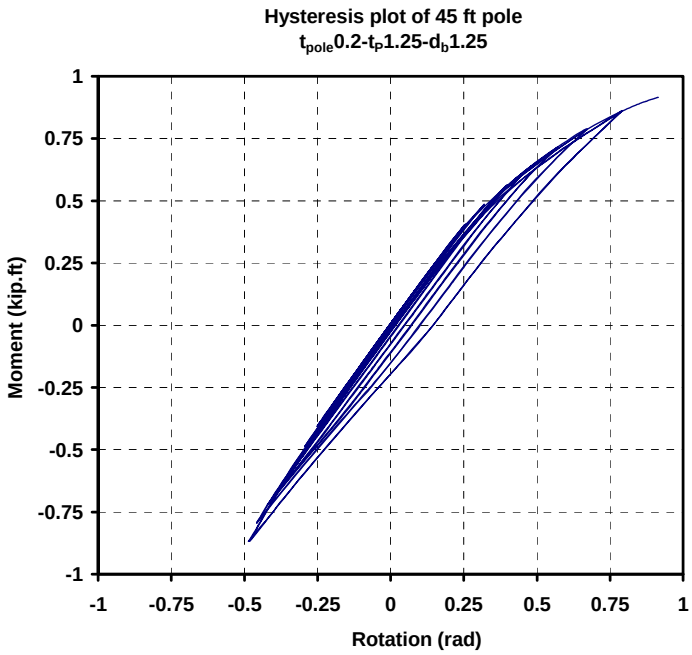

Figure D.11 Hysteresis plot of case 11

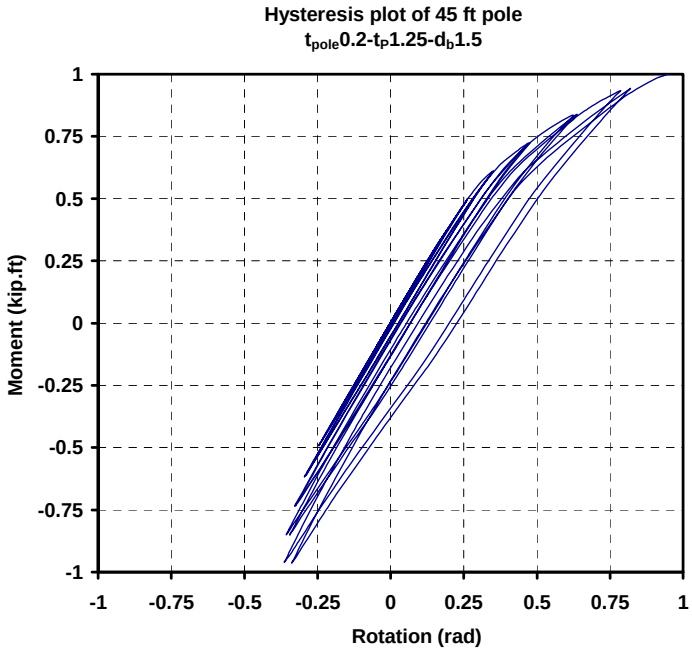

Figure D.12 Hysteresis plot of case 12

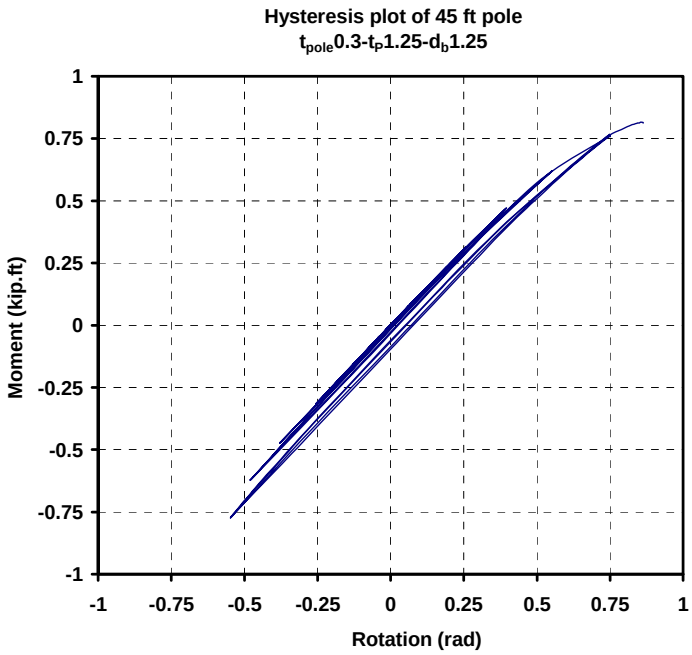

Figure D.13 Hysteresis plot of case 13

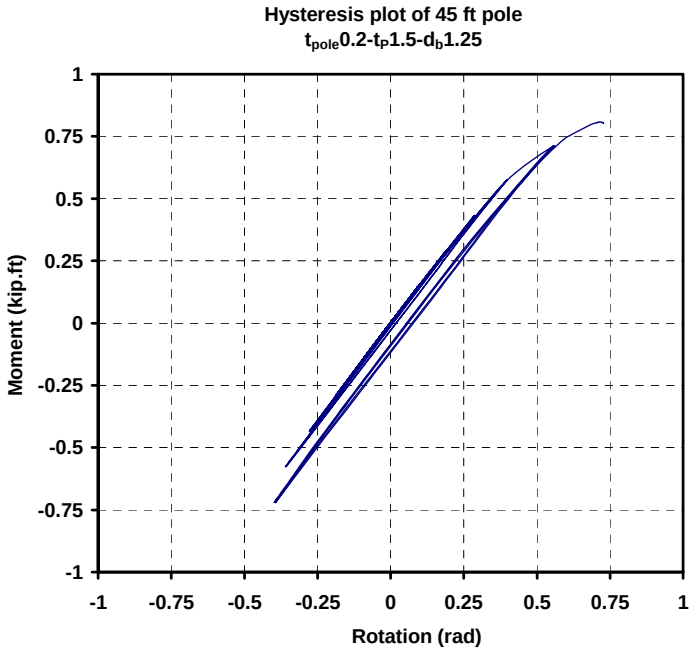

Figure D.14 Hysteresis plot of case 14

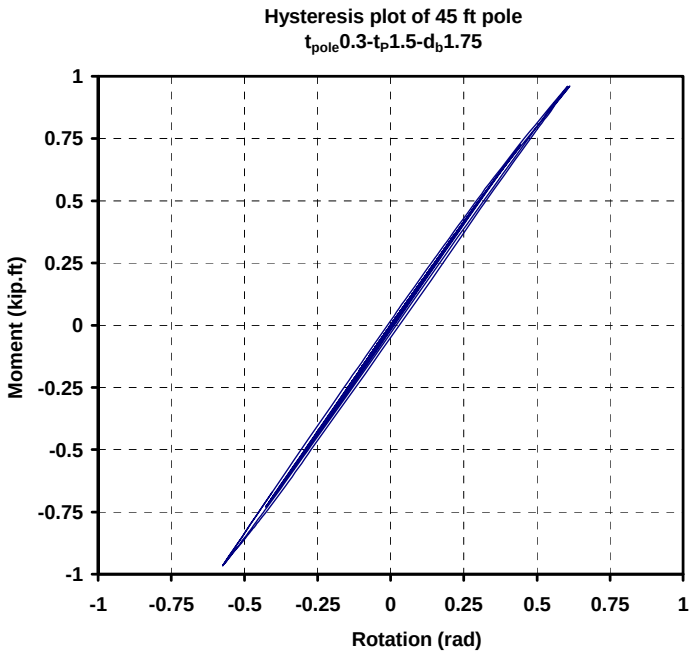

Figure D.15 Hysteresis plot of case 15

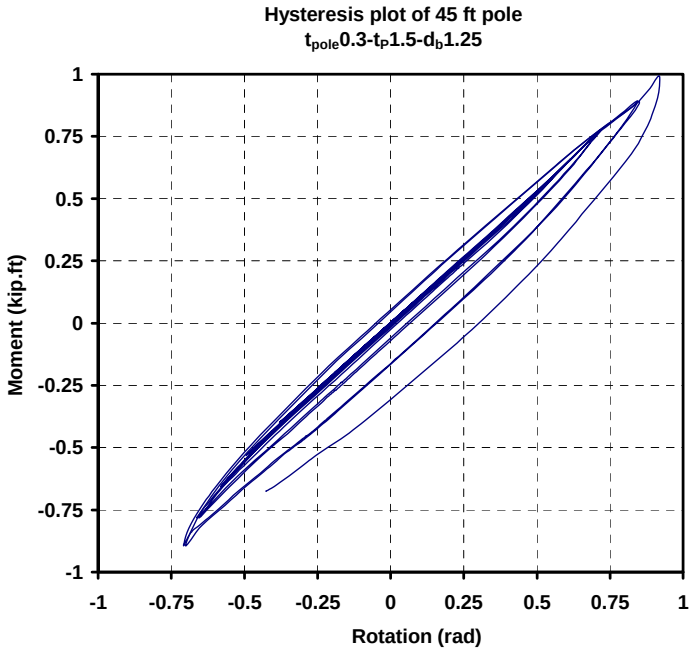

Figure D.16 Hysteresis plot of case 16

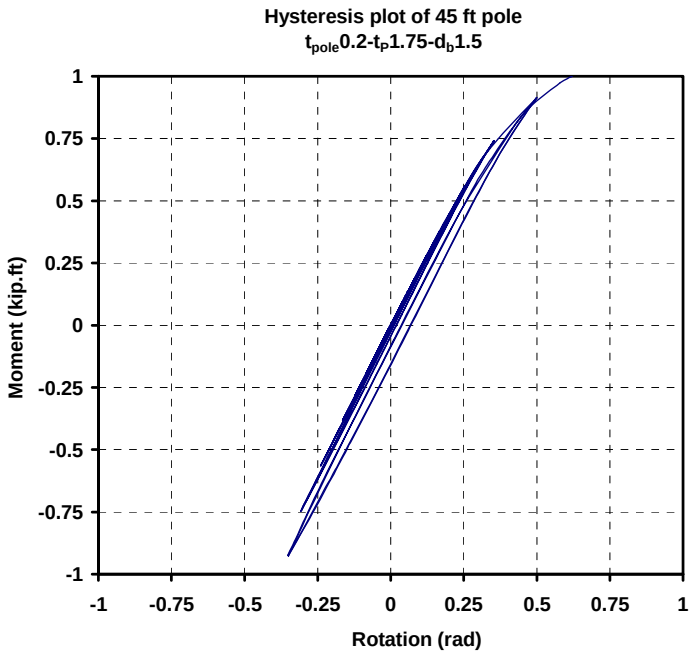

Figure D.17 Hysteresis plot of case 17

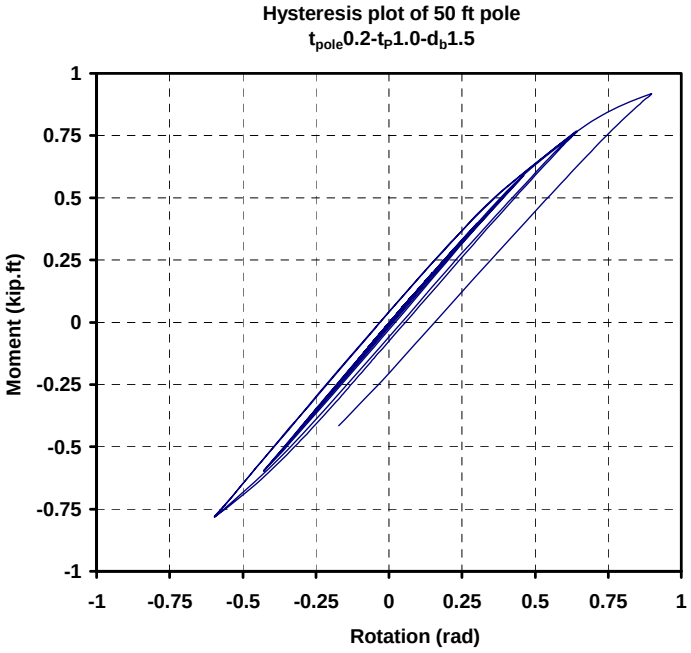

Figure D.18 Hysteresis plot of case 18

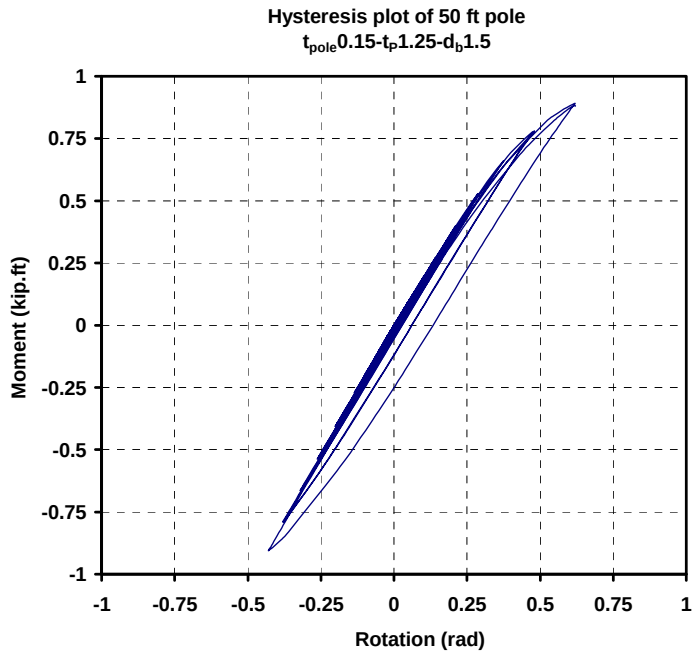

Figure D.19 Hysteresis plot of case 19

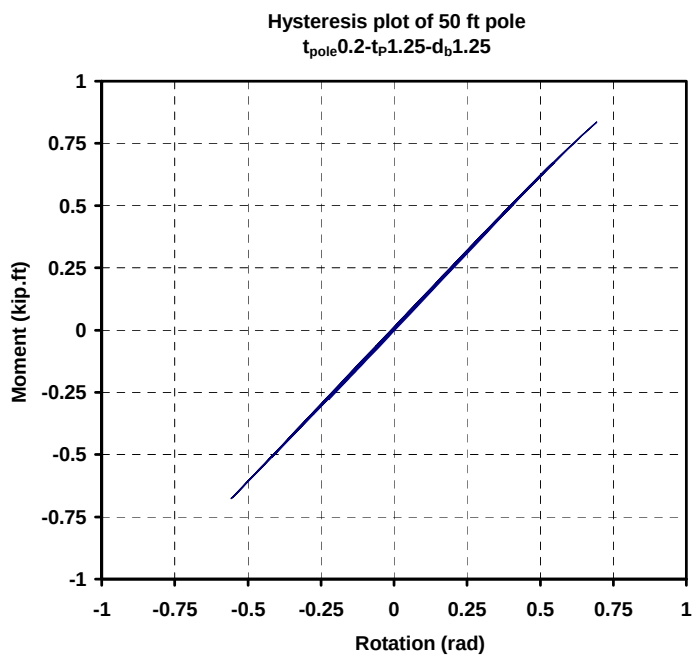

Figure D.20 Hysteresis plot of case 20

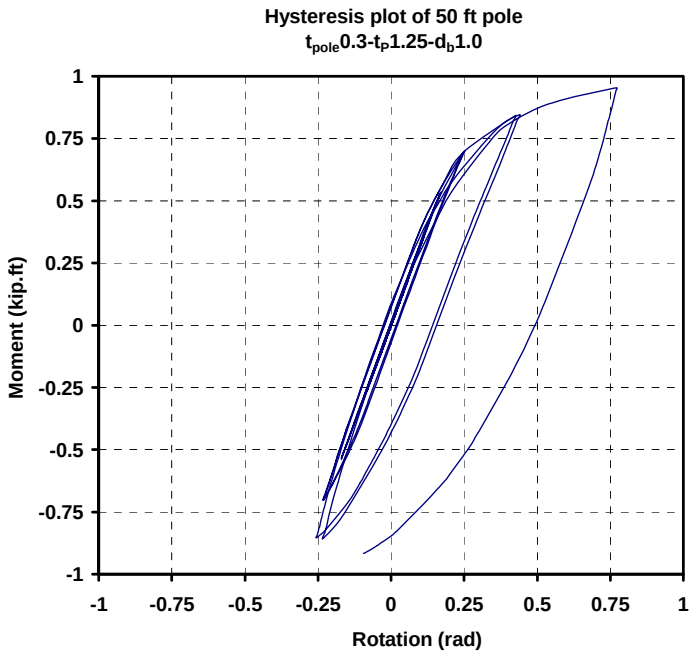

Figure D.21 Hysteresis plot of case 21

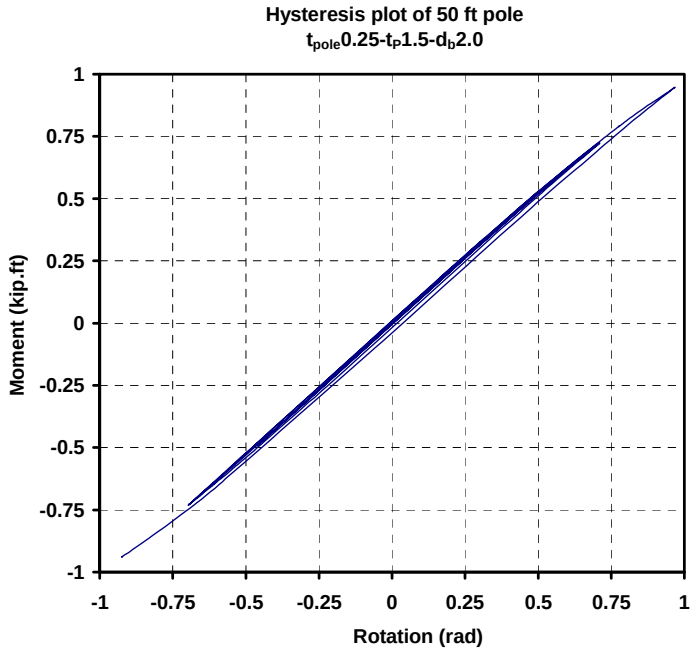

Figure D.22 Hysteresis plot of case 22

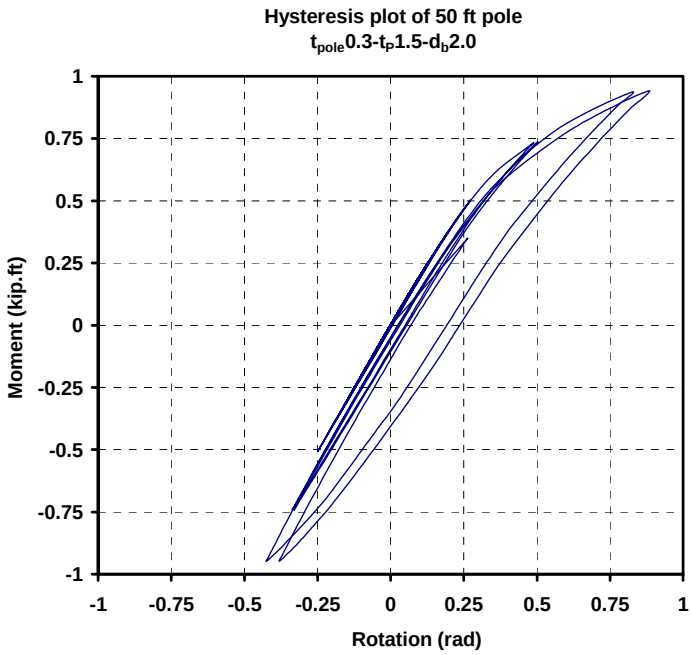

Figure D.23 Hysteresis plot of case 23

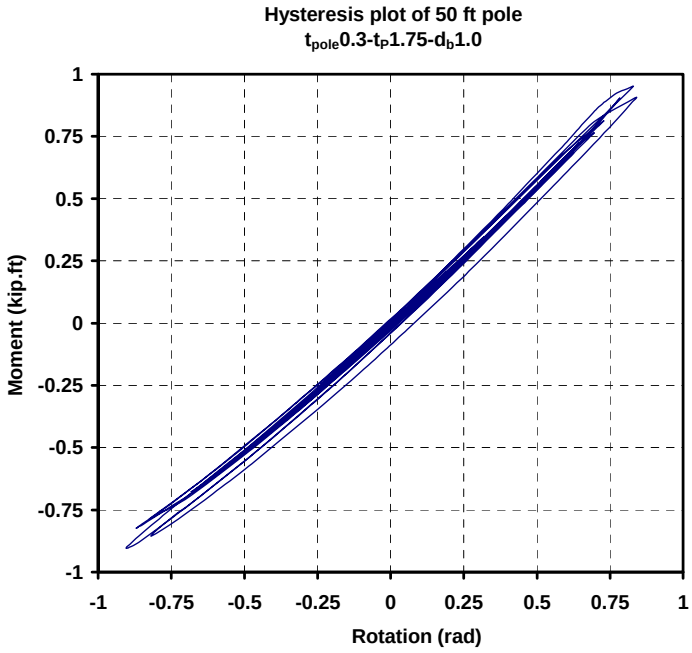

Figure D.24 Hysteresis plot of case 24

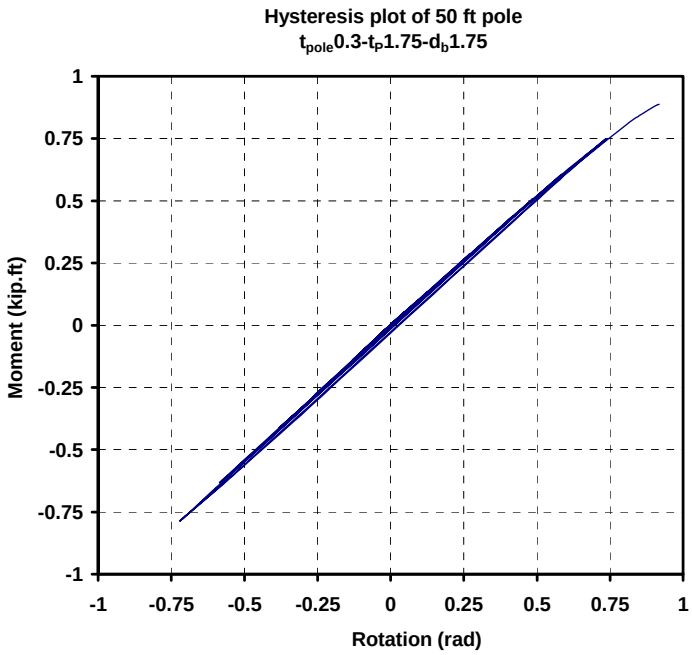

Figure D.25 Hysteresis plot of case 25

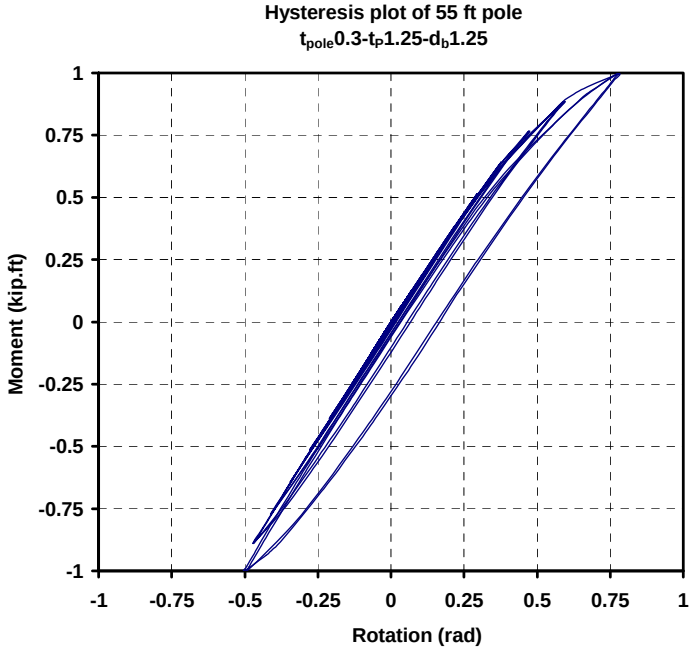

Figure D.26 Hysteresis plot of case 26

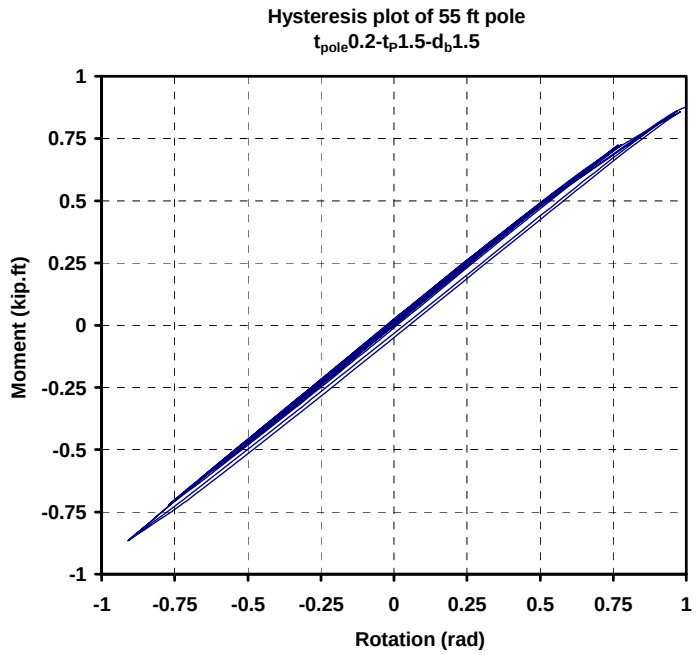

Figure D.27 Hysteresis plot of case 27

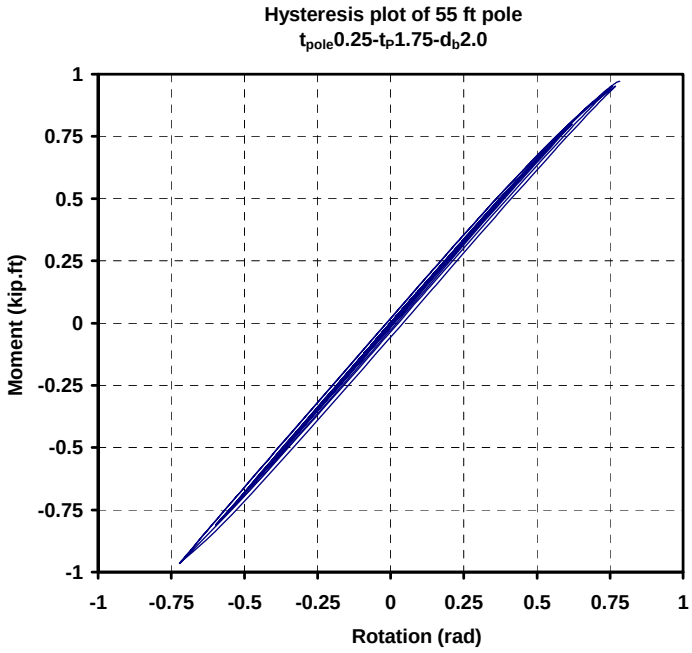

Figure D.28 Hysteresis plot of case 28

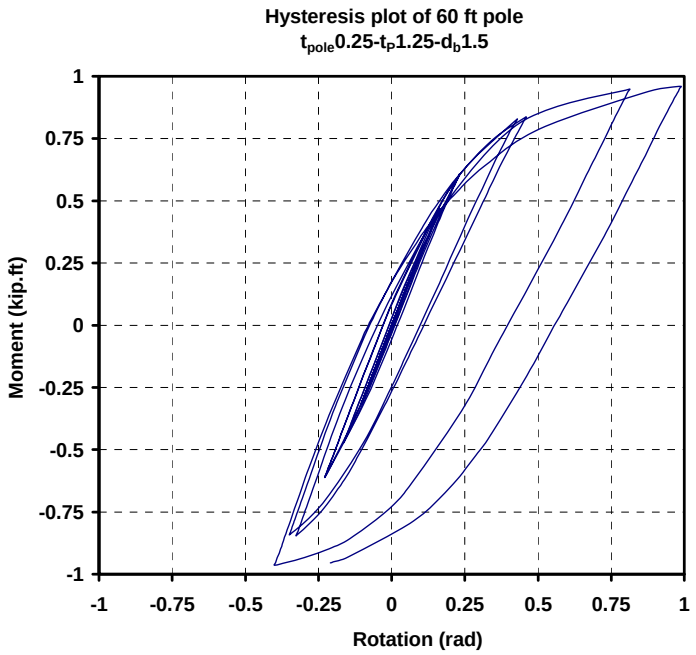

Figure D.29 Hysteresis plot of case 29

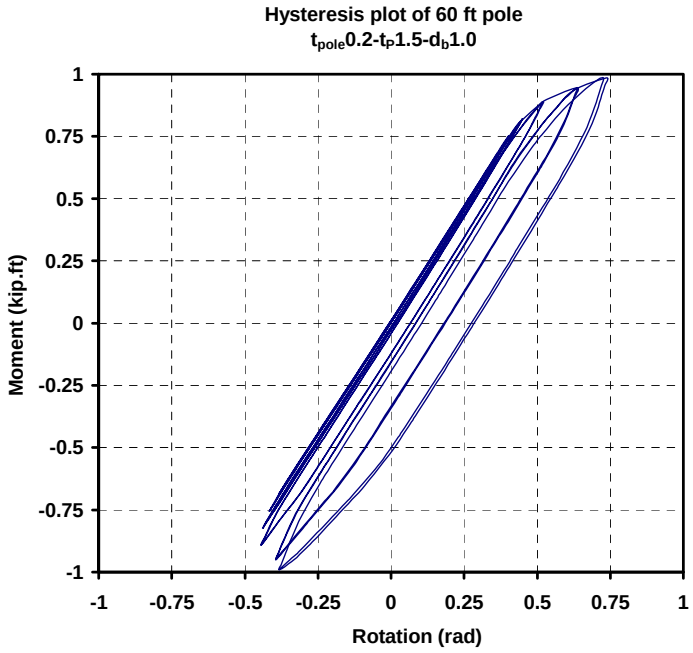

Figure D.30 Hysteresis plot of case 30

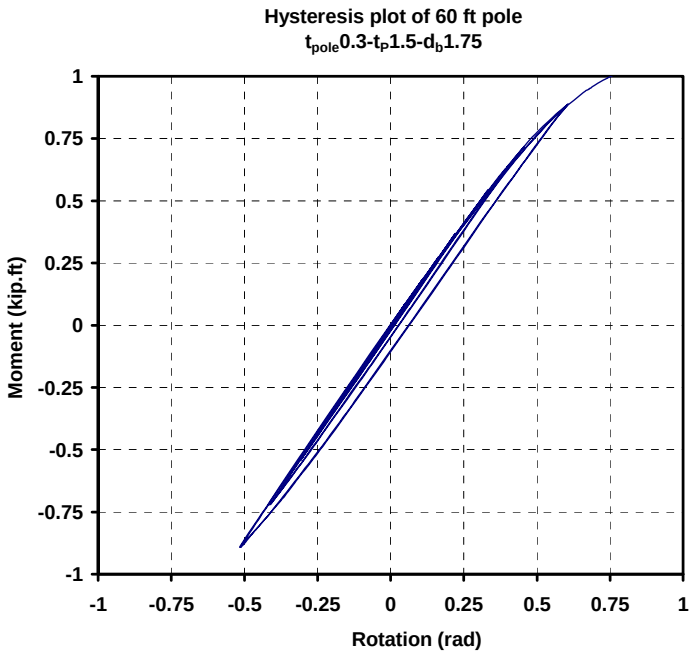

Figure D.31 Hysteresis plot of case 31

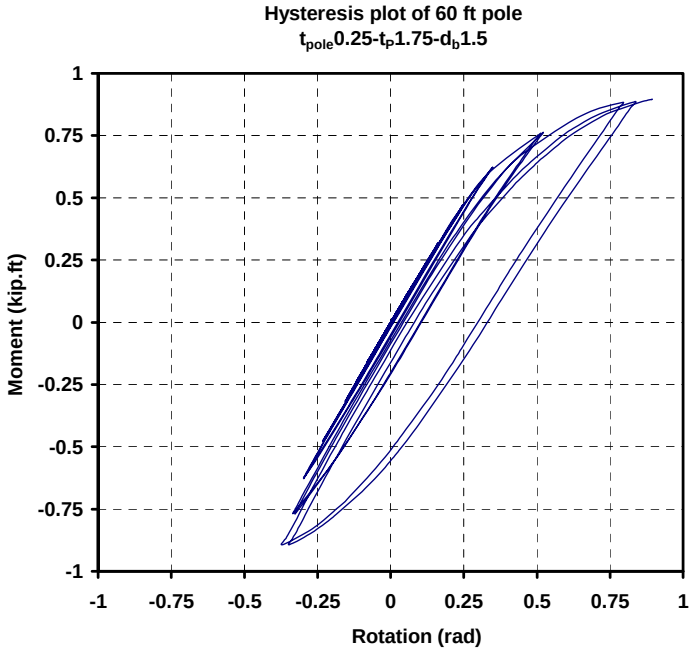

Figure D.32 Hysteresis plot of case 32

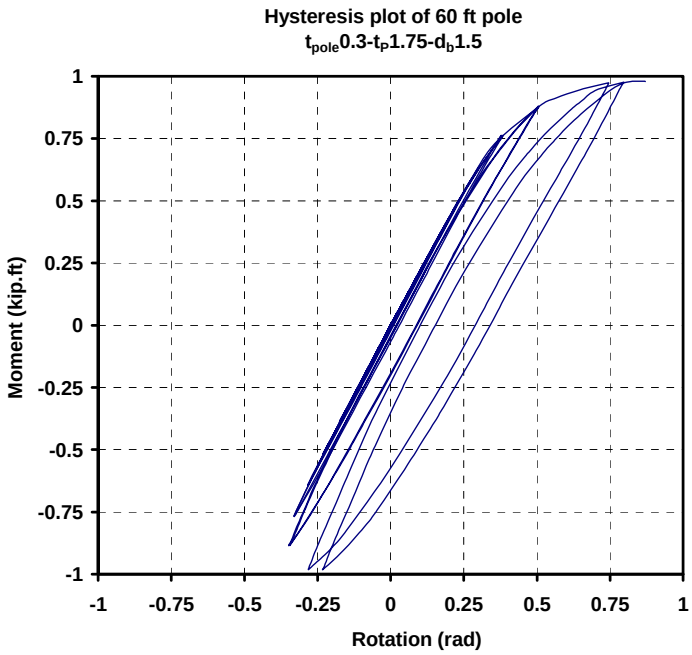

Figure D.33 Hysteresis plot of case 33

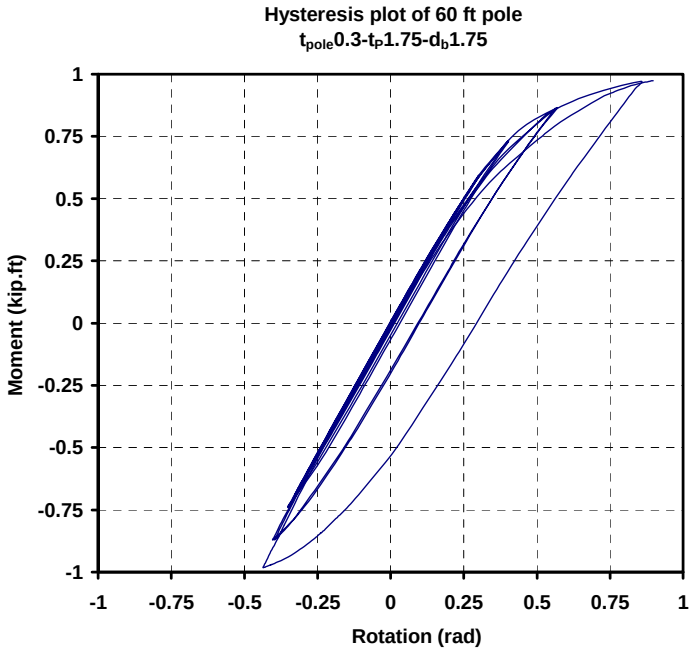

Figure D.34 Hysteresis plot of case 34

APPENDIX E

IMAGE CORRECTION OF MECHANICAL DEVICE

Rigid Mounted With Isolator

(a)

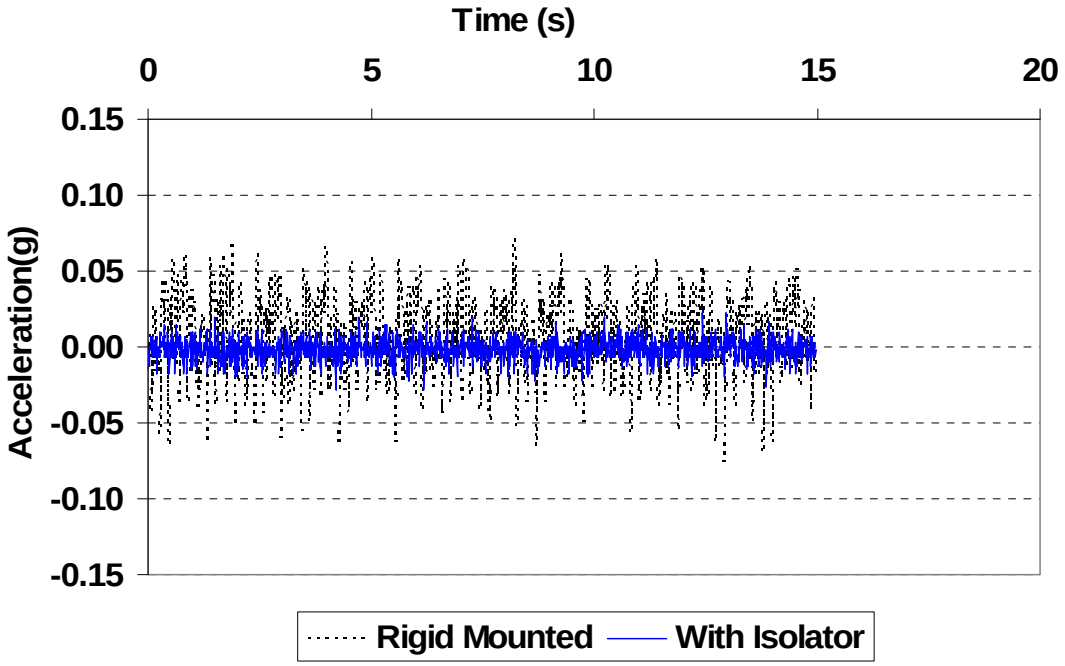

(b)

Figure E.1 Comparison between the uncorrected and corrected images for: Mode1-60ft-R-I-01-0.94 Hz (a) Images and (b) Acceleration data Percentage Correction: Max: 67.83 %; Min: 62.91 %; Avg: 65.37 %.

Rigid Mounted With Isolator

(a)

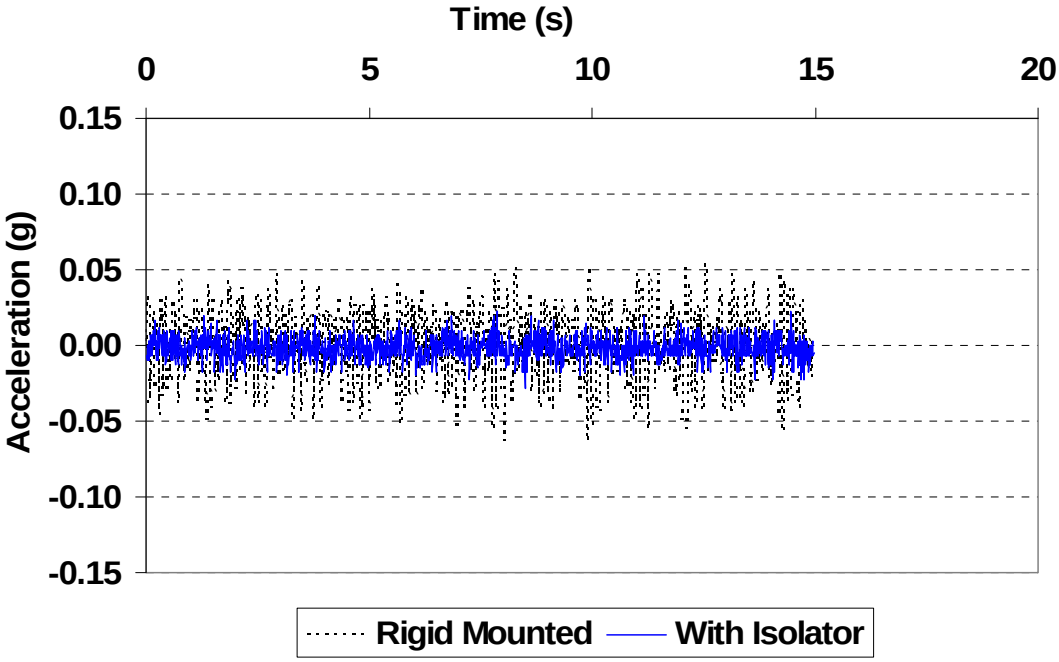

(b)

Figure E.2 Comparison between the uncorrected and corrected images for: Mode1-60ft-R-I-02-0.94 Hz (a) Images and (b) Acceleration data Percentage Correction: Max: 57.01 %; Min: 55.20 %; Avg: 56.10 %.

Rigid Mounted

With Isolator

(a)

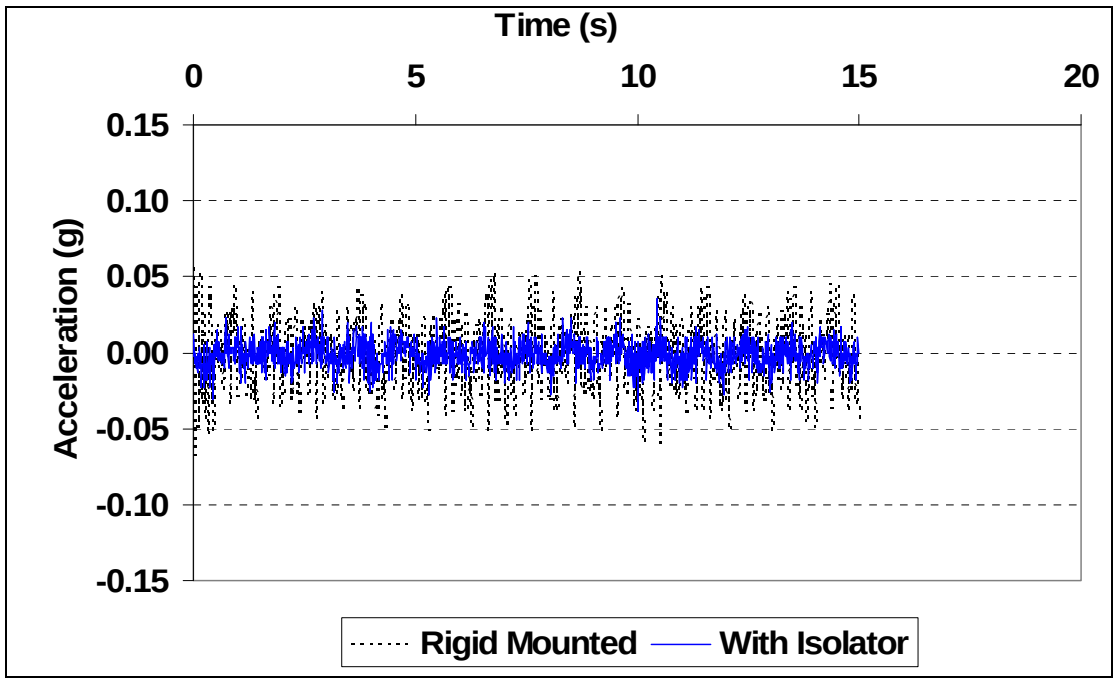

(b)

Figure E.3 Comparison between the uncorrected and corrected images for: Mode1-60ft-R-I-03-0.94 Hz (a) Images and (b) Acceleration data Percentage Correction: Max: 36.28 %; Min: 42.22 %; Avg: 39.25 %.

Rigid Mounted With Isolator

(a)

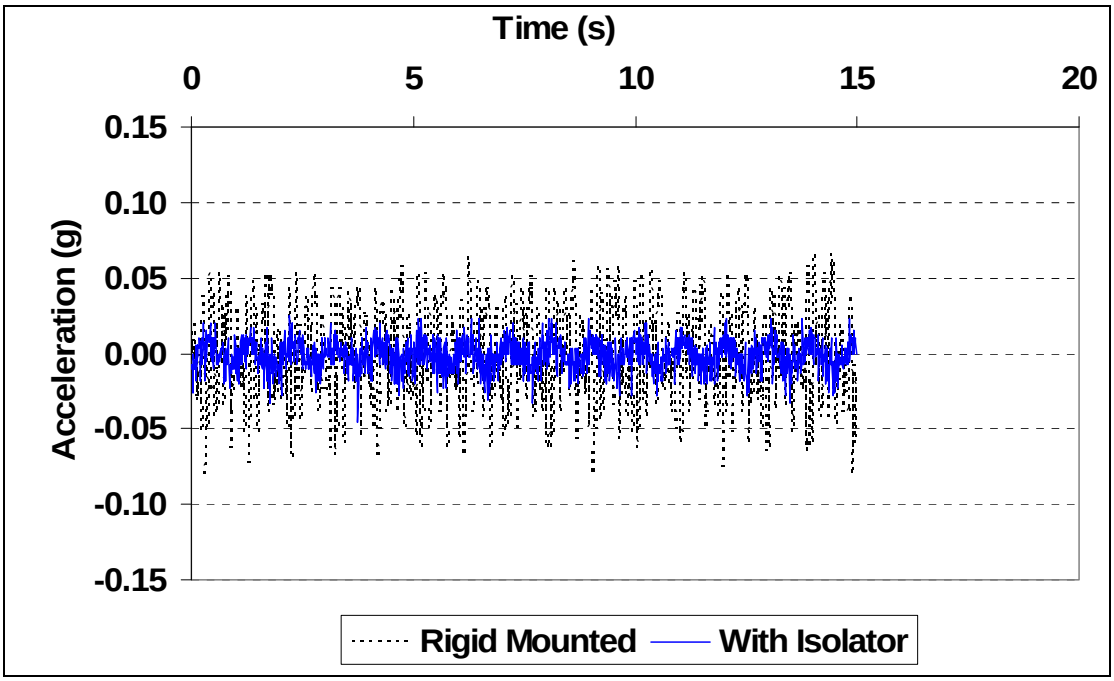

(b)

Figure E.4 Comparison between the uncorrected and corrected images for: Mode1-60ft-R-I-04-1.02 Hz (a) Images and (b) Acceleration data Percentage Correction: Max: 62.41 %; Min: 44.24 %; Avg: 53.32 %.

Rigid Mounted With Isolator

(a)

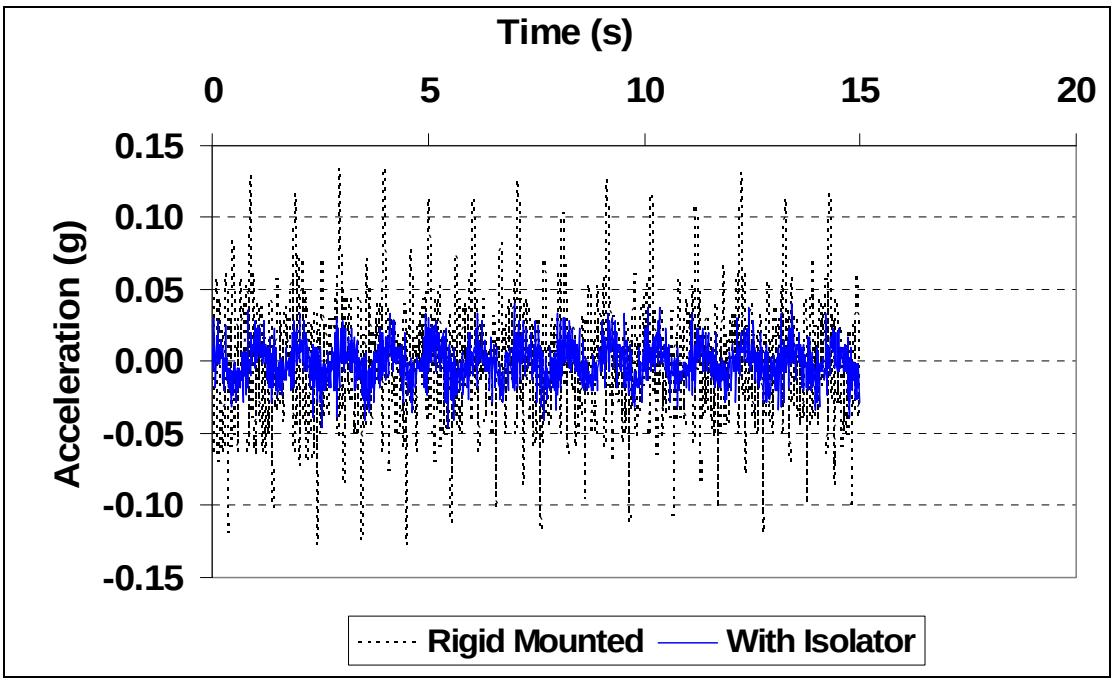

(b)

Figure E.5 Comparison between the uncorrected and corrected images for: Mode1-60ft-R-I-06-1.02 Hz (a) Images and (b) Acceleration data Percentage Correction: Max: 69.52 %; Min: 63.92 %; Avg: 66.72 %.

Rigid Mounted With Isolator

(a)

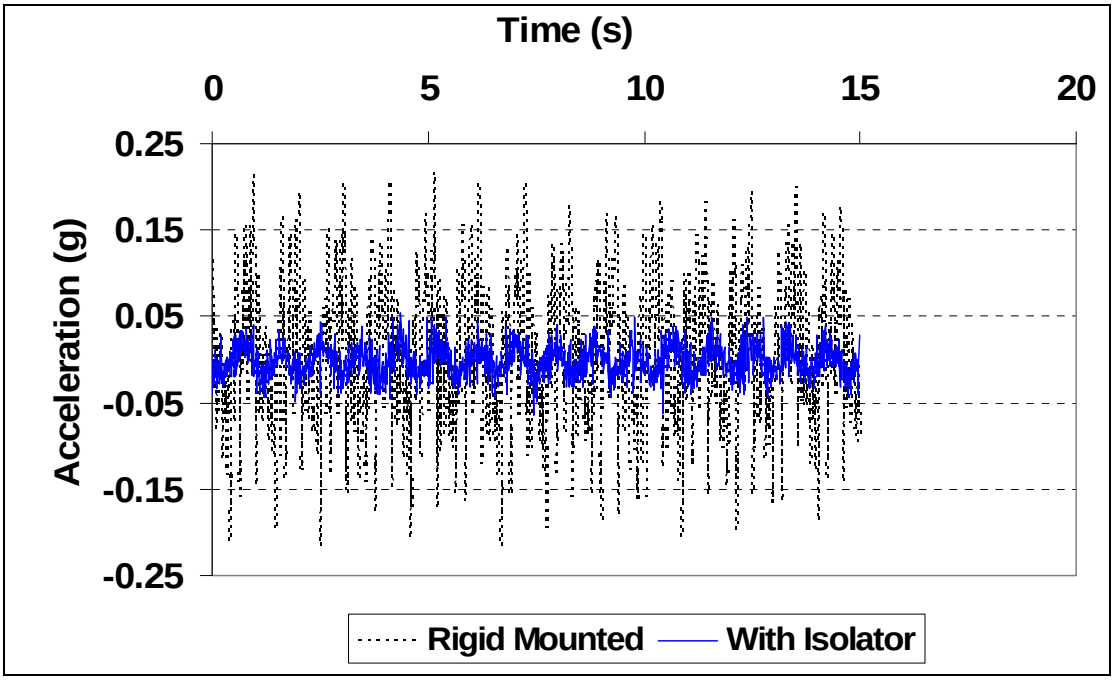

(b)

Figure E.6 Comparison between the uncorrected and corrected images for: Mode1-60ft-R-I-10-1.02 Hz (a) Images and (b) Acceleration data Percentage Correction: Max: 75.17 %; Min: 69.84 %; Avg: 72.51 %.

Rigid Mounted With Isolator

(a)

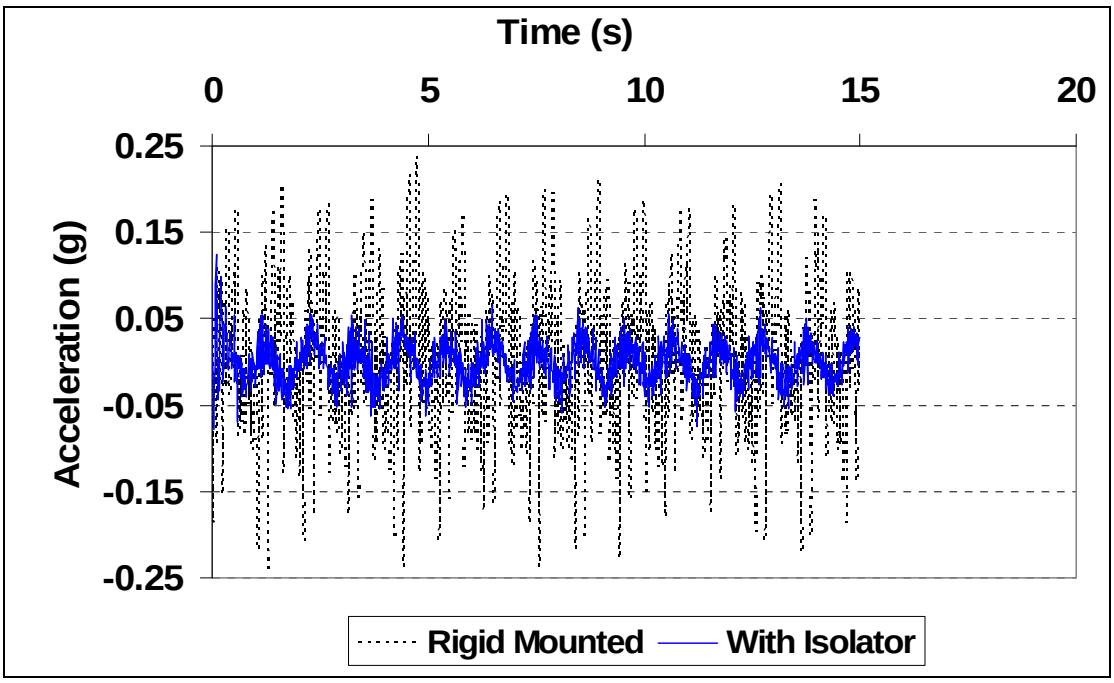

(b)

Figure E.7 Comparison between the uncorrected and corrected images for: Mode1-60ft-R-I-15-1.02 Hz (a) Images and (b) Acceleration data Percentage Correction: Max: 48.01 %; Min: 67.97 %; Avg: 57.99 %.

Rigid Mounted With Isolator

(a)

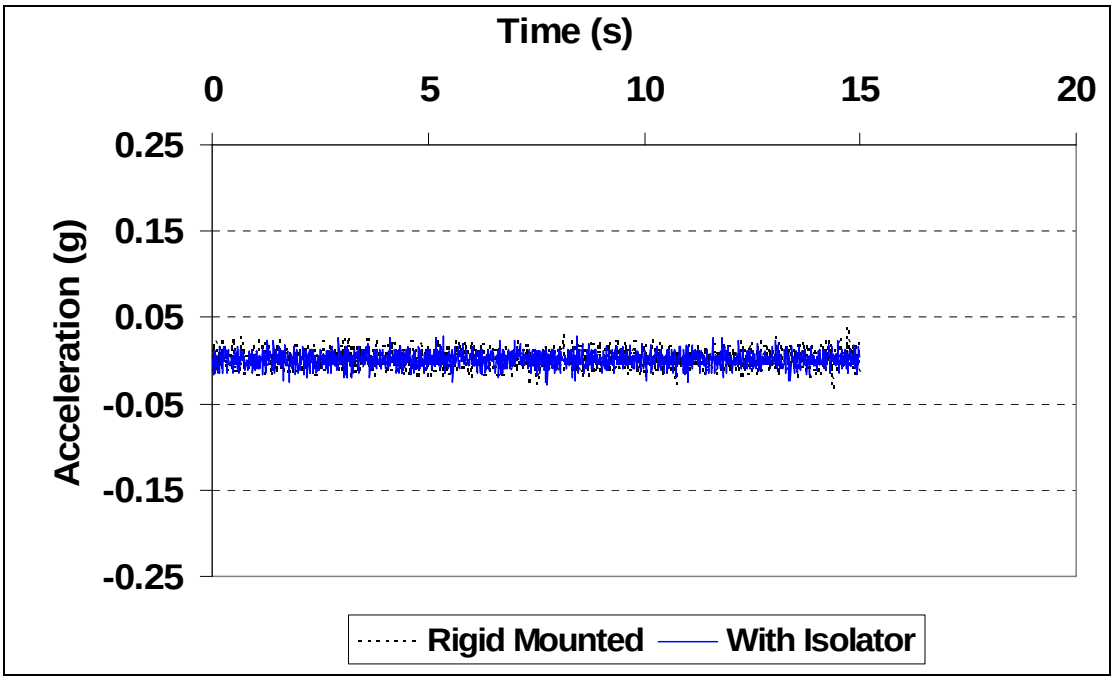

(b)

Figure E.8 Comparison between the uncorrected and corrected images for: Mode2-60ft-R-I-01-4.8 Hz (a) Images and (b) Acceleration data Percentage Correction: Max: 29.63 %; Min: 17.91 %; Avg: 23.77 %.

Rigid Mounted With Isolator

(a)

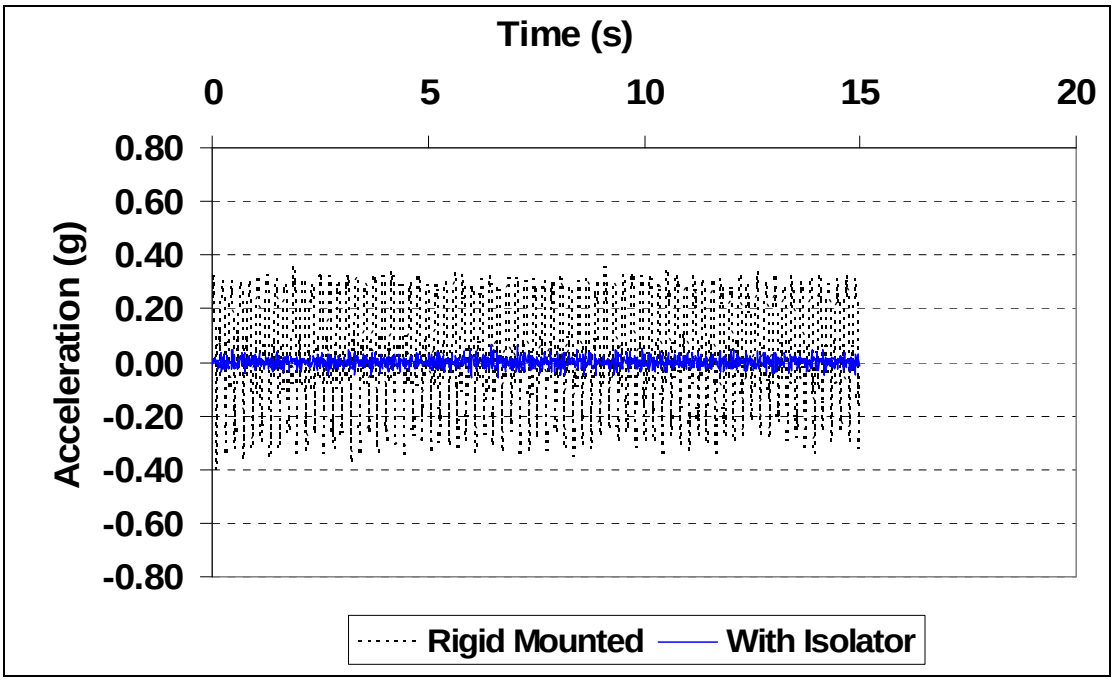

(b)

Figure E.9 Comparison between the uncorrected and corrected images for: Mode2-60ft-R-I-02-4.8 Hz (a) Images and (b) Acceleration data Percentage Correction: Max: 81.83 %; Min: 85.47 %; Avg: 83.65 %.

Rigid Mounted With Isolator

(a)

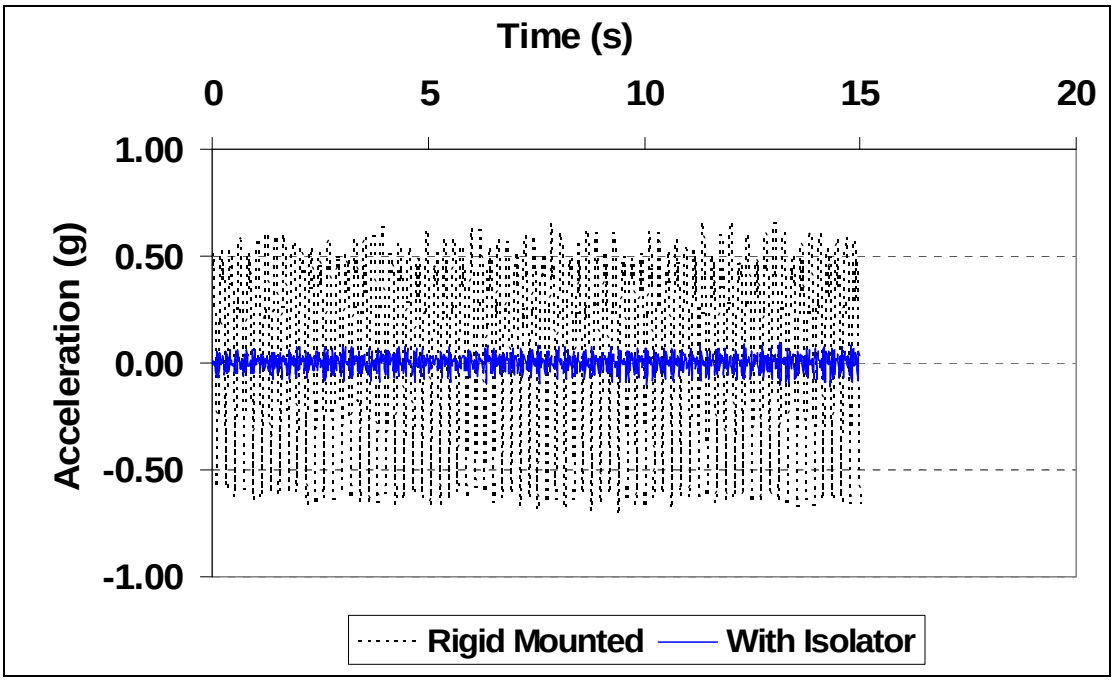

(b)

Figure E.10 Comparison between the uncorrected and corrected images for: Mode2-60ft-R-I-03-4.8 Hz (a) Images and (b) Acceleration data Percentage Correction: Max: 85.41 %; Min: 83.93 %; Avg: 84.67 %.

Rigid Mounted With Isolator

(a)

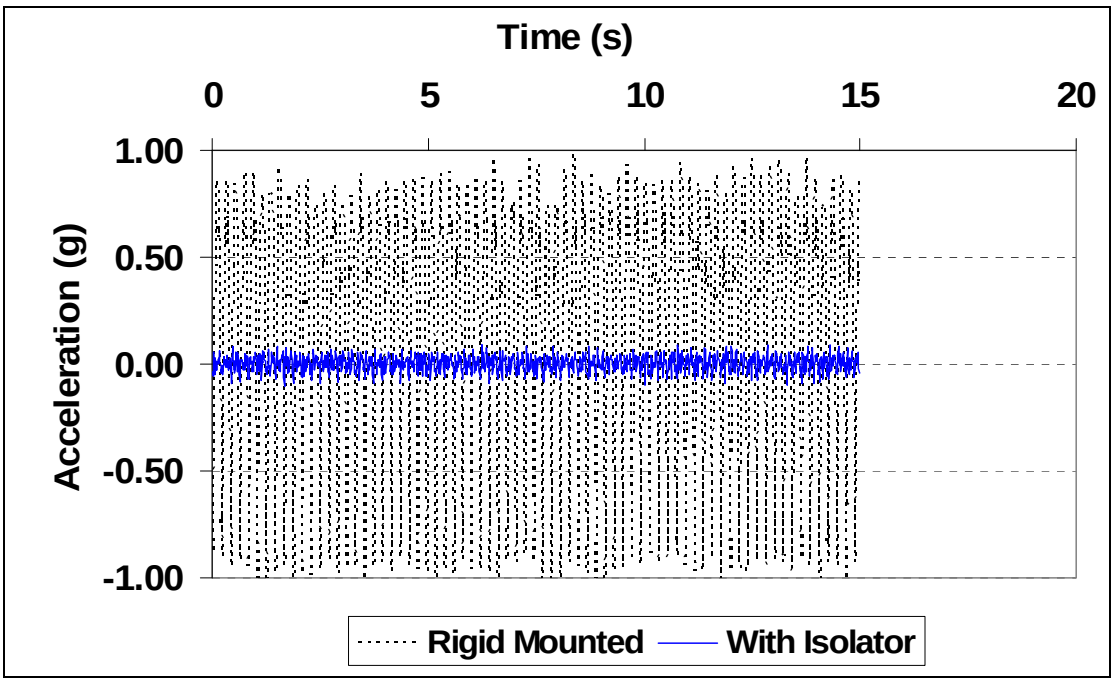

(b)

Figure E.11 Comparison between the uncorrected and corrected images for: Mode 2-60ft-R-I-04-4.8 Hz (a) Images and (b) Acceleration data Percentage Correction: Max: 90.49 %; Min: 90.60 %; Avg: 90.55 %.

Rigid Mounted With Isolator

(a)

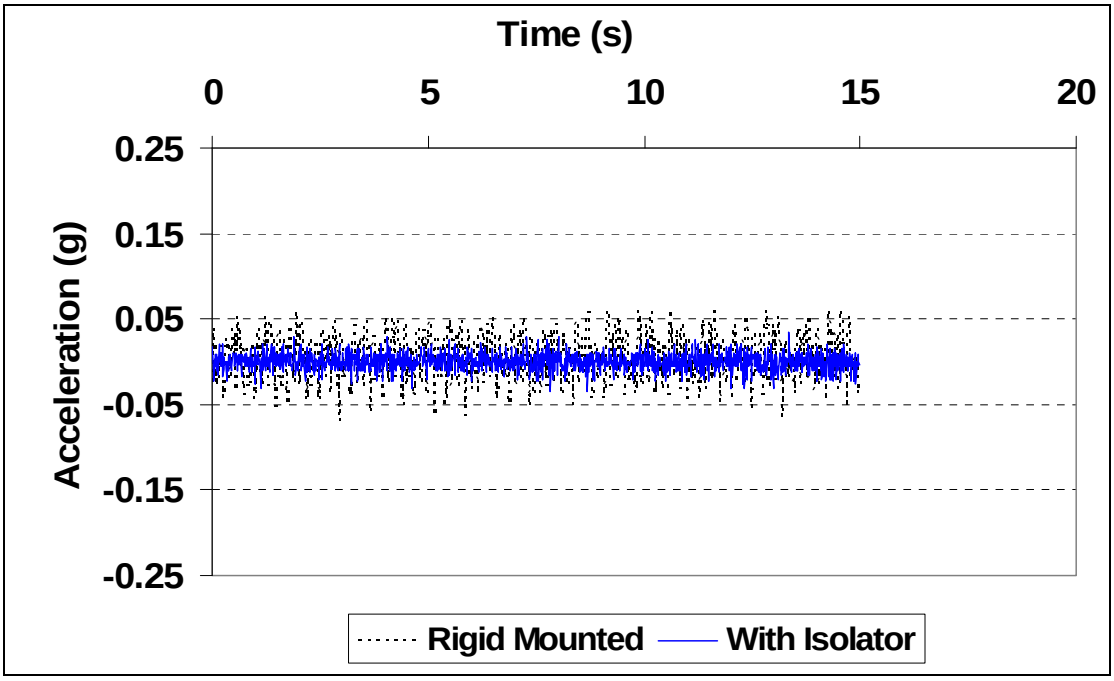

(b)

Figure E.12 Comparison between the uncorrected and corrected images for: Mode1-50ft-R-I-02-1.3 Hz (a) Images and (b) Acceleration data Percentage Correction: Max: 47.29 %; Min: 51.08 %; Avg: 49.18 %.

Rigid Mounted With Isolator

(a)

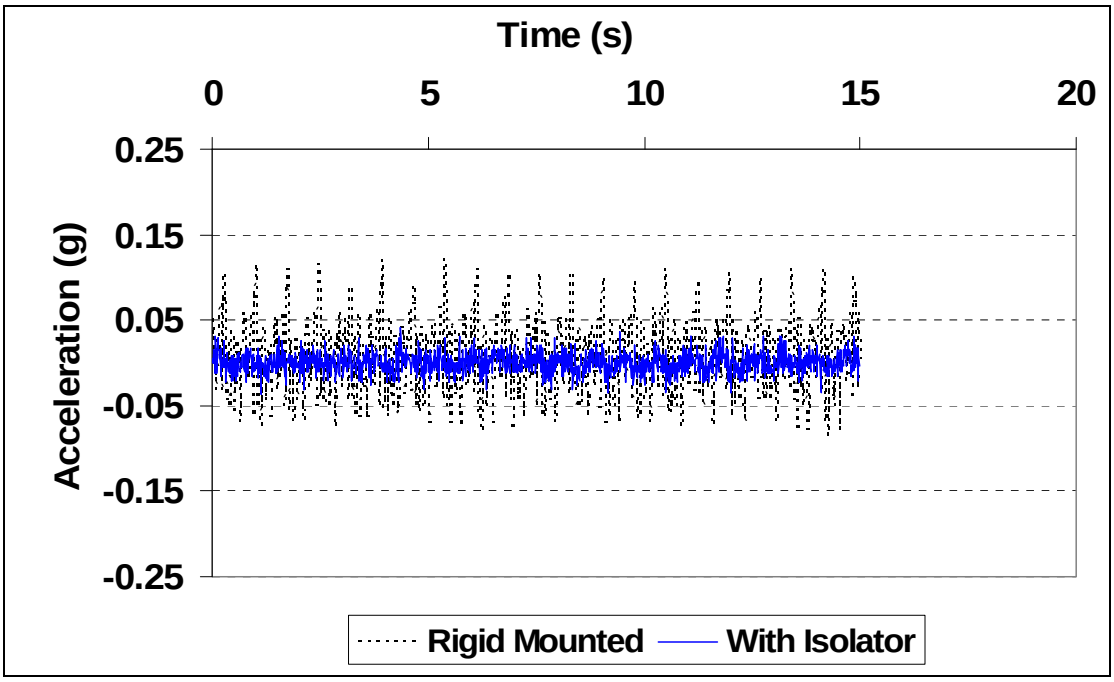

(b)

Figure E.13 Comparison between the uncorrected and corrected images for: Mode1-50ft-R-I-03-1.3 Hz (a) Images and (b) Acceleration data Percentage Correction: Max: 65.99 %; Min: 57.89 %; Avg: 61.94 %.

Rigid Mounted With Isolator

(a)

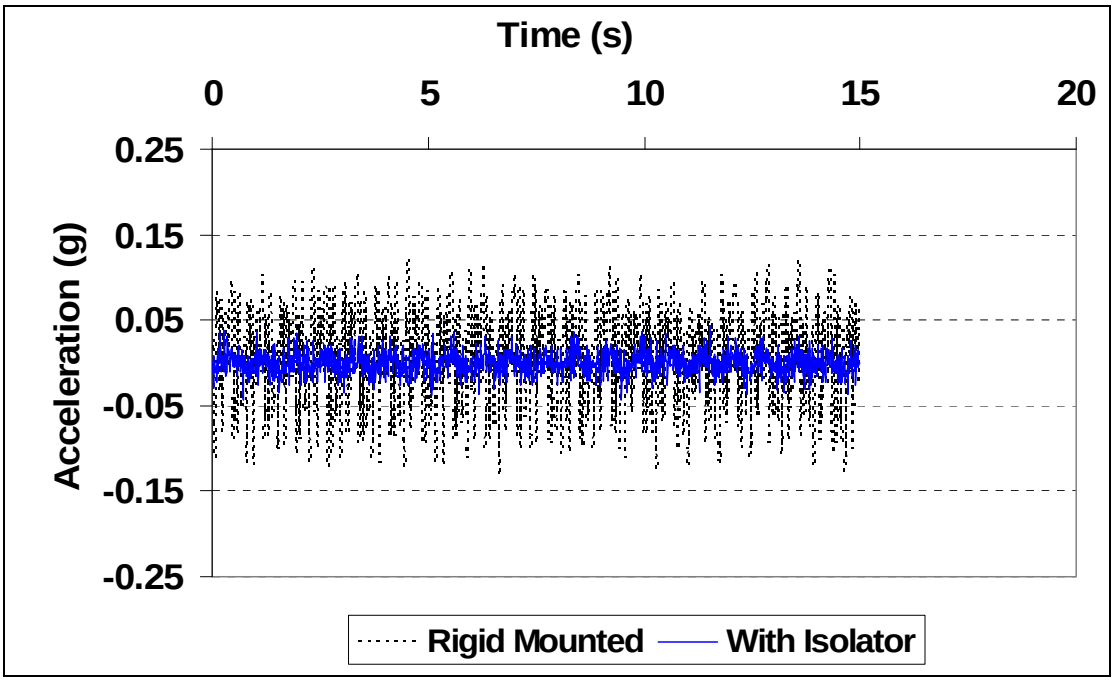

(b)

Figure E.14 Comparison between the uncorrected and corrected images for: Mode1-50ft-R-I-04-1.3 Hz (a) Images and (b) Acceleration data Percentage Correction: Max: 64.37 %; Min: 66.79 %; Avg: 65.58 %.

Rigid Mounted With Isolator

(a)

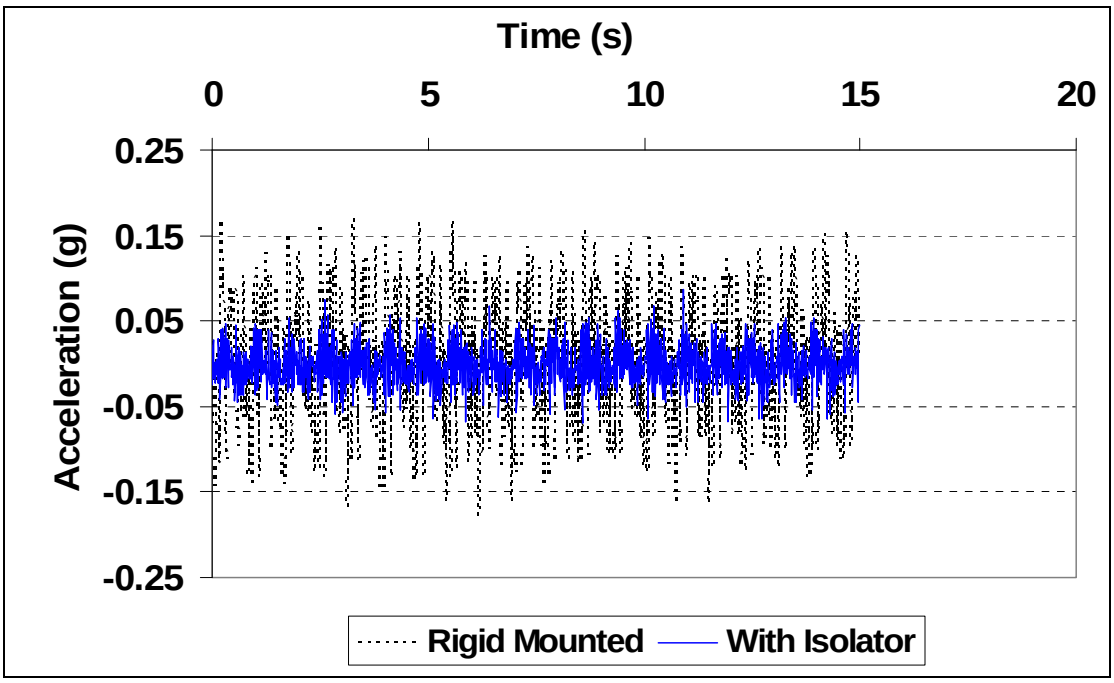

(b)

Figure E.15 Comparison between the uncorrected and corrected images for: Mode1-50ft-R-I-06-1.3 Hz (a) Images and (b) Acceleration data Percentage Correction: Max: 49.56 %; Min: 60.34 %; Avg: 54.95 %.

Rigid Mounted With Isolator

(a)

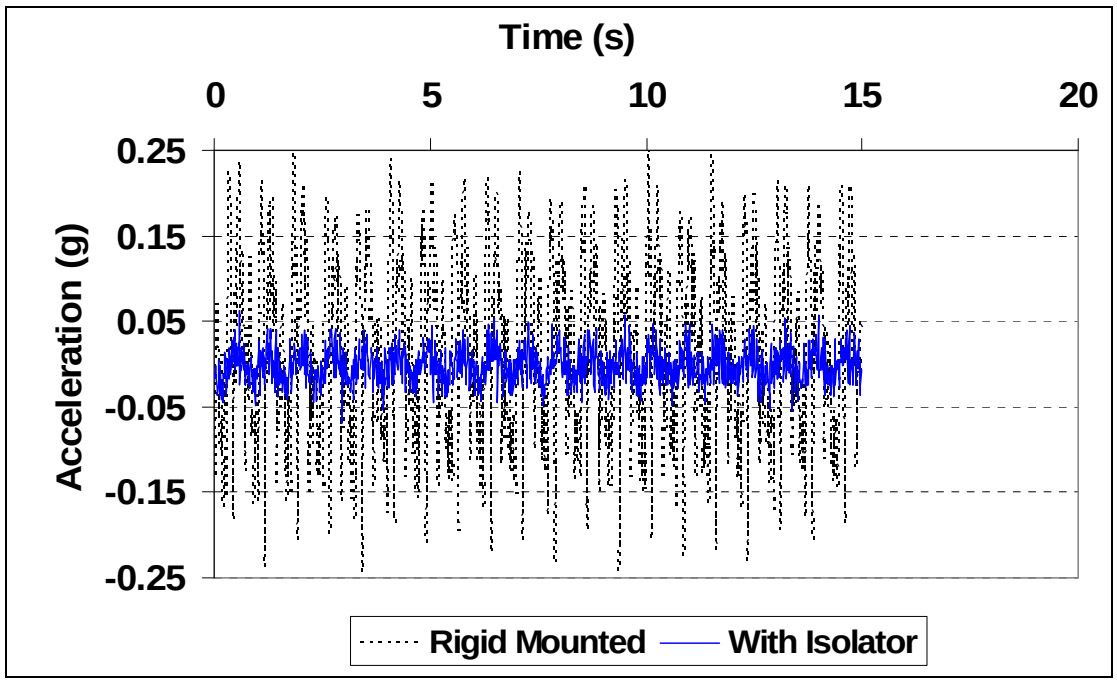

(b)

Figure E.16 Comparison between the uncorrected and corrected images for: Mode1-50ft-R-I-10-1.3 Hz (a) Images and (b) Acceleration data Percentage Correction: Max: 75.35 %; Min: 71.25 %; Avg: 73.30 %.

Rigid Mounted With Isolator

(a)

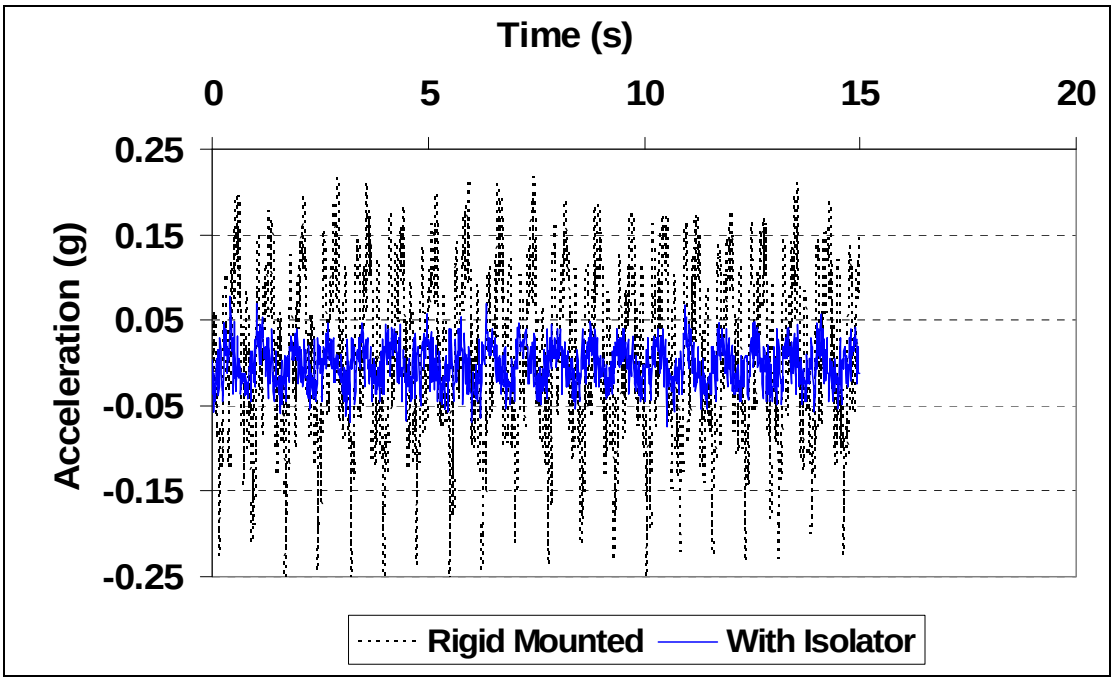

(b)

Figure E.17 Comparison between the uncorrected and corrected images for: Mode1-50ft-R-I-15-1.3 Hz (a) Images and (b) Acceleration data Percentage Correction: Max: 64.46 %; Min: 71.64 %; Avg: 68.05 %.

Rigid Mounted With Isolator

(a)

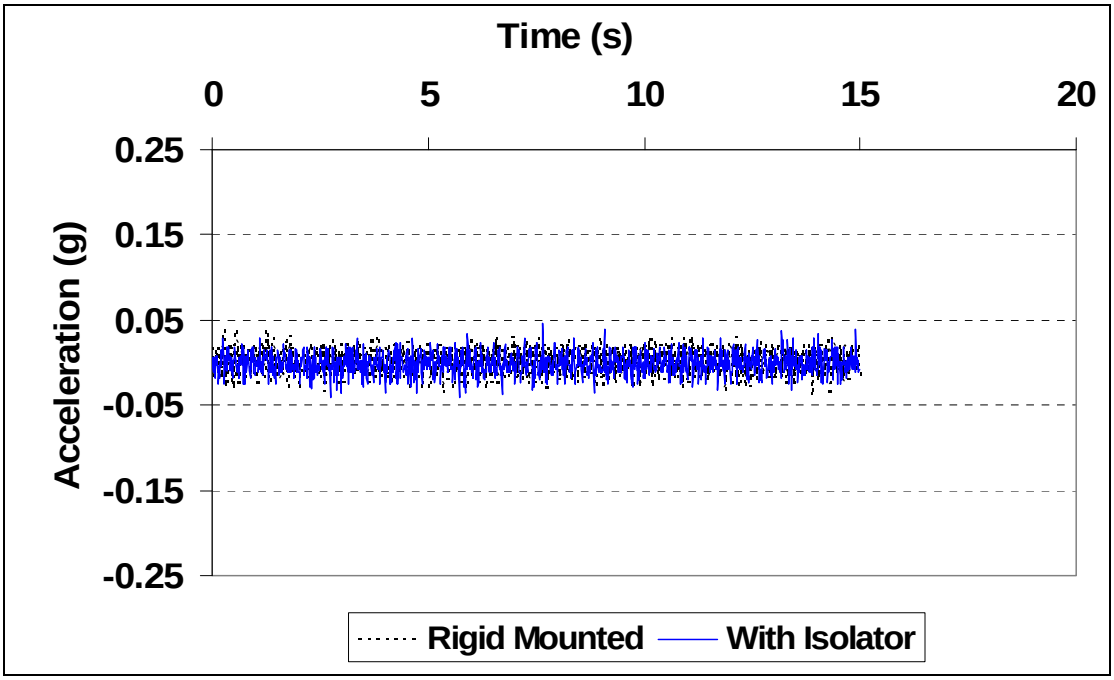

(b)

Figure E.18 Comparison between the uncorrected and corrected images for: Mode2-50ft-R-I-01-6.9 Hz (a) Images and (b) Acceleration data Percentage Correction: Max: 22.07 %; Min: 6.49 %; Avg: 14.29 %.

Rigid Mounted With Isolator

(a)

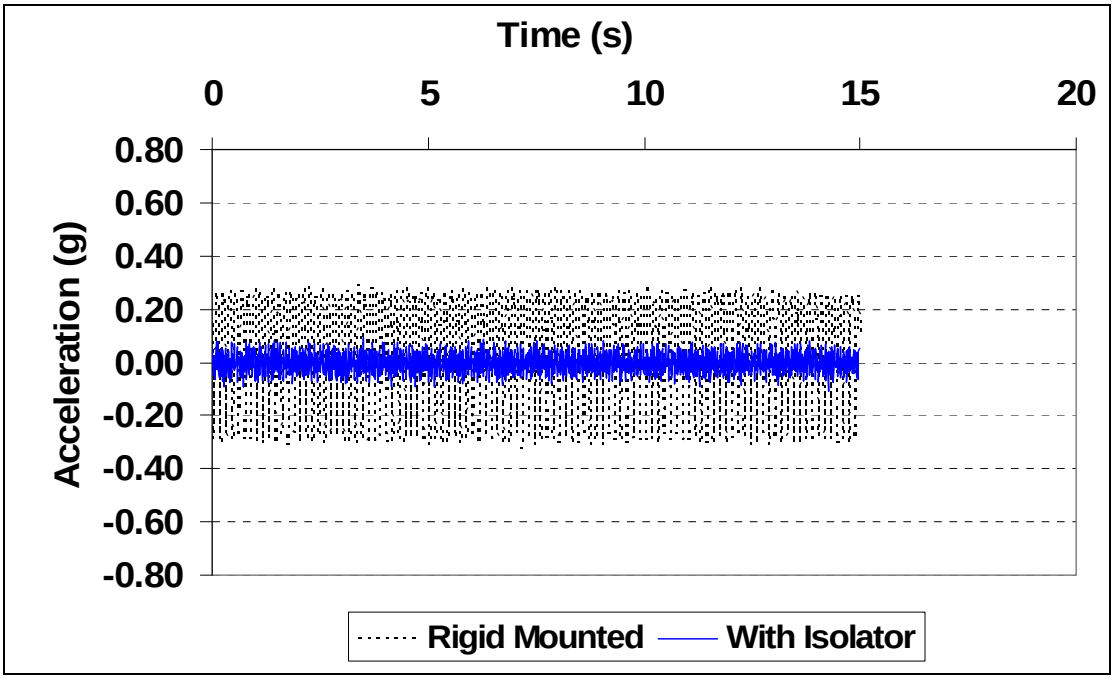

(b)

Figure E.19 Comparison between the uncorrected and corrected images for: Mode2-50ft-R-I-02-6.9 Hz (a) Images and (b) Acceleration data Percentage Correction: Max: 68.67 %; Min: 67.33 %; Avg: 68.00 %.

Rigid Mounted With Isolator

(a)

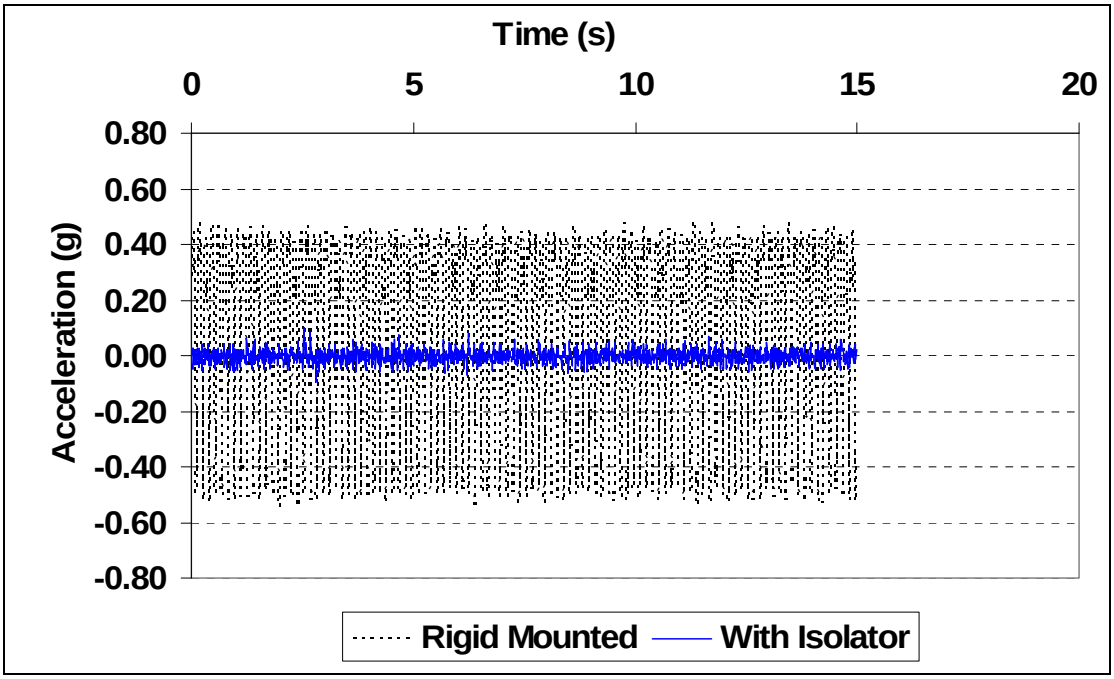

(b)

Figure E.20 Comparison between the uncorrected and corrected images for: Mode2-50ft-R-I-03-6.9 Hz (a) Images and (b) Acceleration data Percentage Correction: Max: 84.02 %; Min: 81.59 %; Avg: 82.81 %.

Rigid Mounted With Isolator

(a)

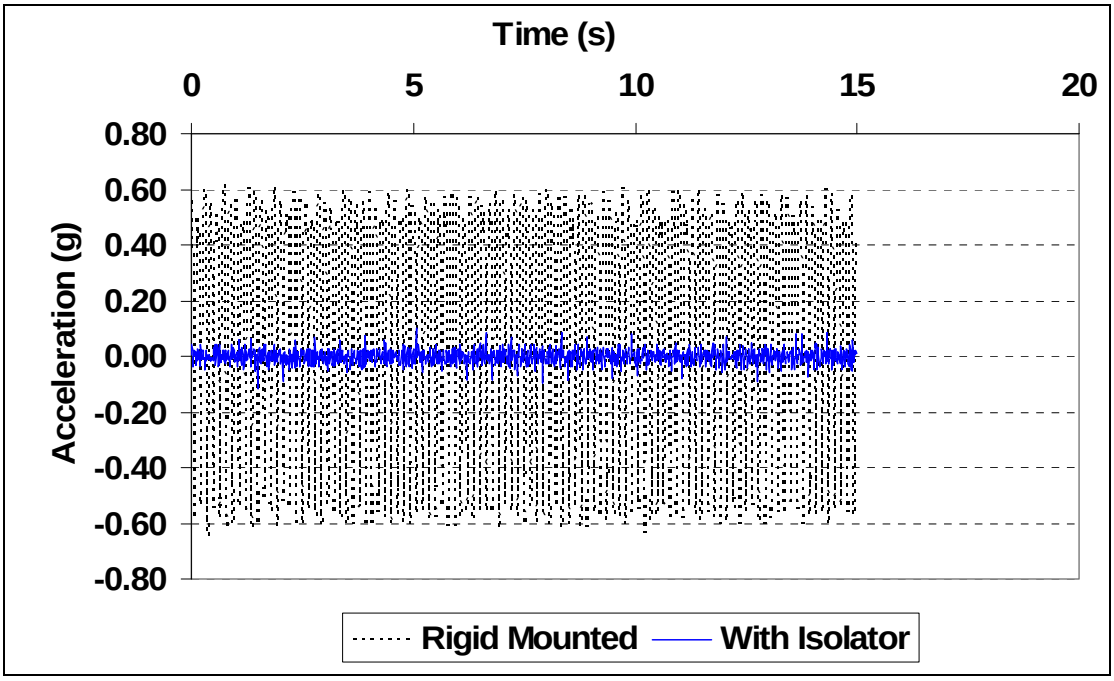

(b)

Figure E.21 Comparison between the uncorrected and corrected images for: Mode2-50ft-R-I-04-6.9 Hz (a) Images and (b) Acceleration data Percentage Correction: Max: 79.69 %; Min: 82.10 %; Avg: 80.90 %.

Rigid Mounted With Isolator

(a)

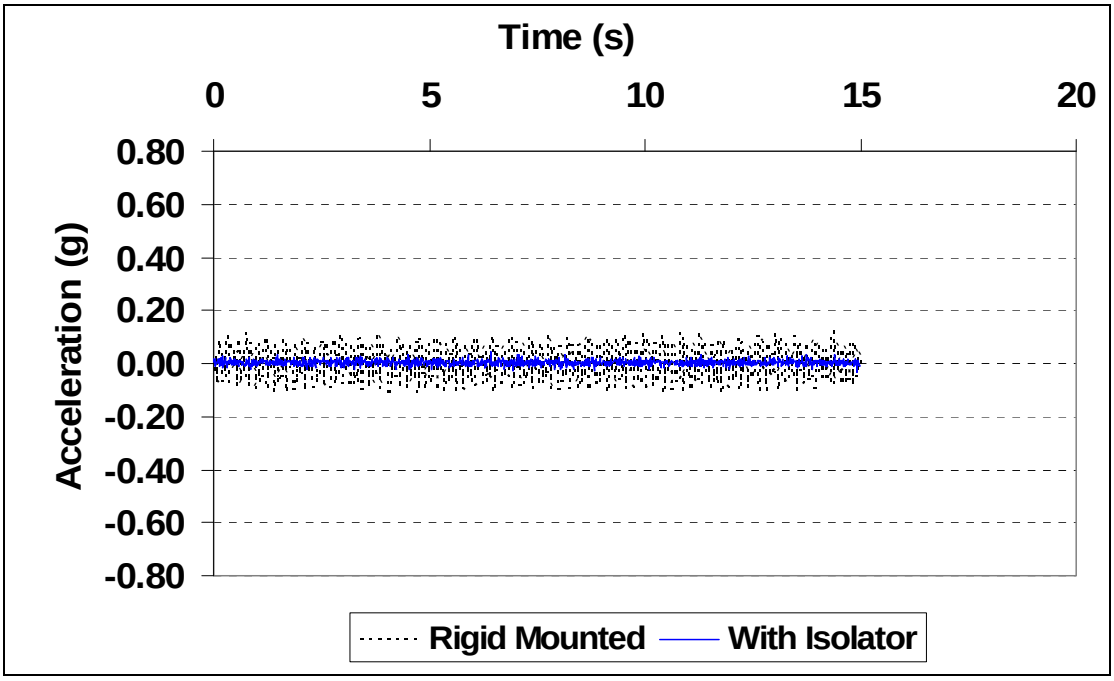

(b)

Figure E.22 Comparison between the uncorrected and corrected images for: Mode1-40ft-R-I-01-2.0 Hz (a) Images and (b) Acceleration data Percentage Correction: Max: 65.85 %; Min: 74.38 %; Avg: 70.12 %.

Rigid Mounted With Isolator

(a)

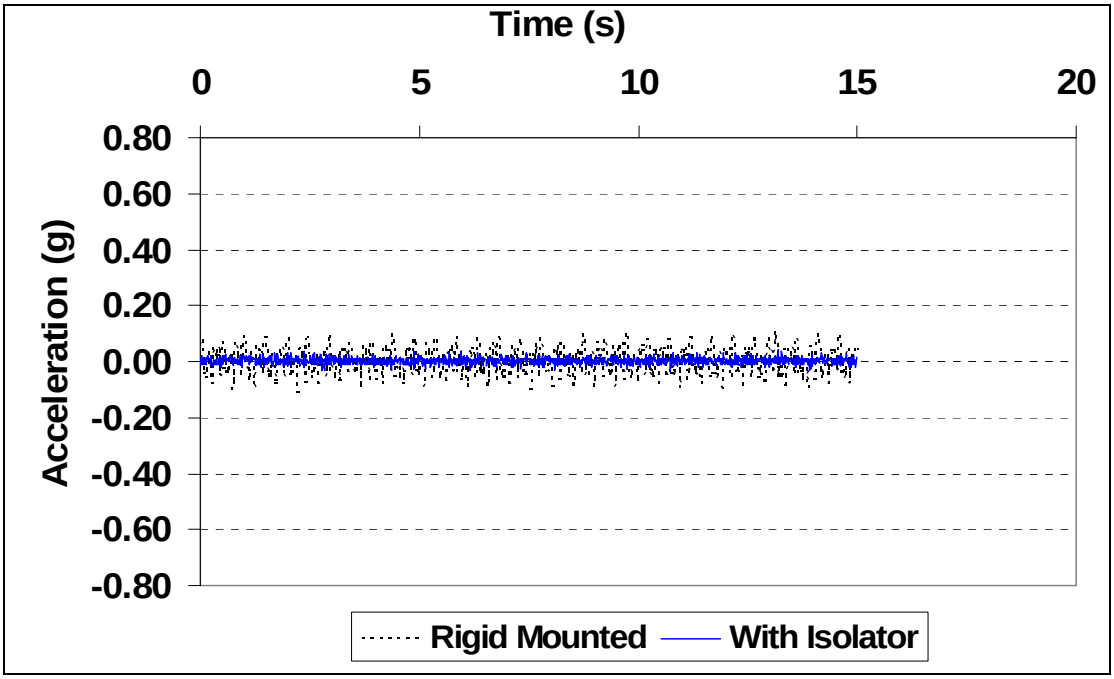

(b)

Figure E.23 Comparison between the uncorrected and corrected images for: Mode1-40ft-R-I-02-2.0 Hz (a) Images and (b) Acceleration data Percentage Correction: Max: 61.82 %; Min: 65.49 %; Avg: 63.65 %.

Rigid Mounted With Isolator

(a)

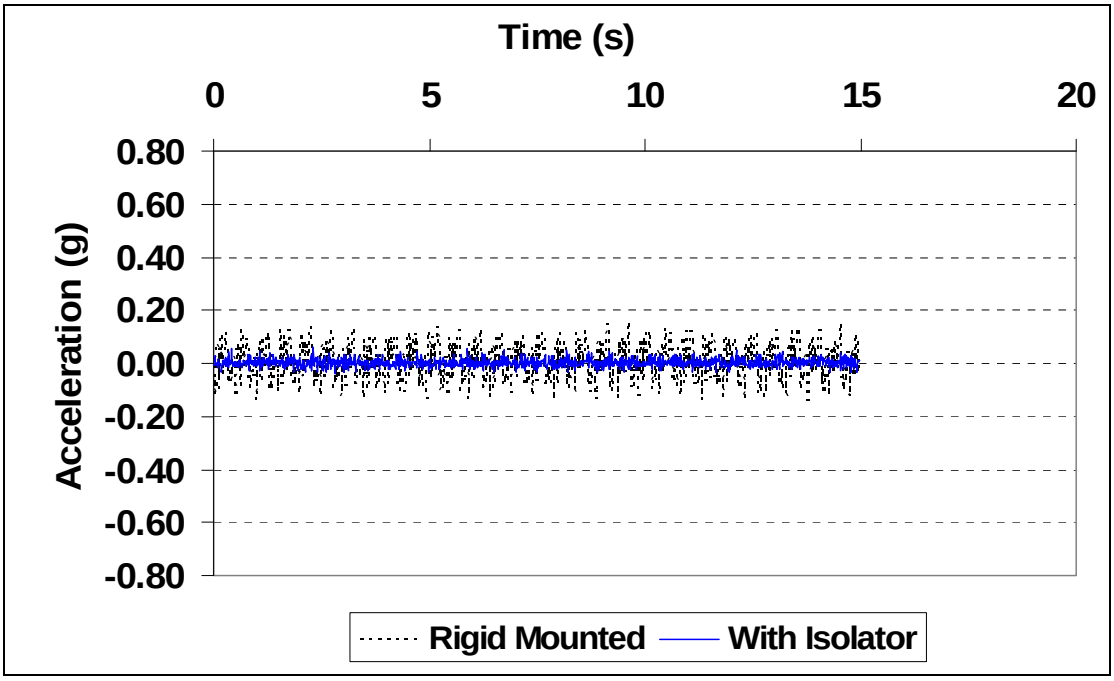

(b)

Figure E.24 Comparison between the uncorrected and corrected images for: Mode1-40ft-R-I-03-2.0 Hz (a) Images and (b) Acceleration data Percentage Correction: Max: 61.01 %; Min: 72.54 %; Avg: 66.77 %.

Rigid Mounted With Isolator

(a)

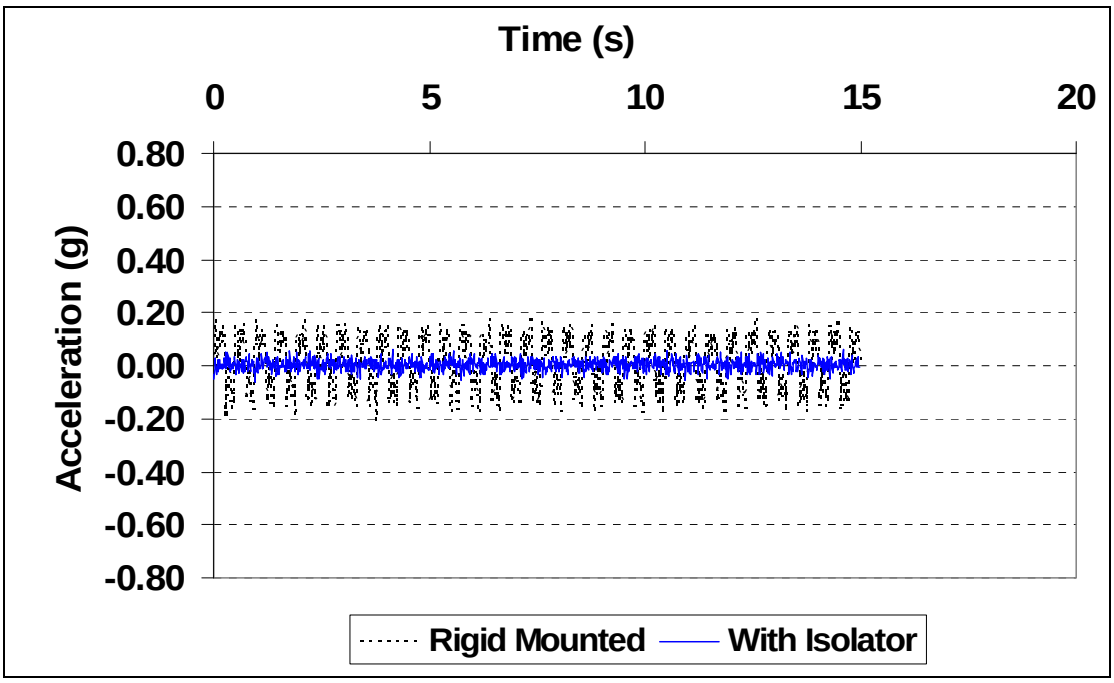

(b)

Figure E.25 Comparison between the uncorrected and corrected images for: Mode1-40ft-R-I-04-2.0 Hz (a) Images and (b) Acceleration data Percentage Correction: Max: 67.37 %; Min: 70.73 %; Avg: 69.05 %.

Rigid Mounted With Isolator

(a)

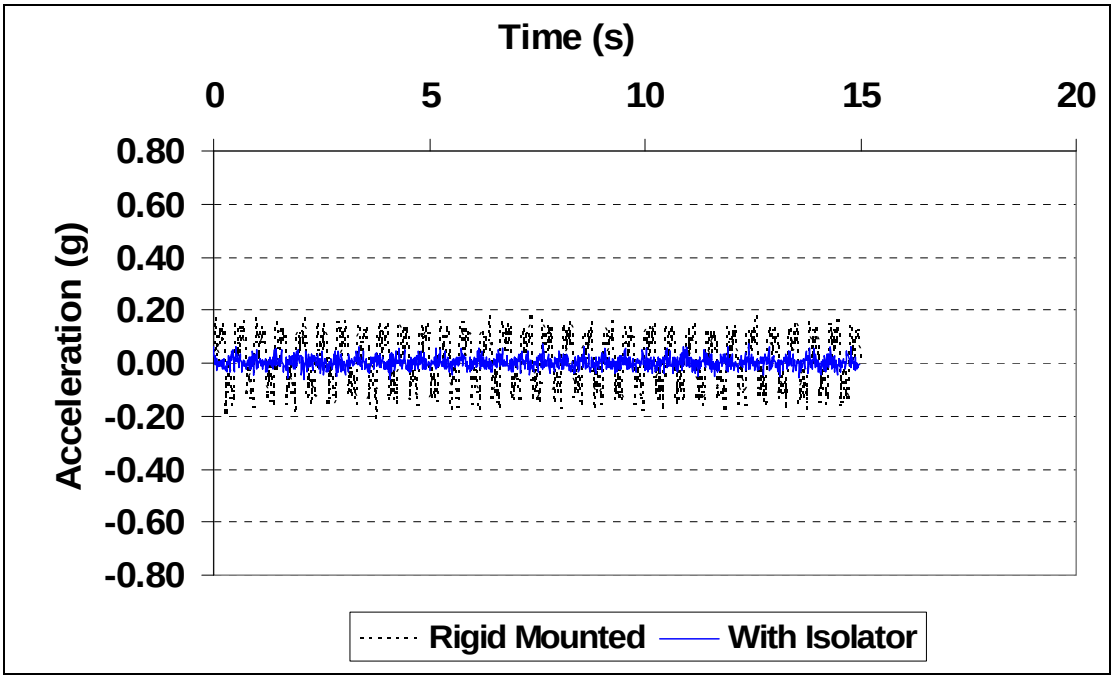

(b)

Figure E.26 Comparison between the uncorrected and corrected images for: Mode1-40ft-R-I-06-2.0 Hz (a) Images and (b) Acceleration data Percentage Correction: Max: 60.52 %; Min: 69.27 %; Avg: 64.90 %.

Rigid Mounted With Isolator

(a)

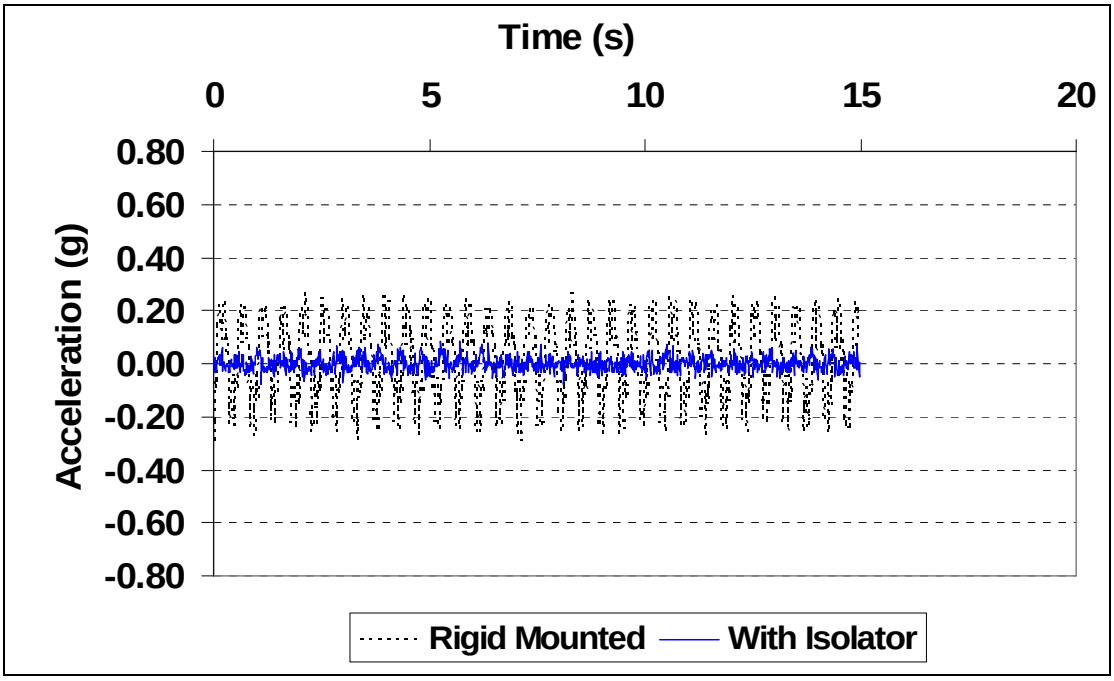

(b)

Figure E.27 Comparison between the uncorrected and corrected images for: Mode1-40ft-R-I-10-2.0 Hz (a) Images and (b) Acceleration data Percentage Correction: Max: 68.63 %; Min: 72.82 %; Avg: 70.73 %.

Rigid Mounted With Isolator

(a)

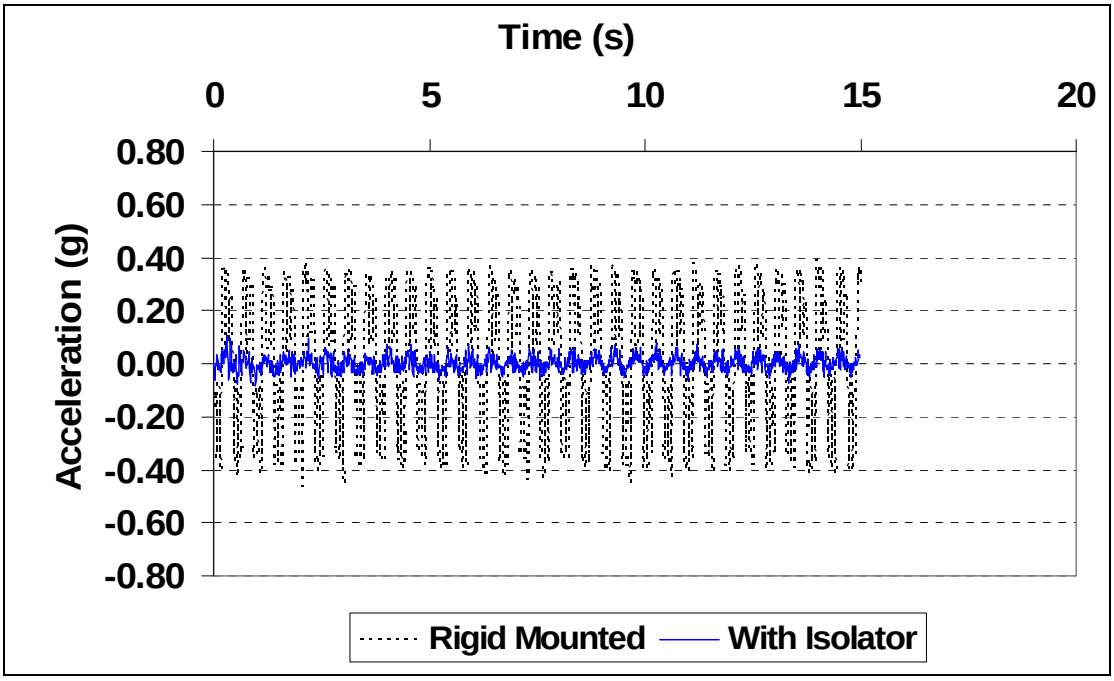

(b)

Figure E.28 Comparison between the uncorrected and corrected images for: Mode1-40ft-R-I-15-2.0 Hz (a) Images and (b) Acceleration data Percentage Correction: Max: 73.03 %; Min: 81.51 %; Avg: 77.27 %.

Rigid Mounted With Isolator

(a)

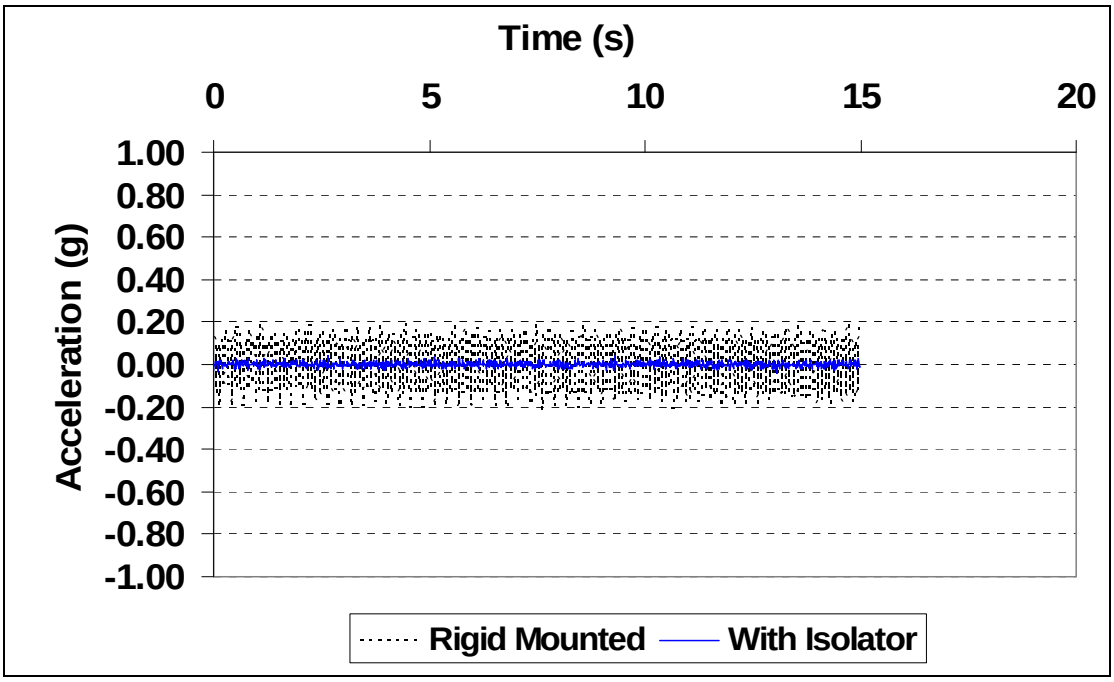

(b)

Figure E.29 Comparison between the uncorrected and corrected images for: Mode1-30ft-R-I-01-3.5 Hz (a) Images and (b) Acceleration data Percentage Correction: Max: 80.30 %; Min: 80.19 %; Avg: 80.25 %.

Rigid Mounted With Isolator

(a)

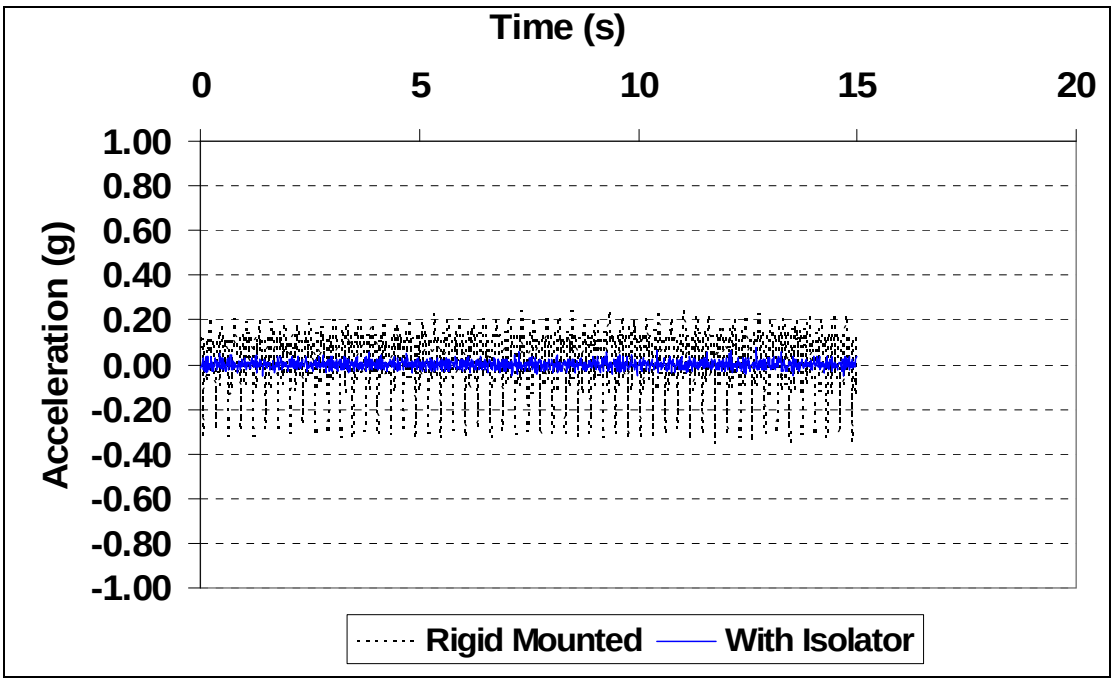

(b)

Figure E.30 Comparison between the uncorrected and corrected images for: Mode1-30ft-R-I-03-3.5 Hz (a) Images and (b) Acceleration data Percentage Correction: Max: 77.93 %; Min: 80.71 %; Avg: 79.32 %.

Rigid Mounted With Isolator

(a)

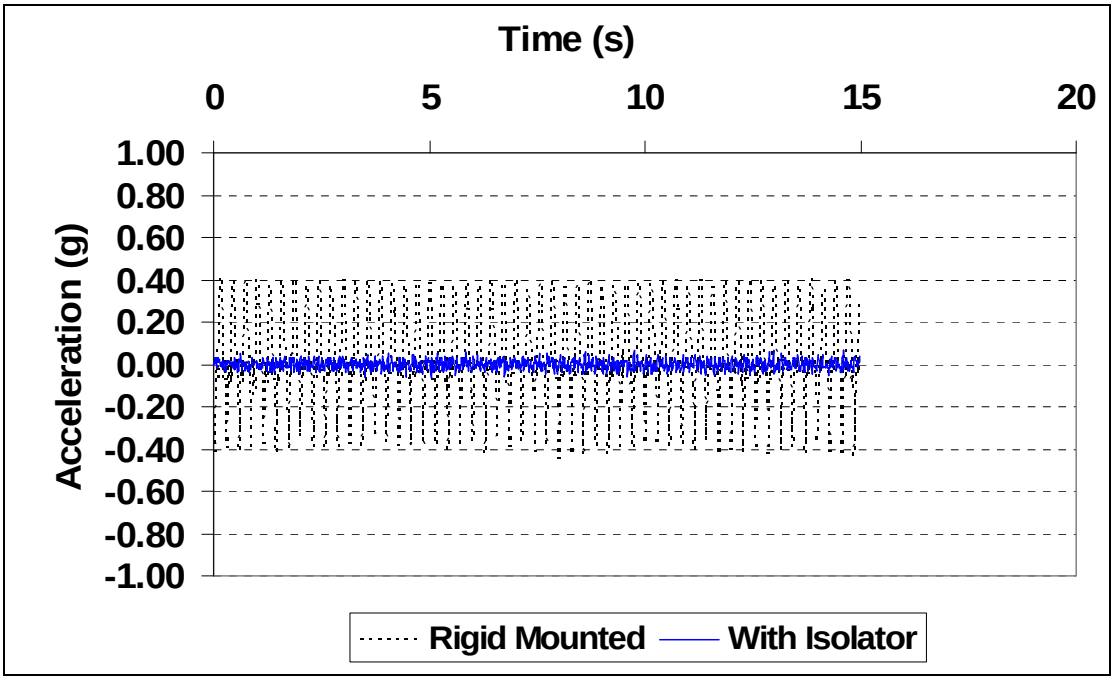

(b)

Figure E.31 Comparison between the uncorrected and corrected images for: Mode1-30ft-R-I-04-3.5 Hz (a) Images and (b) Acceleration data Percentage Correction: Max: 83.45 %; Min: 84.79 %; Avg: 84.12 %.

Rigid Mounted With Isolator

(a)

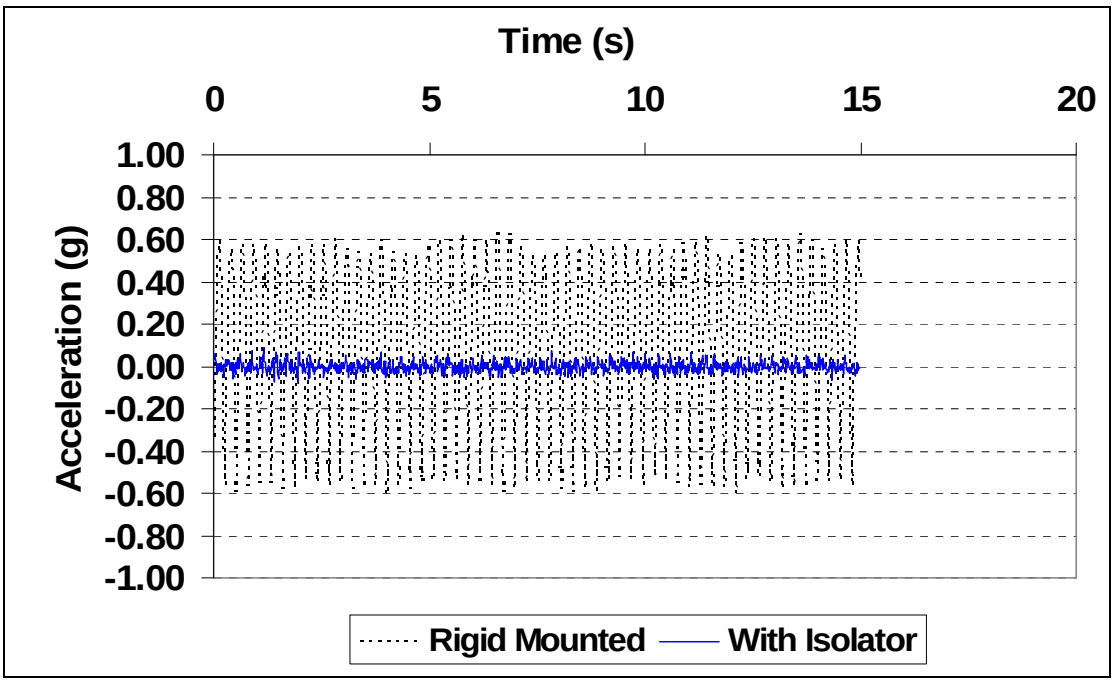

(b)

Figure E.32 Comparison between the uncorrected and corrected images for: Mode1-30ft-R-I-06-3.5 Hz (a) Images and (b) Acceleration data Percentage Correction: Max: 86.13 %; Min: 86.63 %; Avg: 86.38 %.

Rigid Mounted With Isolator

(a)

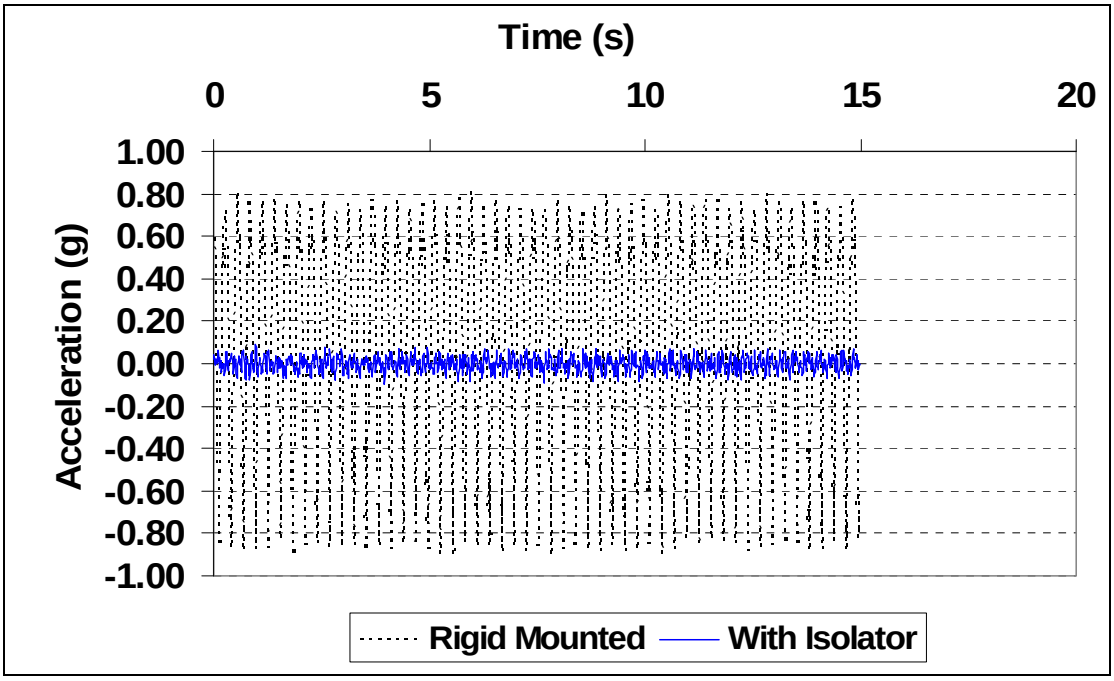

(b)

Figure E.33 Comparison between the uncorrected and corrected images for: Mode1-30ft-R-I-10-3.5 Hz (a) Images and (b) Acceleration data Percentage Correction: Max: 88.56 %; Min: 89.39 %; Avg: 88.98 %.

Rigid Mounted With Isolator

(a)

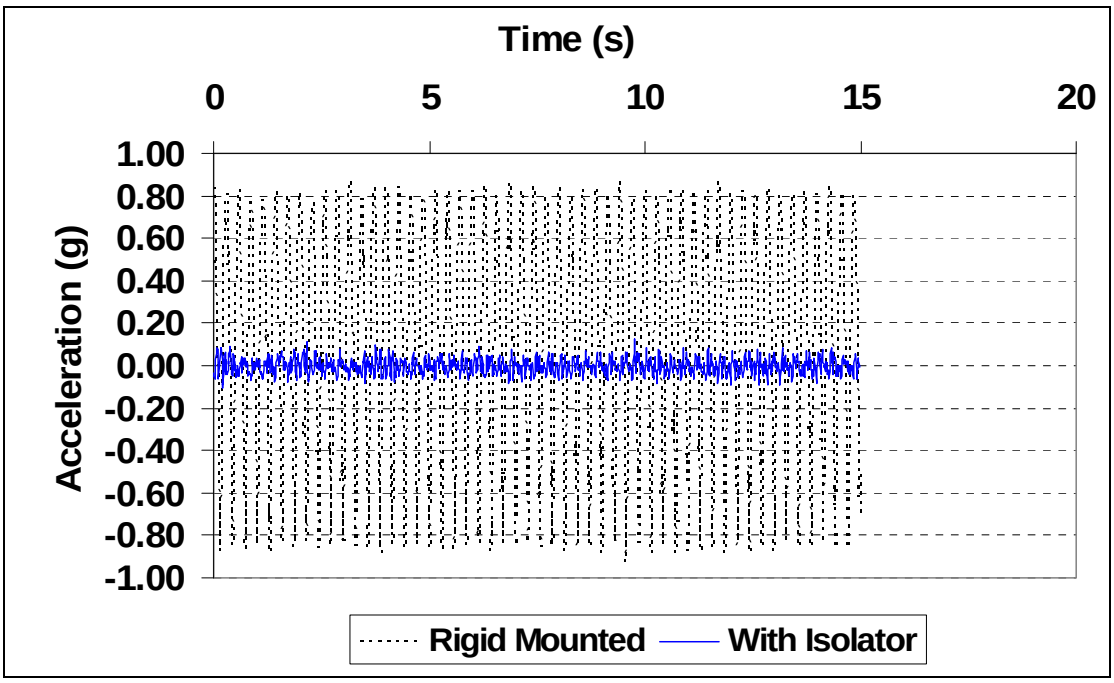

(b)

Figure E.34 Comparison between the uncorrected and corrected images for: Mode1-30ft-R-I-15-3.5 Hz (a) Images and (b) Acceleration data Percentage Correction: Max: 85.49 %; Min: 88.77 %; Avg: 87.13 %.

APPENDIX F

IMAGE CORRECTION OF ELECTRICAL DEVICE

Uncorrected Corrected

Figure F.1 60 ft pole-Amplitude =2mm- 0.94 Hz.

Uncorrected Corrected

Figure F.2 50 ft pole-Amplitude =2mm- 1.35 Hz.

Uncorrected

Corrected

Figure F.3 30 ft pole-Amplitude =1mm- 3.57 Hz.

Uncorrected

Corrected

Figure F.4 50 ft pole-Amplitude =2mm- 6.94 Hz.

REFERENCES

ABAQUS/Standard User's Manual version 6.6, Hibbit, Karlson & Sorenson, Pawtucker, RI, 2006.

ABAQUS/Standard User's Manual version 6.6, Hibbit, Karlson & Sorenson, Pawtucker, RI, 2007.

AISC (1980). Manual of steel construction, American Institute of Steel Construction ,Chicago, IL.

AISC (1999), Load and resistance factor design specification for structural steel building, American Institute of Steel Construction, Chicago, IL.

"RSI installs first modular composite utility pole." Reinforced Plastics, Vol. 49, No. 1, January 2005, p. 7.

Abolmaali, A., Matthys, J. H., Farooqi, M., and Choi, Y. (2003). "Development of moment-rotation model equations for flush end-plate connection." Journal of Constructional Steel Research, In Press, Corrected Proof, Available online 14 June 2005.

Abolmaali, A., Yuan, R. L., Choi, Y., and Shah, A. (2005). "Stiffness Characteristics of Closed Circuit Television Camera Steel Poles." Proceedings of the 84th Transportation Research Board Conference, January 9-13, on CD Rom.

Aref A.J.and Zaoyang Guo (2001). Framework for finite-element-based large increment method for nonlinear structural problems," Journal of Engineering Mechanics, 127(7), pp. 739-746.

Azizinamini, A. (1985). "Cyclic characteristics of bolted semi-rigid steel beam to column connections." Ph.D. thesis, University of South Carolina, Columbia.

Bahaari, M. R., and Sherbourne, A. N. (2000). "Behavior of eight-bolt large capacity endplate connections." Computers and Structures, Vol. 77, pp. 315-325.

Bathe, K. J. (1996). "Finite element procedures." Prentice-Hall, Upper Saddle River, NJ.

Battaini, M., Casciati, F., and Faravelli, L. (1998). "Fuzzy Control of Structural Vibration. an Active Mass System Driven by a Fuzzy Controller." Earthquake Engineering and Structural Dynamics, 27, 1267-1276.

Bursi O.S. and Jaspart J.P. (1997). "Benchmarks for finite element modeling of bolted steel connections." Journal of Constructional Steel Research, Vol 44, pp. 225-262.

Bursi, O. S., and Jaspart, J. P. (1998), "Basic Issues in the Finite Element Simulation of Extended End Plate Connections," Computers & Structures, Vol. 69, pp. 361-382.

Caracoglia, L., and Jones, N. P. (2005). "In-plane dynamic behavior of cable networks. Part 1: Formulation and basic solutions." Journal of Sound and Vibration, Vol. 279, No. 3-5, pp. 969-991.

Chen, W. F., and Han, D. J. (1988). "Plasticity for structural engineering." Springer-Verlag Publications, New York.

Choi, C. K., and Chung, G. T. (1996). "A gap element for three-dimensional elasto-plastic contact problems." Computers and Structures, Vol. 61, No. 6, pp. 1155-1167.

Chung, K. F., and Ip, K. H. (2001). "Finite element investigation on the structural behavior of cold-formed steel bolted connections." Engineering Structures, Vol. 23, pp. 1115-1125.

Chutima, S., and Blackie, A. P. (1996). "Effect of pitch distance, row spacing, end distance and bolt diameter on multi-fastened composite joints." Composites Part A, Vol. 27, Vol. 2, pp. 105-110.

Citipitioglu, A. M., Haj-Ali, R. M., and White, D. W. (2002). "Refined 3D finite element modeling of partially-restrained connections including slip." Journal of Constructional Steel Research, Vol. 58, pp. 995-1013.

Crisfield, M. A. (1997). "Non-linear Finite Element Analysis of Solids and Structures." John Wiley & Sons, New York.

Daniel, I. M., and Ishai, O. (2005). "Engineering Mechanics of Composite Materials." Second Edition, Oxford University Press.

Dicleli, M. (1997). "Computer-aided optimum design of steel Tubular telescopic pole structures." Computers and Structures, Vol. 62, No. 6, pp. 961-973.

Dyke, S. J., Spencer Jr, B. F., Sain, M. K., and Carlson, J. D. (1996a).“Experimental Verification of Semi-Active Structural Control Strategies Using Acceleration Feedback.” Third International Conference on Motion and Vibration Control, Chiba, Japan, 291-296.

Dyke, S. J., Spencer, B. F., Sain, M. K., and Carlson, J. D. (1996b). “Modeling and Control of Magnetorheological Dampers for Seismic Response Reduction.” Smart Materials and Structures, 5, 565-575.

Dyke, S. J., Spencer Jr, B. F., Sain, M. K., and Carlson, J. D. (1998). “An Experimental Study of MR Dampers for Seismic Protection.” Smart Materials and Structures, 7 (Special Issue on Large Civil Structures), 693-703.

Gantes, C. J., and Lemonis, M. E. (2003). “Influence of equivalent bolt length in finite element modeling of T-stub steel connections.” Computers and Structures, Vol. 81, pp. 595-604.

Gebbeken N., Rothert H. and Binder B. (1994). “On the Numerical Analysis of Endplate Connections.” J. of Constructional Engrg., Vol. 30 , 177-196.

Hassan, T., Zhu, Y. and Matzen, V.C. (1996). Simulation of Ratcheting in Straight Pipes Using ANSYS with an Improved Cyclic Plasticity Model. In Seismic Engineering, the 1996 ASME Pressure Vessels and Piping Conference, Montreal, Canada.

Housner, G.W., Bergman L.A., Caughey T.K., Chassiakos A.G. (1997). Structural control: past, present, and future,Journal of Engineering Mechanics, ASCE, 123(9): pp. 897-971

Hurrel P. (2000). “Good practice in modeling of pressure vessel bolted joints for stress and fatigue analysis.” Analysis of Bolted Joints, ASME, pp. 123–134

Ibrahim, S., Polyzois, D., and Hassan, S. K. (2000). “Development of glass fiber reinforced plastic poles for transmission and distribution lines.” Canadian Journal of Civil Engineering, Vol. 25, No. 2, pp. 850-858.

Ibrahim, S., and Polyzois, D. (1999). “Ovalization analysis of fiber-reinforced plastic poles.” Composite Structures, Vol. 45, pp. 7-12.

Jacobsen, L, and Ayre, R. (1958). “Engineering Vibrations,” McGraw Hill Publishing.

Jansen, L. M., and Dyke, S. J. (2000). “Semi-Active Control Strategies for MR Dampers: A Comparative Study.” Journal of Engineering Mechanics, 126(8), 795-803.

Johnson, E. A., Christenson, R. E., and Spencer Jr., B. F. (2001). "Smart Stay Cable Damping - Effects of Sag and Inclination." 8th International Conference on Structural Safety and Reliability (ICOSSAR'01), Newport Beach, CA.

Jung J., Abolmaali A., and Choi, Y. (2006). "Finite-Element Analysis of Tapered Steel and Fiber-Reinforced Plastic Bridge Camera Poles." J. Bridge Eng., 11(5), pp. 611-617.

Jung J. (2005). "Development of finite element method-based model equations for hollow tapered poles." Ph. D. Dissertation, University of Texas at Arlington, TX.

Kishi, N., and Chen, W. F. (1990). "Moment-rotation relations of semi-rigid connections with angles." Journal of Structural Engineering, ASCE, Vol. 116, No. 7, pp. 1813-1834.

Kishi, N., Ahmed, A., Yabuki, N., and Chen, W. F. (2001). "Nonlinear finite element analysis of top- and seat-angle with double web-angle connections." Structural Engineering and Mechanics, Vol. 12, No. 2, pp. 201-214.

Kocer, F. Y., and Arora, J. S. (1996). "Optimal design of steel transmission poles." Journal of Structural Engineering, November, pp. 1347-1356.

Kocer, F. Y., and Arora, J. S. (1997). "Standardization of steel pole design using discrete optimization." Journal of Structural Engineering, March, pp. 345-349.

Komuro, M., and Kishi, N. (2003). "Quasi-static loading tests on moment-rotation behavior of top- and seat-angle connections." STESSA Conference, pp. 329-334.

Krishnamurthy, N., Huang, H. T., Jefferey, P. K., and Avery, L. K. (1979). "Analytical M-θ Curves for End-Plate Connections." Journal of Structural Engineering. ASCE, Vol. 105, No. ST1, pp. 133-145.

Krishnamurthy, N. (1980). "Modeling and prediction of steel bolted connection behavior." Computers and Structures, Vol. 11, pp. 75-82.

Krishnamurthy N., Krishna V.R.. (1981). "Behavior of splice–plate connections with multiple bolt rows". Report submitted to the Metal Building Manufacturers Association.

Kukreti, A.R., and Abolmaali, A. (1998). "Moment-Rotation Hysteresis Models for Top and Seat Angle Semi-Rigid Connections," Proceedings of the XIX Southeastern Conference on Developments in Theoretical Mechanics, Vol. XIX, College of Engineering, Florida Atlantic University, Boca Raton, Florida, May 3-5, pp. 235-245.

Kukreti, A.R., Murray, T.M., and Abolmaali, A. (1984). "Finite Element Analysis of Two Tension Bolt Flush End-Plate Connections," Project Report FSEL/MBMA 87-02, School of Civil Engineering and Environmental Science, University of Oklahoma, Norman, Oklahoma, July 1984, 233 pages, submitted to the Metal Building Manufacturers Association.

Kulak, G. L., and Birkemoe, P. C. (1993). "Field studies of bolt pre-tension." Journal of Steel Research, Vol. 25, pp. 95-106.

Kuruta, N., Kobori, T., Takahashi, M., Niwa, N., and Midorikawa, H. (1999). Actual Seismic Response Controlled Building with Semi-Active Damper System." Earthquake Engineering and Structural Dynamics, 28, 1427-1447.

Kuruta, N., Kobori, T., Takahashi, M., Ishibashi, T., Niwa, N., Tagami, J., and Midorikawa, H. (2000). "Forced Vibration Test of a Building with Semi-Active Damper System." Earthquake Engineering and Structural Dynamics, 29, 629- 645.

Lacoursiere, B. (1999). "Steel utility poles: Advantages and application." IEEE Conference Paper, No. 99B2.

Lin, Z. M. (1995). "Analysis of pole-type structures of fiber-reinforced plastics by finite element method." Ph.D. Dissertation, University of Manitoba, Canada.

McClure, G., Boire, L., and Carriere, J. C. (1992). "Applications of advanced composite materials in overhead power lines and telecommunications structures." Advanced Composite in Bridges and Structures, First International Conference, pp. 543-549.

McDonald, J. R., Mehta, K. C., Oler, W. W., and Pulipaka, N. (1995). "Wind load effects on signs, luminaries and traffic signal structures." Texas Tech University Research Study, Lubbock, Texas, No. 11-5-92-1310.

Mofid M., Ghorbani Asl M., McCabe S.L. (2001). "On the analytical model of beam-to-column semi-rigid connections, using plate theory." Thin-Walled Structures, Vol. 39, pp. 307-325

Morozov, E. V. (2004). "Mechanics and analysis of fabric composites and structures." AUTEX Research Journal, Vol. 4, No. 2, pp. 60-71.

Oldfield, M., Ouyang, H., and Mottershead, J. (2003). "Modeling and simulation of bolted joints under harmonic excitation." Materials Science Forum, Vol. 440-441, pp. 421-428.

Pagnini, L. C., and Solari, G. (2001). “Damping measurements of steel poles and tubular structures.” Engineering Structures, Vol. 23, pp. 1085-1095.

Patten, W. N., Sun, J., Li, G., Kuehn, J., and Song, G. (1999). “Field Test of an Intelligent Stiffener for Bridges at the I-35 Walnut Creek Bridge.” Earthquake Engineering and Structural Dynamics, 28, 109-126.

Polyzois, D., Ibrahim, S., and Raftoyiannis, I. G. (1999). “Performance of fiber-reinforced plastic tapered poles under lateral loading.” Journal of Composites Materials, Vol. 33, No. 10, pp. 941-960.

Polyzois, D., Raftoyiannis, I. G., and Ibrahim, S. (1998). “Finite elements method for the dynamic analysis of tapered composite poles.” Composite Structures, Vol. 43, pp. 25-34.

Raj, N. S., Dattaguru, B., Krishnamurthy, T., and Ramamurthy, T. S. (1987). “Analysis of flange joints with elastic bolt.” Nuclear Engineering Design, Vol. 100, pp. 41-48.

Ramallo, J. C., Johnson, E. A., and Spencer Jr., B. F. (2002). “"Smart" Isolation for Seismic Control.” Journal of Engineering Mechanics, 128(10), 1088-1099.

Razavi, H., Abolmaali, A., and Ghassemieh, M. (2006). “Invisible Elastic Bolt Model Concept for Finite Element Analysis of Bolted Connections.” Journal of Constructional Steel Research, Vol. 63, No. 5, pp. 647-657.

Richard, R. M. and Abbott, B. J., (1975). “Versatile elastic-plastic stress-strain formula.” Journal of the Engineering Mechanics Division, ASCE, Vol. 101, No. EM4, pp. 511-515.

Richard, R. M., Gillet, P. E., Kriegh, J. D., and Lewis, B. A. (1980). “The analysis and design of single plate framing connections.” AISC Engineering Journal, Second Quarter, pp. 38-52.

Rothert, H., Gebbeken, N. and Binder, B., 1992. “Non-linear three-dimensional finite element contact analysis of bolted connections in steel frames”. Int. J. Numer. Meth. Engng. Vol. 34, pp. 303–318.

Sherbourne, A. N., and Bahaari, M. (1994). “Finite element prediction of end plate bolted connection behavior. I: Parametric Study.” Journal of Structural Engineering, Vol. 123, No. 2, pp. 157-164.

Solberg, J. M., and Papadopoulos, P. “A finite element method for contact/impact.” Finite Elements in Analysis and Design, Vol. 30, pp. 297-311.

Sommer, W. H. (1969). “Behavior of welded-header-plate connections.” M. S. Thesis, University of Toronto.

Soong, T. T., and Spencer Jr., B. F. (2002). “Supplemental Energy Dissipation: State-of-the-Art and State-of-the-Practice.” Engineering Structures, 24, 243- 259.

Soong T.T., and Dargush G.F. (1997). “Passive energy dissipation systems in structural engineering”, Wiley, New York

Spencer Jr., B. F., and Soong, T. T. (1999).“New Applications and Development of Active, Semi-Active and Hybrid Control Techniques for Seismic and Non-Seismic Vibration in the USA.” International Post-SMiRT Conference Seminar on Seismic Isolation, Passive Energy Dissipation and Active Control of Vibration of Structures, Cheju, Korea.

Statik, H., Gebeken, N., and Binder, B. (1992). “Nonlinear three dimensional finite element contact analysis of bolted connections in steel frames.” International Journal of Numerical Methods in Engineering, Vol. 34, No. 11, pp. 3122-3136.

Stallings, J. M., and Hwang, D. Y. (1992). “Modeling pre-tensions in bolted connections.” Computers and Structures, Vol. 45, No. 4, pp. 801-803.

Swanson J.A., Kokan D.S., Leon R.T. (2002). “Advanced finite element modeling of bolted T-stub connection components.” Journal of Constructional Steel Research, Vol. 58, pp. 1015–1031.

Symans, M. D., Constantinou, M. C., Taylor, D. P., and Garnjost, K. D. (1994). “Semi-Active Fluid Viscous Dampers for Seismic Response Control.” First World Conference on Structural Control, Los Angeles, CA, FA4-3 - FA4-12.

Symans, M. D., and Constantinou, M. C. (1999). “Semi-active Control Systems for Seismic Protection of Structures: a State-of-the-Art Review.” Engineering Structures, 21, 469-487.

Tsai, S. W., and Wu, E. M. (1971). “A general theory of strength for anisotropic material.” Journal of Composites Materials, Vol. 5, pp. 58-80.

Vanderbilt, M. D., and Criswell, M. E. (1988). “Analysis and design of single-pole transmission structures.” Computers and Structures, Vol. 28, No. 4, pp. 551-562.

Wanzek, T., and Gebbeken, N. (1999). “Numerical aspects for the simulation of end plate connections.” Report of Working Group 6 – Numerical simulation of semi-rigid connections by the finite element method, Brussels, Luxembourg, pp. 13-31.

Yang, J. G. (1997). “Double angle framing connections subjected to shear and tension.” Ph. D. Thesis, Virginia Polytechnic Institute and State University, Blacksburg, VA.

Yang, J. G., Murray, T. M., and Plaut, R. H. (2000). “Three-dimensional finite element analysis of double angle connections under tension and shear.” Journal of Constructional Steel Research, Vol. 54, pp. 227-244.

Yang, G. (2001). “Large-Scale Magnetorheological Fluid Damper for Vibration Mitigation: Modeling, Testing and Control,” Dissertation, University of Notre Dame, Notre Dame, Indiana.

Yee, Y. L., and Melchers, R. E. (1986). “Moment-rotation curves for bolted connections.” Journal of Structural Engineering, ASCE, Vol. 112, No. ST3, pp. 615-635.

Yi, F., and Dyke, S. J. (2000). “Performance of Smart Structures.” Proceedings of SPIE - The International Society for Optical Engineering, Newport Beach, CA, pp. 94-104.

Yorgun, C., Dalc1, S., and Altay, G. A. (2004). “Finite element modeling of bolted steel connections designed by double channel.” Computers and Structures, Vol. 82, pp. 2563-2571.

Yoshioka, H., Ramallo, J. C., and Spencer Jr., B. F. (2002). “"Smart" Base Isolation Strategies Employing Magnetorheological Dampers.” Journal of Engineering Mechanics, 128(5), 540-551.

Youssef, N. F. G., Bonowitz, D., and Gross, J. L. (1995). A survey of steel moment-resisting frame buildings affected by the 1994 Northridge earthquake. Report No. NISTIR 5625, National Institute of Standards and Technology, US Department of Commerce.

Zadoks R I., Kokatam D.P.R. (2001). “Investigation of the axial stiffness of a bolt using a three-dimensional finite element model” Journal of Sound and Vibration, 2001, 246(2), pp. 349-373.

BIOGRAPHICAL INFORMATION

Tri Dai Le was born October 20, 1980 in Tien Giang province, Vietnam to Thanh Nguyen and Liet Le. He spent his childhood in a peaceful countryside in Mekong delta where he finished high school in 1997. Then he moved to Hochiminh, the largest and most crowded city in Vietnam, for his bachelor degree in Civil Engineering at the University of Technology, one of the famous universities in Vietnam. He graduated in 2002. Right after graduation, he worked for a state owned company for six months as a technician staff member who estimated building cost and prepared documents for tender. After that he worked for a British company, Atlas Co.Ltd., where he worked for 18 months as an AutoCAD detailer. Tri became an expert in detailing precast panels, reinforced slab and retaining wall drawings. In January 2004, he entered the graduate program in Structural and Applied Mechanics at the University of Texas at Arlington (UTA) where he completed his Master degree in August 2005 and Doctor of Philosophy in Civil Engineering with the minor field of finite element modeling in May 2008. Under the supervision of Dr. Ali Abolmaali, Tri Le has four papers published and two under reviewed. Tri Le was offered the Post Doctoral research position at UTA; he will start his job in May 2008.